The Chemical Evolution of Chondrite Components: Implications for Mixing in the Solar Nebula

Sanjana Sridhar

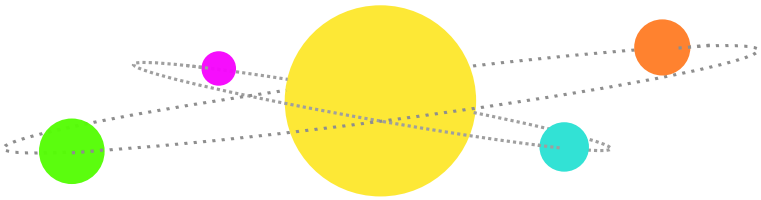

A thesis submitted for the degree of
Doctor of Philosophy

Department of Earth Sciences
University of Oxford

January 2025

Abstract

Chondrites provide invaluable insight into the conditions present in the early protoplanetary disk. In this study, the coupled ε^{54}Cr compositions and plateau volatile element concentrations of various non-carbonaceous (NC) and carbonaceous (CC) chondrites were measured to investigate the mechanisms of planetesimal accretion throughout the solar system. A new subsampling method was utilised to determine the ε^{54}Cr compositions of chondrules and matrix present in each chondrite group.

Ordinary chondrites contain chondrules and matrix that display similar ε^{54}Cr compositions, implying that they form from local material and reflect limited mixing in the inner solar system. Rumuruti (R) chondrites display higher average ε^{54}Cr compositions, though their chondrule and matrix compositions were difficult to determine. This higher ε^{54}Cr value indicates that R chondrites accrete with small fractions of CC-like material, likely due to their accretion in the outer regions of the inner disk, close to the NC/CC barrier.

CC chondrites accrete in the outer solar system. CO, CM, CV, and C2-Ung chondrites share a similar average chondrule composition, and exhibit CI-like matrix compositions. This implies that CC groups form from varying mixtures of isotopically distinct chondrules and CI-like matrix, and groups that exhibit higher matrix proportions display correspondingly higher ε^{54}Cr compositions. CR chondrites may have initially formed in a similar manner but were then subjected to reprocessing which formed a population of chondrules with higher ε^{54}Cr compositions. These chondrules mixed with CI-like dust, and additional chondrules that are isotopically similar to those observed in other CC groups, to form the CR parent body. Accretion of isotopically distinct chondrules and matrix implies that the CC chondrites accrete from solids sourced from different regions of the outer solar system. Both inward and outward migration of chondritic components are required to produce the CC chondrite parent bodies. These motions imply widespread mixing of solids in the outer solar system to form the CC chondrites, contrary to what is observed in the inner solar system, indicating distinct dynamic environments across the protoplanetary disk.

Acknowledgements

This PhD would not have been possible without the support and guidance of the people I have met over the last four years. These have been the hardest, and yet most rewarding years of my life, and I owe thanks to everyone listed below who has helped me through this process.

First of all, I would like to thank my supervisor James Bryson for developing this project and allowing me the opportunity to conduct research in a field that I love. His unwavering support throughout the course of the PhD was invaluable and greatly appreciated, and I have become a better scientist, critical thinker, and writer because of his efforts. I would also like to thank my supervisor Jon Wade for his guidance during this project, the interesting chats, and for his help in securing additional funding when needed. Thank you also to Greg Brennecka and Jan Render, who I consider as my supervisors in all but name, I will always be grateful for the opportunity they provided me to work at LLNL whilst the labs were shut in Oxford, and appreciate the kindness and hospitality they showed me whilst I was there. They have provided invaluable assistance every time I have had questions, and helped talk over my issues from afar whenever I have been stumped.

This project would not have been possible without the guidance and knowledge provided by Jane Barling. I am exceedingly grateful for the time and effort she dedicated in teaching me how to use the clean labs and helping me troubleshoot my column chemistry the many (many) times it failed. I also have to thank Nick Belshaw for helping me understand the mechanics of the TIMS, and for his continual support in ensuring the instrument kept working throughout the course of my PhD. I would like to thank Pierre Bonnand for helping me set up the dynamic run on the TIMS, and Tim Elliot and the researchers at

Bristol for helping organise alternative arrangements when they were needed. Thank you to Phil Holdship for teaching me how to use the Quad and for his patience in allowing me so much instrument time during the endless period of developing the column chemistry. I am also grateful to Darren Hillegonds for teaching me how to use the noble gas mass spectrometer during my brief foray into noble gas isotopes, and since then providing a sympathetic ear and second set of eyes when I was running into issues with the TIMS. Thank you to James King for lending me equipment from the workshop, helping me fix the degasser, and always providing support and dog therapy when needed! I also have to thank Claire Nichols for her endless moral support throughout the whole PhD process. Allowing me to demonstrate on the Assynt field course and get back out into the field helped re-establish my passion for this subject when times were difficult.

The development of the column chemistry and measurement of Cr isotopes would not have been possible without the help of many researchers who kindly took the time to discuss their methodology with me. These people include Ke Zhu, Elishevah van Kooten, and especially Zack Torrano. I am grateful for all the knowledge and tips they provided me that eventually helped me to develop a working protocol.

Thank you also to my examiners, Alex Halliday and Yves Marrocchi, for taking the time to read this work, and for the enjoyable discussion and insightful comments during my viva.

The friends I've made during the course of this PhD have been equally important in making the last few years so enjoyable. To Susie, Bei Bei, and Vikki, I'm so glad we all met at the beginning of our PhDs and words can't express how grateful I am to know you. These last four years have been some of the best thanks to your friendship, unending support, and willingness to take me on some much needed adventures! Hannah, Rebecca, Sjef, Emily, Biao, Ian, Toby, Ronnie, and Fish, I'm so happy we met over the course of the PhD - thank you for your kindness and support, chats over coffee, adventures in the field, and escapes to the climbing wall. The PhD was more enjoyable for knowing you all. Madeline, Lewis, Lot, and Vicky, thank you for being the best clean lab gang, and for providing moral support throughout the adventure that is isotope geochemistry. To Richard and Annika, I'll always be grateful to you for making me feel so welcome in office

20.16 when I first joined, and to Adam, Miguel, Dongwoo, Ed, and Red, thank you for making the office a pleasure to come into every day! I would also like to thank all the interns and staff at LLNL that helped make my visit so enjoyable, especially Ade and Autumn, for showing me all that California had to offer!

Finally I would like to thank my family and friends at home for their continuous support throughout this process. Thank you for visiting me here at Oxford, and for letting me escape for a few days to enjoy life outside this bubble. This would not have been possible without your help.

Contents

1 Introduction **1**

1.1 General background 1

1.1.1 Formation of the Solar System 1

1.1.2 Extraterrestrial sample material 3

1.1.3 Chondrites 5

1.1.4 Nucleosynthetic anomalies in the solar system 8

1.1.5 A bifurcated disk 11

1.2 Aim of this study 15

1.3 Thesis outline 20

2 Methods **23**

2.1 Sample preparation 23

2.1.1 Novel subsampling procedure 23

2.1.2 Sample selection 25

2.1.3 Sample digestion 26

2.2 Chromium separation 27

2.2.1 Theory 27

2.2.2 Column 1 29

2.2.3 Column 2 30

2.2.4 Columns 3 & 4 30

2.2.5 Column 5 31

2.2.6 Column chemistry elution curves 33

2.3 Analytical methods 36

2.3.1 Chromium Isotopic measurements: Thermal Ionisation Mass Spectrometry . . . 36
2.3.2 Plateau Volatile Element concentrations and column yields: Quadrupole ICP-MS . . . 44
2.3.3 Determination of matrix volume fraction . . . 44
2.3.4 Determination of matrix mass fraction . . . 46
2.4 Mixing line . . . 48

3 Accretion in the non-carbonaceous reservoir 51
3.1 Introduction . . . 51
3.1.1 Background . . . 51
3.1.2 This work . . . 55
3.2 Methods . . . 57
3.3 Results . . . 59
3.3.1 LL chondrite LoV 171 chemical and isotopic composition . . . 59
3.3.2 Mixing line through LL chondrite LoV 171 . . . 62
3.3.3 R chondrite MIL 07440 chemical and isotopic composition . . . 63
3.3.4 Mixing line through R chondrite MIL 07440 . . . 66
3.4 Discussion . . . 67
3.4.1 Ordinary chondrites . . . 67
3.4.2 R chondrites . . . 74
3.4.3 Comparison of formation of the R chondrites and OCs . . . 80
3.4.4 Pebble vs planetesimal accretion and the NC/CC barrier . . . 81
3.5 Conclusions . . . 83

4 Formation of the carbonaceous chondrite parent bodies 85
4.1 Introduction . . . 85
4.1.1 Background . . . 85
4.1.2 This work . . . 90
4.2 Methods . . . 91
4.3 Results . . . 93
4.3.1 CO: Chemical and isotopic composition . . . 93

4.3.2 CO: Mixing line . . . 94
4.3.3 Allende: Chemical and isotopic composition . . . 95
4.3.4 Allende: Mixing line . . . 96
4.3.5 CM: Chemical and isotopic composition . . . 97
4.3.6 CM: Mixing line . . . 98
4.3.7 Tarda: Chemical and isotopic composition . . . 99
4.3.8 Tarda: Mixing line . . . 100
4.3.9 CO, CM, CV, C2-Ung Mixing line . . . 105
4.3.10 Subsample composition vs mass . . . 106
4.4 Discussion . . . 108
4.4.1 Composition of bulk chondrites . . . 108
4.4.2 ε^{54}Cr compositions of chondrules and matrix . . . 110
4.4.3 Formation of the CC parent bodies . . . 116
4.4.4 Dynamics of solid transport in the CC reservoir . . . 118
4.5 Conclusions . . . 121

5 Accretionary history of the CR chondrites 123
5.1 Introduction . . . 123
5.1.1 Background . . . 123
5.1.2 This work . . . 126
5.2 Methods . . . 127
5.3 Results . . . 128
5.3.1 MIL 090001 chemical and isotopic composition . . . 128
5.3.2 Mixing line . . . 131
5.4 Discussion . . . 134
5.4.1 Bulk composition . . . 134
5.4.2 ε^{54}Cr composition of chondrules and matrix . . . 135
5.4.3 Isotopic evidence for different chondrule populations . . . 136
5.4.4 Evidence of reprocessing and an initial CR reservoir . . . 137
5.4.5 Formation of the CR parent body . . . 141
5.5 Conclusions . . . 145

6 Synthesis **147**

6.1 Summary 147

6.2 Suitability of the subsampling method 150

6.3 Chondrite formation and solid dynamics in the inner and outer solar system 153

6.4 Formation of the CC chondrites vs CR chondrites: changing conditions over time 160

7 Conclusions **163**

List of Figures

1.1 Planetesimal vs Pebble accretion 2
1.2 Chondrite components 5
1.3 ε^{50}Ti variations within bulk chondrites and their chondritic components . 10
1.4 Plots of ε^{54}Cr vs ε^{50}Ti and ε^{95}Mo vs ε^{94}Mo displaying the isotope dichotomy 12
1.5 Plots displaying the PVE concentrations in chondrites and their relationship to matrix volume and mass fraction 16
1.6 Zn concentration (normalised to CI) plotted against ε^{54}Cr composition of chondrites in the inner and outer solar system 18

2.1 Subsampling procedure 24
2.2 Elution curves for column chemistry procedure to purify Cr 35
2.3 Measured ε^{54}Cr compositions of unprocessed and processed standard NIST-979 40
2.4 NIST-979 standard compositions from static and dynamic runs on the TIMS 41
2.5 Processed standard values compared to those reported in the literature . . 42
2.6 ε^{54}Cr compositions of CR chondrite MIL 090001 subsamples measured at the University of Oxford and LLNL 43
2.7 BSE and SE images of different CM chondrite subsamples used to determine matrix proportions 45

3.1 Planetesimal vs pebble accretion in the inner solar system 53
3.2 Bulk ε^{54}Cr and Zn compositions of NC and CC chondrites 55
3.3 ε^{54}Cr vs matrix fractions of subsamples of OC LoV 171 59
3.4 LL LoV 171 subsample mass plotted against Zn and ε^{54}Cr compositions . 60

3.5 Isotopic mixing line through subsamples of LL LoV 171 62
3.6 ε^{54}Cr vs matrix fractions of subsamples of R MIL 07440 63
3.7 R MIL 07440 subsample mass plotted against Zn and ε^{54}Cr compositions 64
3.8 Isotopic mixing line through subsamples of R MIL 07740 66
3.9 Bulk composition of LL LoV 171 67
3.10 Comparison of recovered LoV 171 chondrule ε^{54}Cr compositions to literature values 69
3.11 Mechanism of OC accretion 71
3.12 Isotopic mixing line through bulk OCs and K chondrites 73
3.13 Average ε^{54}Cr and Zn composition of MIL 07440 75
3.14 Plot displaying the PVE concentrations in NC chondrites 77
3.15 Recovering R chondrite compositions through mixing of OC chondrules and CI chondrites 78
3.16 Mechanism of R chondrite accretion 79

4.1 CC group classifications 86
4.2 Mixing line plot through the ε^{54}Cr compositions and CI-normalised Zn concentrations of bulk CC chondrites 87
4.3 ε^{54}Cr vs matrix fractions of subsamples of CO DOM 08006 93
4.4 Isotopic mixing line through subsamples of CO DOM 08006 94
4.5 ε^{54}Cr vs matrix fractions of subsamples of CV Allende 95
4.6 Isotopic mixing line through subsamples of CV Allende 96
4.7 ε^{54}Cr vs matrix fractions of subsamples of CM NWA 11345 97
4.8 Isotopic mixing line through subsamples of CM NWA 11345 98
4.9 ε^{54}Cr vs matrix fractions of subsamples of C2-Ung Tarda 99
4.10 Isotopic mixing line through subsamples of C2-Ung Tarda 100
4.11 Isotopic mixing line through subsamples of CO DOM 08006, CV Allende, CM NWA 11345, and C2-Ung Tarda 105
4.12 Matrix volume fractions and ε^{54}Cr compositions of CC subsamples plotted against their mass 107

4.13 Bulk ε^{54}Cr compositions and CI-normalised Zn concentrations of CO DOM 08006, CV Allende, CM NWA 11345, and C2-Ung Tarda 109
4.14 CC chondrule ε^{54}Cr compositions 111
4.15 Comparison of mixing line through CC chondrite groups generated from this study with the mixing line proposed in previous literature 114
4.16 Variation in chondrule and matrix fractions observed in different CC chondrite groups 116
4.17 Formation of CC chondrules and accretion of the CC chondrite parent bodies 119

5.1 ε^{50}Ti vsε^{54}Cr and matrix volume fraction of CC chondrites 124
5.2 Average ε^{54}Cr compositions of CC chondrite groups and CR and CC chondrules 125
5.3 ε^{54}Cr vs matrix fractions of subsamples of CR MIL 090001 128
5.4 CR MIL 090001 subsample mass plotted against Zn and ε^{54}Cr compositions 129
5.5 Isotopic mixing line through subsamples of CR MIL 090001 131
5.6 Isotopic mixing line through subsamples of CR MIL 090001, Al Rais, and GRO 95577 133
5.7 Average composition of MIL 090001 compared to literature data 134
5.8 Composition of the initial CR reservoir 139
5.9 ε^{50}Ti plotted against updated CR chondrite matrix volume fraction 141
5.10 Mechanism of CR parent body accretion 142
5.11 Chondrite accretion age plotted against updated CR chondrite matrix volume fraction 143

6.1 Summary of NC and CC chondrite formation on a plot of ε^{54}Cr compositions against CI-normalised Zn concentrations 148
6.2 Summary of CR chondrite formation on a plot of ε^{54}Cr compositions against CI-normalised Zn concentrations 149
6.3 Effect of subsample size on recovery of chondrule and matrix compositions 152
6.4 Locations of accretion of NC and CC chondrites in the protoplanetary disk 157

List of Tables

2.1 List of samples 25
2.2 Column chemistry procedure: Column 1 29
2.3 Column chemistry procedure: Column 2 30
2.4 Column chemistry procedure: Columns 3 and 4 31
2.5 Column chemistry procedure: Column 5 32
2.6 Cup configuration for TIMS measurements 37
2.7 Bulk and grain density of chondrites groups used to calculate matrix mass fraction of subsamples 47

3.1 ε^{54}Cr compositions and PVE concentrations of OC LoV 171 subsamples . 61
3.2 Matrix volume and mass fractions of OC LoV 171 subsamples 61
3.3 ε^{54}Cr compositions and PVE concentrations of R MIL 07440 subsamples . 65
3.4 Matrix volume and mass fractions of R MIL 07440 subsamples 65

4.1 ε^{54}Cr compositions and PVE concentrations of all CC chondrite subsamples 102
4.2 Matrix volume and mass fractions of all CC chondrite subsamples 103
4.3 Matrix area fractions of CM chondrite subsamples derived from SEM images 104
4.4 Inferred chondrule, matrix, RI abundances in CC groups 117
4.5 Measured bulk, chondrule, and matrix compositions of CC chondrites . . . 121

5.1 ε^{54}Cr compositions and PVE concentrations of CR MIL 090001 subsamples 130
5.2 Matrix volume and mass fractions of CR MIL 090001 subsamples 130

6.1 Average chondrule diameters in NC and CC chondrites 151

7.1 Measured bulk, chondrule, and matrix compositions of NC and CC chondrites165

Chapter 1

Introduction

1.1 General background

1.1.1 Formation of the Solar System

Our solar system formed ∼4.6 billion years (Ga) ago through the gravitational collapse of an interstellar molecular cloud. At the centre of this cloud, compressional forces caused compaction and heating, leading to the formation of a protostar - our Sun. To conserve angular momentum of this rotating, collapsing cloud of dust and gas, a flattened accretionary protoplanetary disk formed around the proto-sun. This model, the nebula hypothesis, remains the most widely accepted theory for the formation of the solar system.

The protoplanetary disk is thought to have lasted approximately 3 - 10 million years (Ma) before its dissipation by photoevaporative stellar winds (Alexander et al., 2014). Soon after the disk formed and started to cool, the first solids began to condense at temperatures of ∼1400 K. These solids are highly refractory objects (called calcium aluminium-rich inclusions (CAIs)) that record of the age of the solar system. As the disk slowly cooled and dust continued to condense out and settle in the mid-plane, these particles experienced extensive radial mixing and transport. Volatile depleted solids formed at distances closer to the Sun, while solids with ice accreted at further distances beyond the ice line (∼3 AU), where the disk was colder (Morbidelli et al., 2021).

Various models have been proposed to explain the formation of the inner terrestrial planets

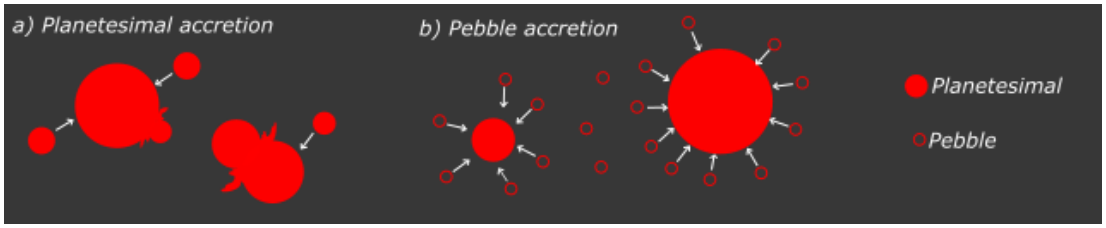

Figure 1.1: Schematic depicting the mechanisms of planetesimal and pebble accretion. Planetesimals models favour large impacts between planetesimal-sized bodies and pebble accretion involves the accretion of small, pebble-sized objects onto a growing planetesimal. Not to scale.

and the gas and ice giants that inhabit the outer solar system. The two prevailing theories for terrestrial planet formation include pebble accretion and planetesimal accretion (Fig. 1.1). During pebble accretion, 100 km sized planetesimals are modelled to have formed by the collapse of self gravitating clumps of pebbles via the streaming instability (Youdin and Goodman, 2005; Johansen et al., 2021). In this scenario, pebbles are solids whose movements are marginally coupled to the gas in the protoplanetary disk by viscous drag. Pebbles are often linked to small, millimetre-centimetre sized objects in the inner solar system (e.g., chondrules, see subsection 1.1.3). The streaming instability facilitates the spontaneous concentration of dust due to gas drag, and requires an enhanced dust-to-gas ratio in the protoplanetary disk (approximately unity) (Youdin and Goodman, 2005). These conditions could arise within the rings of protoplanetary disks (Drazkowska et al., 2022).

The planetesimal accretion model relies on gravitational focusing effects to collide successively larger planetesimals to form planets. The formation of the initial planetesimals are facilitated by the streaming instability. In this framework, the efficiency of planetesimal formation decreases as the planetesimal gets larger and also reduces with increasing distance from the star. Due to this, it is hard to form larger planetary cores beyond the snow line within the lifetime of the disk, meaning that the planetesimal accretion model struggles to replicate the formation of gas giants. The pebble accretion model also encounters difficulties with rapid formation of planetary cores due to the assumed reduction in pebble flux in the outer solar system, however, this can be overcome under specific conditions (e.g., enhanced dust-to-gas ratios formed by photoevaporation of the disk, or ring-like substructures acting as particle traps). An important distinction between pebble

and planetesimal accretion lies in the provenance of the material accreted onto the planet. Planetesimal accretion involves bodies local to the region, while pebble accretion samples a larger feeding zone as pebbles are smaller and are subject to more radial drift.

The outer envelopes of gas and ice giants are thought to form in the outer disk either through gravitational instability (the instantaneous gravitational collapse of clumps of gas) (Drazkowska et al., 2022) or via core formation followed by increasingly rapid gas accretion as the planets mass increases. Both models enable large planetary cores to form and accrete a gaseous envelope before the gas in the disk dissipated (Meech and Raymond, 2019). During the rapid gas accretion phase, the orbits of nearby planetesimals are disrupted and these objects can be scattered inwards into the feeding zone of planetesimals in the inner solar system.

All models of planetesimal formation broadly match what has been observed around circumstellar disks, as many display rings where the first asteroids and protoplanets are proposed to be accreting (Drazkowska et al., 2022). However, problems relating to timing and efficiency still arise in all scenarios, and the efficacy of each model is highly dependent on the dust-to-gas ratio, mass flux, viscosity, and turbulence of the disk at the time - all parameters which are currently poorly constrained.

Identifying the governing mechanisms of planet formation would therefore provide invaluable information on the dynamical evolution of our solar system, and the physical and chemical properties of planets and asteroids we see today. This is because different planet formation scenarios could sample compositionally distinct material from different regions of the solar system (local vs "global" sampling in the case of planetesimal vs pebble accretion). To better constrain models of planetesimal formation (and therefore disk evolution) we need to understand how and where solids formed in our solar system, and their histories of mixing, transport, and accretion.

1.1.2 Extraterrestrial sample material

We have limited resources to help us understand the evolution of our own solar system; for the last few decades the only samples in our collections that were recovered in-situ are materials from the Earth and the Moon. However, due to recent sample return missions,

we also have samples from near-earth asteroids Ryugu, Bennu, and Itokawa. Studying the chemical and isotopic composition of these samples allows us to infer the accretionary history of these bodies and their provenance, granting insight into their approximate formation locations and conditions in the protoplanetary disk. This allows us to start deciphering the dynamic history of our solar system.

Meteorites can also provide us with an important record of the material present in the early protoplanetary disk, which went on to form the large asteroids and planets observed in our solar system today. The majority of the meteorite samples in our collections are thought to originate from asteroids located in the asteroid belt, currently situated between the orbits of Mars and Jupiter at 2 - 3 AU. These samples have been linked to objects populating the asteroid belt by comparison of their spectral properties (Bates, 2020).

Though the asteroid belt formed at ∼2.7 AU, the compositional variety of asteroids suggests they were sourced from both the inner and outer solar system. The growth and migration of the giant planets (during the lifetime of the disk) is thought to have scattered bodies from the inner ($<$ 2.7 AU) and outer solar system (5 - 20 AU) into the asteroid belt (Raymond and Izidoro, 2017). The diverse population represented in the asteroid belt then implies that the meteorites in our collections represent samples of material formed from across the protoplanetary disk. A few meteorite samples originate from the Moon, Mars, and Vesta, confirmed by their chemical and isotopic composition and spectral properties (McCord et al., 1970; Greenwood et al., 2020).

Meteorites have themselves been subjected to a range of geological conditions, including aqueous alteration, heating, melting, and recrystallisation. This is largely dependent on the accretionary history of the meteorites parent body, for example, if the parent body accretes early with large amounts of short-lived, radiogenic ^{26}Al and ^{60}Fe, it will have experienced greater amounts of heating and could undergo complete melting and differentiation. This process can result in the formation of the iron and achondrite meteorites we see today; the former representing the core of a differentiated parent body, and the latter representing the mantle and crust. Another important class of meteorites that have escaped significant heating - and so are undifferentiated and essentially "pristine" - are called chondrites.

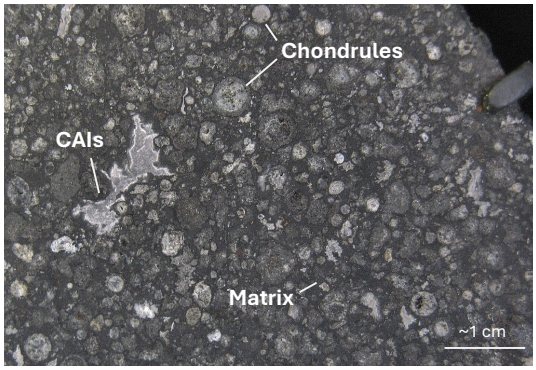

Figure 1.2: Photograph of a typical carbonaceous chondrite with labels identifying irregularly shaped CAIs and spherical chondrules set in a dark, fine-grained matrix. Image sourced and adapted from Wikipedia.

1.1.3 Chondrites

Chondrites are aggregates of sub-millimeter sized solids that formed between 0 - 4 Ma. They consist of varying proportions of chondrules (rounded, millimetre-sized particles that were partially or fully molten in the solar nebula), metallic Fe,Ni grains, and refractory inclusions (CAIs and amoeboid olivine aggregates (AOAs)), all set in a fine grained matrix (Scott and Krot, 2004). Unlike iron and achondrite meteorites which formed between 0 - 2 Ma and have undergone melting and differentiation, chondrites accreted slightly later (from 2 - 4 Ma), and avoided pervasive heating, preserving their pristine components (Kruijer et al., 2020). Chondrites form 85% of our meteorite collection and have been studied extensively to help understand the evolution of our solar system.

CAIs represent the main refractory component seen in chondrites, representing < 5 vol% and range from μms to 1 cm in diameter. These inclusions are some of the oldest dated solids in the solar system, with ages of 4567.3 $\pm$ 0.16 Ma recovered from U-corrected Pb-Pb dating (Connelly et al., 2012). CAIs are thought to have condensed at temperatures of 1400 K, from a gas of approximately solar composition within 0.1 AU from the proto-Sun (Ebel, 2006; Bekaert et al., 2021). The age of the solar system and all subsequent processes are reported relative to the condensation age of CAIs. CAIs are composed of a variety of minerals including: corundum, hibonite, grossite, perovskite, melilite, spinel, and anorthite, which are all rich in Ca and Al (MacPherson et al. 2005). Some CAIs display textural evidence for melting and alteration of previous condensates. AOAs are fine grained, 0.1 - 5 mm, porous aggregates of grains of forsterite, aluminum-diopside,

spinel, anorthite, and Fe,Ni-metal that condensed in the solar nebula in the CAI forming region (Scott and Krot, 2004)

Chondrules contribute between ∼0 to 80% of the total volume of chondrites and range in size from a few micrometers to 1 cm in length (Scott and Krot, 2004). They have igneous textures and are typically composed of olivine and pyroxene, whilst also containing variable amounts of interstitial glass (mesostastis), feldspars, sulfides, oxides, and Fe,Ni metal. Chondrules are also commonly surrounded by fine grained rims (FGRs): higher porosity regions with a distinct mineralogical signature compared to the interchondrule matrix (Pinto et al., 2022). The mineralogical composition of chondrules reflects the redox state of their surroundings during their formation, and so can inform on the conditions in the solar nebula at that time. Many chondrules show evidence of relict grains, relict olivines, and igneous rims, reflecting: a high-temperature thermal history; episodes of remelting and resolidification; and multiple episodes of chondrule generation. The oldest chondrules form contemporaneously with CAIs, with formation ages ranging from 4567.32 ± 0.42 to 4564.71 ± 0.30 Ma, recovered from U-corrected Pb-Pb dating (Connelly et al., 2012). The process of chondrule formation is enigmatic, with proposed models divided into nebula and planetary formation mechanisms. Nebula formation models assume chondrules formed through rapid heating events in the protoplanetary disk; shock-induced processing (bow shocks) (Morris et al., 2016) or solar nebula lightning (Horányi et al., 1995) could provide the necessary conditions for this mechanism. In planetary formation mechanisms, chondrules are remnants of impact melts formed during protoplanet collisions (Johnson et al., 2015; Lichtenberg et al., 2018).

The interchondrule matrix of chondrites consists of < 5 μm grains of olivine, pyroxene, amorphous silicates, Fe-Ni sulphides, feldspar, Fe,Ni metal, organics, refractory metal nuggets, CAI and chondrule fragments, and presolar grains (Scott and Krot, 2004). Presolar grains are extra-solar material formed before the birth of our solar system, and these exist as a range of different highly refractory, insoluble minerals including: silicon carbide (SiC) grains, nanodiamonds, spinels, hibonite, graphite (Zinner, 2014; Qin and Carlson, 2016).

Different chondrites have experienced various extents of thermal and aqueous alteration,

altering their pristine mineralogical inventory. Extensive aqueous alteration of chondrites can lead to the alteration of matrix silicates to phyllosilicates, and the destruction of metal grains and formation of sulfides and oxides (Rubin et al., 2007; Suttle et al., 2021). The amount of aqueous alteration experienced by a chondrite is dependent on the volatile inventory of the chondrite parent body. Certain chondrite groups display evidence of minimal parent body aqueous alteration (Ordinary, CV, and CO chondrites) (Doyle et al., 2015), whilst others are suspected to have accreted greater quantities of water ice and exhibit evidence for extensive alteration (CI and CM chondrites) (King et al., 2015b; Marrocchi et al., 2018). Terrestrial weathering is another significant source of aqueous alteration.

Studying the formation of chondrites is relevant to understanding the general evolution of our solar system, as the bulk chemical composition of chondrites closely match those of the solar photosphere (with a few exceptions including Li and the highly volatile elements H, He, C, and N) (Krot et al., 2014). In particular, the CI chondrites are mostly composed of matrix (Krot et al., 2014) (though they contain the occasional CAI (Frank et al., 2023)) and most closely match the chemical composition of the Sun (Palme et al., 2014). As the Sun accounts for ∼99.89% of the mass of the solar system, this indicates that chondrites provide an invaluable record of the material present in the early stages of the solar system that eventually condensed to form the planets and asteroids we see today. Additionally, chondrites display similar refractory element ratios to Earth and Mars, suggesting that they are a good elemental proxy for the terrestrial planets (McDonough and Sun, 1995).

The complex inventory of chondrites and the compositional variation between groups is likely a reflection of their accretionary history, however, this is still poorly understood. There are two proposed models of chondrite accretion that attempt to match the chemical compositions observed in the chondrules and matrices of these meteorites. The first model suggests that there is chemical complementarity between chondrules and matrix, based on observations of superchondritic (above CI) ratios of Si/Mg, Fe/Mg, Ca/Al, and Ca/Ti in matrix and correspondingly subchondritic (below CI) ratios in chondrules (Bland et al., 2005; Friend et al., 2017; Braukmüller et al., 2018; Hezel et al., 2018a). This is interpreted

as the evaporative loss of elements during chondrule formation, and their subsequent recondensation into the matrix. These ratios are then thought to reflect a joint heritage of matrix and chondrules within a chondrite, with both components being sourced from the same reservoir and being formed in close proximity. This model is also supported by patterns of volatile fractionation, assuming a volatile depleted, CI-like initial reservoir (Bland et al., 2005).

The second model of chondrite accretion proposes that chondrules and matrix did not necessarily have to form from the same reservoir, and that the apparent complementarity observed is an artefact of aqueous alteration. This is supported by recent studies showing little evidence of complementarity in pristine chondrites samples that have undergone minimal aqueous alteration (Patzer et al., 2021). These studies suggest that alteration of metal sulfides on the rims of chondrules, and leaching of Fe and siderophile elements could lead to the superchondritic ratios seen in the matrix of chondrites (van Kooten et al., 2019). Since an initial shared chondrule-matrix reservoir is not necessary for chondrite formation in this model, it is possible that chondrules and matrix could have formed in different locations in the disk and later accreted to form the chondrite parent body. Understanding the accretionary history of chondrites is therefore crucial for developing a comprehensive model of solid transport and mixing in the protoplanetary disk, as chondrules occupy the size range of pebbles, and chondrules and chondrite parent bodies form within the lifetime of the protoplanetary disk.

1.1.4 Nucleosynthetic anomalies in the solar system

Since the 1960s it has been recognised that meteorites display measurable isotopic anomalies compared to terrestrial rocks. These anomalies have been observed in the noble gases Xe and Ne (Reynolds and Turner, 1964; Black and Pepin, 1969), and also in N, Si, and C (Lewis et al., 1987; Zinner et al., 1987). These isotope anomalies can be categorised into various types: those caused by radioactive decay; anomalies induced by particle irradiation; differences caused by mass-dependent fractionation; and mass-independent anomalies.

Radioactive decay introduces isotopic anomalies through the decay of radiogenic parent

isotopes and the subsequent enrichment of the daughter isotopes. Common radiogenic isotope anomalies include those arising from the short-lived isotope systems ^{26}Al-^{26}Mg, ^{182}Hf-^{182}W, and ^{53}Mn-^{53}Cr (Anand and Mezger, 2023) and the long lived dual decay systems of ^{238}U-^{206}Pb and ^{235}U-^{207}Pb (Connelly et al., 2017). The Pb-Pb chronometer is a powerful tool for providing an absolute age date for solar system materials (including CAIs and chondrules), whilst the Al-Mg chronometer is used for relative age dating of these materials (Connelly et al., 2019; Gregory et al., 2020; Piralla et al., 2023). The timing of core formation on planets and planetesimals and the formation of chondrules is dated using ^{182}Hf-^{182}W chronometry (Halliday et al., 1996; Budde et al., 2016b; Kruijer et al., 2017; Budde et al., 2018; Pape et al., 2019), and ^{53}Mn-^{53}Cr is used to determine the age a chondrite experienced aqueous alteration (Fujiya et al., 2013; Jilly-Rehak et al., 2017)

Cosmogenic nuclides form during interaction of cosmic rays with the surface of planets, asteroids and meteorites. This process can form both stable and radioactive nuclides, including stable ^{10}Be, ^{21}Ne, and radiogenic ^{180}W. Cosmogenic nuclides serve as useful tools for determining the cosmic ray exposure age (CRE) of a meteorite; the time a surface is exposed to cosmic rays during its orbit around the sun (David and Leya, 2019; Krietsch et al., 2021). In general this is used to determine the time period between an asteroid break-up and the later arrival of the meteorite to Earth. Before it is exposed during asteroid break-up, and after entry into the Earth's atmosphere, the meteorite surface is assumed to be shielded from cosmic ray exposure.

Mass-dependent anomalies in meteorites are generated by fractionation between isotopes of the same element due to their masses. These fractionations are caused by equilibrium fractionation or kinetic effects. These stable isotope anomalies are measured to investigate volatile depletion in chondrites; systems used include Te isotopes (Hellmann et al., 2020), Zn isotopes (Mahan et al., 2018), and Cr isotopes (Zhu et al., 2019b).

Mass-independent anomalies in meteorites are not due to isotopic fractionation based on mass, but are instead formed by: photochemical reactions in the solar nebula (e.g., O isotope anomalies (Clayton and Mayeda, 1999; Clayton, 2008; Krot et al., 2020)); the magnetic isotope effect (Fukami et al., 2024); or by enrichments/depletions of various

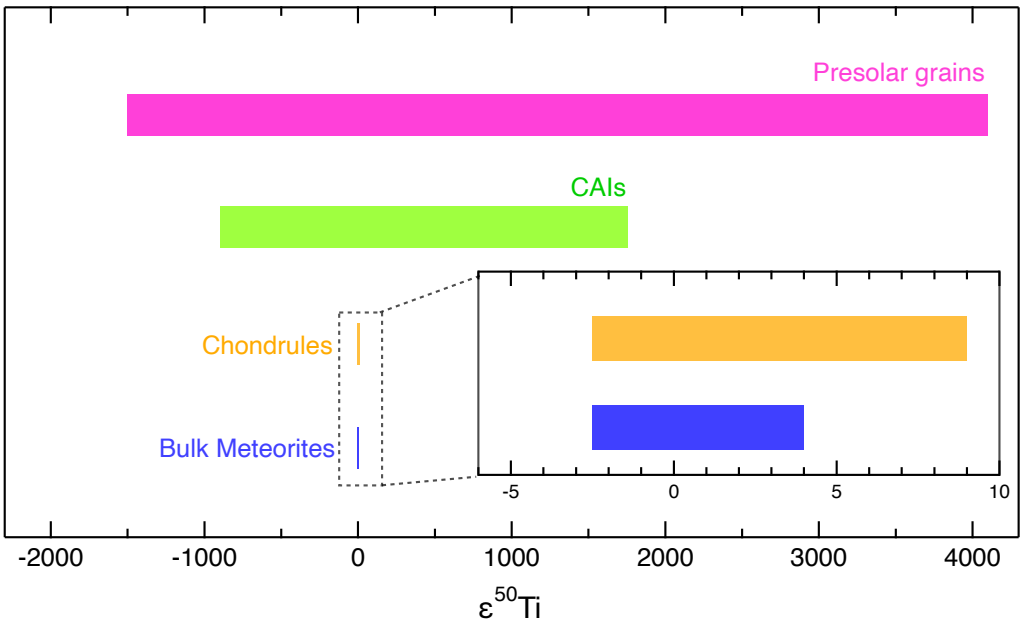

Figure 1.3: Schematic depicting the range in ε^{50}Ti compositions of bulk chondrites, chondrules, CAIs, and presolar grains. Graph adapted from Bermingham et al. (2020), with references listed within.

nucleosynthetic isotopes formed during different stellar processes not native to our solar system (Brennecka et al., 2013). These processes include the r-process, s-process, and p-process.

The s-process (slow-neutron-capture) occurs in low-intermediate mass ($\sim$1.5 – 3 Solar mass) stars, particularly asymptotic giant branch (AGB) stars. This involves the addition of neutrons to a seed nucleus at a slow rate, at low temperatures and low neutron densities. During this process, successively heavier isotopes of the same element are formed. If the isotope is stable, another neutron is added forming increasingly heavier isotopes. If the new isotope is unstable, beta-decay occurs, forming a new element that is one atomic number higher.

r-process (rapid-neutron-capture) isotopes are made through the rapid addition of neutrons to a seed nucleus (or involves the formation of a seed nucleus), at a rate faster than beta-decay. Heavy isotopes until the "neutron drip line" are formed, after which these unstable heavy nuclei undergo a series of radioactive decay steps eventually forming heavy stable isotopes of higher proton number elements. The r-process requires extremely high neutron-fluxes, sites of which are hypothesised to include core-collapse supernovae and

binary neutron star mergers, though locations that fit this criteria are still debated.

The *p*-process (previously referenced as proton-capture, however, now referring to any process forming *p*-nuclei) forms proton-rich nuclei. This process is poorly understood but is theorised to occur via the gamma-process, where heavy nuclei are rapidly heated and undergo disintegration to form proton-rich, neutron-poor species within the shells of exploding massive stars of in supernovae (Bermingham and Meyer, 2024).

The preservation of *s*-, *r*-, and *p*-process anomalies in meteorites indicates wide-scale isotopic heterogeneity in the solar system during the formation of chondrites. These nucleosynthetic anomalies are thought to be carried by presolar grains, with a heterogenous distribution of these grains controlling the isotopic anomalies observed (Qin and Carlson, 2016; Bermingham et al., 2020). This is evidenced by the large range of anomalies seen in isolated presolar grains (∼1%), while "bulk" meteorites show a much narrower range, indicating an averaging effect (see Fig. 1.3) (Bermingham and Meyer, 2024).

Different theories have been proposed to address why meteorites show variable enrichments in *s*-, *r*-, and *p*-process material, and how these isotopic heterogeneities were introduced into the protoplanetary disk. These include: variable thermal processing of presolar grains (Colmenares et al., 2024); grain size sorting within the protoplanetary disk; heterogeneity of the solar system molecular cloud (Burkhardt et al., 2019; Nanne et al., 2019); and late injection of clouds of isotopically distinct material (Brennecka et al., 2013).

1.1.5 A bifurcated disk

The advancement of high precision mass-spectrometry has enabled researchers to study the mass-independent isotopic anomalies of meteorites in greater detail. Plotting different isotope anomalies against each other has lead to the observation that bulk chondrites display a compositional dichotomy (Warren, 2011). This bi-modal grouping is consistently seen in plots across multiple isotope systems, including in siderophile (e.g., Mo, W, Ru, Ni) (Burkhardt et al., 2011; Peters et al., 2017; Worsham et al., 2019; Render et al., 2018), lithophile (Cr, Ti, O) (Clayton and Mayeda, 1999; Trinquier et al., 2007, 2008, 2009), and refractory (Ti, Mo, Ru), and non-refractory (Cr, Ni) (Steele et al., 2011) elements (Fig. 1.4a). These two groups are called the non-carbonaceous (NC) and the carbonaceous (CC)

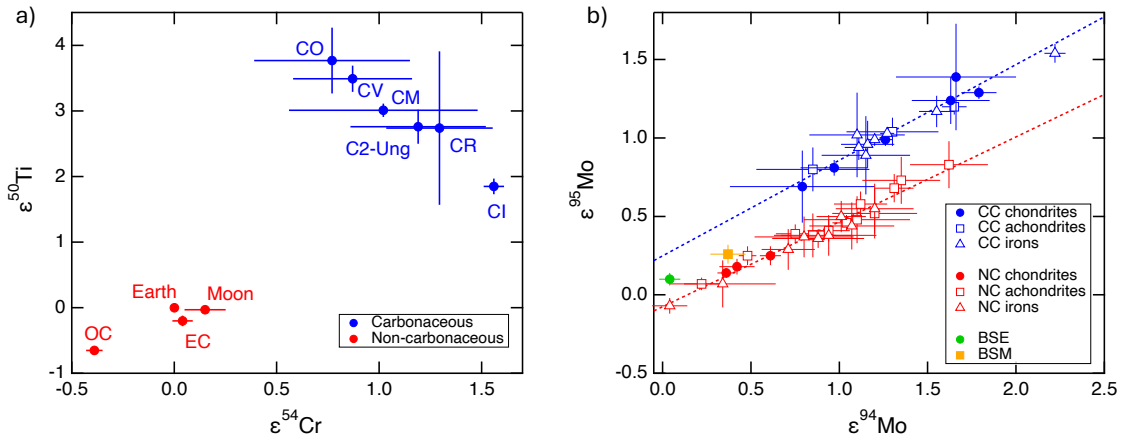

Figure 1.4: Plots of a) ε^{54}Cr vs ε^{50}Ti, and b) ε^{95}Mo vs ε^{94}Mo displaying the isotope dichotomy between NC and CC meteorites. Data is sourced from: Bryson and Brennecka (2021), Burkhardt et al. (2019) and Budde et al. (2019).

groups; the term "carbonaceous" refers to the higher carbon content observed in a few of the CC chondrites (Warren, 2011; Krot et al., 2014). This isotopic dichotomy is also observed in iron meteorites and achondrites that form at earlier ages (0 - 1.5 Ma) compared to chondrites (Kruijer et al., 2017), indicating that the mechanism(s) responsible for the preservation of this dichotomy was present for a prolonged period during the early solar system. Anomalies are also observed in Ca (Dauphas et al., 2014), Zr (Render et al., 2022), Pd (Mayer et al., 2015), Sr, Ba, Nd, and Sm (Brennecka et al., 2013; Bermingham and Meyer, 2024) in CAIs and irons and achondrites.

Detailed studies of Mo isotopes reveal that CC meteorites (irons and chondrites) display a consistent r-process excess when compared to NC meteorites (Fig. 1.4b). This excess is uniform in all CC meteorites, implying that the CC reservoir was isolated from the NC reservoir when this anomaly was introduced, and that the reservoirs remained separated as the r-process enriched material was well mixed within the CC reservoir (Burkhardt et al., 2011; Budde et al., 2016a). The CC reservoir also shows enrichment of other heavy isotopes, including ^{50}Ti and ^{54}Cr (Trinquier et al., 2009; Kleine et al., 2020).

A plethora of evidence suggests that the CC reservoir was located in the outer solar system beyond the orbit of Jupiter, including: spectral similarity of CC chondrites to C- and D-type asteroids which are thought to form in the outer solar system (Alexander et al., 2018; Bates et al., 2024); higher accreted water contents indicating formation past the snowline

(Garenne et al., 2014; Alexander et al., 2018; Marrocchi et al., 2018); the observation of pristine aliphatic-rich organics (thought to be derived from cold, distal locations in the disk) (Alexander et al., 2017; Bates et al., 2024); and palaeomagnetic evidence for distal formation in the protoplanetary disk (Bryson et al., 2020a,b).

The presence and preservation of this compositional dichotomy between the NC and CC meteorites has been used as evidence to suggest that these two families of meteorites accreted concurrently in spatially separate regions of the protoplanetary disk, isolated by a barrier to the transport of solids. Various barriers to the movement of solids in the early solar system have been proposed, including: the growth of Jupiter's core (Kruijer et al., 2017); a pressure maximum (Brasser and Mojzsis, 2020); a snow line (Lichtenberg et al., 2021); and magnetic field lines (Fu et al., 2021)). However, the exact mechanisms, how effective they are, and how long they persisted are still poorly understood.

The NC and CC meteorites can be further divided into distinct groups, based on their chemical and isotopic compositions. Meteorites from each group are thought to originate from similar parent bodies or similar regions in the protoplanetary disk. Some argue that these regions indicate additional, distinct substructures of the protoplanetary disk, even within the NC and CC reservoirs (Rüfenacht et al., 2023).

Expanding this model, recent studies indicate that the compositions of CC chondrites reflect mixtures of material from across the protoplanetary disk, including contribution from both NC-like and CC-like material (Alexander, 2019a; Burkhardt et al., 2019; Bryson and Brennecka, 2021; van Kooten et al., 2021). This is evidenced by observations of individual CC chondrules that appear to plot out of the CC region in ε^{50}Ti-ε^{54}Cr isotope space, and instead show intermediate compositions (Williams et al., 2020; Schneider et al., 2020). In particular, studies by Bryson and Brennecka (2021) on geochemical mixing and van Kooten et al. (2021) on the radial compositions of chondrules demonstrate that the composition of chondrules in CC chondrites could be explained by the addition of varying amounts of CI-dust to NC-like chondrules, implying that chondrules of intermediate composition measured by Williams et al. (2020) and Schneider et al. (2020) could reflect snapshots of this process.

Since these studies demonstrate that CC chondrites contain inner solar system derived material from the NC reservoir, this implies that these regions were not completely isolated and that there was limited transport and mixing of material between the reservoirs. More recent evidence also lends credence to this idea as rare, isotopically CC-like chondrules and CAIs have been observed in NC chondrites, implying that there is some amount of shared material in both reservoirs (Marrocchi et al., 2024). These studies raise further questions regarding the presence, nature, timescale, and permeability of the potential barriers to transport of material previously proposed.

Since the presumed notion of a completely bifurcated protoplanetary disk with non-interacting reservoirs is being challenged, more research is being conducted to better understand the motion of solids in the early solar system. In time, this will lead to a better understanding of the dynamic regimes present in the protoplanetary disk, which will place vital constraints on the mechanisms and timescales of solid aggregation and planetary body formation.

How planetary bodies formed, and what dynamic regimes they experienced during their accretion play important roles in determining their chemical and isotopic compositions, their subsequent evolution, and the architecture of the solar system. Constraining the provenance of material that makes up protoplanets can help us identify whether pebble accretion or planetesimal accretion dominated in different regions of the solar system. Understanding the chemical composition of protoplanets can also inform us on the role that barriers played in the transport of material to planetary forming regions, which will allow us refine our models disk dynamics and planetary accretion. A more complete understanding of the history of solid transport in the protoplanetary disk will allow us to explain the physical and chemical properties of solar system material we see today. This work aims to contribute to this growing field of research by using a geochemical approach to probe the formation history of chondrite parent bodies and explore the transport and movement of solids in the early solar system.

1.2 Aim of this study

As highlighted in the previous section, our understanding of chondrite formation and solar system dynamics is incomplete. More work needs to be done to uncover the formation mechanisms of planetesimals, and the complex compositional histories of chondrites.

Recent work in the field has begun to address this question, with researchers using geochemical and modelling approaches to replicate the compositions of chondrite groups by admixtures of various "primitive" solar system materials. Comprehensive models have been proposed that attempt to address the observed nucleosynthetic anomalies and link these with the chemical compositions of chondrites (such as those by Alexander (2019a,b)), however, these tend to treat the inner and outer solar system reservoirs as separate, non-interacting entities, when there is growing evidence that this is not necessarily the case. This thesis will instead take a geochemical approach to investigate the formation of both inner and outer solar system material, and will probe the possible exchange of material between the NC and CC reservoirs. I will then integrate these results with the published literature to form a larger model of evolution of solid formation and mixing throughout the early solar system.

In particular, this study will focus on the coupled chromium isotopic and "plateau volatile element" (PVE) composition of subsamples of primitive meteorites to isolate the carriers of different nucleosynthetic anomalies and probe the formation of early solar system solids.

This approach is based off recent work by Bryson and Brennecka (2021), who argue that the amount of CI-like material present in a CC chondrite can be traced by its chromium isotopic composition, and Hellmann et al. (2020) who demonstrate that PVE concentrations (Ag, Pb, Sn, In, Te, Se, S, Cd, Tl, and Zn) recorded by carbonaceous chondrites can serve as proxies for the mass and volume fraction of matrix present (Fig. 1.5b and c).

Plateau volatile elements (defined by Braukmüller et al. (2018), also including Bi) are a subset of the moderately volatile elements (MVEs) with 50% condensation temperatures ($T_{C,50}$) between 800 - 500 K (Lodders, 2003). Unlike the MVEs with higher $T_{C,50}$s (1250

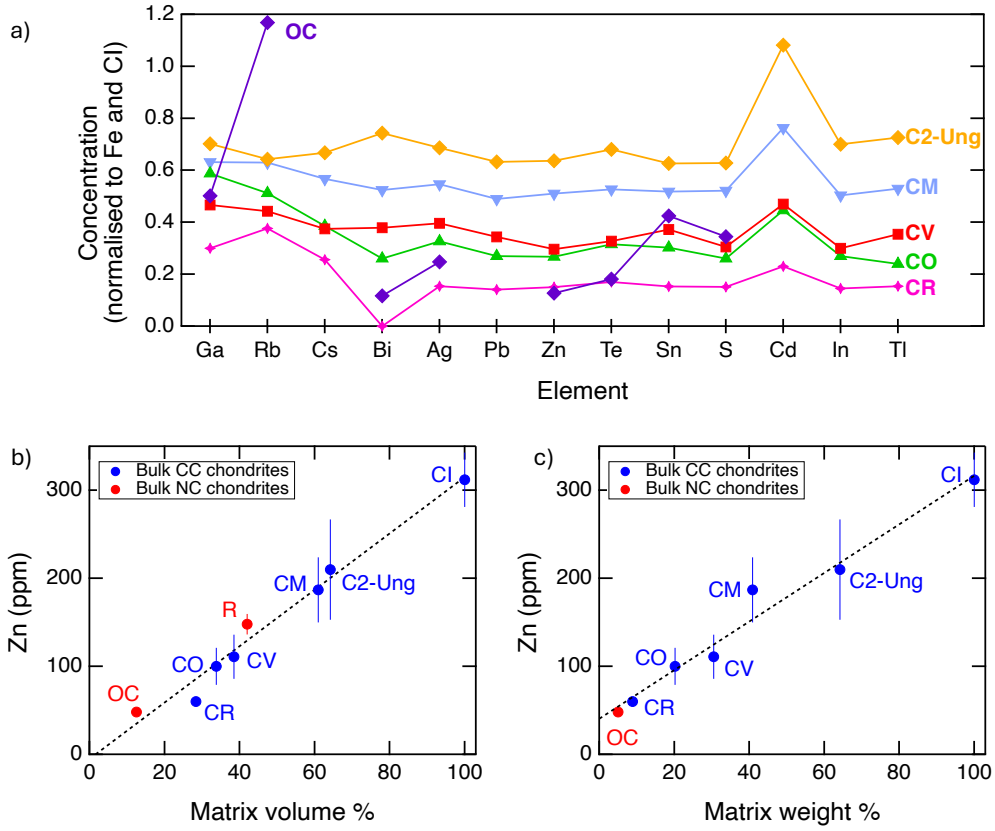

Figure 1.5: a) PVE concentrations of CC groups and OCs normalised to Fe and CI. b) Zn concentrations of chondrites plotted against their matrix volume fraction and c) matrix mass fraction. Data sourced from: Wasson and Kallemeyn (1988), Braukmüller et al. (2018), Abreu et al. (2020), Hellmann et al. (2020), Bryson and Brennecka (2021), Palme and Zipfel (2022), and references therein.

- 800 K) which show increasing depletion in CC chondrites, the PVEs are, in general, unfractionated from each other (Fig. 1.5a).

Chromium isotopes are useful tracers of CI-like material in chondrites as Cr is a main group element with a relatively high $T_{C,50}$ and so its concentration and composition is expected to be relatively unchanged during mild thermal processing (Alexander, 2019a). This allows us to see through the effects of low-level alteration on the chondrite parent body. Chondrules and matrix contain similar concentrations of chromium (approx 2960 ppm and 2620 ppm, respectively (Schneider et al., 2020; Bryson and Brennecka, 2021)), whilst CAIs contain comparatively minimal concentrations (Yamakawa and Yin, 2014). Though CAIs show large excesses in ^{54}Cr, their low abundances (Bryson and Brennecka, 2021) and low Cr concentrations mean that they do not majorly influence the isotopic composition of bulk chondrites. This enables Cr isotopes to effectively trace the contribution of chondrule

and matrix material to the bulk isotopic composition, whilst ignoring contributions from refractory components. The carrier phase of the Cr anomaly is thought to be <100 nm presolar spinel grains, which show large ^{54}Cr enrichments compared to solar (Dauphas et al., 2010). Chromium isotopic compositions are often reported in epsilon notation (ε), as a parts per 10 000 deviation from a terrestrial standard (detailed in equation 1.1).

$$\varepsilon^{54}Cr = \left(\frac{\frac{^{54}Cr}{^{52}Cr\,sample}}{\frac{^{50}Cr}{^{52}Cr\,standard}} - 1 \right) \times 10000 \tag{1.1}$$

Probing the composition of chondrites within this framework allows us to investigate the formation of different chondrite parent bodies. This will help answer various outstanding questions, including if all chondrites share similar mechanisms of formation, and whether chondrite formation samples local material or material from across the disk.

When the ε^{54}Cr and volume fraction of matrix present in different chondrite groups are plotted against each other (Fig. 1.6), the CO (Ornans-like), CM (Mighei-like), C2-Ung (Ungrouped), CV (Vigarano-like) and CI chondrites plot on an a possible mixing line, with CI chondrites as an end member composed of ∼100% matrix. When a mixing line is fitted through these groups with one fixed end member composition defined by CI chondrites, the second, freely varying end-member agrees within error to the average chondrule composition reported by Schneider et al. (2020), implying that each of these chondrite groups isotopic and chemical compositions could be recovered from mixtures of varying proportions of isotopically distinct chondrules and matrix (mixing line details in section 2.4). This would challenge the assumption of complementarity and the theory that chondrites accrete from local material (Bland et al., 2005; Ebel, 2006; Friend et al., 2017), as in that scenario, chondrules and matrix might be isotopically similar.

To unambiguously determine the contribution of matrix and chondrule to the bulk chondrite composition, the ideal approach would be to isolate and measure the isotopic composition of both components. This should be a fairly simple test, however, in reality it is very difficult to accurately measure the isotopic composition of chondrule and matrix separates due to the small sizes of these components (many micrometer scale chondrule fragments exist within the matrix), and the ease of chemical exchange between chondrules and ma-

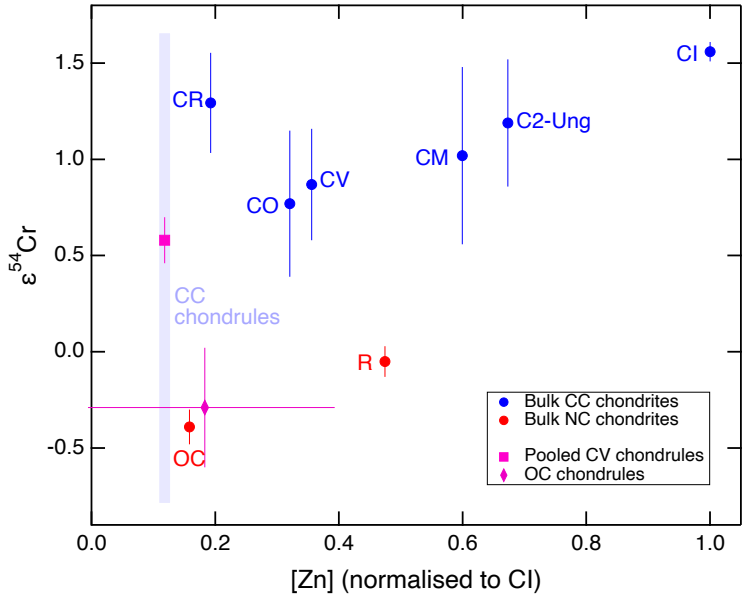

Figure 1.6: ε^{54}Cr compositions of NC and CC chondrite groups plotted against their CI-normalised Zn concentrations. The pooled CV chondrule and average OC chondrule compositions are also plotted. A blue shaded region indicates the range of CC chondrule compositions observed. Data is from: Rubin and Pernicka (1989), Shukolyukov and Lugmair (2006), Trinquier et al. (2006), Trinquier et al. (2007), Qin et al. (2010), Petitat et al. (2011), Qin et al. (2011), Göpel et al. (2015), Bollard et al. (2017), Braukmüller et al. (2018), Hellmann et al. (2020), Schneider et al. (2020), Williams et al. (2020), Bryson and Brennecka (2021), Marrocchi et al. (2021b), Torrano et al. (2021), Zhu et al. (2021b), Zhu et al. (2021c), Hellmann et al. (2023), Yokoyama et al. (2023), Schrader et al. (2024b), and references therein.

trix during parent body metamorphism and aqueous alteration (Bland et al., 2009). This work will utilise a novel subsampling procedure to address this issue, detailed in section 2.1.1. This subsampling procedure will exploit the inherent heterogeneity of chondrites to sample differing amounts of chondrule and matrix in each subsample to investigate if these components exhibit compositional variation.

The NC ordinary chondrites (OC) and Rumuruti-like chondrites (R) plot in a separate regions compared to the CC chondrites. By examining the compositions of these NC groups, we can investigate if all chondrites formed via the same mechanisms, or whether the NC and CC chondrites experienced different formation histories in different regions of the disk. Additionally, there is limited evidence for CC-like contribution to the OC and R chondrites. Rare, small chondrules in OCs have CC-like oxygen isotopic compositions (Marrocchi et al., 2024). Relict grains in R chondrite chondrules seem to have formed from ^{16}O-poor precursors (trending towards carbonaceous values) possibly indicating mi-

nor contribution from the CC reservoir (Varela et al., 2012; Miller et al., 2017; Regnault et al., 2022), and R chondrites display matrix abundances more similar to CC chondrites (40 - 50%) than OCs (10 - 15%) (Bischoff et al., 2011; Krot et al., 2014). Better understanding their formation history will shed light on possible mixing between the NC and CC reservoirs.

The CC CR (Renazzo-like) chondrites plot off the apparent CC mixing line in Fig. 1.6. It has been previously reported that the CR chondrites have undergone multiple episodes of heating, remelting, and re-equilibration, and formed at a later time to the main-group CC chondrites (Budde et al., 2018; Davidson et al., 2019; Marrocchi et al., 2022). We can investigate whether these processes are reflected in the formation history inferred from this study, and how this differs from the formation of other chondrite groups.

1.3 Thesis outline

This chapter provides a brief introduction to the field of nucleosynthetic anomalies in chondrites, and discuses our current understanding of the dynamics of solid formation and planetesimal accretion in the early solar system. The following chapters detail how this work will investigate the compositional variations exhibited by chondrites and their components, and how these results can inform us on the mechanisms of chondrite parent body accretion in the inner and outer solar system over time.

The methodology used in this study is provided in Chapter 2. This describes the unique subsampling protocol utilised in this work, and provides a detailed commentary on sample selection, processing, measurement, and data analysis.

Chapter 3 investigates the mechanisms of accretion of planetesimals in the inner solar system by characterising the bulk, chondrule and matrix compositions of OC and R chondrites. This chapter discuses the extent of solid migration and mixing recorded in inner solar system chondrites, and how this relates to the different formation mechanisms proposed for the terrestrial planets. The potential addition of CC-like, outer solar system derived material into the NC reservoir is also discussed.

The general formation of CC chondrites is explored in Chapter 4, by characterising the bulk, chondrule, and matrix compositions of various CC groups. This chapter investigates if all CC chondrite groups share similar or different chondrule and matrix compositions, and whether different CC groups simply form from varying mixtures of chondritic components. The source regions and formation reservoirs of CC chondrules and matrix is discussed here, as well as the general accretion mechanism of the CC chondrite parent bodies. These results are then used to comment on the inferred dynamics of solid movement in the outer solar system, and how this motion relates to models of planetesimal accretion.

Chapter 5 investigates how the formation of chondritic components and accretion of CC chondrites may have varied over time, by characterising the bulk, chondrule, and matrix compositions of a CR chondrite. This chapter compares the average chondrule compositions observed in CR chondrites to those recovered from other CC groups to discuss how

reprocessing events altered the compositions of CR chondrites and their components. The formation history of the CR chondrites is then discussed, with comparisons made to the earlier formed CC groups.

Chapter 6 provides a concise summary of the results of Chapters 4, 5, and 6, and evaluates the effectiveness of the new subsampling method used in this work. The mechanisms of chondrite formation in the inner and outer solar system are compared and discussed, with a focus on the provenance of chondritic components, the locations of accretion of chondrite parent bodies, and the dynamic regimes experienced in the NC and CC reservoirs over time.

Chapter 7 provides a brief summary of the results, discussions, and conclusions discussed previously in Chapters 3, 4, 5 and 6.

Chapter 2

Methods

2.1 Sample preparation

2.1.1 Novel subsampling procedure

To determine the ε^{54}Cr composition of matrix and chondrules in chondrites, previous work has relied on physical separation of chondritic components. As discussed in section 1.2, this approach presents issues due to the preferential measurement of larger chondrules that are easier to isolate; the presence of many un-separable micrometer-sized chondrule fragments within chondritic matrix; and the effect of chemical exchange between chondrules and matrix. In particular, Bland et al. (2009) show that extensive localised isotopic and chemical exchange can occur at small length scales (100s μm) between chondritic components (such as chondrules and matrix), even in pristine chondrites. This exchange means that measuring the compositions of isolated chondritic components may not provide a reliable value for their respective compositions.

To circumvent these issues, in this study I will measure the compositions of several small subsamples of representative chondrites, aiming to sample variations in the relative amounts of chondrules and matrix within each subsample - possible due to chondrite heterogeneity - whilst averaging out small, local chemical exchange between the components (as seen in Fig. 2.1a). A subsample mass between 10 - 40 mg provides: 1) multiple subsamples from a $\sim$1 g sample; 2) large enough subsamples to average out alteration

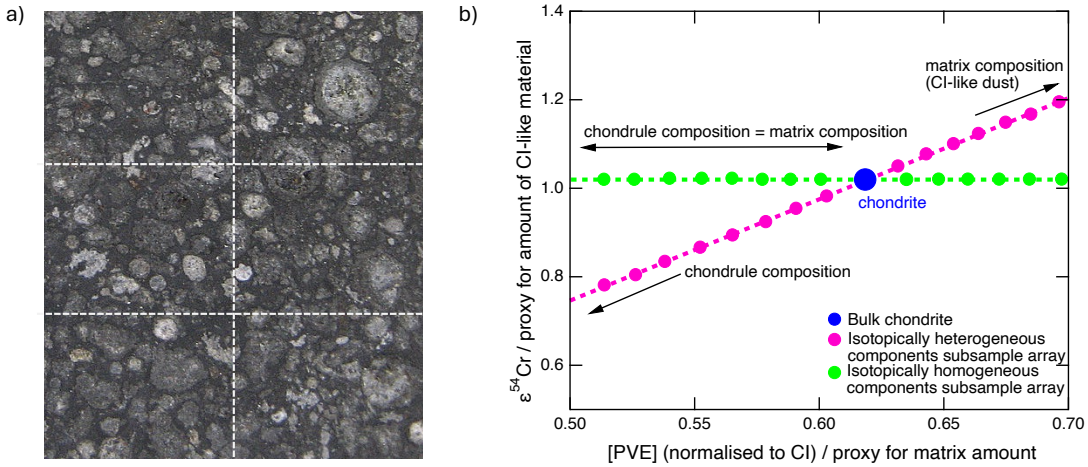

Figure 2.1: a) Sectioning a larger mass of chondrite into smaller subsamples, each containing varying amounts of chondrules and matrix. b) Coupled ε^{54}Cr compositions and CI-normalised PVE concentrations of a hypothetical array of subsamples. CI-normalised PVE abundances are a proxy for matrix volume fractions within each subsample. If chondrules and matrix display different ε^{54}Cr compositions, subsamples should plot on a slope trending towards each end member composition (pink line). If chondrules and matrix display homogenous compositions, subsamples will define a flat line (green slope). Image sourced and adapted from Wikipedia.

effects and provide measurable concentrations of PVEs (Bland et al., 2009; Stracke et al., 2012); and 3) small enough subsamples (<600 mg) to provide heterogeneous isotopic and chemical concentration values which could indicate that the subsamples contain heterogeneous amounts of matrix and chondrules. Confirmation of heterogeneity can be assessed by whether the relative standard deviation (RSD) of PVE concentrations is >4% (Stracke et al., 2012).

Assuming that small subsamples of chondrites contain varying proportions of matrix and chondrules, if both components were formed in separate regions of the protoplanetary disk and their compositions differ then each subsample should display varying ε^{54}Cr compositions, proportional to the fraction of matrix present. On a plot of ε^{54}Cr vs matrix fraction, these subsamples would fall on a mixing line between the compositions of their chondrules and matrix, as shown in Fig 2.1b. However, if chondrites formed in a similar region from locally sourced material, the chondrules and matrix of each subsample should acquire the same ε^{54}Cr composition, regardless of the amount of matrix present. On a plot of ε^{54}Cr vs matrix fraction, subsamples of each chondrite group would then define lines of 0 gradient, also seen in Fig 2.1b.

Subsampling should serve as a powerful tool for identifying if there is significant variation in the average compositions of chondrules and matrix in different chondrites. Additionally, the mixing line fit through subsamples of each meteorite on a plot of ε^{54}Cr against matrix fraction will allow me the extract the ε^{54}Cr compositions of the matrix and chondrules of each chondrite (method detailed in section 2.4). This may be an effective method of determining the average chondrule and matrix composition within each chondrite group, without needing to isolate and measuring each individual chondrule and avoiding issues due to small chondrule size and element remobilisation. Identifying the compositions of chondrules in each chondrite group will allow me to investigate the formation of chondrules and chondrites, and probe the history of mixing in the protoplanetary disk by tracing changing ε^{54}Cr compositions.

2.1.2 Sample selection

Sample Name	**Classification**	**Weathering Grade**
Los Vientos (LoV) 171	OC LL	W0/1
Miller Range (MIL) 07440	R4	Be
Allende	CV3	Fall
Dominion Range (DOM) 08006	CO3	A/B
Northwest Africa (NWA) 11345	CM2	Low
Tarda	C2-Ung	W0
Miller Range (MIL) 090001	CR2	B

Table 2.1: List of samples studied in this work. Classification and weathering grade sourced from the Meteoritical Bulletin.

I acquired ∼0.5 - 1 g samples of a range of carbonaceous and non-carbonaceous meteorites to sample the breadth of primitive meteorite groups observed in the solar system. One sample of a Vigarano-like (CV), Ornas-like (CO), Mighei-like (CM), C2 Ungrouped (C2-Ung), Renazzo-like (CR), Rumuruti-like (R) and Ordinary chondrite (OC) was requested from various institutions including: ANSMET, CEREGE, eBay, and personal loans. A full list of samples is provided in table 2.1.

Ideally, each sample would be minimally weathered and of petrological grade 3, displaying unequilibrated mineral assemblages and no extensive aqueous alteration (Van Schmus and Wood, 1967). This would ensure minimal remobilisation of elements within the sample

to lessen the effects of chemical and isotopic exchange between chondritic components. R chondrite MIL 07440 has a petrological grade of 4, indicating that it has experienced low degrees of equilibration, displaying a "slightly recrystallised matrix" according to the Meteorical Bulletin classification. CM chondrite NWA 11345, C2-Ung chondrite Tarda, and CR chondrite MIL 09001 are all petrological grade 2, indicating little to no thermal alteration, and the presence of abundant hydrated minerals. These samples have had to be used due to the scarcity of grade 3 chondrites within each group; many more suitable candidates are of too low mass and so are difficult to obtain, or have experienced greater degrees of weathering. Each chondrite was selected after careful review of literature data which indicated that they exhibit relatively low levels of alteration.

2.1.3 Sample digestion

Each chondrite sample was cut into 10 - 25 mg subsamples using either a diamond wire saw or a scalpel. Each subsample was then crushed using a ceramic pestle and mortar, and transferred to Teflon beakers.

Subsamples were digested by refluxing in a mixture of 1.2 ml concentrated (conc.) Nitric acid (HNO_3, ∼15M) and 0.8 ml conc. Hydrofluoric acid (HF, 28M) at 180°C for >7 days. The amount of HF used was calculated to provide the minimum amount of fluoride ions necessary to digest the silicates present in each subsample to reduce the likelihood of forming insoluble fluorides. Estimates of silicate contents were determined by previously reported silicon concentrations in chondrites (Braukmüller et al., 2018). After refluxing in conc. HNO_3 and HF, subsamples were dried down and refluxed in 2 ml 6M Hydrochloric acid (HCl) at 120°C for >2 days. Finally, if necessary, subsamples were refluxed in aqua regia (0.6 ml conc. HCl and 0.2 ml conc. HNO_3) at 100°C to destroy any remaining organic material. Subsamples were then brought up in 2 ml 6M HCl; a 0.8 ml aliquot was reserved for PVE and pre-column chemistry concentration measurements and a 0.5 ml aliquot was reserved for Cr purification. The remaining sample was stored for future repeats or measurement of different isotope systems.

2.2 Chromium separation

2.2.1 Theory

To accurately determine the mass-independent Cr isotopic anomalies preserved in the selected chondrites, Cr was isolated from the matrix elements present in the samples via ion exchange chromatography. This technique utilises the differing partition constants (K_D) of elements with cation and anion exchange resins to isolate specific species. Near-complete separation of Cr from the matrix is required to avoid atomic isobaric interferences from ^{50}V, ^{50}Ti, and ^{54}Fe, and to ensure stable ionisation during measurement which is affected by high Mg, Na, and Ca contents.

Mass-independent Cr isotopic measurements require typically high (>95%) purification yields to avoid the effects of equilibrium stable isotope fractionation induced by column chemistry (Larsen et al., 2016). Effects of this fractionation on the isotopic ratio of the sample are sometimes in excess of the uncertainty reported for Cr isotope analysis using Thermal Ionisation Mass-Spectrometry (TIMS) and Multi-Collector Inductively Coupled Plasma Mass-Spectrometry (MC-ICP-MS).

The column chemistry procedure developed for this study is an amalgamation of methods used by various authors, including those published by Torrano et al. (2021); Schneider et al. (2020); van Kooten et al. (2017); Larsen et al. (2016); Trinquier et al. (2008) and Zhu et al. (2021a), and uses 5 - 6 columns.

The main difficulty with achieving high yields during ion exchange chromatography lies in the difficulty in converting all chromium present to the appropriate redox state and forming the required chromium-species. A study by Larsen et al. (2016) shows that during cation-based ion exchange column chromatography there is significant isotopic fractionation between Cr(VI) and Cr(III), with Cr(VI) being enriched in ^{54}Cr. Additionally, there is a smaller but measurable fractionation between Cr(III) peaks with Cr(III)-chloride (Cl) complexes eluting faster on AG50w-x8 cation columns and being enriched in lighter isotopes, and Cr^{3+} eluting much later and being isotopically heavier. This highlights the necessity in ensuring that all the Cr present in a sample is in the correct oxidation state and complexes, which elutes in one aliquot during the chemistry procedure.

To ensure that all Cr is present in the correct oxidation state, this chemistry relies on the effective reduction of Cr(VI) to Cr(III). Cr(III) can exist as Cr^{3+} in nitric solutions, and Cr^{3+}, $CrCl^{2+}$, $CrCl_2{}^{+}/CrCl_3{}^{0}$ complexes in hydrochloric acid solutions. During hydrochloric acid chemistry, effective conversion of all Cr to $CrCl^{2+}$ and $CrCl_2{}^{+}/CrCl_3{}^{0}$ complexes allows for the Cr to be eluted in a single initial step. To achieve this, following the procedures developed in Larsen et al. (2016), the sample is heated to 50°C in weak nitric acid for multiple days to ensure conversion to Cr(III), and for hydrochloric solutions the sample is refluxed for multiple hours in concentrated hydrochloric acid at high temperatures (>120°C) to ensure the formation of chloride complexes, before the solution is diluted to a weaker acid and quickly loaded. Even with these conversion steps, loss of 10 - 20% of Cr can regularly occur during the first hydrochloric acid based cation exchange chemistry, presumably from incomplete formation of Cr(III)-Cl complexes. To overcome this, the matrix cut (assumed to contain the remaining Cr in Cr^{3+}) was collected, subjected to the same treatment procedure and passed through the column again to lead to a more complete recovery of Cr.

A brief summary of the column chemistry procedure used is provided below:

1. A HCl based anion column that aims to remove Fe.
2. A HCl based cation column that removes Mg, Ca, and Ti. This commonly suffers from low yields, so the matrix cut is collect, subjected to the column again and combined with the first Cr cut.
3. Repeat of column 2 using the collected matrix cut, from which the Cr is collected and combined with the Cr collected in column 2.
4. A HCl based cation column that is a repeat of the second column to remove additional Ti and Mg.
5. A HNO_3 based cation column that aims to eliminate Ti, Na, and HFSEs. This column sometimes suffers from Cr loss during the initial nitric cut. If this occurs, the nitric cut is subjected to the same column, and the Cr is collected again.

A detailed breakdown of each column, along with elution curves, is provided in the fol-

lowing subsections. The elution curves were conducted on an aliquot of the CM chondrite NWA 11345 and display at which stages Cr, Ti, Mg, Fe, Na, and Ca elute during the chemistry (Fig. 2.2). V was measured, but was present below the instrument detection limit (IDL) of the Quadrupole ICP-MS used to determine the composition of each elution cut, and so is excluded.

2.2.2 Column 1

Column 1 is adapted from Yamakawa et al. (2009) and Hibiya et al. (2019), and uses 1 ml anion resin (AG® 1-X8, 200-400 mesh), in a 3 ml pipette type column, cut shorter to 1 ml pipette volume. All resins used were pre-cleaned with 10 repeated rinses in conc. HCl and Milli-Q® (MQ), and stored in MQ. All columns used (1 - 5) were cleaned before and after use by submersion in 6M HCl for at least a week.

During the first column Cr elutes first, followed by Cu, Fe, and Zn. The Cu, Fe, and Zn elutions were not routinely collected, due to lack of interest for this study. Details of pre-treatment and column chemistry are provided in Table 2.2. The elution curves for this column are provided in Fig. 2.2a, and show how Fe is effectively removed at this stage. The Cr cut (5 ml 6M HCl) is collected and subjected to the next column.

Pre-column chemistry		
Step	**Reagent**	**Volume**
Reflux sample in HCl for 24 hrs at 140°C	6M HCl	1 ml

Column chemistry		
Step	**Reagent**	**Volume**
Wash resin	3M HNO_3	10 ml
Wash resin	MQ	18 ml
Wash resin	6M HCl	12 ml
Condition the column	6M HCl	5 ml
Load the sample and elute Cr	6M HCl	1 ml
Elute Cr	6M HCl	4 ml
Elute Cu	6M HCl	13 ml
Elute Fe	0.5M HCl	8 ml
Elute Zn	3M HNO_3	6 ml

Table 2.2: Pre-treatment and column chemistry protocol for column 1.

2.2.3 Column 2

Column 2 is adapted from Yamakawa et al. (2009) and Torrano et al. (2021). This column consists of 1 ml cation resin (AG® 50-X8, 200-400 mesh) in a Bio-Rad column. Details of pre-treatment and column chemistry are provided in Table 2.3. The elution curves for this column are provided in Fig. 2.2b, and show how Mg, Ti, and Ca are removed during this column. A small amount of Cr elutes during the matrix collection (7 ml 6M HCl) due to the incomplete conversion of all the Cr to Cr(III)-Cl ligands, therefore both the Cr cut (8 ml 1M HCl) and the matrix cut is collected and the matrix cut is passed through the column again.

Pre-column chemistry		
Step	**Reagent**	**Volume**
Dry sample in conc. HNO_3 at 120°C (repeat x2)	Conc. HNO3	0.2 ml
Dry sample in HCl at 120°C	6M HCl	0.2 ml
Reflux sample in HCl for 24 hrs/overnight at 130°C	6M HCl	1 ml
Reflux sample in conc HCl for 5 hrs at 130°C	Conc. HCl	∼0.2 ml
Dilute samples with MQ to 2.4ml 1M HCl	MQ	∼2.2 ml

Column chemistry		
Step	**Reagent**	**Volume**
Wash resin	6M HCl	10 ml
Wash resin	1.8M HCl	10 ml
Condition the column	1M HCl	10 ml
Load the sample and elute Cr	1M HCl	2.4 ml
Elute Cr	1M HCl	5.6 ml
Elute matrix elements + residual Cr	6M HCl	7 ml

Table 2.3: Pre-column treatment and column chemistry protocol for column 2.

2.2.4 Columns 3 & 4

Columns 3 and 4 are a repeat of column 2. The same resin and Bio-Rad columns are used, with the resin in each having been cleaned with x3 rinses of 4 ml 6M HCl and 4 ml MQ, repeatedly. The only difference in the column chemistry is during the pre-condition of the resin where 1M HCl is used instead of 1.8M HCl. Details are provided in Table 2.4.

The matrix cut collected during column 2 is put through column 3, and the Cr scavenged is collected in the same beaker as the Cr collected during column 2. This combined Cr

sample from columns 2 and 3 is then processed through column 4, where the Cr elution is collected. If the Cr elution dries down to a small green dot, then the sample is passed through column 5. If the sample does not dry down to a small green dot and instead appears white/yellow, then it is passed through column 4 again to remove excess Mg and Ca before moving onto column 5.

The elution curves for these columns are provided in Figs. 2.2c and d, and show where small amounts of Cr are scavenged in column 3, and how Ti is removed in column 4.

Pre-column chemistry		
Step	**Reagent**	**Volume**
Dry sample in conc. HNO_3 at 120°C (repeat x2)	Conc. HNO3	0.2 ml
Dry sample in HCl at 120°C	6M HCl	0.2 ml
Reflux sample in HCl for 24 hrs/overnight at 130°C	6M HCl	1 ml
Reflux sample in conc HCl for 5 hrs at 130°C	Conc. HCl	∼0.2 ml
Dilute samples with MQ to 2.4 ml 1M HCl	MQ	∼2.2 ml

Column chemistry		
Step	**Reagent**	**Volume**
Wash resin	6M HCl	10 ml
Condition the column	1M HCl	10 ml
Load the sample and elute Cr	1M HCl	2.4 ml
Elute Cr	1M HCl	5.6 ml
Elute matrix elements	6M HCl	8 ml

Table 2.4: Pre-column treatment and column chemistry protocol for columns 3 and 4.

2.2.5 Column 5

Column 5 is adapted from Yamakawa et al. (2009) and Torrano et al. (2021), and uses 0.3 ml cation resin (AG® 50-X8, 200-400 mesh), in a shrink-wrap Teflon columns (4.05 mm diameter and 23.3 mm height). Details of pre-treatment and column chemistry are provided in Table 2.5. The elution curves for this column are provided in Fig. 2.2e, and show how Na and Ti are removed during this column. Occasionally a small amount of Cr elutes during the initial HNO_3 elution matrix collection (4 ml 0.5M HNO_3) due to the incomplete conversion of all the Cr to Cr^{3+}. This can be seen when a small green dot is visible during the dry down of the nitric elution; if this is present, this cut is passed through column 5 again in an attempt to recover the Cr. However, repeating this column

possibly causes greater Mg contents in the final Cr collection, affecting sample ionisation during isotopic measurement. An elution curve for this additional repetition was not done as it was unnecessary for the sample.

After purification, a small aliquot of the final purified sample is taken to check the yield and purity. Following these steps, this procedure can result in yields of up to 90% for pure chromium standard NIST®SRM®979 (henceforth referred to as NIST-979), and yields of typically 80 - 95% for meteorite samples.

Samples are then dried down twice in 200 μl conc. HNO_3 at 120°C and once in 100 μl 30% H_2O_2 at 60°C to destroy any remaining organics from the resin (Zhu et al., 2021a). Following this, samples are dried down twice in 200 μl 6M HCl at 120°C before they are dissolved in the appropriate amount of 6M HCl to form a 500 ppm solution for Cr isotopic measurements.

Pre-column chemistry		
Step	**Reagent**	**Volume**
Dry sample in conc. HNO_3 at 120°C (repeat x2)	Conc. HNO3	0.2 ml
Dry sample in HCl at 120°C	6M HCl	0.2 ml
Reflux sample in HNO_3 for 24 hrs at 50°C	1M HNO_3	1.5 ml
Dilute samples with MQ to 3 ml 1M HNO_3	MQ	1.5 ml

Column chemistry		
Step	**Reagent**	**Volume**
Wash resin	6M HCl	4 ml
Wash resin	1.8M HCl	4 ml
Wash resin	MQ	1 ml
Condition the column	0.5M HNO_3	3 ml
Load the sample and elute matrix elements	0.5M HNO_3	3 ml
Rinse matrix elements	0.5M HNO_3	1 ml
Rinse matrix elements	1M HF	3 ml
Rinse matrix elements	1M HCl	6 ml
Elute Cr	6M HCl	6 ml

Table 2.5: Pre-column treatment and column chemistry protocol for column 5.

2.2.6 Column chemistry elution curves

Elution curves depicting the success of the column chemistry protocol are provided in Fig. 2.2. These were conducted on aliquots of CM NWA 11345, displaying the success of this method in purifying chondrite samples.

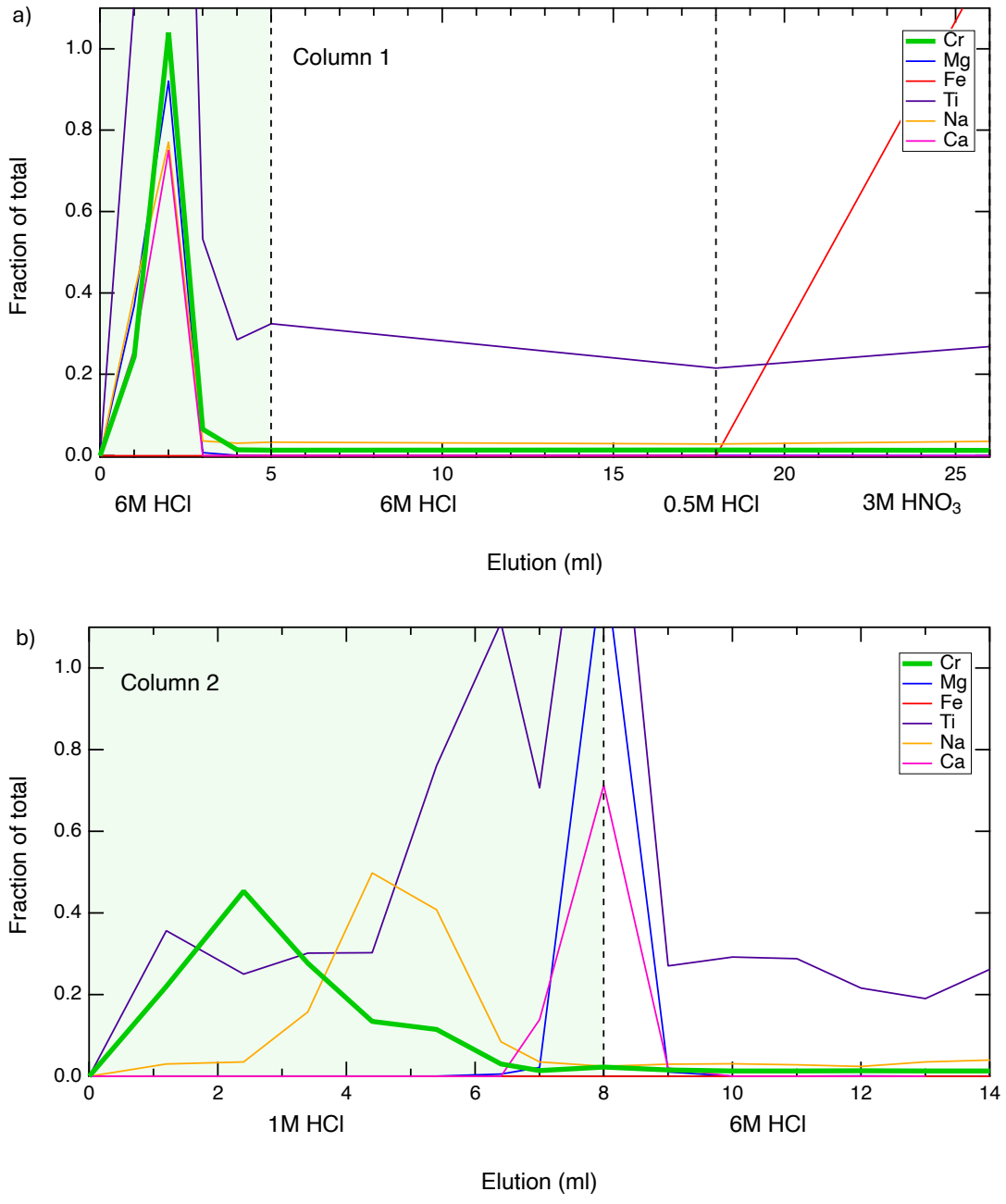

Figure continued on the next page.

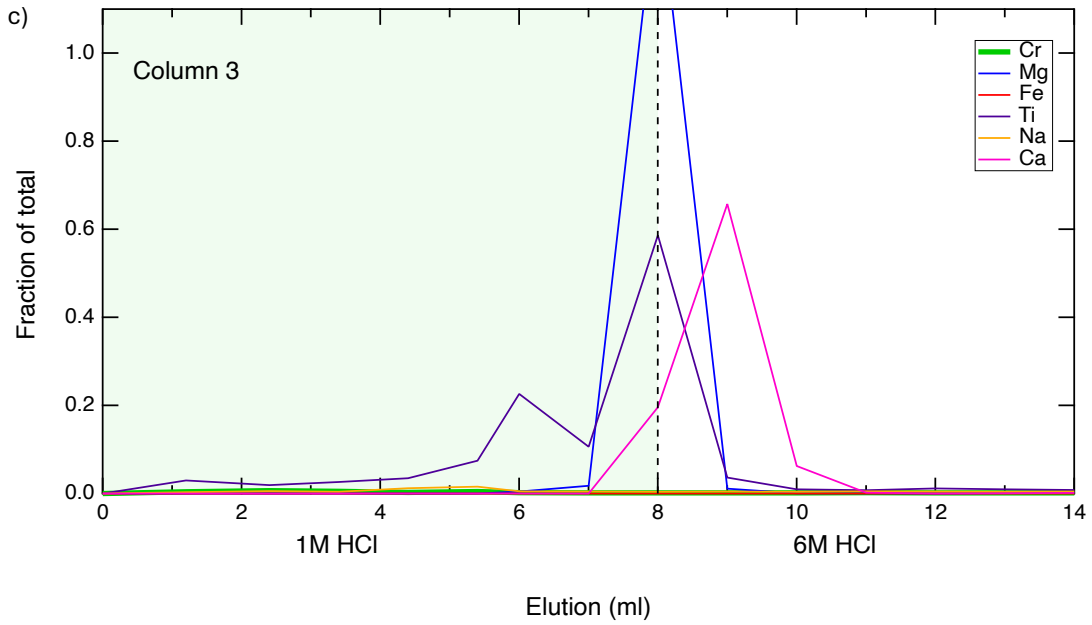

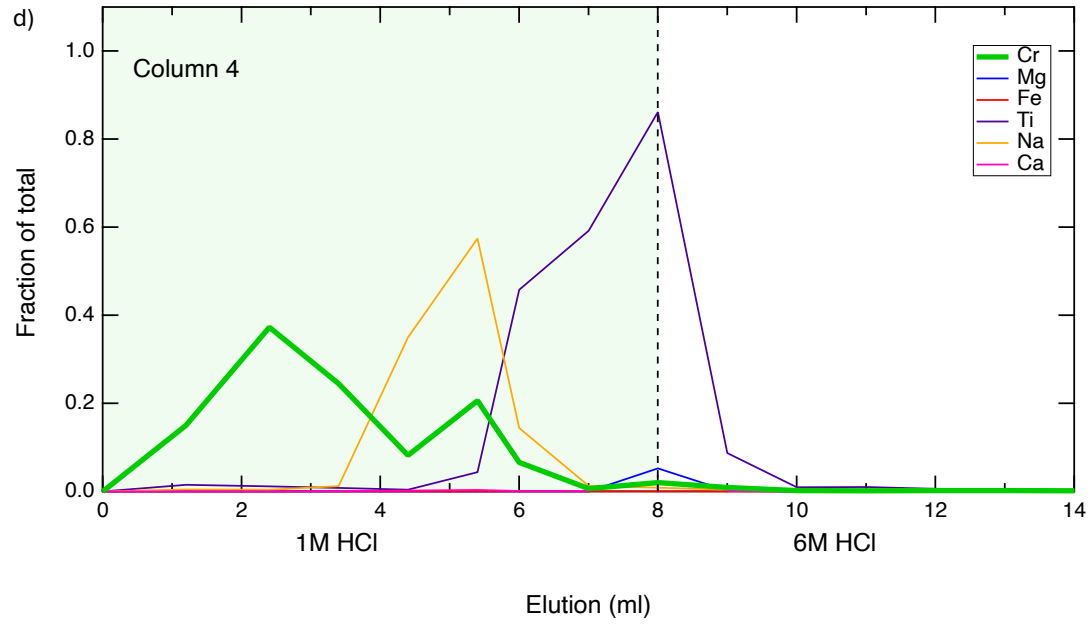

Figure continued on the next page.

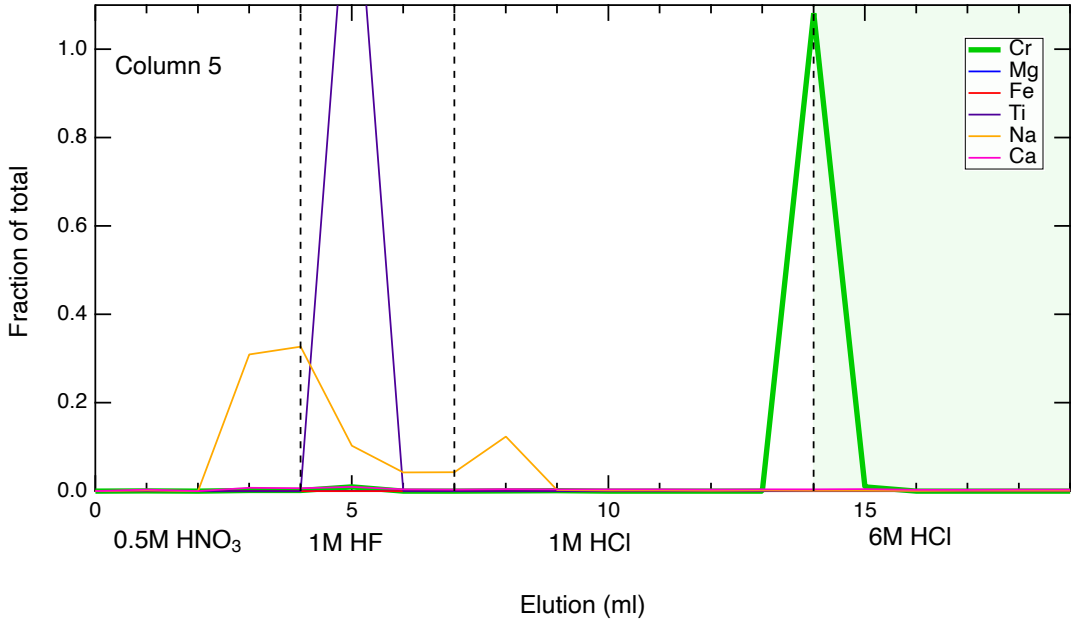

Figure 2.2: Elution curves for the Cr purification procedure, conducted on CM chondrite NWA 11345. The Cr elution step is indicated by a green shaded region. The fraction of each element is the amount measured in each aliquot compared to the total amount loaded onto column 1. Column 3 does not show resolvable amounts of Cr in the Cr elution step as this is the matrix cut that is being scavenged for any Cr that did not speciate correctly in column 2. In this case negligible Cr was present in the matrix cut, resulting in no recovered Cr during this round of column chemistry. Column 5 displays how an ∼100% yield of Cr is achieved for meteorite samples.

2.3 Analytical methods

2.3.1 Chromium Isotopic measurements: Thermal Ionisation Mass Spectrometry

Thermal Ionisation Mass Spectrometry (TIMS) is commonly used to measure the Cr isotopic composition of meteorites due to the increase in signal stability and low mass fractionation experience by samples compared to measurement on plasma based instruments (i.e., MC-ICP-MS). Samples are typically dried down onto a metal filament, and a current is passed through the filament allowing for heating, ionisation, and measurement of the isotopic composition of the sample using an array of collectors. Isotopic fractionation during the measurement is corrected for offline, with the method detailed below.

2.3.1.1 Fractionation correction

Fractionation during measurement occurs due to lighter isotopes evaporating and ionising off the filament first. This leads to the measured ratio of $\frac{^{54}Cr}{^{52}Cr}$ changing over the course of a run from lower values (due to greater ionisation ^{52}Cr) to higher values at the end of the run as proportionally greater amounts of the heavier isotope are ionised. This mass fractionation approximately follows the exponential law, detailed in equation 2.1.

$$\gamma[\Delta(lnM)] = \gamma(0) + \Delta(lnM)f + \theta[(\Delta(lnM))^2] \tag{2.1}$$

where $\Delta(lnM)$ is the mass log difference of the two masses of interest (M_1 and M_2); γ is the fractionation, f is the mass independent coefficient; and $\theta[(\Delta(lnM))^2]$ represents the higher order terms. The first term of the expansion assumes that $\Delta M = 0$ and that the measured isotopic ratio r is equivalent to the true isotopic ratio R.

Equation 2.1 can be evaluated to provide the following mass fractionation correction:

$$\frac{^{54}Cr}{^{52}Cr}_T = \frac{^{54}Cr}{^{52}Cr}_M \times \left(\frac{\frac{^{50}Cr}{^{52}Cr}_T}{\frac{^{50}Cr}{^{52}Cr}_M} \right)^{\beta} \tag{2.2}$$

where $\frac{^{x}Cr}{^{y}Cr}_T$ is the true isotopic ratio of isotopes of atomic masses x and y, and $\frac{^{x}Cr}{^{y}Cr}_M$ is

the measured isotopic ratio, and:

$$\beta = \frac{ln(^{54Cr}m) - ln(^{52Cr}m)}{ln(^{50Cr}m) - ln(^{52Cr}m)} \tag{2.3}$$

where ^{x}m is the atomic mass of each isotope x.

It is also assumed that this exponential correction also corrects for residual fractionation that arises from incomplete recovery of Cr during column chemistry.

2.3.1.2 Dynamic run

Isotopic measurements conducted with a one-line run are susceptible to errors in measured signals due to the collection of different isotopes in different collectors, which each have varying efficiencies and amplifiers. To minimise the error associated with differences in cup and amplifier efficiencies a two-line dynamic run was conducted, with the cup configuration listed in Table 2.6.

Cup	**L4**	**L3**	**L2**	**L1**	**CC**	**H1**	**H2**	**H3**	**H4**
Line 1	-	-	^{50}Cr	^{51}V	^{52}Cr	^{53}Cr	^{54}Cr	-	^{56}Fe
Line 2	-	-	-	^{49}Ti	^{50}Cr	^{51}V	^{52}Cr	^{53}Cr	^{54}Cr

Table 2.6: Cup configuration for a two-line dynamic run conducted at the University of Oxford

This eliminates any errors associated with a specific cup in the following manner:

$$\frac{^{54}Cr}{^{52}Cr}_{T} = \left(\frac{^{54}Cr}{^{52}Cr}_{M} \times \frac{G_{H2}}{G_{CC}}\right) \times \left(\frac{\frac{^{50}Cr}{^{52}Cr}_{T}}{\frac{^{50}Cr}{^{52}Cr}_{M} \times \frac{G_{CC}}{G_{H2}}}\right)^{\beta} \tag{2.4}$$

where $\frac{^{x}Cr}{^{x}Cr}_{M}$ is the true fractionated isotopic ratio, and G_y is the gain error associated with the cup and amplifier combination found in cup y. $\frac{^{54}Cr}{^{52}Cr}_{M}$ is recovered from Line 1 and $\frac{^{50}Cr}{^{52}Cr}_{M}$ from Line 2. As $\frac{^{50}Cr}{^{52}Cr}_{T}$ is a constant (used here as 0.051859), and β can be approximated to -1, equation 2.4 can be simplified to:

$$\frac{^{54}Cr}{^{52}Cr}_{T} \propto \left(\frac{^{54}Cr}{^{52}Cr}_{M} \times \frac{G_{H2}}{G_{CC}}\right) \times \left(\frac{^{50}Cr}{^{52}Cr}_{M} \times \frac{G_{CC}}{G_{H2}}\right) \tag{2.5}$$

As seen in equation 2.5, the gains associated with the H2 and CC cup cancel out in the calculation of $\frac{^{50}Cr}{^{52}Cr\,T}$.

2.3.1.3 Iron correction

Despite chemical purification, trace amounts of Fe remain in the samples, contributing to an isobaric inference on ^{54}Cr collected in line 1. To eliminate this, collected data was subjected to an iron correction defined in equation 2.6.

$$^{54}Cr_{corrected} = ^{54}\,Cr_{measured} - \left(^{56}Fe_{measured} \times \left(\frac{^{54}Fe}{^{56}Fe\,M}\right)\right) \tag{2.6}$$

where $\frac{^{54}Fe}{^{56}Fe\,M}$ is the measured ratio of ^{54}Fe to ^{56}Fe. This $^{54}Cr_{corrected}$ is used in the term $\frac{^{54}Cr}{^{52}Cr\,M}$ in equation 2.2. As ^{54}Fe is not directly measured, the ratio is calculated by equations 2.7 and 2.8 which model how Fe is fractionated during the measurement:

$$\frac{^{54}Fe}{^{56}Fe\,M} = \frac{^{54}Fe}{^{56}Fe\,T} \times \left(\frac{\frac{^{50}Cr}{^{52}Cr\,T}}{\frac{^{50}Cr}{^{52}Cr\,M}}\right)^{-\gamma} \tag{2.7}$$

where $\frac{^{54}Fe}{^{56}Fe\,T}$ is the standard reference ratio of the naturally occurring abundance of these isotopes (used here as 0.063703)

$$\gamma = \frac{ln(^{54}Fe m) - ln(^{56}Fe m)}{ln(^{50}Cr m) - ln(^{52}Cr m)} \tag{2.8}$$

where ^{x}m is the atomic mass of each isotope x.

To check that there was no remaining contribution from ^{54}Fe, the signal of $^{56}Fe_{measured}$ was plotted against $\frac{^{54}Cr}{^{52}Cr\,T}$ to determine if there was any correlation. If all the contribution of ^{54}Fe is successfully corrected for, then there should be no correlation between $^{56}Fe_{measured}$ and $\frac{^{54}Cr}{^{52}Cr\,T}$. During this study no correlation was observed between $^{56}Fe_{measured}$ vs $\frac{^{54}Cr}{^{52}Cr\,T}$.

2.3.1.4 Loading samples

Samples were loaded using a single rhenium filament assembly for measurement on the TIMS. Rhenium filaments were outgassed by heating under a vacuum to remove adsorbed gaseous species. The outgassed filaments were stored at atmosphere for at least 2 days before loading.

One ug of sample (2 μl of 500 ppm solution in 6M HCl) was loaded onto the centre of the filament and a filament loading device was used to heat the filament at 0.7 A until the sample was dry (10 min). Following this, 1 μl of 500 ppm Al solution (in 2% HNO_3) was loaded directly on top of the sample and allowed to dry down at 0.7 A (10 min). The presence of small quantities of Al helps to increase the stability of Cr ionisation during measurement. Once the Al solution was completely dried down, 2 μl of a Silica-gel-H_3BO_3 mixture was placed on top of the sample and was dried at 0.7 A. This mixture was ultrasoniced for 45 mins prior to use. When the Silica-gel-H_3BO_3 mixture turned white (8 min), an additional 1 μl was added to ensure complete coverage of the sample. After the sample was completely dry and homogenised (18 min) the current was slowly increased to 1.2 A and held at this current for 30 seconds, before the current was slowly increased again to 1.8 A and the filament was allowed to flash heat for 5 seconds before the current was immediately switched off.

2.3.1.5 TIMS measurement procedure

Samples were measured on a Triton Thermo Scientific instrument at the University of Oxford. To achieve Cr ionisation, filaments were heated at a rate of 30 mA/min to 1800 - 1950 mA. Collector gains were measured once a day during filament heating. Ion beam intensities were simultaneously monitored using Faraday cups with 10^{11} Ω resistors. The signal strength of the beam on the centre cup (CC) of line 1 (^{52}Cr) at the beginning of each measurement was typically between 7 - 10 V. The ion beam was focused using the autofocus function and wheel finetuning was carried out to ensure that the maximum signal was being achieved. The peaks were centred on CC for ^{52}Cr (line 1) and ^{50}Cr (line 2) and a peak scan was conducted before each measurement. Peak centring on line 2 was added to the method protocol after October 2024. Samples were measured over 30 blocks,

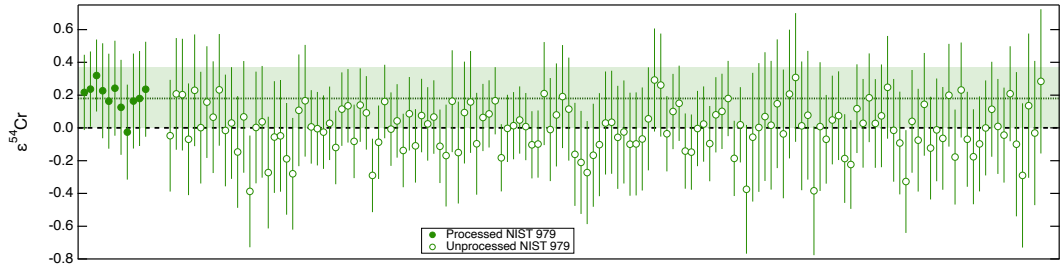

Figure 2.3: Measured ε^{54}Cr compositions of unprocessed and processed standard NIST-979. Processed standards underwent the column chemistry procedure described in section 2.2 and are depicted as solid points. Unprocessed standards were measured throughout the course of this study and are depicted as open points. The green dotted line indicates the average value of the processed NIST-979 standards, and the green shaded region depicts the associated 2σ. The bold black dashed line indicates the average of all unprocessed NIST-979 standards.

each containing 20 cycles. Filaments were typically run twice. Within the measurement method a baseline was taken every block, a lens focus was carried out every 3rd block, and a peak centre on line 1 and line 2 was conducted every 5th block. Interblock heating was programmed to automatically heat the filament and increase the ion beam intensity if the signal fell to less than 80% the initial voltage. The integration time for each line was 8.389 s, and the idle time was 3 s. The abort intensity was programmed at 4 V.

Within each sample wheel, >7 standards of unprocessed standard NIST-979 were run to check for instrument drift and for error analysis.

2.3.1.6 Data analysis

The Cr isotopic data collected from measurement on the TIMS was processed offline. Initially an iron correction (equations 2.6 and 2.7) was applied to measured ^{54}Cr signals (line 1, H2) to recover the true ^{54}Cr signal without isobaric interference of ^{54}Fe. Following this, the correction detailed in equation 2.2 was applied to recover $\frac{^{54}Cr}{^{52}Cr}_T$ of each cycle. The calculated isotopic ratios from each cycle in a run were subjected to a 3SD filter to remove outliers. The final isotopic ratio reported is the weighted average of $\frac{^{54}Cr}{^{52}Cr}_T$ for each sample across repeated filament runs (to account for incomplete runs).

For calculation of ε^{54}Cr, the calculated $\frac{^{54}Cr}{^{52}Cr}_T$ of each sample was normalised to the average of NIST-979 standards that had also been processed through column chemistry. This is because NIST-979 standards subjected to column chemistry exhibited systematically

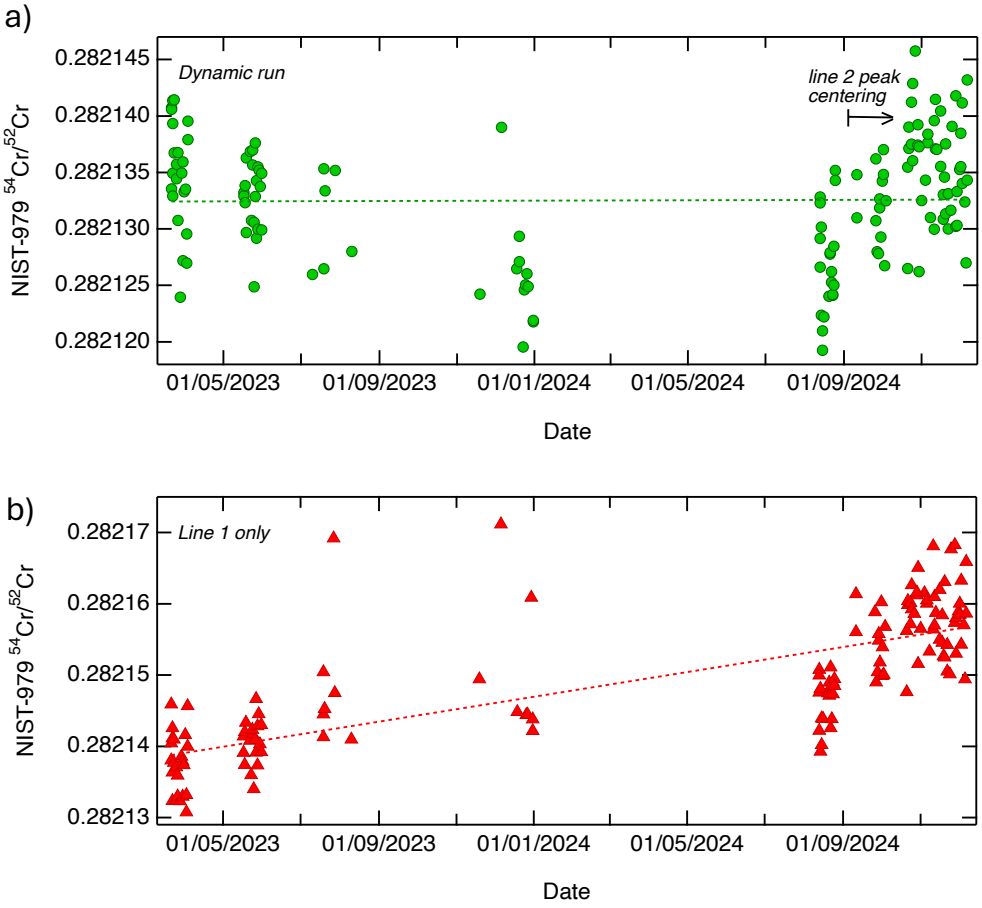

Figure 2.4: NIST-979 standard compositions from a) dynamic measurements on the TIMS using line 1 and line 2, and b) NIST-979 compositions recovered from using only line 1 data collected from the dynamic run on the TIMS. Lines of best fit are given by dotted lines to show the drift over time. The long term drift observed in the line 1 measurements indicates the effectiveness on the dynamic run in reducing long term drift. R chondrite MIL 07440 was measured in the time period 01/09/2023 - 01/09/2024 where drift was observed in the dynamic run, before line 2 peak centring was added into the measurement protocol.

heavier ε^{54}Cr values (0.19 ± 0.19, 2SD (2σ)) when normalised to unprocessed NIST-979 samples (average of 0.00 ± 0.26, 2σ) (Fig. 2.3). The cause of this isotopic shift is likely due to effects associated with the column chemistry procedure, however, Larsen et al. (2016) note that any associated effects from incomplete Cr recovery should lead to negative shifts in isotopic ratios.

2.3.1.7 Accuracy and precision

Errors for each chondrite subsample are given as the 2SD (2σ) of the unprocessed NIST-979 standards run during the same time period. This error range spans ±0.22 - 0.39 ε^{54}Cr.

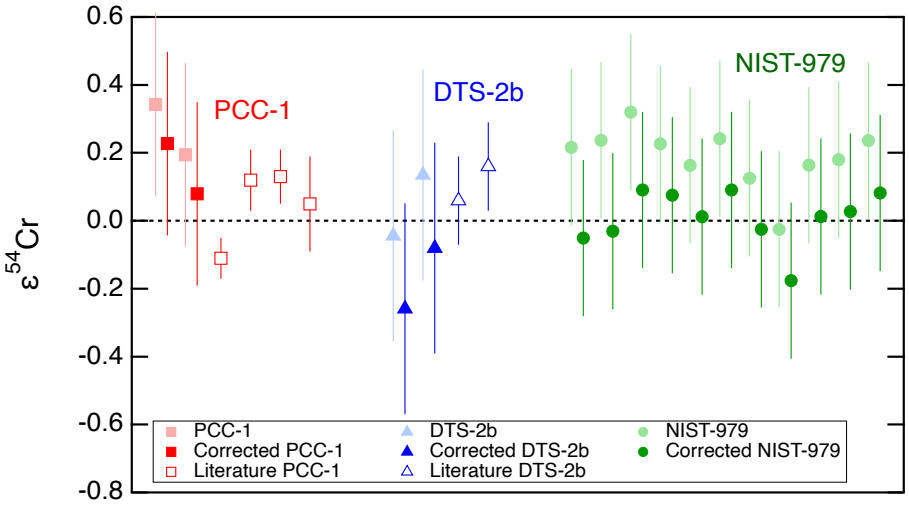

Figure 2.5: Processed standard values compared to those reported in the literature. Shaded points represent the measured ε^{54}Cr compositions of NIST-979, PCC-1, and DTS-2b. Solid points represent the compositions of these standards after a correction was applied for column-induced fractionation. Open points display standard compositions reported in the literature by Zhu et al. (2021b), Zhu et al. (2019a), van Kooten et al. (2021), Qin et al. (2010) and Schneider et al. (2020).

The $\frac{^{54}Cr}{^{52}Cr}$ compositions of unprocessed NIST-979 measured throughout this study for error analysis and drift observation are displayed in Fig. 2.4a. Compared to the long-term drift observed in $\frac{^{54}Cr}{^{52}Cr}$ calculated from only Line 1 measurements (57 ppm, Fig. 2.4b), there is minimal long-term drift observed from $\frac{^{54}Cr}{^{52}Cr}$ calculated from both Line 1 and Line 2 (3.5 ppm), demonstrating the success of a Dynamic run in addressing issues relating to variations between, and degradation of, collectors.

Drift of the instrument observed between 01/09/2023 - 01/09/2024 via the Dynamic run is due to uncorrected drift of Line 2 related to the lack of peak centring on the centre cup of Line 2. Peak centring on this cup was introduced in October 2024 and is indicated on Fig. 2.4a.

External reproducibility of this work was assessed by measuring isotopic and terrestrial standards and comparing them to published literature. NIST-979 was routinely processed through column chemistry over the course of this study, and the measured ε^{54}Cr compositions of these standards is shown in Fig. 2.5. Terrestrial samples DTS-2b and PCC-1 were also measured and the recovered ε^{54}Cr values are compared to those reported in literature data in Fig. 2.5. Processed terrestrial standards display larger errors ($\pm$ 0.27, 2σ) than

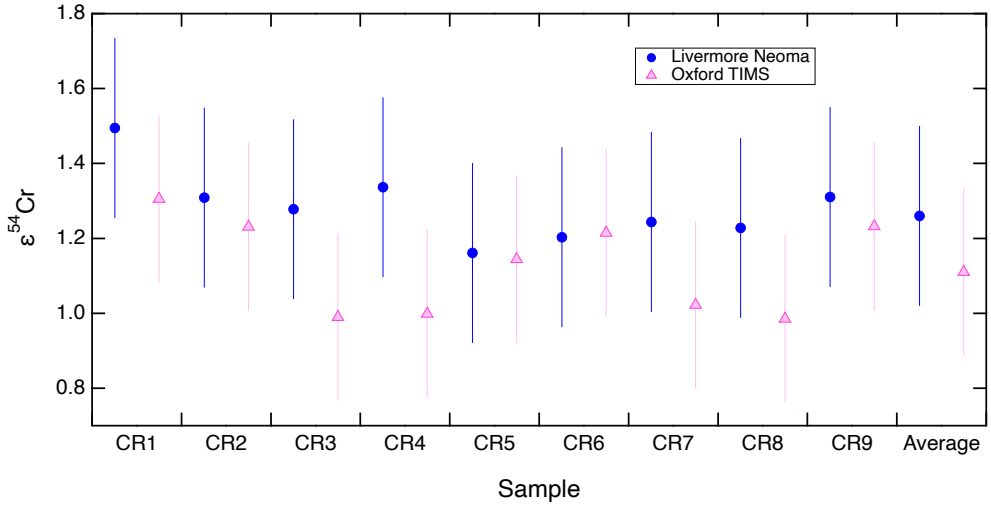

Figure 2.6: ε^{54}Cr compositions of CR MIL 090001 subsamples measured on the TIMS at the University of Oxford compared to those measured on a Neoma™ Multicollector ICP-MS at LLNL.

those reported in literature (± 0.06 - 0.14, 2σ), however, this is likely due to the errors reported in this study being the 2σ of the local NIST-979 standard, whilst literature errors are the 2σ of repeated measurements of the standards (often n>4). Direct comparison of these types of errors is therefore not practical due to the low number of samples processed in this study (n=2 of both DTS-2b and PCC-1). Both terrestrial standards and NIST-979 standards which have been subjected to column chemistry routinely display an isotopically heavier signature compared to unprocessed NIST-979 (normalising standard, Figs. 2.3 and 2.5). As described previously, isotopic fractionation due to insufficient yields during column chemistry typically results in isotopically lighter samples which are not observed here, and therefore cannot fully explain the observed heavier signatures. However, PCC-1 and DTS-2b values reported by Zhu et al. (2021b), Zhu et al. (2019a), van Kooten et al. (2021), Qin et al. (2010), and Schneider et al. (2020) also show slightly elevated ε^{54}Cr compositions. After correction for heavy isotopic enrichment (discussed in section 2.3.1.6), compositions of PCC-1 reported in this study agree within error with literature values and DTS-2b samples agree within error to all but one literature value, indicating that results in this study are comparable to published literature.

Duplicated measurements of processed chondrite subsamples by external laboratories also confirm the external reproducibility of the ε^{54}Cr results reported in this study. Subsamples of CR chondrite MIL 090001 were measured using the TIMS at the University of

Oxford and on a Neoma™ Multicollector ICP-MS located at Lawrence Livermore National Laboratory. Measurements on the Neoma™ were conducted by Dr. Jan Render using sample splits. A comparison of the results are shown in Fig. 2.6. All subsamples measured using the TIMS plot within error to those measured on the Neoma™, indicating that these results are reproducible. Additionally, this shows that the sample purification was effective as measurement on MC-ICP-MS typically requires near-total removal of Fe (Torrano et al., 2021). The errors from both techniques are also comparable, with a calculated 2σ of $\pm$ 0.22 from measurements on the TIMS and $\pm$ 0.21 from the Neoma™.

2.3.2 Plateau Volatile Element concentrations and column yields: Quadrupole ICP-MS

Compositions of each chondrite subsample were measured pre- and post-chemistry to determine initial PVE concentrations, column chemistry yields, and the purity of the Cr isolated from each sample. Initial PVE and Cr compositions were measured from 0.8 ml aliquots of each subsample after digestion, and column chemistry purity and yields were measured from small (<1.5%) aliquots of the processed subsamples.

Samples were measured for trace element compositions by inductively coupled plasma mass spectrometry (ICP-MS). A quadrupole Perkin Elmer NexION350D ICP-MS was used, which was coupled with an Element Scientific prepFAST M5 autosampler and autodiluter. Indium and rhodium were added as internal standards used to normalise for instrument sensitivity and drift. Cr and Zn were measured pre-chemistry and diluted manually by a factor of approximately 8, and then by a factor of 50 using the prepFAST. Te, Ge, Sn, Se, Cd, and Pb were measured undiluted. Post-chemistry measurements of Cr, Mg, Fe, Ti, V, Na, Ni, and Ca were diluted manually by a factor of 60. Repeated analysis of in-house standards provided reproducibilities of <4%, calculated by twice the Relative Standard Deviation (2RSD).

2.3.3 Determination of matrix volume fraction

Following studies by Hellmann et al. (2020) and Bryson and Brennecka (2021), the matrix volume fraction present in each chondrite subsample was assumed to equal their

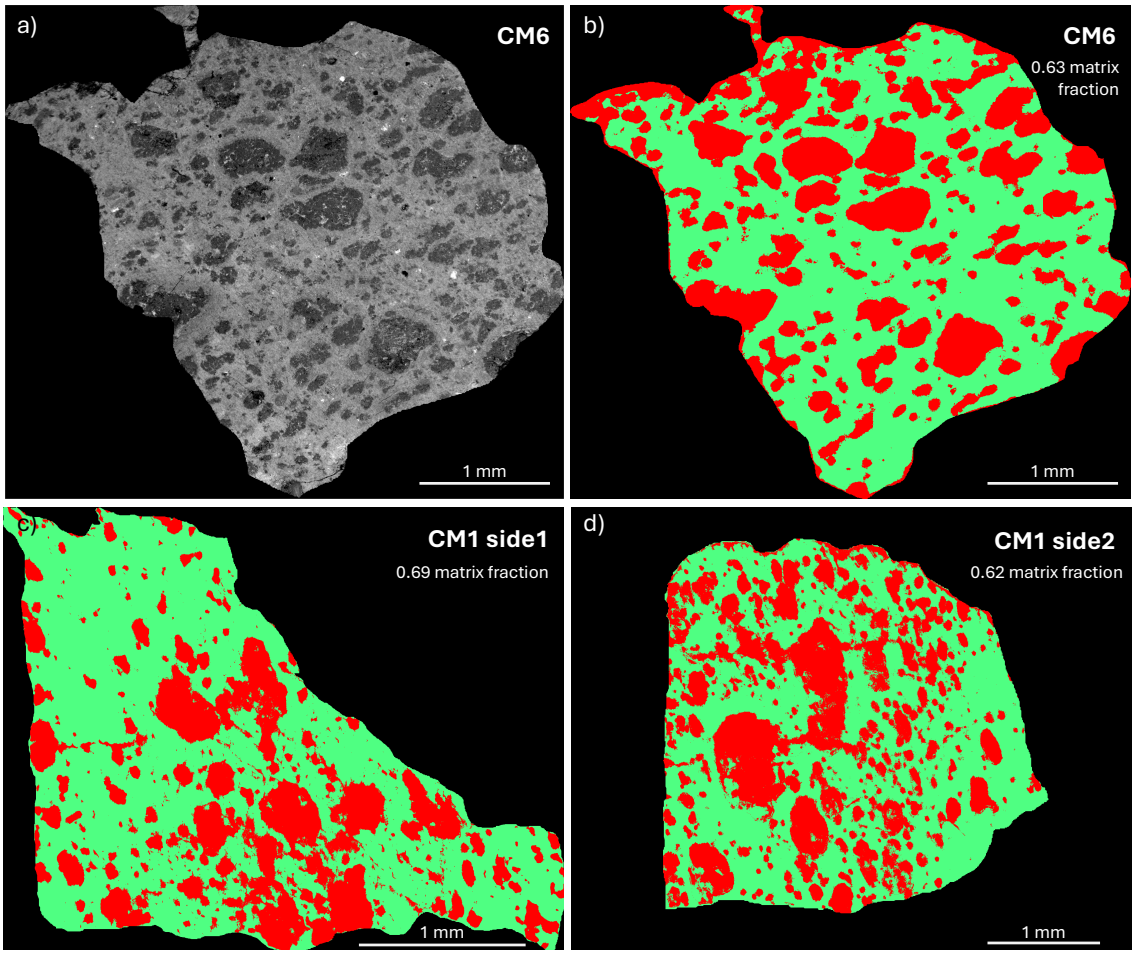

Figure 2.7: BSE and SE images of different CM chondrite subsamples used to determine matrix proportions. a) BSE image of subsample CM6. b) Processed BSE image of CM6, where regions of matrix (green) and non-matrix (red) were identified using *Trainable Weka Segmentation*. This recovers a matrix fraction of 0.63. c) Processed SE image of one side of the CM1 subsample chip, which recovers a matrix fraction of 0.69. d) Processed SE image of a different side of the CM1 subsample chip, which recovers a matrix fraction of 0.62.

CI-normalised PVE concentration (see Fig. 1.5b). A range of PVEs were measured in this study including: Zn, Te, Ge, Sn, Se, Cd, and Pb. Despite all PVEs displaying good correlation with matrix fraction in the literature (Hellmann et al., 2020), Te, Ge, and Pb are present in low abundances in measured subsamples (typically $<$1 ppm) and Sn tends to provide calculated matrix fractions greater than 1. Due to these factors, this study reports matrix fraction as the Zn concentration of each subsample (normalised to CI), though the measured concentrations of Te, Ge, Sn, Cd, Se, and Pb are also provided.

To assess whether imaging provides better estimates of matrix proportion, a FEI Quanta 450 Scanning Electron Microscope (SEM) was used to image the individual subsamples of

CM chondrite MIL NWA 11345 before it was digested. This was conducted at Lawrence Livermore National Laboratory. An accelerating potential of 15 and 20 kV was used, with a 5.5 μm spot size, and dwell time of 3 s. Scanning electron (SE) and backscattered electron (BSE) images of each subsample chip were taken. The matrix amount was determined by analysis of the BSE images, however, if the sample chip orientation or surface topography resulted in a poor image, the SE image was used instead.

Images were processed using the *Trainable Weka Segmentation* plugin in ImageJ. As differences in contrast in BSE images reflect changes in the mean atomic number (and therefore in composition), the algorithm was trained to identify regions of matrix and non-matrix by these differences. An example of this process is seen in Fig. 2.7a and b. Total calculated matrix proportions from image analysis are listed in section 4.3 and roughly agree with proportions calculated by PVE concentrations. Importantly, images of different sides of the same subsample (CM1) provide a calculated matrix estimate range of ∼8%, which is comparable to the range of some of the chondrite subsamples measured in this study (see Fig. 2.7c, d, and section 3.3). This demonstrates the uncertainty associated with calculation of matrix by imaging of samples, as the heterogeneity of chondrites ensures that different sides of the same sample display differing matrix fractions. This problem is compounded by the inability of processing techniques to accurately identify all non-matrix components present in an image. To ensure all non-matrix components are identified, manual selection would be necessary which is time consuming and not feasible when working with large sample sets. Instead, calculation of matrix volume fraction via PVE abundances samples the entire chondrite subsample so is not biased by heterogeneous sections, and this method is able to represent contribution by components too small to identify (e.g., μm sized chondrule or CAI grains), supporting its use in this study.

2.3.4 Determination of matrix mass fraction

The matrix mass fractions of chondrite subsamples were calculated following the methods stated in Bryson and Brennecka (2021), based on the relationships proposed in Hellmann et al. (2020). This converts the matrix volume fraction recovered from CI-normalised PVE concentrations into a mass fraction using equation 2.9:

$$f = 1 - \frac{\rho_g}{\rho_b}(1 - x) \tag{2.9}$$

where f represents the matrix mass fraction present in a chondrite, ρ_g and ρ_b are the grain and bulk densities of each chondrite group, and x represents the matrix volume fraction present in a chondrite. The values of ρ_g and ρ_b for each chondrite group are provided in Table 2.7. The grain density of a chondrite is assumed to be equal to the density of non-matrix components (i.e., chondrules and CAIs) (Bryson and Brennecka, 2021). The bulk and grain densities have not previously been reported for R chondrites, therefore the matrix mass fractions of samples from this group were not calculated.

Chondrite group	**Bulk density** ρ_b (kg m^{-3})	**Grain density** ρ_g (kg m^{-3})
OC	3350	3650
CO	3000	3500
CV	3000	3500
CM	2300	2900
C2-Ung	1800	2550
CR	3100	3400

Table 2.7: Bulk density and grain density of chondrite groups used to calculate matrix mass fraction of subsamples. Values sourced from Bryson and Brennecka (2021) and references within.

2.4 Mixing line

To determine the Cr isotopic composition of chondrules and matrix in the measured chondrite subsamples, an isotopic mixing line was plotted through their coupled ε^{54}Cr compositions and PVE concentrations. This mixing line is derived below, from the equations 2.10 and 2.11:

$$I_B C_B = I_M C_M f + I_C C_C (1 - f) \tag{2.10}$$

$$C_B = C_M f + C_C (1 - f) \tag{2.11}$$

where I_B and C_B are the ε^{54}Cr compositions and Cr concentrations of the bulk chondrite, respectively. I_M and C_M are the ε^{54}Cr compositions and Cr concentrations of the matrix (M), respectively. I_C and C_C are the ε^{54}Cr compositions and Cr concentrations of the chondrules (C), respectively. f represents the mass fraction of matrix present in a chondrite, including R chondrites.

On a plot of ε^{54}Cr against Zn concentration (normalised to CI), I_B represents the ε^{54}Cr of samples, and the measured Zn concentration represents the Zn contribution from both chondrules and matrix. To fit equation 2.10 to samples on a plot of ε^{54}Cr vs Zn, we need to represent f in terms of Zn (normalised to CI), and take into account the contribution of chondrules towards the measured Zn concentrations. The concentration of Zn in chondrules of carbonaceous chondrites is calculated to be 36.8 μg/g (Hellmann et al., 2020), leading to a CI normalised value of ∼0.118. The Zn concentrations of NC chondrules have a measured average of 57.2 ppm (Rubin and Pernicka, 1989; Bollard et al., 2017), resulting in a CI normalised value of 0.183. To plot a mixing line on a graph of CI-normalised Zn concentrations, knowing that at least ∼0.118 (or 0.183) of the total Zn concentration of a sample is due to chondrules, it is possible to relate f to measured Zn concentrations using equation 2.12, where x represents the CI-normalised Zn concentration of a sample.

$$x = 0.882 f + 0.118 \tag{2.12}$$

Equation 2.12 is an empirical relationship based on Zn concentrations in CC chondrites and chondrules, and matrix mass fractions calculated by Hellmann et al. (2020), in a similar method as described in section 2.3.4. Importantly however, this is independent of ρ_g and ρ_b, allowing this conversion to be applied across all chondrite groups.

The composition of Cr in chondrules and matrix can be related by equation 2.13, where j represents the compositional ratio of chondrules to matrix in a chondrite.

$$C_C = C_M \times j \tag{2.13}$$

Values for j can vary between chondrite classes, Schneider et al. (2020) report an average chondrule Cr composition of 2960 pmm in a CC CV chondrite, whilst chondrules from a NC OC display a higher average of 4307 ppm. Rubin and Wasson (1987) measure the Cr composition of matrix in a carbonaceous CV chondrite to be ∼3100 ppm. These compositions provide j values of ∼1 and ∼1.39 for carbonaceous and non-carbonaceous chondrites, respectively.

Combining equations 2.10, 2.11 and 2.13 allows the ε^{54}Cr composition of samples (I_B) to be represented by the following equation:

$$I_B = \frac{I_M C_M f + I_C C_M j(1-f)}{C_M f + C_M j(1-f)} \tag{2.14}$$

Which, via substitution of equation 2.12, can be evaluated to:

$$I_B = \frac{I_M(x-0.118) + I_C j(1-x)}{(x-0.118) + j(1-x)} \tag{2.15}$$

When equation 2.15 is fit through measured ε^{54}Cr (I_B) and Zn concentrations (x) of subsamples of chondrite groups, and I_M and I_C are allowed to freely vary to best fit the data, the best fit values for I_M and I_C can be evaluated for each chondrite group. This provides estimates of the ε^{54}Cr composition of chondrules and matrix present in a chondrite, allowing me to determine if there is a difference in the isotopic compositions of different components in different chondrite groups.

Fitting of equation 2.15 is done through the *Curve fitting* package in IGOR Pro®. Parameters I_M and I_C are allowed to freely vary, but are given initial starting values of either: 1.56 and 0.58, respectively, if the subsamples appear to show a positive trend (based on the composition of CI matrix and pooled CV chondrules); or the average ε^{54}Cr composition of the subsamples if there is no obvious trend. Uncertainties associated with the fit of the mixing line are displayed as a 95% confidence envelope, and errors associated with the recovered chondrule and matrix ε^{54}Cr compositions are provided as 2σ.

Chapter 3

Accretion in the non-carbonaceous reservoir

3.1 Introduction

3.1.1 Background

The mechanisms controlling terrestrial planet formation in the protoplanetary disk are highly debated, and to date, no consensus has been reached on a model that explains all the dynamical and chemical constraints observed in inner solar system bodies (Levison et al., 2015; Lambrechts et al., 2019; Johansen et al., 2021). The classical model of terrestrial planet formation involves collisions and accretion of increasingly larger planetesimals from an initial feedstock of km-sized bodies. This model can successfully reproduce the required size distribution and orbits of the planets observed today (Nesvorný et al., 2021; Raymond and Morbidelli, 2022). Planetesimal formation by this mechanism is expected to result in non-carbonaceous (NC) isotopic signatures of the terrestrial planets due to the modelled accretion of local, inner solar system derived material (assumed to display NC-like signatures) (Morbidelli et al., 2025). NC-like ε^{54}Cr and ε^{50}Ti compositions are observed in the terrestrial planets, the Moon, and inner solar system asteroids, consistent with their formation in the inner regions of the protoplanetary disk via planetesimal accretion (Fig. 1.4a). In particular, Earth most closely matches the isotopic composi-

tions of enstatite chondrites (ECs) (Warren, 2011; Dauphas, 2017; Dauphas et al., 2024; Burkhardt et al., 2021). Interestingly, bulk silicate Earth (BSE) and bulk silicate Mars (BSM) display isotopic signatures that are not wholly consistent with a NC origin, as their Mo and Zn isotopic compositions plot between the NC and CC trends (Fig. 1.4b). Studies explain this deviation as the effect of late-stage, CC-like impactors modifying the BSE composition towards a *s*-process enriched signature (Budde et al., 2016a; Dauphas, 2017; Burkhardt et al., 2021; Savage et al., 2022; Steller et al., 2022; Martins et al., 2023).

Recently however, isotopic studies of μ^{48}Ca, μ^{54}Fe, and μ^{30}Si have suggested that the trend towards CC-like compositions seen in BSE and BSM could be due to formation of the terrestrial planets by pebble accretion, which allows pebbles sourced from the CC-like outer regions of the protoplanetary disk to contribute towards 15 - 42 % of Earths total mass (Schiller et al., 2018, 2020; Onyett et al., 2023). This eliminates the requirement of impactors delivering CC-like, volatile enriched material to BSE that hinders traditional models of planetesimal accretion. Pebble accretion is generally accepted as the dominant mechanism of planet formation of the outer solar system's gas and ice giants due to its ability to allow planets to form sufficiently large masses at greater heliocentric distances within the lifetime of the protoplanetary disk (Levison et al., 2015). A unifying theory of pebble accretion across the protoplanetary disk is then highly attractive as it would imply common methods of accretion in the inner and outer solar system. Determining the mechanisms of chondrite accretion would then help to constrain different parameters of the protoplanetary disk, e.g., turbulence, dust-to-gas ratio, and the disk's physical structure.

Current work seeks to resolve whether the terrestrial planets of the inner solar system formed via pebble or planetesimal accretion (Fig. 3.1). Studies have attempted to use compositional (Dauphas et al., 2024), dynamical (Levison et al., 2015; Lambrechts et al., 2019; Johansen et al., 2021), and chronological (Johansen et al., 2023) constraints to determine the accretionary mechanism dominant in the inner solar system. Characterising the isotopic compositions of chondrites which are thought to form in the inner solar system, and their chondrule and matrix compositions, would allow us to investigate the provenance of material that is present in the terrestrial planet forming region. If pebble

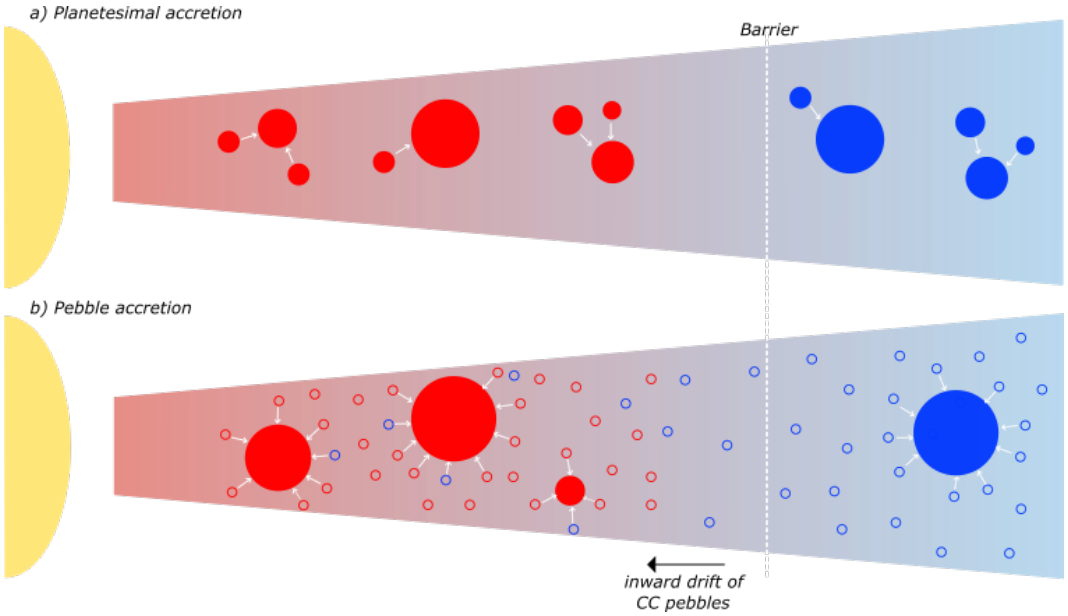

Figure 3.1: Schematic depicting the mechanisms of a) planetesimal vs b) pebble accretion. Planetesimal accretion involves collisions between successively larger planetesimals in a local reservoir. Pebble accretion involves the accretion of cm - mm sized pebbles onto rapidly growing planetesimals. These pebbles are sourced form across the disk, with expected inward drift of CC-like pebbles sourced from the outer solar system into the inner solar system. Not to scale.

accretion played a significant role in the formation of inner solar system bodies, signatures of contribution from pebbles sourced from the outer solar system would be reflected in the isotopic compositions of NC chondrites and their components.

NC chondrites are thought to form in the inner regions of the protoplanetary disk, at 0.6 - 2.2 Ma, between 1.94 - 2.8 AU (Desch et al., 2018). These chondrites are considered to represent the composition of material present in the inner solar system and typically display r-process depleted isotopic signatures. NC chondrites exhibit volatile-poor compositions linked to their inner solar system origin, though recent studies have shown elevated water contents in the ECs (Piani et al., 2020). NC chondrites fall into three main groups: the ordinary (OC), Rumuruti (R) chondrites, and ECs. Each group is differentiated by their chemical and isotopic compositions, petrology, mineralogy, and oxidation state.

The OCs are the most abundant NC chondrite, comprising 85% of all falls. This group is subdivided into the H, L, and LL classifications, with chondrites displaying high, low, or very low metal abundances, respectively. OCs display mineralogical assemblages dominated by pyroxenes, olivines, and various amounts of metal. These chondrites contain high

proportions of chondrules (∼80%) (Marrocchi et al., 2020), specifically FeO-rich type II chondrules, which indicate chondrule formation in an oxidising environment (Krot et al., 2014). Chondrules and matrix in OCs are shown to display very similar, restricted ε^{54}Cr compositions (Trinquier et al., 2007, 2008; Pedersen et al., 2019; Qin et al., 2010), indicating little isotopic variation in chondritic components. Recent studies suggest that the Mg/Si ratios of chondrules and matrix in OCs appear complementary, providing an additional chemical constraint suggesting that they sample a restricted reservoir (Ebel et al., 2024), similar to mechanisms described in planetesimal accretion.

R chondrites display similar bulk chemical compositions as OCs but are characterised by: comparatively higher matrix abundances (∼50%); the absence of Fe,Ni metal; enrichments in Zn and Se; and elevated Δ^{17}O compositions (Krot et al., 2014). R chondrites also display enriched ε^{54}Cr signatures compared to OCs, with compositions trending towards CC-like values (Fig. 3.2) (Larsen et al., 2011; Zhu et al., 2021b). R chondrites are thought to accrete at greater radial distances and at later times compared to OCs due to their r-process enriched signature and high degrees of oxidation (Desch et al., 2018). Due to the differences in timing and location of R chondrite parent body formation compared to OCs, this group provides an insight into how chondrite formation may have varied spatially and temporally in the inner solar system. Their enrichment in ^{54}Cr could indicate the contribution of inwardly drifting CC-like material, similar to what is proposed in models of pebble accretion.

ECs are the third major NC group, subdivided into EH and EL based on the presence of either high and low metal abundances, respectively. The ECs display a very reduced mineralogy, with abundant sulfides and enstatite-rich chondrules. Originally thought to be depleted in water, recent studies indicate that ECs contain large amounts of hydrogen (Piani et al., 2020). This, alongside observations that BSE most closely matches ECs in oxygen and nitrogen isotopic compositions, and that its composition can be modelled by accretion of EC-like ε^{54}Cr, ε^{50}Ti, ε^{48}Ca, ε^{64}Ni, ε^{92}Mo, ε^{100}Ru, and μ^{142}Nd compositions (Javoy, 1995; Dauphas, 2017; Dauphas et al., 2024), provides a compelling argument that ECs make up the main building blocks of Earth. This negates the requirement for major CC contribution during accretion to explain the volatile contents of BSE, arguing against

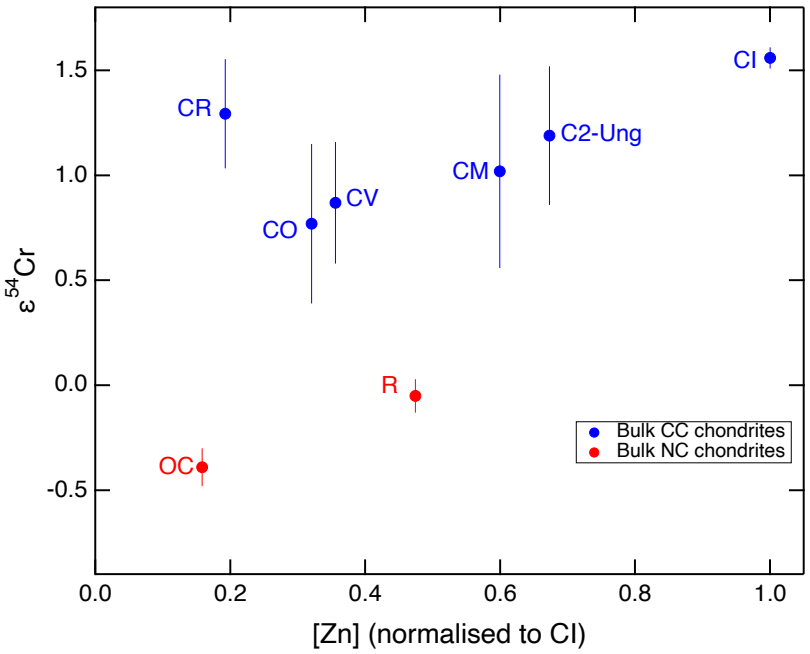

Figure 3.2: Bulk ε^{54}Cr and CI-normalised Zn compositions of NC and CC chondrites. R chondrites display enriched ε^{54}Cr compositions compared to OCs. Data is sourced from references listed in Fig. 1.6.

the action of pebble accretion in the inner solar system .

It is clear that the bulk compositions of different NC groups provide contradictory evidence for which mechanisms of planetesimal accretion were dominant in the inner solar system. Instead, determining the isotopic composition of the chondrules and matrix in these chondrites may allow us to explore their provenance, and gain insight into the dynamics of solid movement in the inner protoplanetary disk. This will enable us to determine whether the composition of material present in the inner solar was isotopically homogenous over time, favouring the action of planetesimal accretion, or whether some NC chondrites record evidence of significant CC-like contributions, implying that pebble accretion played a major role in terrestrial planet formation.

3.1.2 This work

In this chapter I will probe the formation history of chondrites in the inner solar system by measuring the coupled ε^{54}Cr and Zn concentration of OC LoV 171 and R chondrite MIL 07440. These results will be used to determine the compositions of chondrules and matrix in OC and R chondrites, and will allow me to explore whether each chondrite

group accreted from locally derived (isotopically homogenous) material. Any potential contribution from the CC-reservoir towards the inner solar system is discussed, with ε^{54}Cr compositions of R chondrites providing evidence for a small CC-like enrichment. The carrier of the ε^{54}Cr anomaly is not identified in this work, however, the magnitude of the observed enrichment is discussed and provides an argument against terrestrial planet formation via pebble accretion in the NC-reservoir.

3.2 Methods

Two NC chondrites, OC LoV 171 and R MIL 07440, were analysed to determine the coupled ε^{54}Cr isotopic compositions and PVE concentrations of their subsamples. LoV 171 belongs to the LL group of OCs due to its low metal content.

OC LoV 171 was cut into 11 subsamples, digested, and purified by Dr. Greg Brennecka and Dr. Jan Render at Lawrence Livermore National Laboratory (LLNL), USA. These subsamples ranged in mass between 14.1 - 34.2 mg. Yields of 73 - 100% were achieved during column chemistry. Measurements of sample masses, column chemistry yields, and concentrations of Cr, Zn, Ge, Cd, Sn, and Pb were conducted at LLNL. Cr isotopic measurements were conducted on the purified subsamples using the TIMS at Oxford.

I acquired a 860 mg sample of R chondrite MIL 07440 from the Johnson Space Centre (JSC) (loan no. 3712) and processed it at the University of Oxford. The sample was cut into 16 subsamples and 13 were used in this study, ranging in weight between 13.7 - 46.6 mg. These subsamples were digested in the protocol described in section 2.1.3, and a 0.8 ml aliquot was preserved for determining PVE concentrations and initial Cr abundance. A 0.5 ml aliquot was then subjected to the Cr purification procedure detailed in section 2.2. Yields of 69 - 97% were achieved during column chemistry, with 13 subsamples displaying yields greater than 80%. Initial Cr concentrations, PVE abundances, and purity and yield of the column chemistry were measured using Quadrupole ICP-MS, as described in section 2.3.2.

The column chemistry associated with the R chondrites had a procedural blank of 100 ng Cr which is higher than other studies (e.g., Torrano et al. (2024)), but insignificant compared to the total amount of measured Cr (20 - 30 μg).

Matrix mass fractions were calculated using the CI-normalised Zn concentrations of each subsample as described in section 2.3.4.

For calculation ε^{54}Cr, normalisation to unprocessed NIST-979 standards measured during the same period was used in this chapter.

Since LoV 171 was purified at LLNL via a slightly different procedure to the one stated

in section 2.2, and the isotopic shift to heavier values of ε^{54}Cr observed in standards is likely due to the column chemistry procedure, it would not be appropriate to normalise the collected ratios to NIST-979 standards processed using the protocol developed at Oxford.

R chondrite MIL 07440 was also normalised to unprocessed NIST-979 standards. This was due to large magnitude short-term drift of the TIMS observed in the $\frac{^{54}Cr}{^{52}Cr}$ of unprocessed NIST-979 standards during the measurement time period between 01/09/2023 - 01/09/2024 (see Fig. 2.4). No processed NIST-979 standards were run during this time period, so it was not possible to correct for both instrument drift and the fractionation induced during column chemistry. In order to correct for the effect of instrument drift, the unprocessed NIST-979 standards measured during this time period were instead used for normalisation.

An isotopic mixing line was fit through the ε^{54}Cr and CI-normalised Zn compositions of subsamples of LoV 171 and MIL 07440 to determine the ε^{54}Cr composition of chondrules and matrix in each chondrite. Details of the mixing line are provided in section 2.4.

The bulk ε^{54}Cr composition and CI-normalised Zn concentration of each chondrite group are calculated using the weighted average of their subsample compositions. The error associated with the bulk ε^{54}Cr composition is the uncertainty associated with the measurement of the isotopic compositions of the subsamples (as described in section 2.3.1.7).

3.3 Results

3.3.1 LL chondrite LoV 171 chemical and isotopic composition

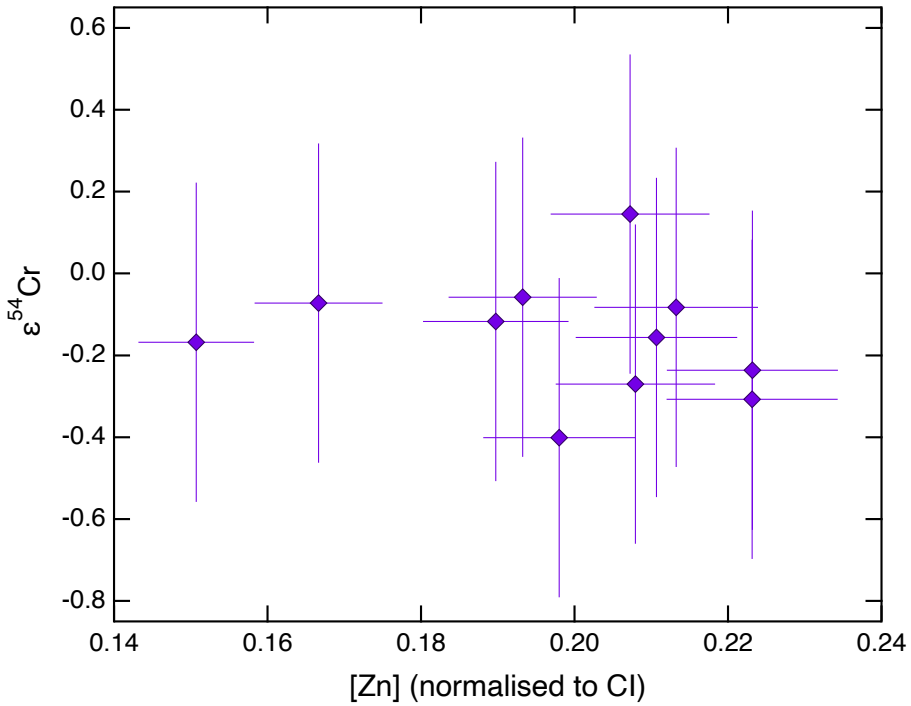

Figure 3.3: Calculated matrix volume fraction of subsamples of OC LoV 171, represented by their CI-normalised Zn concentration, plotted against their ε^{54}Cr composition.

The coupled ε^{54}Cr and PVE composition of 11 subsamples of LL chondrite LoV 171 are reported in Table 3.1. The subsamples span a range of ε^{54}Cr compositions between -0.4 - 0.15, and Zn concentrations between 47 - 67 ppm, resulting in a calculated matrix volume fraction range of 0.151 - 0.223 and mass fraction range of 0.075 - 0.154 (Tables 3.1 and 3.2).

The range of matrix volume fractions in LoV 171 subsamples displays a RSD of 22.9%, indicating a heterogenous population of subsamples (Stracke et al., 2012).

The bulk ε^{54}Cr composition of LoV 171 is -0.16 ± 0.39 and the bulk Zn concentration is 62 ppm. The average matrix volume fraction of the subsamples was 0.199.

The ε^{54}Cr compositions and matrix fractions of LoV 171 subsamples are displayed in Fig. 3.3. There appears to be no correlation between matrix fraction and Cr isotopic compositions, with subsamples roughly defining a flat line (as opposed to a random scatter).

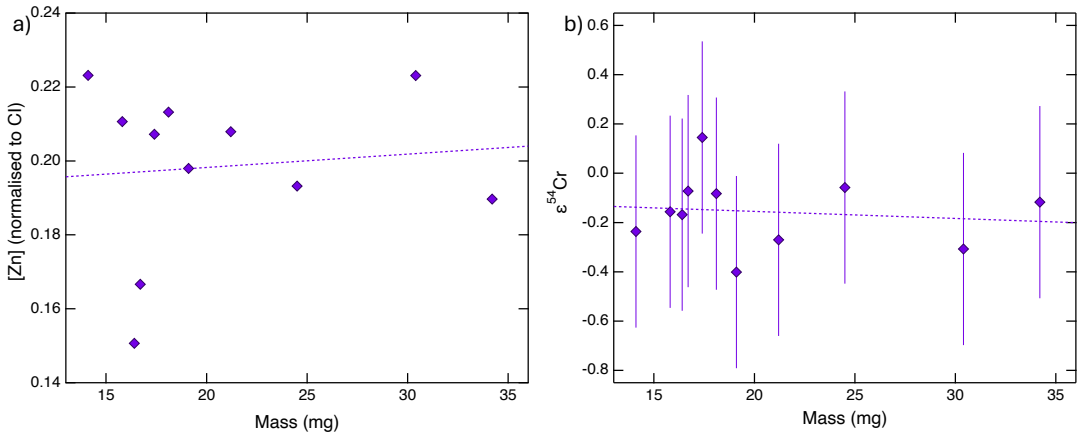

Figure 3.4: Subsample masses of OC LoV 171 plotted against a) CI-normalised Zn concentrations and b) ε^{54}Cr compositions. A line of best fit is plot through both plots.

This is supported by a calculated Pearson correlation coefficient (ρ) of -0.18, indicating little correlation between the ε^{54}Cr value and matrix fraction of the different OC subsamples.

There is also no apparent relationship between the mass of each subsample and the ε^{54}Cr composition or calculated matrix fraction (Fig. 3.4). A linear best fit line plotted through the ε^{54}Cr and Zn compositions of the subsamples shows a very weak correlation with mass, indicating the absence of a strong relationship. Lower subsample masses (<25 mg) appear to show greater variation in Zn concentrations.

I.D.	ε^{54}Cr	Cr (ppm)	Zn (ppm)	Ge (ppm)	Cd (ppm)	Sn (ppm)	Pb (ppm)
	±0.39 2σ	±5% 2RSD	±5% 2RSD	±5% 2RSD	±5% 2RSD	±5% 2RSD	±5% 2RSD
LVA	-0.07	4708	52.0	0.34	0.05	0.42	0.53
LVB	-0.08	6250	66.5	0.38	0.03	0.48	0.45
LVC	-0.16	5562	65.7	0.29	0.06	0.48	0.49
LVD	-0.40	5693	61.8	0.42	0.03	0.39	0.46
LVE	-0.17	5151	47.0	0.18	0.06	0.42	0.84
LVF	-0.06	5668	60.3	0.35	0.03	0.54	0.91
LVG	-0.24	5176	69.6	0.26	0.03	5.12	1.45
LVH	-0.27	6382	64.9	0.37	0.03	0.51	0.89
LVI	0.15	5497	64.7	0.37	0.03	0.43	0.59
LVJ	-0.31	5895	69.6	0.53	0.03	0.41	0.49
LVK	-0.12	5623	59.2	0.57	0.03	0.37	0.60

Table 3.1: ε^{54}Cr compositions and PVE concentrations of OC LoV 171 subsamples. σ = Standard deviation. RSD = Relative standard deviation.

I.D.	Matrix volume fraction	Matrix mass fraction
LVA	0.167	0.092
LVB	0.213	0.143
LVC	0.211	0.140
LVD	0.198	0.126
LVE	0.151	0.075
LVF	0.193	0.121
LVG	0.223	0.154
LVH	0.208	0.137
LVI	0.207	0.136
LVJ	0.223	0.154
LVK	0.190	0.117

Table 3.2: Calculated matrix volume fraction (Zn normalised to CI) and calculated matrix mass fraction of OC LoV 171 subsamples.

3.3.2 Mixing line through LL chondrite LoV 171

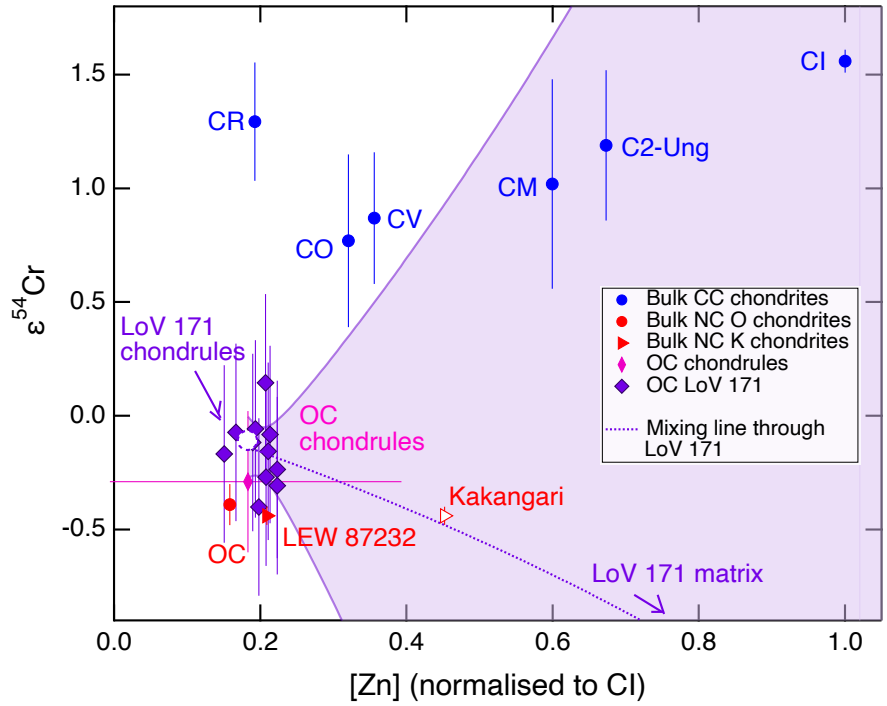

Figure 3.5: Plot displaying the composition of measured subsamples of OC chondrite LoV 171, the reported compositions of OC, R, and CC chondrites, and the average reported composition of OC chondrules. A mixing line has been fitted through subsamples of LoV 171 (purple line) with a shaded 95% confidence interval. Bulk chondrite and chondrule data is sourced from Zhu et al. (2023) and references listed in Fig. 1.6.

An isotopic mixing line was fit though the measured subsamples of LoV 171, and the results are displayed in Fig. 3.5. Details of the mixing line are listed in section 2.4. The average ε^{54}Cr composition of the subsamples, -0.16, was used as the initial isotopic composition of chondrules and matrix due to no obvious trend in the data. Values of 0.183 and 1.39 were used for the concentration of Zn in chondrules (normalised to CI) and the ratio of Cr in chondrules:matrix, respectively, and these values were held constant.

The best fit line and generates a ε^{54}Cr composition of -1.45 ± 5.37 for matrix and -0.14 ± 0.13 for chondrules. This line also has a poor fit demonstrated by large 95% confidence interval.

3.3.3 R chondrite MIL 07440 chemical and isotopic composition

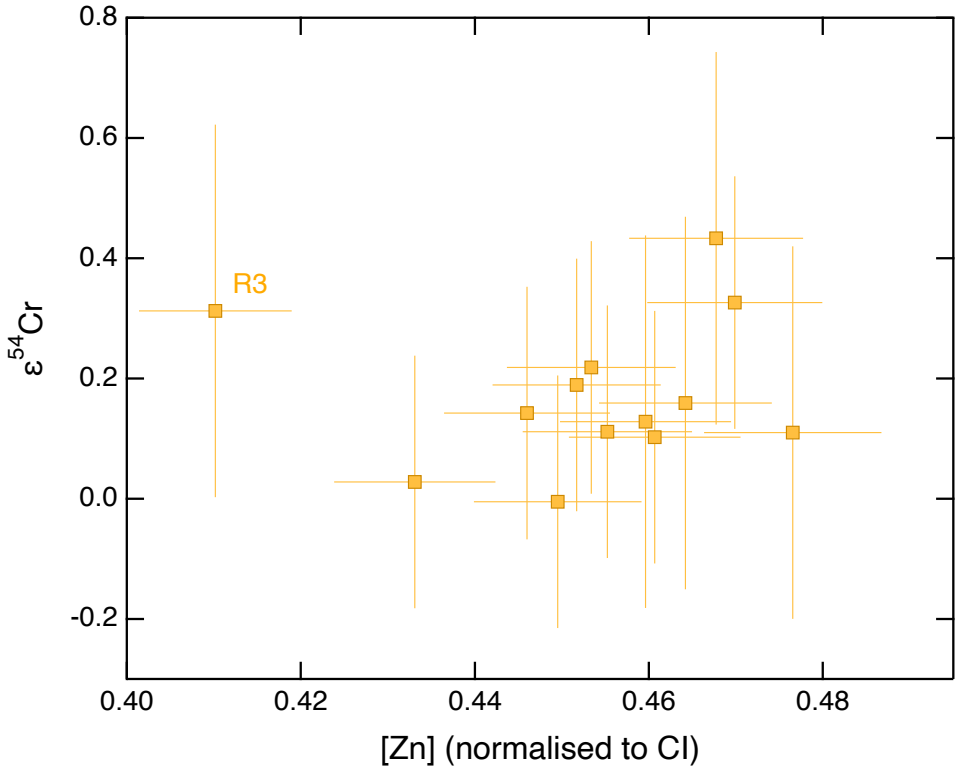

Figure 3.6: Calculated matrix volume fraction of subsamples of R chondrite MIL 07440, represented by their CI-normalised Zn concentration, plotted against their ε^{54}Cr composition.

The coupled ε^{54}Cr and Zn composition of 10 subsamples of R chondrite MIL 07440 are reported in Table 3.3. The subsamples span a range of ε^{54}Cr compositions between -0.04 - 0.33, and Zn concentrations between 128 - 148 ppm, resulting in a calculated matrix volume fraction range of 0.410 - 0.477 (Table 3.4).

The range of matrix volume fractions in MIL 07440 subsamples displays a RSD of 4.5%, indicating a heterogenous population of subsamples (Stracke et al., 2012).

The ε^{54}Cr compositions and matrix fractions of MIL 07440 subsamples are displayed in Fig. 3.6. There appears to be a weak positive correlation between matrix fraction and Cr isotopic composition, with subsample R3 plotting apart from the trend. This is supported by a calculated ρ of 0.52 when considering all subsamples apart from R3, indicating correlation between the ε^{54}Cr value and matrix fraction of the different R subsamples. When subsample R3 is included, ρ is 0.06.

MIL 07440 has an average measured ε^{54}Cr of 0.18 $\pm$ 0.31 and a bulk Zn concentration of

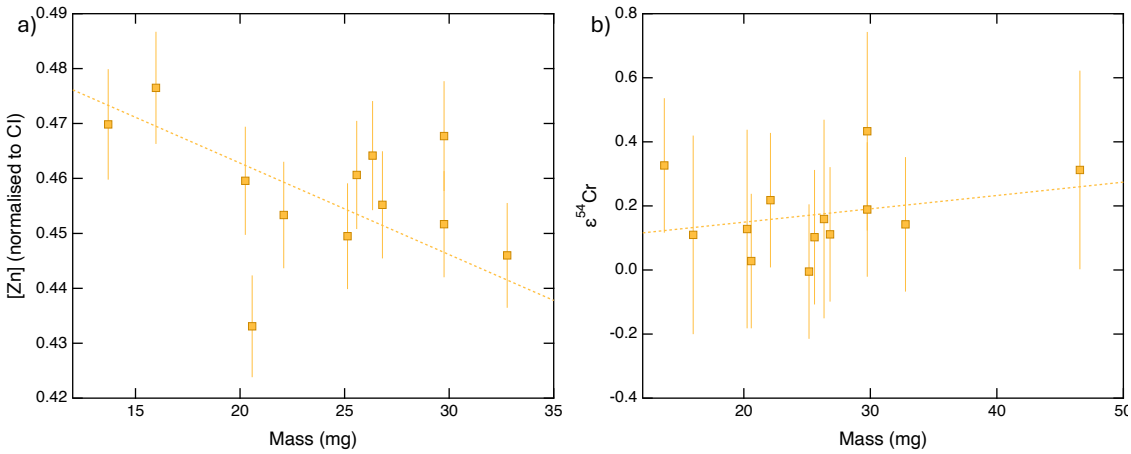

Figure 3.7: Subsample masses of R chondrite MIL 07440 plotted against a) CI-normalised Zn concentrations and b) ε^{54}Cr compositions. A line of best fit is plot through both plots.

142 ppm. The average matrix volume fraction of the subsamples was 0.454.

There is a weak trend between the mass of each subsample and its calculated matrix volume (Fig. 3.7a): as the mass of each subsample increases the calculated matrix volume fraction decreases slightly. This trend is seen when a linear best fit line is plotted through the points, however it is weak. There is no trend between subsample mass and ε^{54}Cr composition, as seen in Fig. 3.7b.

I.D.	ε^{54}Cr	Cr	Zn	Ge	Se	Cd	Sn	Te	Pb
		(ppm)	(ppm)	(ppm)	(ppm)	(ppm)	(ppm)	(ppm)	(ppm)
	±0.21	±3.51%	±2.14%	±1.55%	±2.22%	±1.21%	±0.55%	±2.01%	±0.98%
	2σ	2RSD	2RSD	2RSD	2RSD	2RSD	2RSD	2RSD	2RSD
R1*	0.11	3530	148.7	0.21	16.25	0.52	7.55	0.92	0.96
R2*	0.13	3550	143.4	0.21	15.45	0.54	7.30	0.83	0.93
R3*	0.31	3549	128.0	0.77	12.62	0.49	7.06	0.68	1.01
R4*	-0.04	3534	144.8	0.59	14.37	0.48	7.00	0.75	0.93
R5	0.19	3433	140.9	0.36	15.84	0.52	6.96	0.81	1.00
R6	0.11	3577	142.0	0.31	14.99	0.52	7.46	0.82	0.99
R7	0.03	3374	135.1	0.52	19.21	0.55	9.64	1.06	0.93
R8	0.00	3400	140.2	0.36	17.58	0.54	7.11	0.96	0.92
R9*	0.43	3567	145.9	0.33	14.42	0.51	7.47	0.71	1.32
R11	0.10	3402	143.7	0.23	13.68	0.52	7.26	0.71	0.95
R12	0.14	3317	139.1	0.72	14.40	0.51	7.07	0.76	0.97
R13	0.22	3423	141.5	0.18	17.85	0.56	7.18	0.98	0.92
R14	0.33	3444	146.6	0.20	16.63	0.55	7.95	0.98	0.93

Table 3.3: ε^{54}Cr compositions and PVE concentrations of R chondrite MIL 07440 subsamples. σ = Standard deviation. RSD = Relative standard deviation. Starred samples (*) have a 2σ ε^{54}Cr error of 0.31.

I.D.	Matrix volume fraction
R1	0.477
R2	0.460
R3	0.410
R4	0.464
R5	0.452
R6	0.455
R7	0.433
R8	0.450
R9	0.468
R10	0.413
R11	0.461
R12	0.446
R13	0.453
R14	0.470

Table 3.4: Calculated matrix volume fraction (Zn normalised to CI) and calculated matrix mass fraction of R chondrite MIL 07440 subsamples.

3.3.4 Mixing line through R chondrite MIL 07440

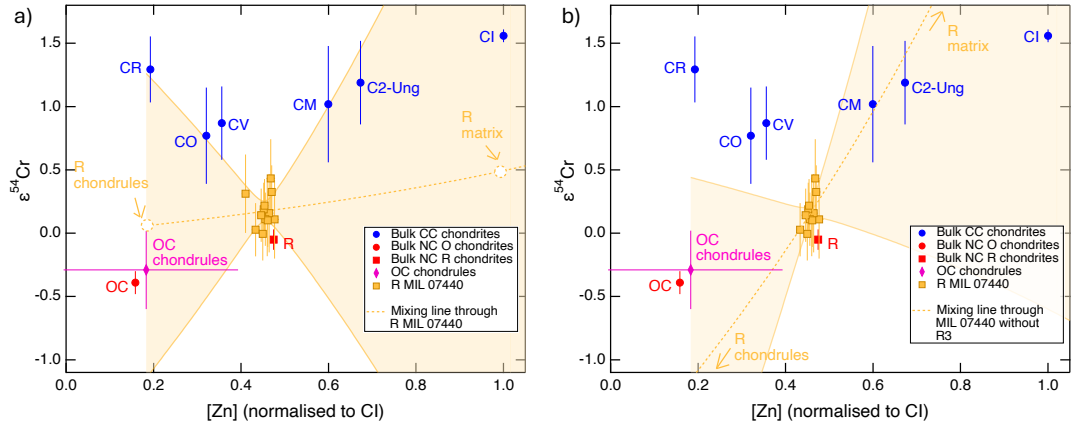

Figure 3.8: Plot displaying the composition of measured subsamples of R chondrite MIL 07440, the reported compositions of OC, R, and CC chondrites, and the average reported composition of OC chondrules. A mixing line (orange line) with a shaded 95% confidence interval has been fitted through a) subsamples of MIL 07440, and b) all subsamples of MIL 07440 excluding R3. Bulk chondrite and chondrule data is sourced from references listed in Fig. 1.6.

An isotopic mixing line was fit though the measured subsamples of MIL 07440, the results displayed in Fig. 3.8. Details of the mixing line are listed in section 2.4. An initial value of -0.29 was used as the ε^{54}Cr composition of chondrules (derived from literature values of OC chondrules), and 1.56 was used for the isotopic composition of the matrix. These values are based on the assumption that R chondrites appear to have elevated ε^{54}Cr compositions compared to OCs, and this could reflect the signature of CI-like material present in the matrix mixing with OC-like chondrules. Values of 0.183 and 1.39 were used for the concentration of Zn in chondrules (normalised to CI) and the ratio of Cr in chondrules:matrix, respectively, and these values were held constant.

A best fit line through all subsamples generates a ε^{54}Cr composition of 0.49 ± 3.28 for matrix and 0.06 ± 1.17 for chondrules (Fig. 3.8a). This line has a poor fit demonstrated by large 95% confidence interval.

A second best fit line was plotted through all subsamples excluding subsample R3, as this appears to plot separate from all others and may be anomalous (Fig. 3.8b). This fit generates a ε^{54}Cr composition of 3.79 ± 4.24 for matrix and -1.16 ± 1.54 for chondrules. This line also has a poor fit demonstrated by its wide 95% confidence intervals and large errors on recovered chondrule and matrix compositions.

3.4 Discussion

3.4.1 Ordinary chondrites

3.4.1.1 Bulk composition

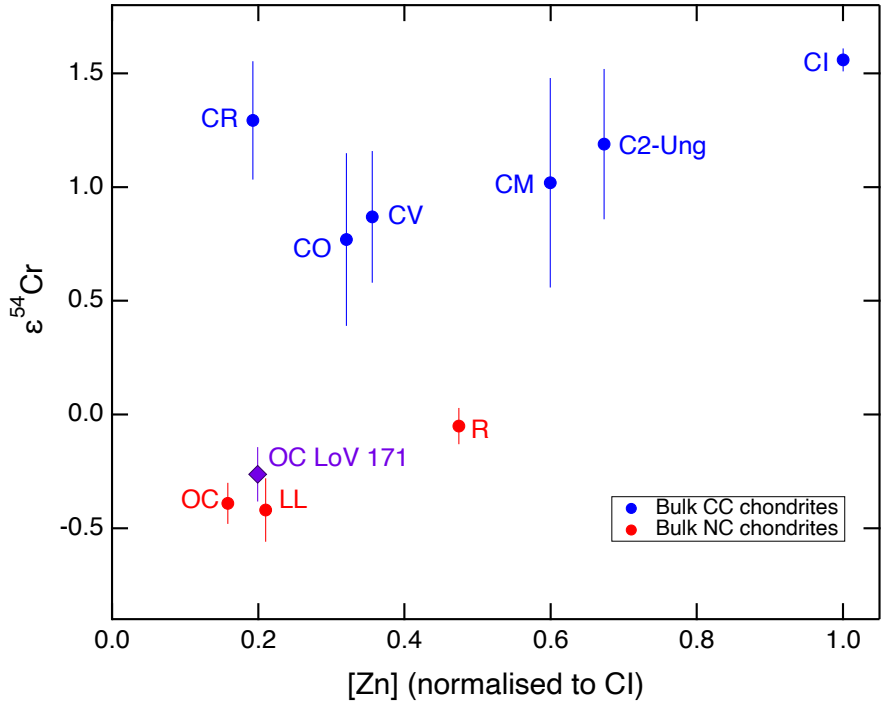

Figure 3.9: Average composition of LoV 171 compared to literature data. Bulk chondrite and chondrule data is sourced from Wasson and Kallemeyn (1988), Kallemeyn et al. (1996), and references listed in Fig. 1.6.

OC chondrites are characterised by their negative ε^{54}Cr composition and depleted PVE concentrations, however, these have not been measured previously for LoV 171. The ε^{54}Cr and PVE compositions of LoV 171 reported here allow us to confirm whether this chondrite displays similar signatures to the OCs, and if it can serve as a representative sample to explore how NC chondrites form.

The average ε^{54}Cr composition of LoV 171 (-0.16 ± 0.39) is isotopically enriched compared to other reported OCs (-0.39 ± 0.09), and more specifically, LL chondrites (-0.4 ± 0.14) (Fig. 3.9, but still lies within error of previously measured OCs (Zhu et al., 2021c)). All but one subsample show slightly higher ε^{54}Cr values than the OC average (see Fig. 3.5). Subsample LVI in particular displays an exceedingly enriched isotopic composition, on the edge of the error margin of the compositions recorded for OC chondrules. It is unlikely

that this anomalous composition is due to alteration as petrographic observations of Fe,Ni metal grains and troilite (reported by the Meteoritical Bulletin) indicate that LoV 171 underwent minimal weathering and is essentially pristine.

The calculated bulk matrix volume fraction of LoV 171 (0.199) lies within the range of matrix fractions reported in the OCs of 0.10 - 0.35 (calculated from reported Zn concentrations) (Creech and Moynier, 2019).

Since the ε^{54}Cr composition of LoV 171 is slightly enriched than all previously reported OCs (the highest to date is H chondrite LAP 03601 at -0.28 $\pm$ 0.11 (Qin et al., 2010), this could indicate that the OCs show a larger range of ε^{54}Cr anomalies that previously reported, and more samples should be measured to obtain a more representative view of the NC reservoir. Overall however, LoV 171 appears to display compositions within error of OCs and therefore can be considered to record the formation history of the OC reservoir. The elevated ε^{54}Cr composition of LoV 171 could indicate a contribution from ε^{54}Cr enriched sources, possibly suggesting a CC-like contribution to the NC reservoir.

3.4.1.2 ε^{54}Cr composition of chondrules and matrix

Characterising the ε^{54}Cr compositions of chondrules and matrix in the OCs will allow us to investigate the provenance of each component, and their histories of formation within the OC reservoir.

Zn concentrations of OC and R chondrites serve as good proxies for the matrix volume fraction present in each chondrite group, as previously discussed by Alexander (2019a). When the calculated matrix volume fractions of LoV 171 subsamples are plotted against their ε^{54}Cr compositions (Fig. 3.3) there is no trend to suggest that subsamples with lower matrix fractions (and correspondingly higher chondrule contents) show different isotopic compositions from those with higher matrix fractions. All but one subsample (LVI) plot within the error of other subsample ε^{54}Cr compositions, indicating that chondrules and matrix in this sample are likely isotopically indistinguishable, and have ε^{54}Cr values of approximately -0.16 (the average ε^{54}Cr composition of LoV 171). This agrees with previous observations by Trinquier et al. (2007) that chondrules and matrix in OCs are isotopically similar and display a limited range of compositions.

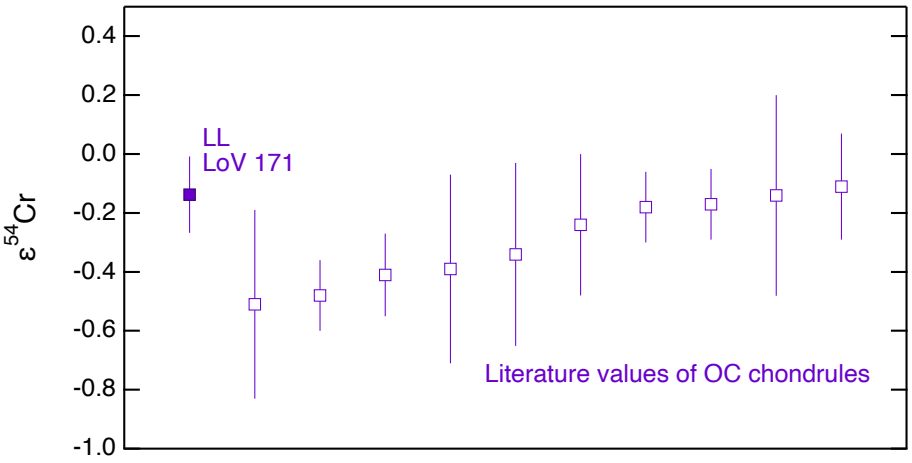

Figure 3.10: Plot displaying the recovered chondrule ε^{54}Cr composition of LoV 171 from Fig. 3.5 in comparison with compositions of OC chondrules previously reported by Trinquier et al. (2007), Qin et al. (2010), and Schneider et al. (2020).

The mixing line shown in Fig. 3.5 recovers ε^{54}Cr compositions of -1.45 ± 5.37 for the matrix of LoV 171, and -0.14 ± 0.13 for chondrules. However, the fit of the generated mixing line is poor, indicated by the wide 95% confidence bands which lead to large uncertainties in the calculated chondrule and matrix compositions. This effect is particularly pronounced in the calculated matrix composition, with the value recovered being more negative than any undifferentiated body or component measured so far (Zhu et al., 2023), indicating that this is likely an unrealistic estimate. The error associated with the recovered matrix value spans the compositions of all measured CC and NC chondrites and their components (Fig. 3.5). This fitted mixing line therefore cannot provide a reasonable estimate for matrix compositions in the OCs.

The recovered chondrule composition (-0.14 ± 0.13) is within the range of measured subsample compositions (Fig. 3.3), again agreeing with previous studies that report compositional similarities between OC chondrules and bulk compositions (Trinquier et al., 2007). This composition is elevated compared to, but within error of, OC chondrule compositions previously reported by Trinquier et al. (2007), Qin et al. (2010), and Schneider et al. (2020) (Fig. 3.10). This similarity supports observations of isotopically r-process depleted OC chondrule compositions compared to CC chondrules (Trinquier et al., 2007; Schneider et al., 2020).

Since the subsamples measured in this study span a limited range of matrix volume fractions (∼0.07), plotting an isotopic mixing line through these samples is probably an unreliable method of determining chondrule and matrix compositions due to the large uncertainties resulting from the narrow range of matrix fraction proportions. This results in a mixing line with a poorly constrained fit and large errors on chondrule and matrix compositions. The effect of this is discussed further in section 6.2.

Irrespective of whether chondrule compositions within LoV 171 are determined via the assumption that they match the bulk ε^{54}Cr composition, or if they are recovered from the mixing line, both methods indicate that their isotopic composition is relatively enriched but still within error compared to chondrule compositions previously reported by Trinquier et al. (2007), Qin et al. (2010), and Schneider et al. (2020). Due to the large errors associated with the fit of the mixing line, it is difficult to ascertain whether chondrules and matrix in the OCs display similar or varying isotopic compositions. From a qualitative assessment of the range of subsample compositions (Fig. 3.3) it is likely that chondrules and matrix share similar ε^{54}Cr compositions, and from the low errors associated with the recovered chondrule compositions, chondrules (and matrix) probably display similar isotopic compositions to the bulk chondrite. If chondrules and matrix in OCs display identical ε^{54}Cr compositions, this could imply that they sample the same local reservoir.

As LoV 171 displays slightly enriched bulk and chondrule ε^{54}Cr compositions compared to other OCs, this could indicate the presence of minor amounts of CC-like material in the OC accretion reservoir (incorporated into either the chondrules and/or matrix). However, this interpretation should be considered with care due to the large errors associated with all measured and recovered compositions. Other evidence for limited outer solar system contribution to the OC reservoir include observations of rare CAIs and the presence of small chondrules with CC-like Δ^{17}O in OC and R chondrites (Marrocchi et al., 2024). It is currently unknown if these Δ^{17}O CC-like chondrules have a correspondingly CC-like ε^{54}Cr composition and it is unlikely that they are present in high enough abundances to explain the magnitude of ^{54}Cr enrichment seen in these samples, however, their existence does support the possibility of outer solar system contamination of regions of the inner solar system.

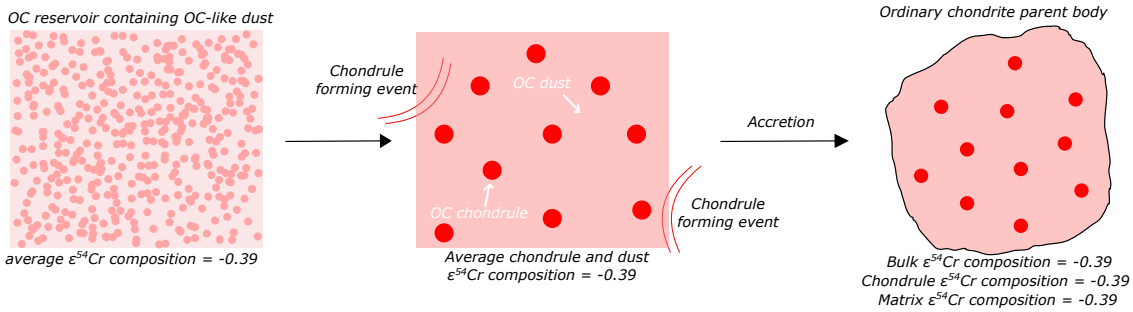

Figure 3.11: OC parent body accretion mechanism. Chondrules form a reservoir containing OC-like dust. Dust and chondrules accrete to form a OC parent body which contains chondrules and matrix that display similar ε^{54}Cr compositions.

3.4.1.3 Formation of OC parent bodies

Comparing the isotopic compositions of chondrules and matrix present in LoV 171 allow us to probe the provenance of these components, and characterise the dynamics of solid movement and accretion in the OC reservoir.

The lack of variation seen in the coupled ε^{54}Cr compositions and PVE abundances of subsamples of LoV 171 indicate that there is likely no isotopic difference between chondrules and matrix in OCs. However, the large uncertainties in the measured and recovered isotopic compositions of the subsamples and chondrules should also be taken into consideration. This observed isotopic homogeneity implies that both chondrules and matrix present in OCs were formed in the same reservoir before accreting to form the OC parent body, or that these chondrites experienced chemical reprocessing that homogenised the compositions of chondrules and matrix. Petrographic observations of LoV 171 indicate that it experienced very little alteration or weathering, however, Cr mobilisation has been observed in chondrites of petrological grades as low as 3.05 (Grossman and Brearley, 2005), implying that small amounts of redistribution may have occurred in this chondrite (grade 3.1). Assuming the isotopic compositions of matrix and chondrules in LoV 171 are not extensively altered and represent their original compositions, then both components reflect signatures of formation in a shared reservoir (Fig. 3.11).

Local formation of OC chondrules and matrix from a shared reservoir has been previously proposed, specifically due to evidence of complementarity in the compositions of chondritic components (Bland et al., 2005; Ebel, 2006; Wasson and Rubin, 2009). Mea-

surements of subsolar Mg/Si matrix elemental compositions and correspondingly enriched Mg/Si chondrule compositions in LL chondrite Semarkona have been used to argue that chondrules and matrices formed and accreted within a single shared, solar-like reservoir, reflecting minimal radial transport of chondritic components (Ebel et al., 2024). Arguments against complementarity highlight the presence and preservation of organic carbon and pre-solar grains, with some present in CI-like abundances (Huss and Lewis, 1995; Davidson et al., 2014; Floss and Haenecour, 2016; Alexander, 2019a). The presence of primitive organics in OCs indicates that the matrix escaped significant heating. This contradicts the assumption in models of complementarity that propose that matrix material represents the components of the reservoir remaining after an unidentified heating event forms chondrules, as it is not expected that organic material would survive this process. Regardless of whether the model of complementarity holds true in relation to the exact formation mechanisms of chondrules and matrix, the results of this study agree that both components formed from the same isotopic reservoir. This finding indicates restricted movements of solids within the inner solar system.

3.4.1.4 Further work: Using Kakangari chondrites to determine chondrule and matrix ε^{54}Cr compositions

As discussed in section 3.4.1.2, the fitted mixing line through the OC data exhibits large uncertainties due to the lack of spread of matrix fractions. To better determine the composition of chondrules and matrix in NC chondrites, a wider range of matrix fractions needs to be sampled to minimise the 95% confidence interval. Few NC chondrite groups display sufficiently large ranges in matrix fractions that would make it possible to extend the range of points available. However, the Kakangari (K) grouplet provides an intriguing case to consider.

The K chondrites contain high matrix volume fractions (33 - 77%), similar to those observed in carbonaceous chondrites (Weisberg et al., 1996; Barosch et al., 2020). The isotopic composition of this grouplet has been scarcely reported, with only one K chondrite, LEW 87232, having a measured ε^{54}Cr composition of -0.44 $\pm$ 0.04 (Zhu et al., 2023). This isotopic composition is within error of the reported average ε^{54}Cr value of

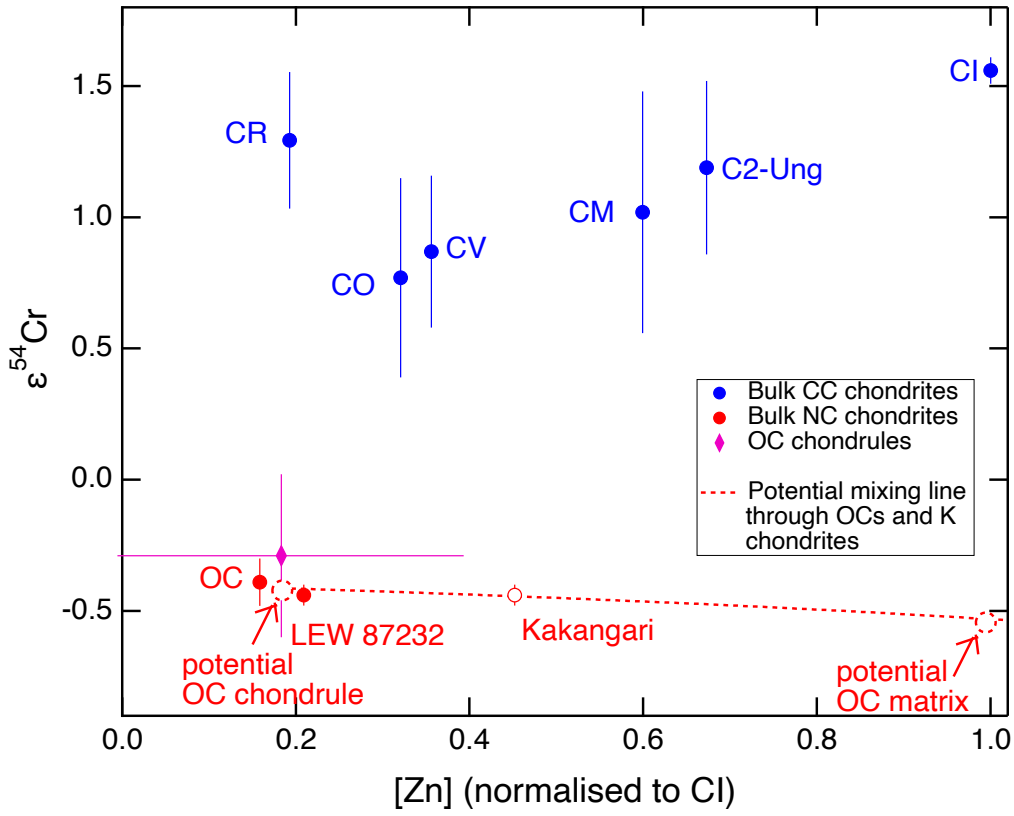

Figure 3.12: Isotopic mixing line plot through bulk OC chondrites and K chondrites LEW 87232 and Kakangari. The isotopic composition of Kakangari has not been measured (and so is represented by an open point) but is assumed to match LEW 87323. The initial values used were: -0.29 for the ε^{54}Cr compositions of matrix and chondrules; 1.39 for the ratio of [Cr] of chondrules:matrix; and 0.118 for [Zn] in chondrules (normalised to CI). Bulk chondrite and chondrule data is sourced from Zhu et al. (2023) and references listed in Fig. 1.6.

OCs (-0.39 ± 0.09) (Zhu et al., 2021c). This chondrite is reported to contain a matrix area of 53.4% (Barosch et al., 2020) but to compare it with the samples reported in this study, its matrix volume fraction was calculated from its CI-normalised Zn concentration, providing a value of 0.209 (Weisberg et al., 1996). Kakangari is also included in Fig. 3.5 and displays a larger calculated matrix volume fraction of 0.452 (Weisberg et al., 1996), though its Cr isotopic composition has not been measured yet and so is assumed to be the same as LEW 87323. This large range of matrix proportions, and similar Cr isotopic compositions to OC, could make this grouplet (in particular the Kakangari chondrite) an ideal candidate for a similar study to determine whether chondrules and matrix are isotopically homogeneous, and therefore form in a similar location.

A preliminary mixing line fit through the bulk OCs, LEW 87323, and Kakangari is shown

in Fig. 3.12, which indicates that OCs and K chondrites may share isotopically similar chondrule and matrix ε^{54}Cr compositions (-0.41 ± 0.02 and -0.53 ± 0.14, respectively). These recovered compositions are within error of the compositions measured of OC chondrules and bulk OCs.

Though their Cr isotopic composition is similar to OCs, the K chondrites do show differences, most notably in their high metal contents and anomalous bulk oxygen isotopic compositions, which are similar to CR chondrites. This highlights that though measuring the compositions of these chondrites could provide additional insight into how OC-like chondrites form, they are not from the same parent body and so correlations should be interpreted with caution.

3.4.2 R chondrites

3.4.2.1 Bulk composition

The Cr isotopic composition of R chondrites has not been extensively measured compared other chondrite groups; the only studies reporting the ε^{54}Cr compositions of R chondrites include those by Zhu et al. (2021b) and Larsen et al. (2011). Prior to this, Qin et al. (2010) reported the composition of EET 96026 which was previously classified as an R chondrite, but has since been reclassified as a CV chondrite (Noronha and Friedrich, 2014). An ε^{54}Cr composition of -0.06 ± 0.07 has been reported for MIL 07440 (Zhu et al., 2021b) which is representative of average R chondrites (-0.06 ±0.08), but is isotopically distinct from the bulk value of 0.18 ± 0.31 reported in this study. Eight subsamples of MIL 07440 do however plot within error of the average reported R chondrites.

The isotopically heavier ε^{54}Cr compositions of MIL 07440 reported here compared to previous studies may be due to uncorrected isotopic fractionation induced during column chemistry. The measured ε^{54}Cr compositions of MIL 07440 subsamples could only be corrected for instrument drift or column-induced fractionation, due to the lack of column standards run during the time period of measurement (see sections 2.3.1.6 and 3.2). As deviations due to drift during this time period were of greater magnitude compared to those of column-induced fractionation (Fig. 2.4), only drift was corrected for. However, column-induced fractionation appears to shift ε^{54}Cr values 0.19 ± 0.19 heavier (see section

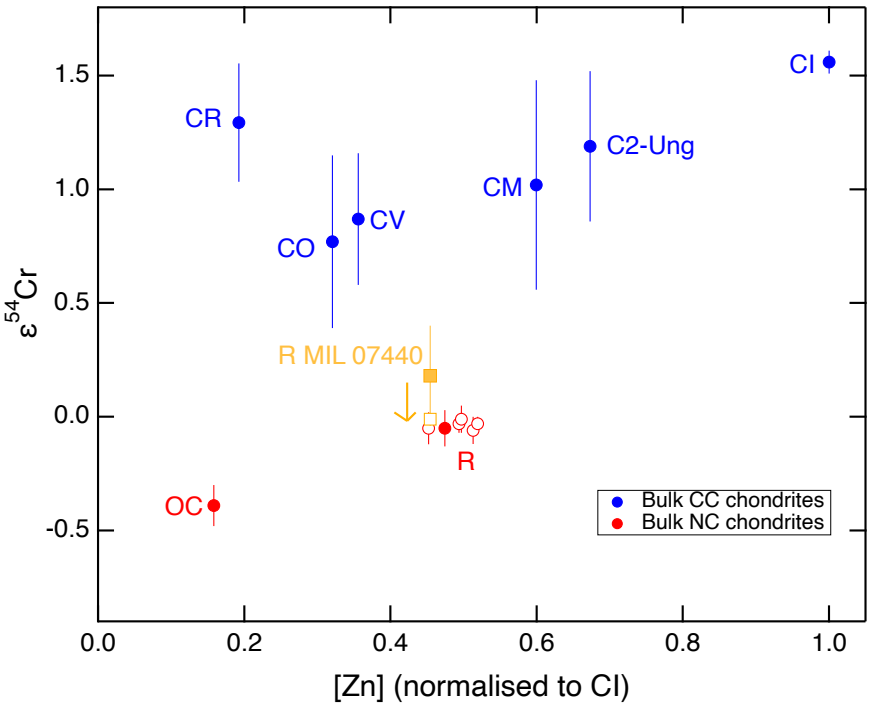

Figure 3.13: Plot of the average ε^{54}Cr and Zn composition of MIL 07440. The open orange square represents a -0.19 ε^{54}Cr shift in the bulk composition of MIL 07440 to approximate a correction for column-induced fractionation. Open red circles represent the literature compositions of various R chondrites that have reported ε^{54}Cr and Zn compositions. Bulk chondrite and chondrule data is sourced from Kallemeyn et al. (1996), Isa et al. (2014), and references listed in Fig. 1.6.

2.3.1.7), implying that the composition of MIL 07440 may in fact agree well with previously reported vales (Fig. 3.13).

Regardless of whether a correction is applied for the potential effects of column-induced isotopic fractionation, R chondrites consistently display enriched ε^{54}Cr compositions compared to OCs. This r-process enrichment could indicate contribution from CC-like material.

MIL 07740 displays a similar bulk Zn composition of 142 ppm compared to the R chondrite average, 148 ppm (Kallemeyn et al., 1996; Isa et al., 2014). This corresponds to a matrix fraction of 0.450, which agrees with the 40 - 50 vol% range reported in previous studies (Bischoff et al., 2011).

3.4.2.2 ε^{54}Cr composition of chondrules and matrix

Zinc concentrations provide a good proxy for matrix volume fractions in R chondrites (Alexander, 2019a), though they show slightly elevated Zn compared to the matrix volume fraction recorded.

Subsamples of MIL 07440 show a weak trend between Zn concentrations (normalised to CI) and ε^{54}Cr, indicating that increasing matrix contents may correlate with higher ε^{54}Cr compositions (Fig. 3.6). This trend is also seen when a mixing line is plotted through the subsamples, both including and excluding subsample R3 (Fig. 3.8). Though it is apparent that there is a trend with increasing Zn concentrations, the range of matrix volume fractions covered by this subsample set is very limited (0.08) and all measured subsamples plot within error of each other. The isotopic mixing line also displays large 95% confidence intervals, making a trend difficult to verify.

If this trend is valid, it suggests that the matrix and chondrules present in R chondrites are isotopically distinct in ε^{54}Cr compositions, with the matrix displaying higher values, trending to CC-like compositions. When subsample R3 is included in the isotopic mixing line (Fig. 3.8a) R chondrite chondrules appear to have ε^{54}Cr compositions within error of OC chondrules, and a matrix composition that is within error to those reported for bulk CC chondrites.

If the trend is coincidental and there is no observable difference between the isotopic compositions of chondrules and matrix, there is still an enrichment of ^{54}Cr in bulk R chondrites compared to OCs seen in both literature data and this study. This difference still indicates that R chondrites record contribution of material with enriched ε^{54}Cr isotopic signatures during their formation, compared to OCs.

3.4.2.3 Formation of R chondrite parent body

R chondrites and OCs, both in this study and in literature, display lower ε^{54}Cr isotopic anomalies compared to all CC chondrite groups. These traits indicate that R chondrites and OCs formed within a similar reservoir, which was distinct from the formation reservoir of CC chondrites. There are limited studies that characterise the mass-independent

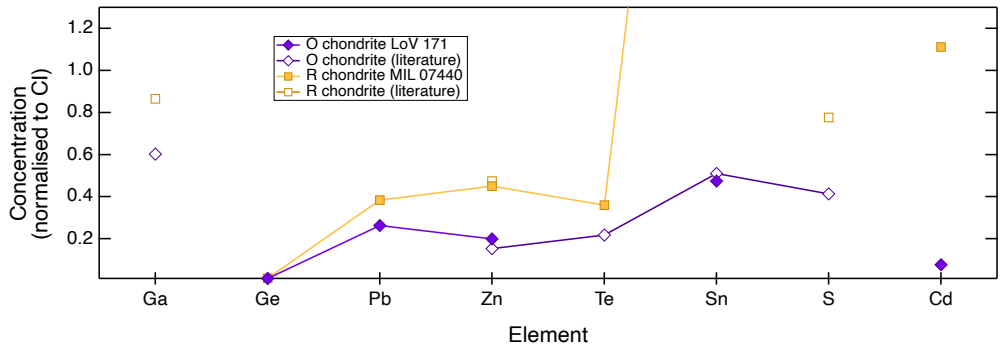

Figure 3.14: CI-normalised PVE concentrations of OC and R chondrites reported in this study (solid points) and in the literature (open points). Sn plots above the range of the graph at 4.79. Data is sourced from references listed in Fig. 1.5.

isotopic composition of R chondrites, with no reported Ti or Ca anomalies. However, the Mo (Marti et al., 2023) and ε^{183}W (Hellmann et al., 2024) compositions of OC and R chondrites are indistinguishable, supporting the conclusion that they form from similar material. This is further supported by their similar major element abundances (Wasson and Kallemeyn, 1988; Ali et al., 2017).

Despite these similarities, R chondrites are comparatively enriched in Zn, Se, and S compared to OCs (Bischoff et al., 2011; Alexander, 2019a). Results from this study agree with the observed Zn enrichment of R chondrites compared to OCs, and extend this observation to other PVEs, including Pb, Te, Sn, and Cd (Fig. 3.14).

If, as assumed in this work, the abundance of most PVEs reflect the amount of matrix present in chondrites, the elevated PVE concentrations (in particular Pb, Zn, and Te) seen in R chondrites could simply represent the increased contribution of these elements to the bulk chondrite composition due to their higher matrix fractions. This would imply that the R chondrites accreted in a region with greater dust concentrations than the OCs, supporting an idea previously suggested by Rubin (2010).

Evolution to higher volatile contents over time in the inner solar system has been proposed by Mahan et al. (2018) who observed that younger OC chondrules record higher volatile contents. Though Mahan et al. (2018) focus on Ag and Sb in OCs, this more broadly implies that components that form, or chondrites that accrete, at later times in the inner solar system (>1 Ma after CAI formation) could be enriched in volatiles and PVEs. If R

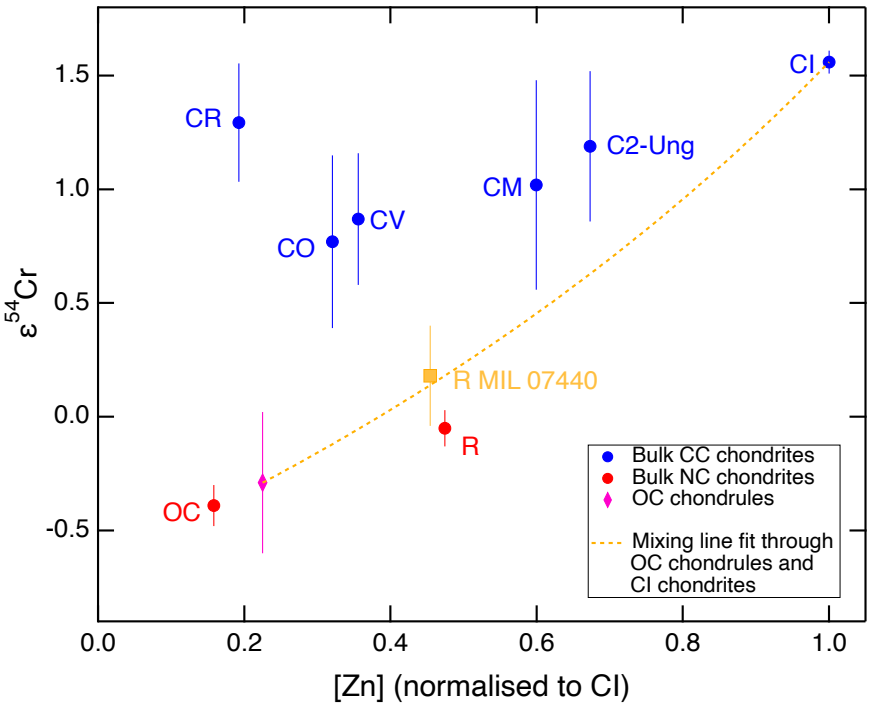

Figure 3.15: Mixing line plot between OC chondrules and CI chondrites. This mixing line passes through the composition of MIL 07440 measured in this study. Bulk chondrite and chondrule data is sourced from references listed in Fig. 1.6.

chondrites accrete at later times compared to the OCs, they could preferentially accrete this volatile-rich material. Modelling by Sugiura and Fujiya (2014) and Desch et al. (2018) also predict the accretion of R chondrites at slightly later times (2.1 - 2.2 Ma) compared to the OCs (2.0 - 2.1 Ma), and at greater distances (∼2.6 AU compared to ∼2.2 - 2.6 AU). Additionally, Desch et al. (2018) remark that the R chondrites require addition of "CI dust" to their formation region to explain their high refractory abundances, which would also increase the volatile contents, as observed. This would also lead to higher ε^{54}Cr compositions in R chondrites compared to OCs, as observed in this study and by Larsen et al. (2011) and Zhu et al. (2021b). The presence of CI-like dust in the formation region of the R chondrites is supported by the bulk ε^{54}Cr composition and Zn concentration of R chondrite MIL 07440 reported in this study, as its composition can be recovered by mixing of OC chondrules and CI-like dust (Fig. 3.15). However, the bulk R chondrite compositions reported in the literature display lower ε^{54}Cr compositions that cannot be recovered by this mixing line, implying that the ^{54}Cr-enriched component added to the R chondrites may display depleted compositions compared to CI chondrites.

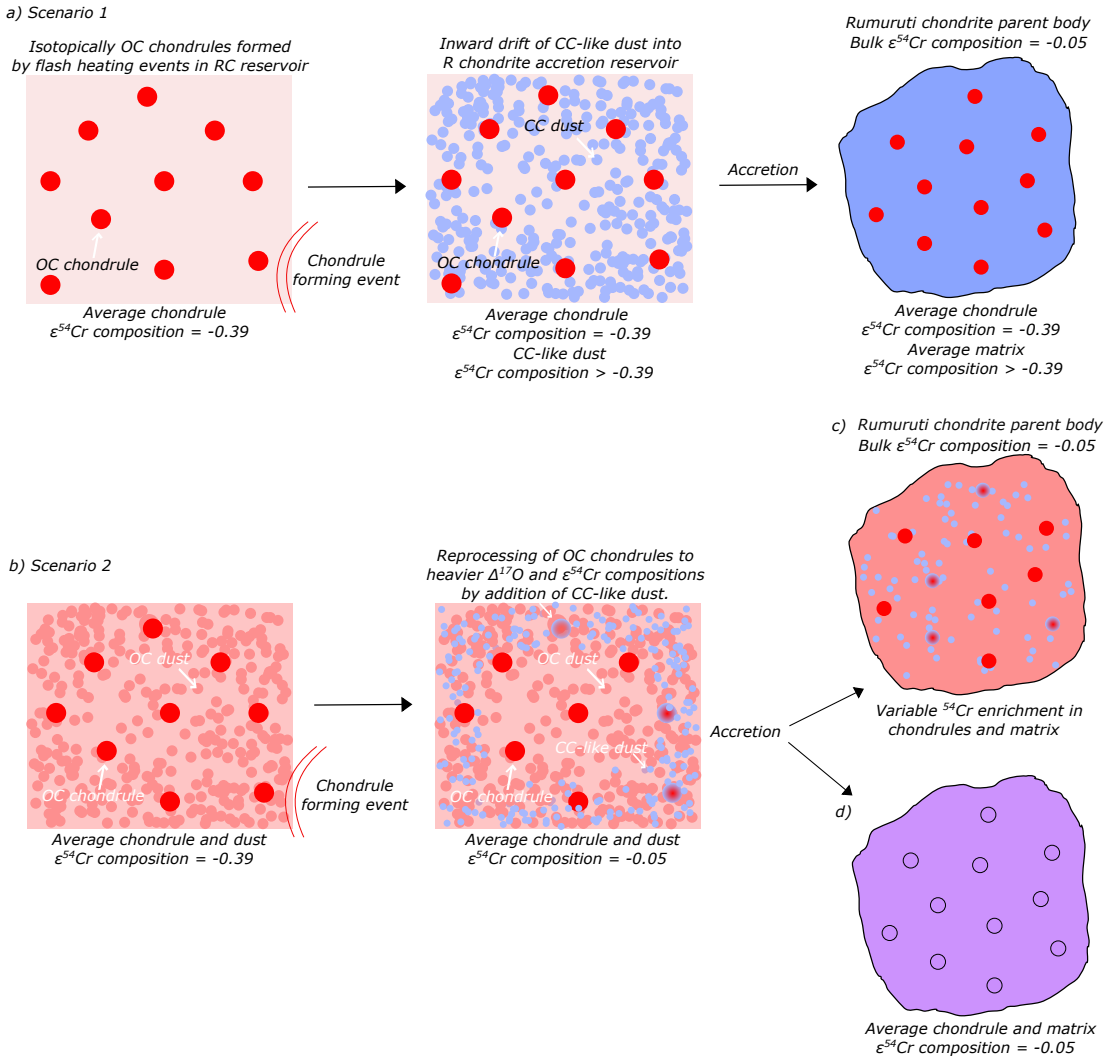

Figure 3.16: Schematic depicting R chondrite accretion to explain the high ε^{54}Cr compositions observed. a) Accretion of R chondrite parent body from mixtures of CC-like dust and OC-like chondrules. b) Accretion of the R chondrite parent body from a reservoir that experienced addition of CC-dust to an OC-like dust population. In c) the chondrules and matrix in the R parent body are variably enriched in ^{54}Cr and display different ε^{54}Cr compositions. In d) the OC-like and CC-like dust mix well, chondrule formation occurs, and chondrules and matrix display similar ε^{54}Cr compositions. Not to scale.

The ε^{54}Cr isotopic enrichment observed in R chondrites could occur in two ways. In the first scenario, chondrules and matrix form in separate regions of the solar system and acquire distinct isotopic signatures, with chondrules displaying similar compositions to OC chondrules and matrix-bound dust sourced from greater radial distances and displaying CC-like compositions. This CC-like dust drifts inwards towards the R chondrite formation reservoir, before mixing with OC-like chondrules and accreting to form the R chondrite parent body (Fig. 3.16a).

In the second scenario the R chondrite parent body accretes within a region that originally displays similar elemental and isotopic compositions to bulk OCs, but subsequently experiences small additions of CC-like material (likely dust) sufficient to alter the bulk reservoir composition to higher PVE concentrations and higher ε^{54}Cr compositions (Fig. 3.16b). In this scenario, the chondritic component hosting the ε^{54}Cr anomaly is not identified. ^{54}Cr-enriched carriers (likely from the CC-like dust) could be incorporated into either the chondrules and/or matrix. This ambiguity reflects the large errors associated with the mixing lines (Fig. 3.8), highlighting that chondrules and matrix could display similar isotopic compositions, or both components could be variably enriched in ^{54}Cr. Both scenarios could feasibly explain the Cr isotopic composition observed in R chondrites; due to the lack of resolution in this study, distinguishing between them is not possible.

The formation of R chondrites from mixtures of OC-like dust and/or chondrules and CC-like dust detailed here supports studies that propose an evolutionary relationship between R chondrites and OCs. Ali et al. (2017) suggest that the Δ^{17}O compositions of R chondrite chondrules indicate they form from alteration of OC chondrules with matrix containing ^{17}O-rich water, under oxidising conditions. CC chondrites display greater abundances of hydrated minerals compared to OCs, and CI chondrites display high Δ^{17}O compositions (Clayton and Mayeda, 1999), implying that CI-like dust may be strong a candidate for the source of ^{17}O-enrichment within R chondrite chondrules. The incorporation of this dust into R chondrite chondrules could lead to the observed enriched ε^{54}Cr compositions of R chondrites (this study and Zhu et al. (2021b)). Increased dust fractions and dust-to-gas ratios in the R chondrite accretion reservoir (from the presence of both OC-like and CC-like dust) could lead to the more oxidising conditions proposed in the R chondrite regions, implied by the abundance of Fe-O rich olivines and oxidised fine grained material observed (Weisberg et al., 1991; Bischoff et al., 2011; Alexander, 2019a; Marrocchi et al., 2024).

3.4.3 Comparison of formation of the R chondrites and OCs

Overall, the ε^{54}Cr isotopic compositions and PVE abundances reported in this study, and observations from wider literature (Larsen et al., 2011; Ali et al., 2017; Alexander, 2019a;

Zhu et al., 2021b; Regnault et al., 2022), indicate that R chondrites and OCs experienced slightly different conditions of formation. As the fits of isotopic mixing lines display large uncertainties (Figs. 3.5 and 3.8), it is difficult to assess whether R chondrites and OCs contain isotopically similar chondrules and matrix. However, R chondrites show higher ε^{54}Cr compositions and higher PVE abundances compared to OCs, indicating that they accrete with greater amounts of ^{54}Cr-enriched material, likely CC-like, as well as greater fractions of volatile-rich dust. This material is likely isotopically CC-like dust preferentially accreted into the R chondrite parent body due to its late accretion age and/or more distal formation location compared to OCs (Fig. 6.4) (Desch et al., 2018). The presence of greater amounts of CC-like dust in the R chondrite reservoir could indicate contribution from CC-like pebbles (though these are typically considered to be chondrule-sized), or a "leaky" barrier that is inefficient at stopping inward drift of small particles.

3.4.4 Pebble vs planetesimal accretion and the NC/CC barrier

The geochemical evidence presented in this chapter allows me to investigate the potential contribution of CC-like material to the inner solar system, and assess whether this is likely a result of pebble accretion.

If accretion of CC-like pebbles during the lifetime of the protoplanetary disk is invoked to explain Earth's μ^{48}Ca, μ^{54}Fe, and μ^{30}Si (Schiller et al., 2018, 2020; Onyett et al., 2023) composition, a corresponding CC enrichment could also be seen in other inner solar system bodies that form before 5 Ma, most notably, in chondrites. OCs show minimal CC-like enrichment and R chondrites, thought to originate from more distal locations closer to the CC reservoir (Desch et al., 2018), show minor ^{54}Cr enrichment. The magnitude of the excess observed in R chondrites compared to OCs (0.45 - 0.57 ε^{54}Cr), from Zhu et al. (2021b) and this study) is not as much as expected if Earth accreted a significant proportion (∼40% (Schiller et al., 2018)) of CI-like pebbles (0.78 ε^{54}Cr). If R chondrites accreted at greater radial distances (∼2.6 AU) they might be expected to accrete greater amounts of CI-like pebbles compared to the Earth due to their proximity to the CC reservoir, though this may be hindered by their smaller mass, leading to a restricted accretion radius. As this large ^{54}Cr enrichment is not observed, inner solar system chondrites do not

record ε^{54}Cr isotopic evidence of significant CC-derived pebble accretion to match what is proposed for Earth's accretion. However, if these pebbles were similar in composition to CC chondrules (ε^{54}Cr of 0.58 (Schneider et al., 2020)), an excess of 0.39 ε^{54}Cr could be generated from accretion of 40% CC chondrule-like material. This could indicate the accretion of proximal outer solar system material into R chondrites (assuming CC chondrules form close to the NC-CC barrier - see Chapter 4), and imply the CC pebbles were chondrule-like instead of CI-like as suggested by Schiller et al. (2018).

These estimates, however, do not exclude the possibility of accretion of pebbles sourced from within the inner solar system to form the terrestrial planets, though this is difficult to interrogate through an isotopic approach. The Δ^{95}Mo isotopic signatures recorded in BSE could then be due to late-stage impactors (Budde et al., 2019). The ^{54}Cr enrichment observed in R chondrites is likely instead due to addition of small amounts of CC-like dust that exhibits higher ε^{54}Cr compositions.

Due to the lack of significant CC-like contribution to the inner solar system, the barrier separating the NC and CC regions must have been fairly effective at preventing mixing between the two reservoirs. The enriched ε^{54}Cr recorded in R chondrites, though, indicates that small amounts of CC-like material may have been present in the R chondrite formation region. Other evidence for CC-like material being present in the NC reservoir is observed, as small chondrules in OCs are reported to display CC-like, sub-TFL (Terrestrial Fractionation Line), ^{16}O-enriched compositions (Clayton et al., 1991; Piralla et al., 2021; Marrocchi et al., 2024), and small CAIs, typically larger and more abundant in CC chondrites, are observed in low abundances in OCs and ECs (Dunham et al., 2023). The existence of these small grains in the NC reservoir could either imply that they were present prior to formation of the barrier between the NC and CC regions (Marrocchi et al., 2024), or that the barrier enabled small particles (well coupled to the gas) to filter through, as suggested by Van Clepper and Ciesla (2023).

3.5 Conclusions

Coupled ε^{54}Cr values and Zn concentrations of OC LoV 171 and R chondrite MIL 07440 were measured to investigate the formation of chondrite parent bodies in the inner solar system.

OC LoV 171 displays an average ε^{54}Cr composition of -0.16 ± 0.39 and Zn concentration of 62 ppm, resulting in a calculated average matrix volume fraction of 0.199. This measured ε^{54}Cr composition is higher than the OC average, but within error of other LL chondrites.

Subsamples of OC LoV 171 do not show resolvable differences in their ε^{54}Cr composition, implying that their chondrules and matrix formed in the same isotopic reservoir before accretion to form the OC parent body. There is minimal CC-like contribution recorded in the isotopic composition of LoV 171, indicating that the barrier between the NC and CC reservoir was effective at isolating these groups of material at the radial distance of formation of the OCs (2.2 - 2.6 AU (Desch et al., 2018)).

R chondrite MIL 07440 displays a bulk ε^{54}Cr composition of 0.18 ± 0.31 and Zn concentration of 140 ppm, resulting in a calculated average matrix volume fraction of 0.450. This measured ε^{54}Cr composition is heavier than the reported R chondrite average, possibly due to the effects of uncorrected column-induced fractionation. This could not be corrected for post-measurement as the fractionation does not appear to follow the exponential fractionation law.

R chondrites, including MIL 07440, show higher ε^{54}Cr compositions compared to OCs. This could be due to: 1) their bulk composition reflecting a mixture of ^{54}Cr enriched matrix and OC-like chondrules, or; 2) addition of isotopically ε^{54}Cr CC-like material to the R chondrite formation region, which is incorporated into both chondrules and matrix. This study is unable to differentiate between these two scenarios. Regardless, this likely reflects addition of CC-like material to the R chondrite formation region.

Though R chondrites provide evidence for small contributions of CC-like material to the outer edges of the inner solar system (∼2.6 AU), pebble accretion did not play a governing

role in the formation of terrestrial planets during the period of chondrite formation.

Chapter 4

Formation of the carbonaceous chondrite parent bodies

4.1 Introduction

4.1.1 Background

Carbonaceous (CC) chondrites are a class of chondritic meteorites that preserve some of the most pristine material from our solar system. The CC chondrites are split into various groups, including the Ivuna-like (CI), Ornans-like (CO), Vigarano-like (CV), Mighei-like (CM), Bencubbin-like (CB), Karoonda-like (CK), Loongano-like (CL), CH (high metal), and Renazzo-like (CR) chondrites. These groupings are based on variations in petrology, and chemical and isotopic compositions. CC chondrites that do not clearly belong to any of these groups are classed as "ungrouped" (C-Ung). The chemical and isotopic compositions of CC chondrites have been extensively studied as their solar-like elemental ratios and preservation of primitive material provide vital insight into the conditions present during their formation in the first 0 - 4 Ma of the protoplanetary disk.

Since 2011 it has been recognised that CC chondrites show systematic enrichments in *r*-process derived neutron rich isotopes (e.g, ^{50}Ti and ^{54}Cr) compared to the more volatile-depleted non-carbonaceous (NC) chondrites (Warren, 2011). As CC chondrites display higher volatile abundances and more extensive aqueous alteration compared to NC chon-

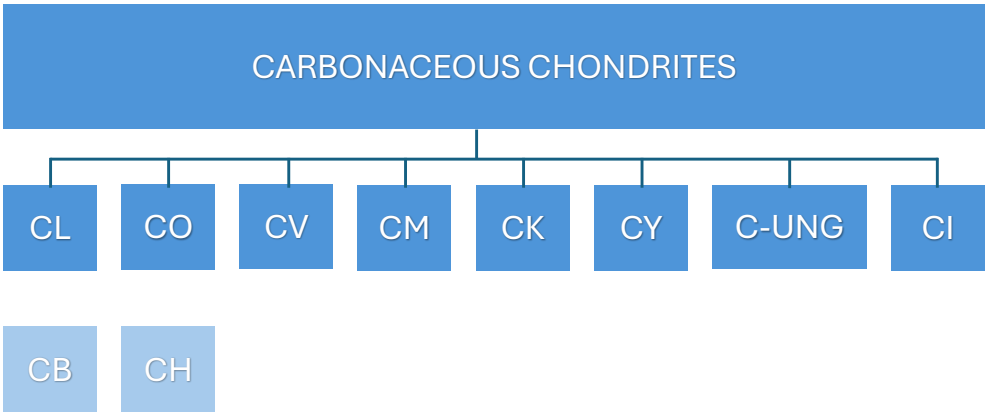

Figure 4.1: Carbonaceous chondrite groups in approximate order of their matrix fractions. CB and CH exhibit anomalous compositions and so are listed separately.

drites, they are though to form at colder, more distal locations in the protoplanetary disk (Lodders, 2003; Krot et al., 2014; Palme et al., 2014). This suggests that different regions of the protoplanetary disk exhibit different mass-independent isotopic compositions, and that these variations may be used to determine the provenance of chondritic material. Understanding how CC chondrite parent bodies form in the outer solar system will help constrain the dynamics of solid movement and planetesimal formation in this region of the protoplanetary disk. The two main formation mechanisms proposed, planetesimal accretion and pebble accretion, source material from different regions of the protoplanetary disk. Planetesimal accretion models the formation of planetary bodies through local collisional and accretionary mechanisms (Drazkowska et al., 2022). Pebble accretion relies on the large scale movement of mm - cm-sized solids in the outer solar to explain the rapid formation of gas giant's cores (Levison et al., 2015). These mechanisms should result in differing isotopic signatures preserved in different CC chondritic components.

CC chondrites contain variable proportions of refractory inclusions (RIs), chondrules, and matrix, with each group displaying characteristic proportions of each component. In particular, CI chondrites contain abnormally few chondrules (<5 vol%), only one observed calcium-aluminium inclusion (CAI) (Leshin et al., 1997; Krot et al., 2014; Frank et al., 2023), and are mostly comprised of extensively hydrated matrix (King et al., 2015a). Various studies have attempted to characterise the isotopic and chemical compositions of these chondritic components to determine how CC parent bodies formed and how planetesimals accreted in the outer solar system.

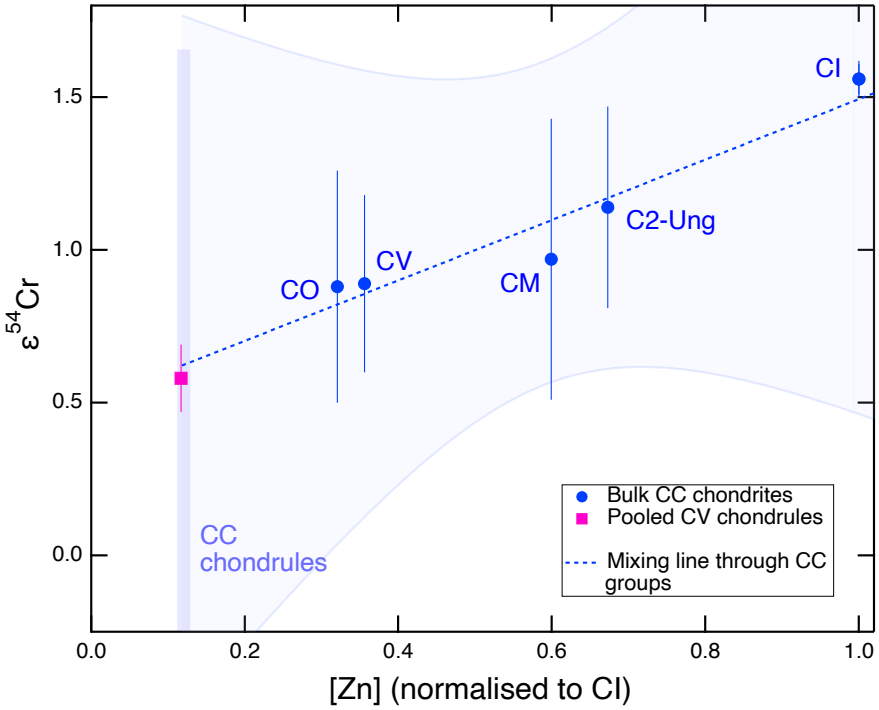

Figure 4.2: Plot of ε^{54}Cr and CI-normalised Zn concentrations of CC chondrites and chondrules. A mixing line plot through the compositions of the CC groups recovers a matrix composition of of 1.52 ± 0.15 and chondrule composition of 0.55 ± 0.17. A 95% confidence region is shaded in blue. This chondrule composition agrees with the values recovered from pooled CV chondrules by Schneider et al. (2020). Bulk chondrite and chondrule data is sourced from references listed in Fig. 1.6.

The two prevailing theories of chondrites formation (discussed previously in section 1.1.3) suggest that either: 1) the chondrules and matrix present in CC chondrites form locally from a shared reservoir of material; or that 2) chondrules and matrix form in different regions of the protoplanetary disk and later accrete to form the different CC parent bodies.

In the first scenario, chondrules and matrix in each CC group accrete from the same reservoir and display complementary elemental ratios due to the evaporative loss of elements during chondrule formation. This is supported by observations of complementary Si/Mg, Fe/Mg, Ca/Al, and Ca/Ti ratios in chondrules and matrix (Friend et al., 2017; Braukmüller et al., 2018; Hezel et al., 2018b; Ebel et al., 2024), as well as patterns of volatile fractionation observed in matrix material (Bland et al., 2005). This initial reservoir may have been CI-like, or may have already been depleted in volatile and moderately volatile (MVE) elements (Bland et al., 2005). The bulk isotopic composition of each chon-

drite then reflects the local isotopic composition of the reservoir. If isotopic differences are observed between chondrules and matrix, this is explained by isotopic fractionation and/or incomplete incorporation of r-process enriched carriers into chondrules (Budde et al., 2016a; van Kooten and Moynier, 2019). Proponents against this theory argue that thermal and aqueous alteration on chondrite parent bodies, as well as the terrestrial alteration experienced by many chondrites, obscures and alters the composition of chondrules and matrix material (van Kooten et al., 2019). This alteration and exchange of elements between chondrules and matrix could induce the complementary elemental and isotopic compositions observed.

In the second scenario, chondrules and matrix form in different regions and so may exhibit different isotopic signatures. Since CI chondrites are almost completely formed from matrix (Krot et al., 2014), and bulk CC chondrite volatile element compositions show CI-like ratios (Braukmüller et al., 2018), some studies have suggested that CIs represent the matrix material present in all CC groups (Alexander, 2019b; Bryson and Brennecka, 2021; Hellmann et al., 2023). The elemental and isotopic compositional variation observed in chondrites is then a reflection of the varying proportions of chondrules, matrix, and RIs present in each group. This scenario is further supported by observations that the ε^{54}Cr compositions of CI, CO, CM, CV, and C2-ung chondrites appear to correlate with matrix fraction, with CI chondrites displaying the highest matrix fractions and largest ε^{54}Cr anomalies and CO chondrites the lowest matrix fractions and most depleted compositions (Fig. 4.2). When a mixing line (detailed in section 2.4) is fit through these chondrite groups, the compositions of each CC group can be expressed as varying mixtures of compositionally CI-like matrix with chondrules that have isotopic compositions close to those measured by Schneider et al. (2020) in CV chondrites. These observations lend support to this formation scenario, however, this needs to be further examined to determine whether the isotopic composition of matrix in CC groups does indeed display CI-like signatures, and if all chondrules share a similar isotopic composition regardless of CC group.

To identify which scenario is responsible for the formation of CC chondrites, the chemical and isotopic compositions of isolated chondrules and matrix from different CC groups should be determined. However, this is difficult due to the pervasive small-scale effects of

thermal and aqueous alteration, and the existence of many small, hard to remove, sub-mm fragments of chondrules and CAIs present in CC matrices. Previous studies have characterised the ε^{54}Cr compositions of CO, CV, CM, CK and CB chondrules, but no values currently exist for the compositions of C2-Ung chondrules (Qin et al., 2011; Yamashita et al., 2010; Olsen et al., 2016; Zhu et al., 2019a; Williams et al., 2020; Schneider et al., 2020; van Kooten et al., 2020). These studies have isolated and measured large chondrules, but fail to fully represent the composition of smaller, < 0.5 mm chondrules. Schneider et al. (2020) have done this for a CV chondrite where pooled chondrules and chondrule fragments were measured for their ε^{54}Cr isotopic composition, and the composition of matrix separates were also determined. These isolated compositions, however, may be affected by small-scale local movement of Cr as previous work by Grossman and Brearley (2005) observes Cr mobilisation in chondrule olivines of pristine chondrites (petrologic type 3.00). More work needs to be conducted to assess the average chondrule and matrix compositions across the different CC chondrite groups to better constrain the formation mechanisms dominant across the CC region.

Local formation of chondrules and matrix implies small-scale, regional formation of chondrite bodies, whose components do not mix. This agrees with the proposals of multiple dust traps or ring like structures that inhibit solid migration and promote local formation of bodies with restricted isotopic compositions (Rüfenacht et al., 2023). This limited mixing agrees with the mechanisms of planetesimal accretion. However, if chondrules and matrix are sourced from different regions of the disk, this implies that extensive movement of material occurred in the outer solar system, similar to the motion of solids described in pebble accretion scenarios. This is also suggested by the presence of isotopically NC-like ε^{50}Ti, ε^{54}Cr, and Δ^{17}O chondrule olivine cores (van Kooten et al., 2021; Fukuda et al., 2024), which could indicate transport and incorporation of NC-like inner solar material into CC chondrules. Determining the mechanisms by which CC chondrites form will help constrain the behaviour of solid movement in the outer solar system. This could also allow us to suggest whether pebble or planetesimal accretion dominated planet formation in the outer protoplanetary disk.

4.1.2 This work

In this chapter I will investigate the formation of CC chondrite parent bodies by measuring the coupled ε^{54}Cr compositions and PVE concentrations of subsamples of CO, CV, CM, and C2-Ung chondrites. By fitting an isotopic mixing line through each subsample set, I aim to identify the ε^{54}Cr compositions of chondrules and matrix in each CC chondrite group and compare these to previously reported values. This includes the first (inferred) ε^{54}Cr composition of C2-Ung chondrules. I will then fit a mixing line through all measured CC chondrite subsamples to assess whether all groups share similar chondrule and matrix isotopic compositions. Using the recovered isotopic compositions of chondrules and matrix I will investigate how the CC chondrite parent bodies accreted, and what this implies about the movement of solids in the outer solar system.

4.2 Methods

Four CC chondrites (CO DOM 08006, CV Allende, CM NWA 11345, and C2-Ung Tarda) were analysed to determine the coupled ε^{54}Cr isotopic compositions and PVE concentrations of their subsamples.

A 373 mg sample of CO chondrite DOM 08006 was acquired on request from JSC (loan no. 3699). A 10.6 g sample of CV chondrite Allende was purchased from eBay. A 879 mg sample of CM chondrite NWA 11345 was acquired from Dr. Jérôme Gattacceca from CEREGE. Multiple chips of C2-Ung chondrite Tarda were received from Dr. Greg Brennecka. All samples were cut into smaller subsamples using a diamond wire saw. DOM 08006 was cut into 11 subsamples, ranging in weight between 9.0 - 34.4 mg. Ten subsamples were cut from the chip of Allende, ranging in weight between 13.5 - 64.7 mg. NWA 11345 was into 18 subsamples and 12 were used in this study, ranging in weight between 23.6 - 46.6 mg. Tarda was cut into 13 subsamples, ranging in weight between 6.9 - 38.6 mg.

All CC chondrite subsamples were digested following the protocol described in section 2.1.3, and 0.8 ml aliquots were preserved for determining initial PVE and Cr chemical concentrations. A 0.5 ml aliquot of each subsample was then subjected to the Cr purification procedure detailed in section 2.2. Yields of 65 - 89% were achieved during column chemistry for the CO, CM, and C2-Ung chondrites. The CV chondrite Allende was processed at the beginning of this study, before incorporation of column 3 to scavenge lost Cr from column 2, and so suffers from lower yields between 53 - 69 %. Initial Cr concentrations, PVE abundances, and purity and yield of the column chemistries were measured using Quadrupole ICP-MS, as described in section 2.3.2. Se, Cd, and Ge concentrations were not measured for Allende as the protocol had not been established at this point.

The column chemistry associated with the CC chondrites in this chapter had a maximum procedural blank of 78 ng Cr which is higher than other studies (Torrano et al., 2024), but insignificant compared to the total amount of measured Cr (4 - 122 μg).

Matrix mass fractions were calculated using the CI-normalised Zn concentrations of each subsample as described in section 2.3.4.

To calculate ε^{54}Cr, measured $\frac{^{54}Cr}{^{52}Cr}$ ratios of each subsamples are normalised to the average processed NIST-979 standard values.

An isotopic mixing line was fit through the ε^{54}Cr and CI-normalised Zn compositions of subsamples of each individual chondrite subset to determine the ε^{54}Cr composition of chondrules and matrix present in each chondrite. A mixing line was also fit through all CC chondrite subsamples to determine the average chondrule and matrix ε^{54}Cr composition of the CC chondrites. Details of the mixing line are provided in section 2.4.

The bulk ε^{54}Cr composition and CI-normalised Zn concentration of each chondrite group are calculated using the weighted average of their subsample compositions. The error associated with the bulk ε^{54}Cr composition is the uncertainty associated with the measurement of the isotopic compositions of the subsamples (as described in section 2.3.1.7).

4.3 Results

4.3.1 CO: Chemical and isotopic composition

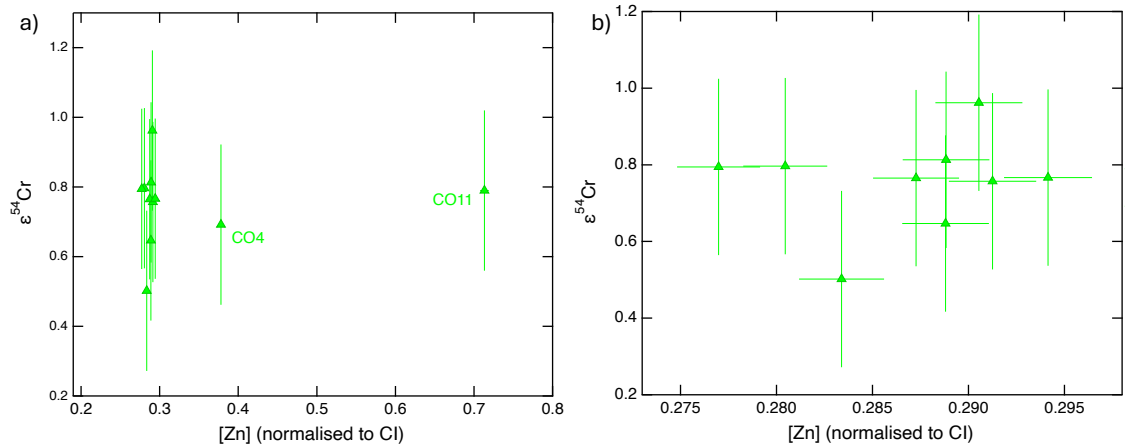

Figure 4.3: a) Calculated matrix volume fractions of subsamples of CO chondrite DOM 08006, represented by their CI-normalised Zn concentration, plotted against their ε^{54}Cr composition. b) Enlarged graph displaying the compositions of all DOM 08006 subsamples excluding CO4 and CO11.

The coupled ε^{54}Cr and PVE composition of 11 subsamples of CO chondrite DOM 08006 are reported in Table 4.1. The subsamples span a range of ε^{54}Cr compositions between 0.50 - 0.96, and Zn concentrations between 86 - 223 ppm, resulting in a calculated matrix volume fraction range of 0.277 - 0.713 and matrix mass fraction range of 0.156 - 0.665 (Tables 4.1 and 4.2). Subsamples CO4 and CO11 display anomalously high Zn concentrations compared to other subsamples.

The range of matrix volume fractions in DOM 08006 subsamples displays a RSD of 77.2%, indicating a heterogenous population of subsamples (Stracke et al., 2012).

The bulk ε^{54}Cr composition of DOM 08006 is 0.73 ± 0.23 and the bulk Zn concentration is 99 ppm. The average matrix volume fraction of the subsamples was 0.317.

The ε^{54}Cr compositions and CI-normalised Zn concentrations of DOM 08006 subsamples are displayed in Fig. 4.3a. An enlarged figure displaying all data points excluding CO4 and CO11 is also provided (Fig. 4.3b) to help identify any trends within the dataset. There appears to be no correlation between matrix fraction and Cr isotopic compositions, with all subsamples plotting within the error ranges of each other's ε^{54}Cr compositions. This is supported by a calculated ρ of 0.07.

4.3.2 CO: Mixing line

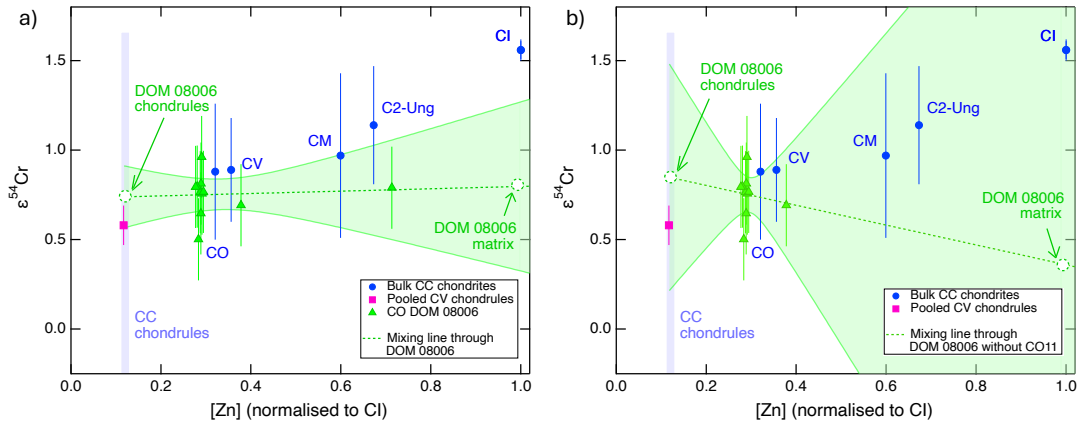

Figure 4.4: a) Plot displaying the composition of measured subsamples of CO chondrite DOM 08006, the reported compositions of CO, CV, CM, C2-Ung, and CI chondrites, the average reported composition of CC chondrules, and the range of CC chondrules. A mixing line has been fitted through subsamples of DOM 08006 (green line) with a shaded 95% confidence interval. b) Mixing line plot through all subsamples except for matrix rich subsample CO11. Bulk chondrite and chondrule data is sourced from references listed in Fig. 1.6.

An isotopic mixing line (details in section 2.4) was fitted to the measured CO chondrite subsamples. The initial values used were: 1.56 and 0.58 for the ε^{54}Cr compositions of matrix and chondrules, respectively. These values were chosen based on the assumption that chondrules and matrix display differing isotopic values, and the compositions of previously measured CO chondrules (Fig. 4.14), however this did not significantly influence the result of the fit. Values of 1.0 for the ratio of [Cr] of chondrules:matrix; and 0.118 for [Zn] in chondrules (normalised to CI) were used.

When the Zn and Cr chemical concentrations in chondrules and matrix are held constant, the best fit mixing line passes through a value of 0.78 ± 0.45 for the ε^{54}Cr composition of matrix and 0.74 ±0.17 for chondrules. This mixing line is plotted in Figure 4.4a. Wide 95% confidence interval bands indicate the poor fit of this mixing line, especially at the Zn concentrations of chondrules and matrix.

To assess if the anomalously matrix rich subsample CO11 affected the recovered chondrule and matrix compositions a second mixing line was fit excluding this subsample, shown in Fig. 4.4b. This recovered a matrix ε^{54}Cr composition of 0.36 ± 2.33 and chondrule value of 0.85 ± 0.60, with wider 95% confidence interval bands.

4.3.3 Allende: Chemical and isotopic composition

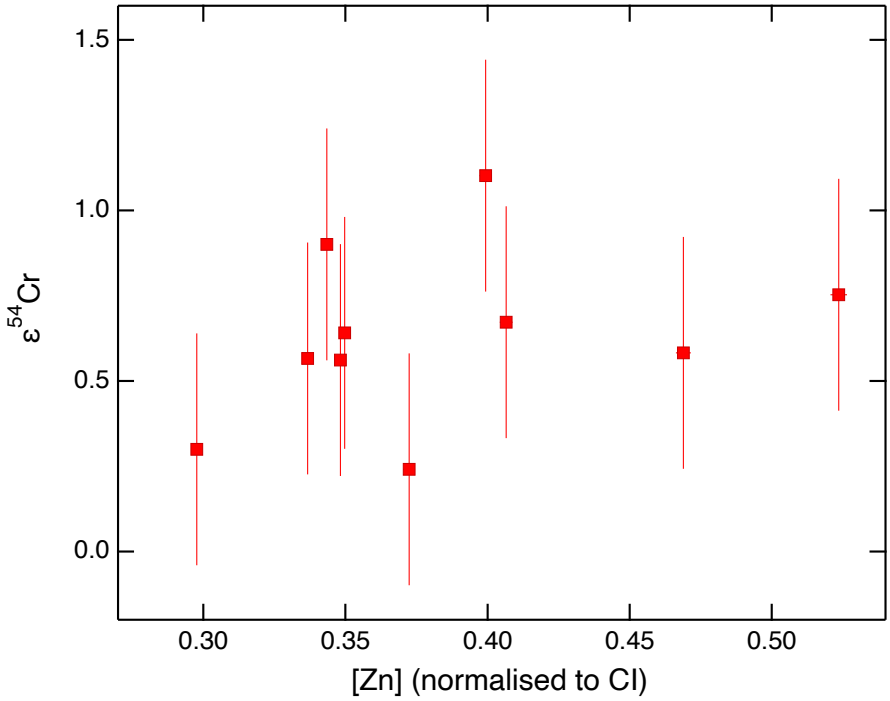

Figure 4.5: Calculated matrix volume fractions of subsamples of CV chondrite Allende, represented by their CI-normalised Zn concentration, plotted against their ε^{54}Cr composition.

The coupled ε^{54}Cr and PVE composition of 10 subsamples of CV chondrite Allende are reported in Table 4.1. The subsamples span a range of ε^{54}Cr compositions between 0.24 - 1.10, and Zn concentrations between 93 - 163 ppm, resulting in a calculated matrix volume fraction range of 0.298 - 0.524 and matrix mass fraction range of 0.181 - 0.444 (Tables 4.1 and 4.2).

The range of matrix volume fractions in Allende subsamples displays a RSD of 35.2%, indicating a heterogenous population of subsamples (Stracke et al., 2012).

The bulk ε^{54}Cr composition of Allende is 0.68 ± 0.34, and the bulk Zn concentration is 118 ppm. The average matrix volume fraction of the subsamples was 0.377.

The ε^{54}Cr compositions and matrix fractions of Allende subsamples are displayed in Fig. 4.5. There appears to be a weak correlation between increasing matrix fractions and higher Cr isotopic compositions, though most subsamples still plot within error of each others ε^{54}Cr compositions. This is supported by a calculated ρ of 0.31, indicating weak correlation between the ε^{54}Cr value and matrix fraction of different CV subsamples.

4.3.4 Allende: Mixing line

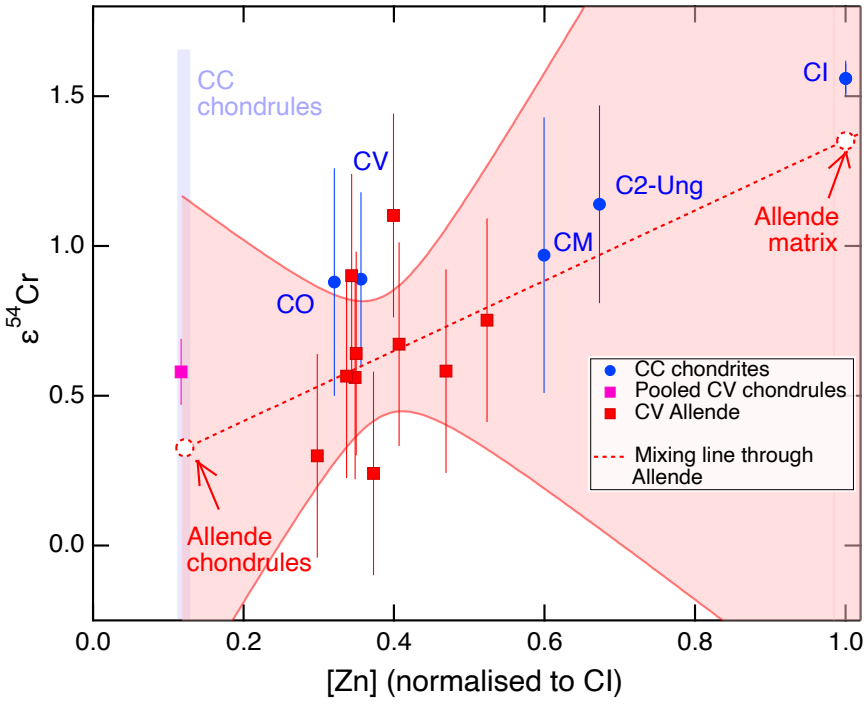

Figure 4.6: Plot displaying the composition of measured subsamples of CV chondrite Allende, the reported compositions of CO, CV, CM, C2-Ung, and CI chondrites, the average reported composition of CC chondrules, and the range of CC chondrules. A mixing line has been fitted through subsamples of Allende (red line) with a shaded 95% confidence interval. Bulk chondrite and chondrule data is sourced from references listed in Fig. 1.6.

An isotopic mixing line (details in section 2.4) was fitted to the measured CV chondrite subsamples. The initial values used were: 1.56 and 0.58 for the ε^{54}Cr compositions of matrix and chondrules, respectively; 1.0 for the ratio of [Cr] of chondrules:matrix; and 0.118 for [Zn] in chondrules (normalised to CI).

When the Zn and Cr concentrations in chondrules and matrix are held constant, the best fit mixing line passes through a value of 1.35 $\pm$ 1.80 for the ε^{54}Cr composition of matrix and 0.32 $\pm$ 0.80 for chondrules. This mixing line is plotted in Figure 4.6a. Wide 95% confidence interval bands and the large errors associated with the calculated chondrule and matrix compositions indicate the poor fit of this mixing line.

4.3.5 CM: Chemical and isotopic composition

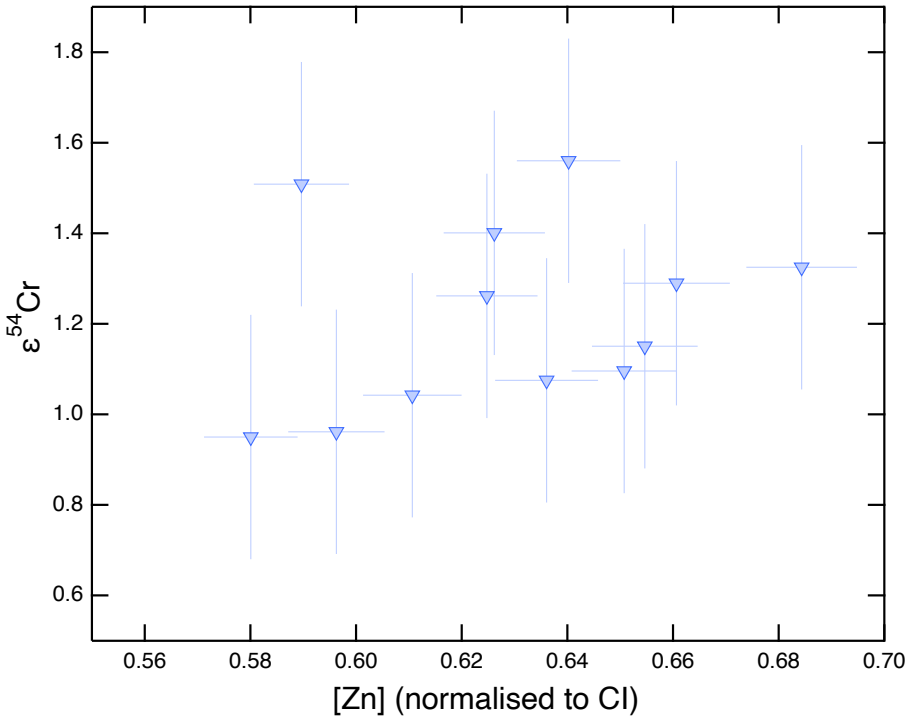

Figure 4.7: Calculated matrix volume fractions of subsamples of CM chondrite NWA 11345, represented by their CI-normalised Zn concentration, plotted against their ε^{54}Cr composition.

The coupled ε^{54}Cr and PVE composition of 12 subsamples of CM chondrite NWA 11345 are reported in Table 4.1. The subsamples span a range of ε^{54}Cr compositions between 0.84 - 1.47, and Zn concentrations between 181 - 206 ppm, resulting in a calculated matrix volume fraction range of 0.580 - 0.661 and matrix mass fraction range of 0.470 - 0.572 (Tables 4.1 and 4.2).

The range of matrix volume fractions in NWA 11345 subsamples displays a RSD of 9.9%, indicating a heterogenous population of subsamples (Stracke et al., 2012).

The bulk ε^{54}Cr composition of NWA 11345 is 1.09 $\pm$ 0.27, and the bulk Zn concentration is 197 ppm. The average matrix volume fraction of the subsamples was 0.631.

The ε^{54}Cr compositions and matrix fractions of NWA 11345 subsamples are displayed in Fig. 4.7. There appears to be a weak-to-no correlation (ρ = 0.12) between increasing matrix fractions and higher Cr isotopic compositions, though most subsamples still plot within error of each others ε^{54}Cr compositions.

4.3.6 CM: Mixing line

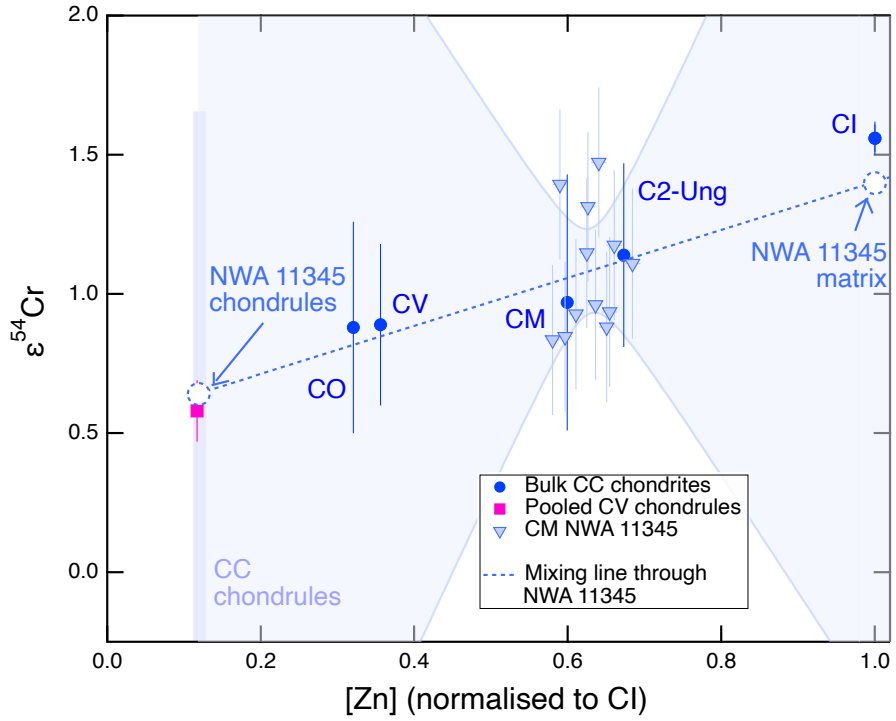

Figure 4.8: Plot displaying the compositions of measured subsamples of CM chondrite NWA 11345, the reported compositions of CO, CV, CM, C2-Ung, and CI chondrites, the average reported composition of CC chondrules, and the range of CC chondrules. A mixing line has been fitted through subsamples of NWA 11345 (blue line) with a shaded 95% confidence interval. Bulk chondrite and chondrule data is sourced from references listed in Fig. 1.6.

An isotopic mixing line (details in section 2.4) was fitted to the measured CM chondrite subsamples. The initial values used were: 1.56 and 0.58 for the ε^{54}Cr compositions of matrix and chondrules, respectively; 1.0 for the ratio of [Cr] of chondrules:matrix; and 0.118 for [Zn] in chondrules (normalised to CI).

When the Zn and Cr concentrations in chondrules and matrix are held constant, the best fit mixing line passes through a value of 1.40 $\pm$ 1.83 for the ε^{54}Cr composition of matrix and 0.64 $\pm$ 2.52 for chondrules. This mixing line is plotted in Figure 4.8a. Wide 95% confidence interval bands and the large errors associated with the calculated chondrule and matrix compositions indicate the poor fit of this mixing line.

4.3.7 Tarda: Chemical and isotopic composition

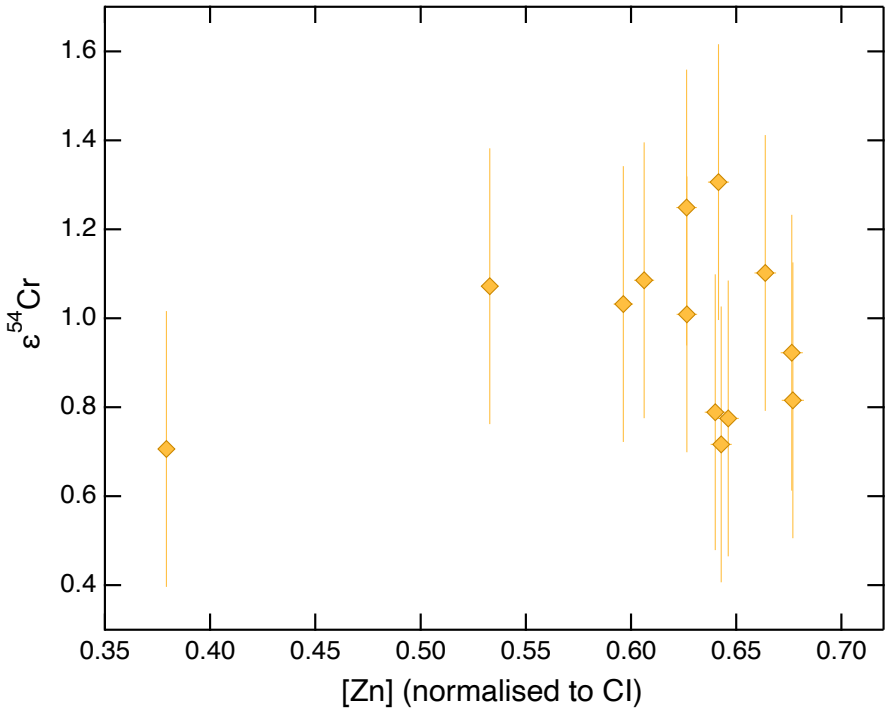

Figure 4.9: Calculated matrix volume fractions of subsamples of C2-Ung chondrite Tarda, represented by their CI-normalised Zn concentration, plotted against their ε^{54}Cr composition.

The coupled ε^{54}Cr and PVE composition of 13 subsamples of C2-Ung chondrite Tarda are reported in Table 4.1. The subsamples span a range of ε^{54}Cr compositions between 0.71 - 1.31, and Zn concentrations between 118 - 211 ppm, resulting in a calculated matrix volume fraction range of 0.379 - 0.677 and matrix mass fraction range of 0.120 - 0.542 (Tables 4.1 and 4.2).

The range of matrix volume fractions in LoV 171 subsamples displays a RSD of 26.0%, indicating a heterogenous population of subsamples (Stracke et al., 2012).

The bulk ε^{54}Cr composition of Tarda is 0.94 $\pm$ 0.31, and the bulk Zn concentration is 194 ppm. The average matrix volume fraction of the subsamples was 0.620.

The ε^{54}Cr compositions and matrix fractions of NWA 11345 subsamples are displayed in Fig. 4.7. There appears to be weak-to-no correlation between increasing matrix fractions and higher Cr isotopic compositions as all subsamples still plot within error of each others ε^{54}Cr compositions regardless of matrix fraction ($\rho = 0.21$).

4.3.8 Tarda: Mixing line

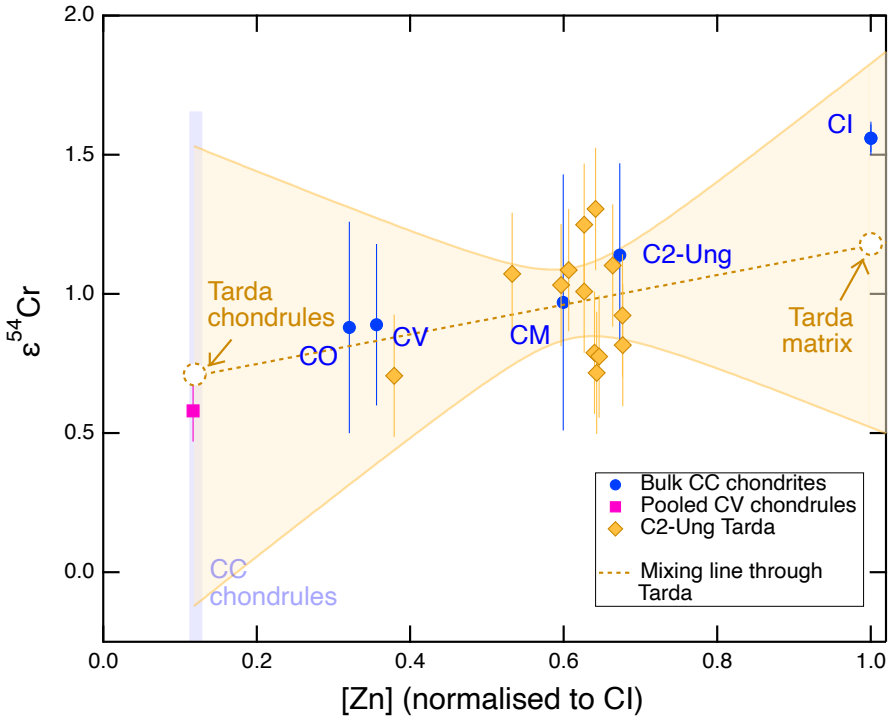

Figure 4.10: Plot displaying the compositions of measured subsamples of C2-Ung chondrite Tarda, the reported compositions of CO, CV, CM, C2-Ung, and CI chondrites, the average reported composition of CC chondrules, and the range of CC chondrules. A mixing line has been fitted through subsamples of Tarda (orange line) with a shaded 95% confidence interval. Bulk chondrite and chondrule data is sourced from references listed in Fig. 1.6.

An isotopic mixing line (details in section 2.4) was fitted to the measured C2-Ung chondrite subsamples.The initial values used were: 1.56 and 0.58 for the ε^{54}Cr compositions of matrix and chondrules, respectively; 1.0 for the ratio of [Cr] of chondrules:matrix; and 0.118 for [Zn] in chondrules (normalised to CI).

When the Zn and Cr concentrations in chondrules and matrix are held constant, the best fit mixing line passes through a value of 1.18 $\pm$ 0.64 for the ε^{54}Cr composition of matrix and 0.71 $\pm$ 0.80 for chondrules. This mixing line is plotted in Figure 4.10a. Wide 95% confidence interval bands indicate the poor fit of this mixing line.

I.D.	ε^{54}Cr	Cr (ppm)	Zn (ppm)	Ge (ppm)	Se (ppm)	Cd (ppm)	Sn (ppm)	Te (ppm)	Pb (ppm)
	±0.23	±0.65%	±0.78%	±2.1%	±6.06%	±2.06%	±1.19%	±3.22%	±2.12%
	2σ	2RSD	2RSD	2RSD	2RSD	2RSD	2RSD	2RSD	2RSD
CO1	0.76	3436	90.9	1.82	6.87	0.34	0.57	0.64	0.69
CO2	0.96	3305	90.6	1.76	7.29	0.33	0.60	0.72	0.67
CO3	0.81	3431	90.1	1.63	6.85	0.34	0.58	0.67	0.68
CO4	0.69	4378	117.9	2.24	8.62	0.40	0.72	0.80	0.83
CO5	0.76	3328	89.6	1.78	6.34	0.31	3.16	0.57	0.65
CO6	0.80	3255	87.5	1.71	6.13	0.29	1.21	0.51	0.65
CO7	0.65	3239	90.1	1.79	6.11	0.29	0.46	0.50	0.64
CO8	0.80	3227	86.4	1.84	6.34	0.30	0.47	0.53	0.67
CO9	0.50	3174	88.4	1.78	6.20	0.31	7.06	0.54	0.64
CO10	0.77	3318	91.8	1.72	6.38	0.30	3.87	0.58	0.65
CO11	0.79	3432	222.5	1.97	10.09	0.94	1.00	1.32	1.56
	±0.34	±0.55%	±0.75%				±1.04%	±1.75%	±35.76%
	2σ	2RSD	2RSD				2RSD	2RSD	2RSD
CV1	0.56	3794	108.6				1.38	0.76	0.90
CV2	1.10	3419	124.6				2.81	0.77	1.07
CV3	0.90	3594	107.1				4.16	0.79	1.97
CV4	0.57	3385	105.0				4.31	0.73	1.82
CV5	0.75	3401	163.3				0.98	0.88	1.22
CV6	0.30	3840	92.9				1.17	0.60	0.52
CV7	0.24	3662	116.2				1.47	0.87	1.12
CV8	0.58	3403	146.3				0.98	0.82	3.26
CV9	0.67	3642	126.8				0.88	0.86	3.21
CV10	0.64	3467	109.1				6.11	0.84	1.13
	±0.27	±1.71%	±1.53%	±1.10%	±3.60%	±0.90%	±1.28%	±3.00%	±8.00%
	2σ	2RSD	2RSD	2RSD	2RSD	2RSD	2RSD	2RSD	2RSD
CM3	1.31	3349	195.4	0.10	10.06	1.35	36.48	1.06	1.55
CM4	0.88	3024	203.0	0.11	5.88	2.20	49.57	0.94	1.82
CM6	1.47	3297	199.7	0.09	7.50	0.72	9.24	1.08	1.50
CM7	1.11	3221	213.5	0.11	7.53	0.99	9.46	1.06	1.47
CM8	1.39	3163	184.0	0.09	7.52	0.78	8.32	0.96	1.32
CM9	1.18	3146	206.1	0.09	8.08	1.31	9.64	1.17	1.61
CM10	0.96	3220	198.5	0.11	10.89	0.82	18.87	1.14	1.38
CM12	1.15	3196	194.9	0.10	7.41	1.25	8.82	1.02	1.53
CM13	0.94	3235	204.2	0.11	9.69	1.27	29.79	1.13	1.55
CM16	0.84	2833	181.0	0.09	8.66	0.93	8.89	1.14	1.42
CM17	0.93	3523	190.5	0.10	8.33	0.87	9.20	1.11	1.41
CM18	0.85	3172	186.0	0.09	8.52	0.71	9.03	1.11	1.35
	±0.31	±0.65%	±0.78%	±2.10%	±6.06%	±2.06%	±1.19%	±3.22%	±2.12%
	2σ	2RSD	2RSD	2RSD	2RSD	2RSD	2RSD	2RSD	2RSD
T1	1.31	2402	200.1	1.30	13.32	0.45	0.97	1.23	1.51
T2	0.92	2558	211.0	1.80	18.50	0.62	1.25	1.48	1.98
T3	0.82	2662	211.2	0.09	12.60	0.46	10.40	1.31	1.78
T4	0.79	2610	199.7	0.08	11.64	0.45	59.78	1.15	1.55
T5	0.71	1587	118.3	0.84	8.30	0.29	1.52	0.72	0.88

ε^{54}Cr compositions and PVE concentrations of CC chondrite subsamples measured in this chapter. Concentrations of Se, Cd, and Ge were not measured for CV chondrite Allende. Table continued on next page.

I.D.	ε^{54}**Cr**	**Cr**	**Zn**	**Ge**	**Se**	**Cd**	**Sn**	**Te**	**Pb**
		(ppm)	(ppm)	(ppm)	(ppm)	(ppm)	(ppm)	(ppm)	(ppm)
	±0.31	±0.65%	±0.78%	±2.10%	±6.06%	±2.06%	±1.19%	±3.22%	±2.12%
	2σ	2RSD	2RSD	2RSD	2RSD	2RSD	2RSD	2RSD	2RSD
T6	0.72	2556	200.6	1.46	12.87	0.44	0.96	1.05	1.46
T7	1.10	2513	207.1	1.53	13.50	0.46	0.96	1.13	1.47
T8	0.77	2514	201.6	1.88	16.41	0.56	1.16	1.30	1.80
T9	1.25	2753	195.4	1.61	12.11	0.46	0.93	1.01	1.34
T10	1.03	2331	186.0	1.56	11.47	0.58	1.03	1.20	1.46
T11	1.09	2424	189.1	1.31	12.52	0.45	3.13	1.07	1.39
T13	1.01	2510	195.5	1.47	12.85	0.45	0.97	1.10	1.42
T14	1.07	2116	166.2	1.23	11.12	0.40	2.48	1.01	1.25

Table 4.1: ε^{54}Cr compositions and PVE concentrations of CC chondrite subsamples measured in this chapter. σ = Standard deviation. RSD = Relative standard deviation

I.D.	Matrix volume fraction	Matrix mass fraction
CO1	0.291	0.173
CO2	0.291	0.172
CO3	0.289	0.170
CO4	0.378	0.274
CO5	0.287	0.168
CO6	0.280	0.161
CO7	0.289	0.170
CO8	0.277	0.156
CO9	0.283	0.164
CO10	0.294	0.176
CO11	0.713	0.665
CV1	0.348	0.240
CV2	0.399	0.299
CV3	0.343	0.234
CV4	0.337	0.226
CV5	0.524	0.444
CV6	0.298	0.181
CV7	0.372	0.268
CV8	0.469	0.380
CV9	0.406	0.308
CV10	0.350	0.241
CM3	0.626	0.529
CM4	0.651	0.560
CM6	0.640	0.546
CM7	0.684	0.602
CM8	0.590	0.483
CM9	0.661	0.572
CM10	0.636	0.541
CM12	0.625	0.527
CM13	0.655	0.565
CM16	0.580	0.470
CM17	0.611	0.509
CM18	0.596	0.491
T1	0.641	0.492
T2	0.676	0.541
T3	0.677	0.542
T4	0.640	0.490
T5	0.379	0.120
T6	0.643	0.494
T7	0.664	0.524
T8	0.646	0.499
T9	0.626	0.471
T10	0.596	0.428
T11	0.606	0.442
T13	0.626	0.471
T14	0.533	0.338

Table 4.2: Calculated matrix volume fraction (Zn normalised to CI) and calculated matrix mass fraction of CC chondrite subsamples.

I.D.	Method	Matrix area fraction
CM1* side 1	SE	0.688
CM1* side 2	SE	0.616
CM2* side 1	SE	0.734
CM2* side 2	SE	0.732
CM3	SE	0.681
CM4	SE	0.816
CM6	BSE	0.629
CM8	BSE	0.764
CM9	BSE	0.683
CM10	BSE	0.716
CM12	BSE	0.568
CM13	BSE	0.676
CM16	BSE	0.576
CM18	BSE	0.643

Table 4.3: Matrix area fractions of CM NWA 11345 subsamples recovered from BSE and SE images. * = The ε^{54}Cr composition and PVE concentrations CM1 and CM2 were not measured in this study. These samples were included in this table to highlight the heterogeneities in recovered area fractions from different sides of the same sample chip.

4.3.9 CO, CM, CV, C2-Ung Mixing line

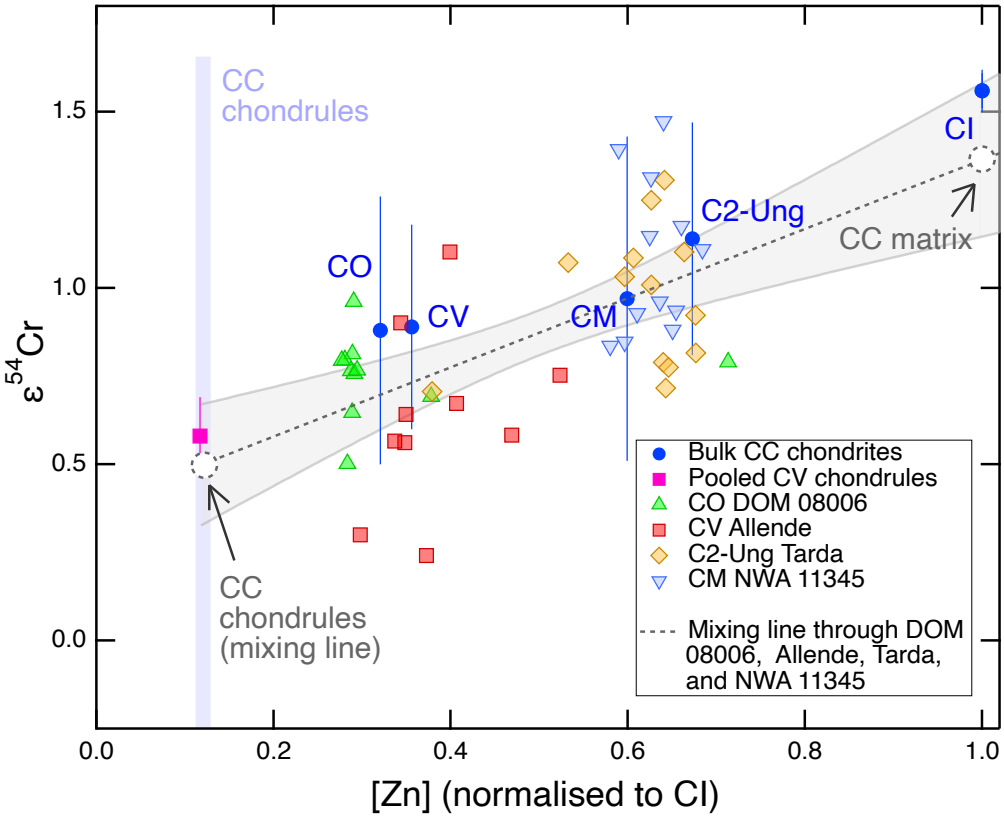

Figure 4.11: Plot displaying the compositions of measured subsamples of CO chondrite DOM 08006, CV chondrite Allende, CM chondrite NWA 11345, and C2-Ung chondrite Tarda. A mixing line has been fitted through all subsamples (grey line) with a shaded 95% confidence interval. Bulk chondrite and chondrule data is sourced from references listed in Fig. 1.6.

An isotopic mixing line (details in section 2.4) was fitted to all measured CC chondrite subsamples (DOM 08006, Allende, NWA 11345, and Tarda). The initial values used were: 1.56 and 0.58 for the ε^{54}Cr compositions of matrix and chondrules, respectively; 1.0 for the ratio of [Cr] of chondrules:matrix; and 0.118 for [Zn] in chondrules (normalised to CI).

When the Zn and Cr concentrations in chondrules and matrix are held constant, the best fit mixing line passes through a value of 1.36 ± 0.22 for the ε^{54}Cr composition of matrix and 0.50 ± 0.17 for chondrules. This mixing line is plotted in Figure 4.11. Narrow 95% confidence interval bands and the small errors associated with the calculated chondrule and matrix compositions indicate a higher quality fit of this mixing line compared to those recovered from each group individually. When considered as one dataset, the ε^{54}Cr values

and matrix fractions of all CC subsamples show a strong correlation, indicated by a ρ of 0.58.

4.3.10 Subsample composition vs mass

For all CC chondrites measured there is no strong relationship between the mass of each subsample and the ε^{54}Cr composition or calculated matrix fraction. A linear best fit line plotted through the ε^{54}Cr and CI-normalised Zn compositions of every subsample shows very weak correlation with mass, indicating that both are independent of mass (see Fig. 4.12). This indicates that the subsampling technique was successful in generating variations in matrix fraction, and possibly ε^{54}Cr compositions, between subsamples within each CC group. In particular, lower subsample masses ($<$25 mg) appear to show greater variation in Zn concentrations in CO, CV, and C2-Ung chondrites (Fig. 4.12a, c, e, and g).

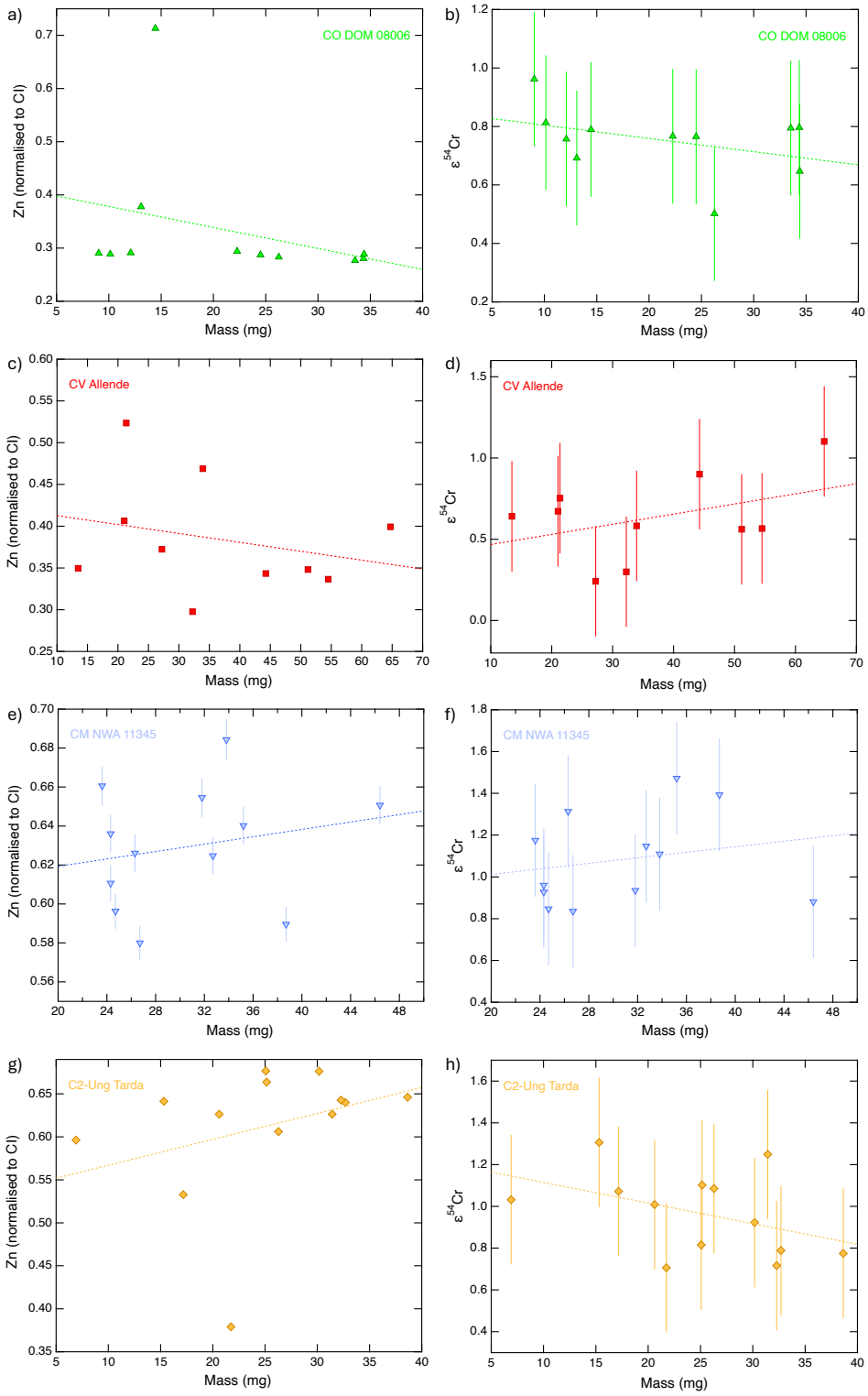

Figure 4.12: Matrix volume fractions (CI-normalised Zn concentrations) and ε^{54}Cr compositions of subsamples of CO chondrite DOM 08006, CV chondrite Allende, CM chondrite NWA 11345, and C2-Ung chondrite Tarda plotted against their mass.

4.4 Discussion

4.4.1 Composition of bulk chondrites

Characterising the bulk composition of each CC chondrite and comparing them to previously reported compositional ranges will allow me to assess whether these samples are representative of each group. In some cases, the bulk composition reported here is the first measurement of specific chondrites, extending the range of reported isotopic compositions for each group. If these chondrites are representative of their groups, then they can later be used to evaluate the formation mechanisms of the CC chondrite parent bodies.

CO chondrite DOM 08006

The bulk ε^{54}Cr composition of DOM 08006 is 0.734 ± 0.23. This is the first reported ε^{54}Cr composition of this CO chondrite, however, it falls in the range of previously reported values of 0.57 (± 0.11) - 1.22 (± 0.04) (Torrano et al., 2021; Zhu et al., 2021c). This composition also agrees with the average reported composition of 0.88 ± 0.38

The bulk Zn concentration of DOM 08006 is 99 ppm, corresponding to a matrix volume fraction of 0.317. This is similar, if slightly lower, than the previously reported average Zn concentrations of CO chondrites (109.8 ppm) (Braukmüller et al., 2018).

CV chondrite Allende

The bulk ε^{54}Cr composition of Allende is 0.68 ± 0.34. This is slightly lower than other reported ε^{54}Cr values of Allende (0.71 (± 0.15) - 0.95 (± 0.1)), however, falls within error of the average of previously reported CV chondrites (0.886 ± 0.29) (Qin et al., 2010; Zhu et al., 2021c).

The comparatively lower ε^{54}Cr compositions of Allende reported in this study may be a result of the low yields achieved during column chemistry (between 53 - 69%). Previous studies have reported that low column yields can result in shifts towards lighter isotopic values (Larsen et al., 2016).

The bulk Zn concentration of Allende is 118 ppm, corresponding to a matrix volume fraction of 0.377. This is similar, if slightly lower, than the previously reported average

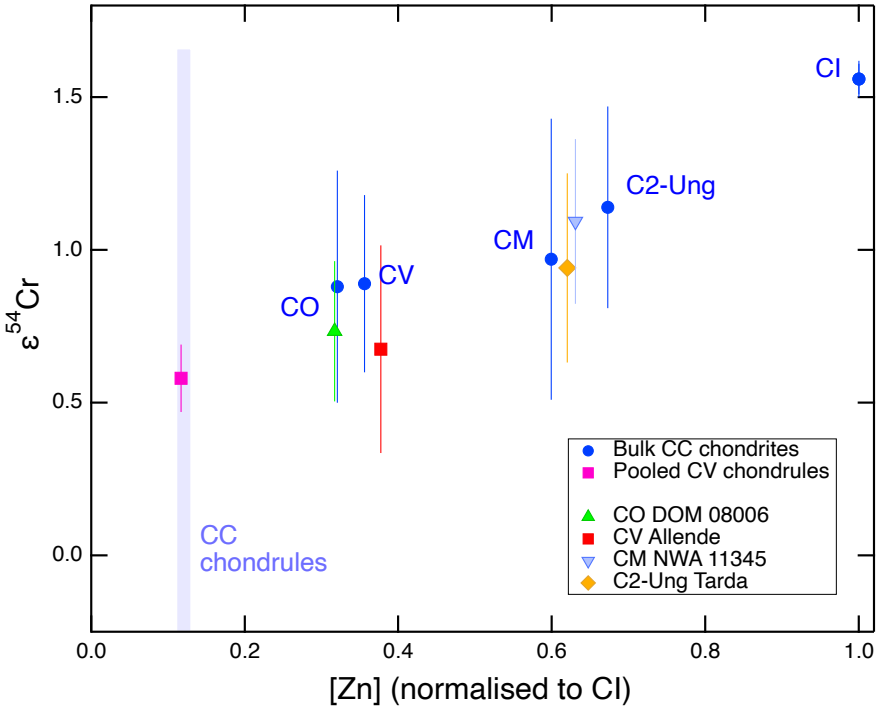

Figure 4.13: Bulk ε^{54}Cr compositions and CI-normalised Zn concentrations of CO chondrite DOM 08006, CV chondrite Allende, CM chondrite NWA 11345, and C2-Ung chondrite Tarda measured in this study. Bulk chondrite and chondrule data is sourced from references listed in Fig. 1.6.

Zn concentrations of CO chondrites (123 ppm) (Braukmüller et al., 2018).

CM chondrite NWA 11345

The bulk ε^{54}Cr composition of NWA 11345 is 1.09 ± 0.27. This is the first reported ε^{54}Cr composition of this meteorite, however, it falls in the range of previously reported CM chondrites values of 0.76 (± 0.04) - 1.37 (± 0.12) (Shukolyukov and Lugmair, 2006; Qin et al., 2010; Göpel et al., 2015; Torrano et al., 2021; Zhu et al., 2021c). This composition also agrees with the average reported composition of 0.97 ± 0.46.

The bulk Zn concentration of NWA 11345 is 197 ppm, corresponding to a matrix volume fraction of 0.631. This agrees well with the reported average by Braukmüller et al. (2018) of 197 ppm, and is slightly higher than the average of 187 ppm reported by Bryson and Brennecka (2021).

C2-ung chondrite Tarda

The bulk ε^{54}Cr composition of Tarda is 0.941 ± 0.31. This is slightly lower, but within error, of previously reported ε^{54}Cr values of Tarda (0.99 (± 0.14) - 1.4 (± 0.16)) (Hellmann et al., 2023; Yokoyama et al., 2023). This composition is slightly lower, but within error, of the average reported values for Tarda and Tagish Lake, the other C2-Ung chondrite that Tarda is commonly paired with (1.14 ± 0.33) (Petitat et al., 2011; Schrader et al., 2024a).

The bulk Zn concentration of Tarda is 194 ppm, corresponding to a matrix volume fraction of 0.620. This is similar, if slightly lower, than the previously reported average Zn concentrations of Tarda and Tagish Lake of 209 ppm (Braukmüller et al., 2018; Hellmann et al., 2020; Marrocchi et al., 2021a; Schrader et al., 2024a). However, this composition matches well with measured reported Zn concentrations of one Tarda subsample measured by Marrocchi et al. (2021a) of 197 ppm.

Overall, the bulk ε^{54}Cr compositions and PVE concentrations of each CC chondrite examined in this work agree within error to the average compositions reported in the literature for each of their respective groups. This implies that the compositions of DOM 08006, Allende, NWA 11345, and Tarda reported here are representative of the CO, CM, CV, and C-Ung chondrites, and trends in the compositions of their subsamples can be used to evaluate the formation mechanisms of the different CC chondrite parent bodies.

4.4.2 ε^{54}Cr compositions of chondrules and matrix

4.4.2.1 Results from individual CC chondrites

Evaluating the chemical and isotopic compositions of chondrules and matrix in CC chondrites allows us to determine whether they share the same provenance, or if they formed in different regions of the disk before they were transported and accreted into the CC parent bodies. If chondrules and matrix are sourced from the same reservoir they may share similar isotopic compositions; if they are formed in different regions, this will be reflected in their differing ε^{54}Cr values.

Mixing lines plotted through the subsamples of each CC chondrite all display large 95%

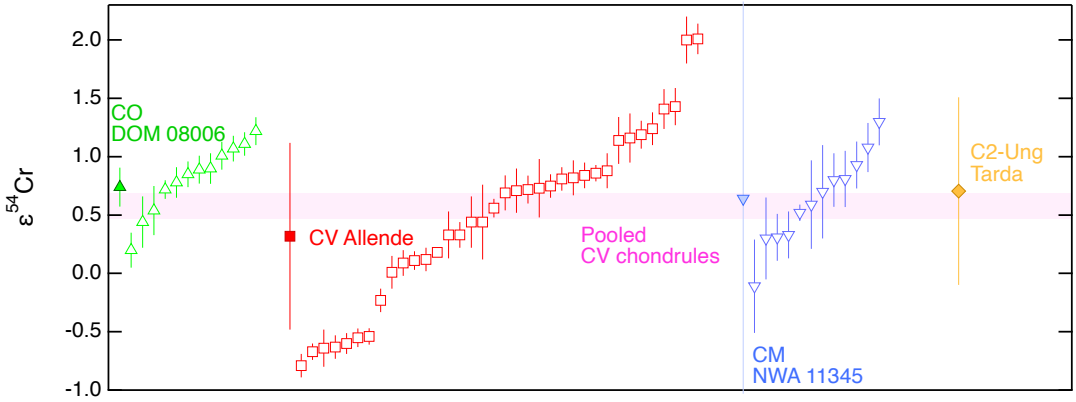

Figure 4.14: Chondrule ε^{54}Cr compositions in CC chondrites. Solid points are compositions recovered from isotopic mixing lines in this study, open points are measured values of CO (green), CV (red), and CM (blue) chondrules reported by Qin et al. (2011); Olsen et al. (2016); Zhu et al. (2019a); Schrader et al. (2020a); van Kooten et al. (2020) and Williams et al. (2020), and the pink shaded region indicates the compositions of pooled CV chondrules reported by Schneider et al. (2020).

confidence intervals, making it hard to accurately determine the ε^{54}Cr compositions of chondrules and matrix (see Figs. 4.4, 4.6, 4.8 and 4.10). Each mixing line could either show slopes of positive gradients implying the presence of isotopically distinct chondritic components, or flat lines indicating homogeneous isotopic compositions of chondrules and matrix. The insensitivity of this mixing line and limitations of this technique are discussed further in section 6.2.

If the mixing lines can determine the chondrule and matrix compositions of these chondrites, taking into account the large associated uncertainties, this study shows that in CV, CM, and C2-ung chondrites, matrix likely displays enriched ε^{54}Cr compositions compared to chondrules. Conversely, CO chondrites display isotopically similar chondrule and matrix isotopic compositions.

The recovered chondrule compositions from Allende (0.32 ± 0.80), DOM 08006 (0.74± 0.17), and NWA 11345 (0.64 ± 2.52) agree with the reported average chondrule compositions of CV, CO, and CM chondrites (0.48 ± 1.49, 0.81 ± 0.59, and 0.63 ± 0.78 respectively) (Qin et al., 2011; Olsen et al., 2016; Zhu et al., 2019a; Schrader et al., 2020a; van Kooten et al., 2020; Williams et al., 2020). The ε^{54}Cr compositions of C2-Ung chondrules have not previously been measured but are reported here as 0.71 ± 0.80.

These inferred chondrule compositions are all within error of the pooled CV chondrule ε^{54}Cr composition of 0.58 (± 0.11) reported by Schneider et al. (2020) (see Fig. 4.14). The recovered chondrule compositions of CM NWA 11345 and C2-Ung Tarda are particularly close to this value.

Due to the lack of spread in matrix fractions within each dataset (barring the CO chondrite DOM 08006), the matrix compositions of CC chondrites are poorly characterised here, with large 95% confidence intervals. The recovered matrix compositions of CO, CV, CM, and C2-Ung chondrites all lie within the range 0.78 (± 0.45) - 1.40 (± 1.83). This range of compositions (excluding uncertainty margins) is higher than the pooled chondrule composition reported by Schneider et al. (2020) (ε^{54}Cr = 0.58) and is broadly more enriched compared to chondrule compositions recovered in this study. This matrix compositional range includes the composition of CI chondrites for all CC chondrites (except the CO chondrites in Fig. 4.4a, though after excluding subsample CO11 in Fig. 4.4b, CI chondrites fall within range again). Schneider et al. (2020) also isolate matrix from CV chondrite Allende and report a matrix ε^{54}Cr compositional range of 0.98 (± 0.13) - 1.18 (± 0.14) , which agrees broadly with the slightly lower-than-CI values observed here.

This similarity in recovered chondrule composition across all measured CC chondrite groups implies that the average compositions of chondrules in the CO, CV, CM, and C2-Ung chondrites are constant. This could imply a shared "chondrule reservoir" for the main CC chondrite groups, an idea previously suggested by Alexander (2019b), Bryson and Brennecka (2021), and Hellmann et al. (2023). However, due to the poor fit of the mixing line, the error associated with these values should be taken into account.

4.4.2.2 Results from pooled CC chondrites

As seen in the previous section, mixing lines generated from the subsamples of each individual chondrite have very large associated errors due to their small range of matrix fractions. This leads to difficulty in determining whether chondrules and matrix in each chondrite have different ε^{54}Cr compositions.

To better assess whether all CC chondrites display differing chondrule and matrix compositions, and if these compositions are similar in all CC groups, a mixing line was fit through

all measured subsamples of CO, CV, CM, and C2-Ung chondrites. This allowed for a wide range of matrix fractions to sampled, reducing the error of the fit and constraining the recovered matrix and chondrule compositions. Models by Bryson and Brennecka (2021) and Alexander (2019b) also support the pooling of all CC groups for fitting of a common mixing line as these studies suggest that all CC groups may share similar chondrule and matrix compositions, with each component present in varying proportions. This mixing line is show in Fig. 4.11.

The mixing line fit through all measured CC subsamples recovers an average CC chondrule ε^{54}Cr composition of 0.50 ± 0.17 and an isotopically distinct matrix composition of 1.36 ± 0.22, with restricted 95% confidence interval bands.

The calculated chondrule composition agrees remarkably well with the pooled CV chondrule ε^{54}Cr value of 0.58 (± 0.11) measured by Schneider et al. (2020) in Allende, indicating that the CO, CV, CM, and C2-Ung chondrites measured here display a similar average chondrule composition compared to those previously reported. This corroborates results reported in the previous section, which suggest that the average chondrule ε^{54}Cr compositions recovered from mixing lines fitted through individual CC groups are all similar.

The matrix composition recovered from this mixing line is significantly enriched in ^{54}Cr compared to CC chondrules, displaying ε^{54}Cr compositions within error of CI chondrites. A CI-like composition of matrix within CC chondrites has also been proposed by Alexander (2019b), Bryson and Brennecka (2021) (Fig. 4.15) and Hellmann et al. (2023). These studies suggest that CI-like material represents one of the key elements that mixes with other chondritic components (e.g., chondrules, RIs, ^{16}O-poor water) in variable amounts to generate the range of CC chondrites seen today. This is because CI chondrites often lie at the end of isotopic trends seen in the CC reservoir (e.g., in plots between ε^{50}Ti-ε^{54}Cr, ε^{64}Ni-ε^{94}Mo, Δ^{17}O-ε^{54}Cr (Kruijer et al., 2020)), and CC chondrites show bulk elemental ratios close to CI (Hezel and Palme, 2008; Friend et al., 2017; Braukmüller et al., 2018; Hezel et al., 2018b). The isotopic composition of CC matrix recovered from the mixing line in this study agrees with these mixing models, as different CC chondrite compositions can be successfully generated through mixing of varying amounts of CI-like matrix with an

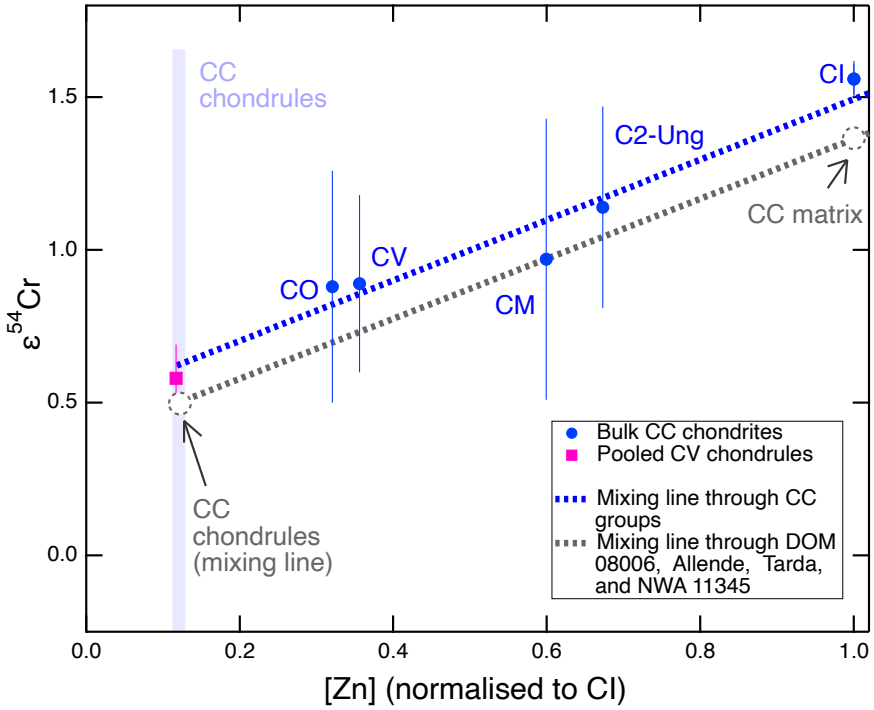

Figure 4.15: Mixing line through all CC chondrite subsamples groups measured in this study (blue line) compared with the mixing line proposed by Bryson and Brennecka (2021) (blue). Bulk chondrite and chondrule data is sourced from references listed in Fig. 1.6.

isotopically distinct chondrule population (Fig. 4.15). Cr isotopic heterogeneity between chondrules and matrix matrix has also been suggested by Sugiura and Fujiya (2014), who observed that chondrule ε^{54}Cr compositions in Allende are isotopically lighter than values recovered from matrix leachates. However, Sugiura and Fujiya (2014) previously associated the lighter chondrule ε^{54}Cr compositions with metamorphism.

4.4.2.3 Isotopic heterogeneity in chondrules

Though the chondrule isotopic compositions recovered in this study agree with the average compositions observed in the CC chondrites, they do not capture the variation in isotopic compositions displayed by individual chondrules. Measurements of isolated chondrules from the CO, CV, and CM chondrites record a large range of ε^{54}Cr values, spanning from -0.79 to 2.01 (see. Fig. 4.14) (Qin et al., 2011; Olsen et al., 2016; Zhu et al., 2019a; Schrader et al., 2020a; van Kooten et al., 2020; Williams et al., 2020).

This range in chondrule composition could manifest as the scatter observed in the ε^{54}Cr compositions of subsamples within each chondrite group. The variability in chondrule

compositions is likely not averaged out within each subsample, leading to deviations away from a clear mixing trend between ^{54}Cr enriched matrix and depleted chondrules. This scatter should be more pronounced in chondrite groups that have larger chondrules, e.g, CV chondrites. This trend is seen in this study as Allende subsamples show the largest variation in ε^{54}Cr compositions (0.24 - 1.10) and CV chondrites also display the largest range in measured chondrule ε^{54}Cr compositions (though this could also be due to the larger number of CV chondrules studied compared to the CM and CO chondrules) (Olsen et al., 2016; Schneider et al., 2020; Williams et al., 2020).

The source of the differing enrichments of ^{54}Cr within individual chondrules is outside the scope of this study, however, it is probably due to incorporation of varying amounts of amoeboid olivine aggregates (AOAs) and isotopically NC-like material into chondrules during their formation (van Kooten et al., 2021; Fukuda et al., 2024; Torrano et al., 2024). This is evidenced by the depleted NC-like ε^{54}Cr observed in large CV chondrule cores van Kooten et al. (2021), and the ability of mixtures of AOAs and NC-like endmembers to reproduce the range of observed chondrule compositions (Torrano et al., 2024).

Regardless of the cause of compositional variation within CC chondrules, the similar average chondrule compositions seen in CC groups implies that they all form within a shared chondrule reservoir. This could indicate that all chondrules form at the same time in the same location, thus recording similar compositions. However, contemporaneous formation disagrees with variations in chondrule ages recovered from Mn-Cr dating, which show that CO chondrules display older ages than CV chondrules (Zhu et al., 2019a). Instead, CC chondrules may continually form in one location which retains a distinct isotopic composition over the time period of chondrule formation ($\sim$0 - 3 Ma after CAI formation (Zhu et al., 2019a; Kruijer et al., 2020)). This agrees with recent work by Hellmann et al. (2023), who suggest that chondrules in all CC groups form locally within a pressure maximum from isotopically heterogeneous dust aggregates which are sourced from across the disk. The pressure maximum is likely related to the water ice line which provides a structure within the disk that facilitates dust enrichment and chondrule formation over an extended time period.

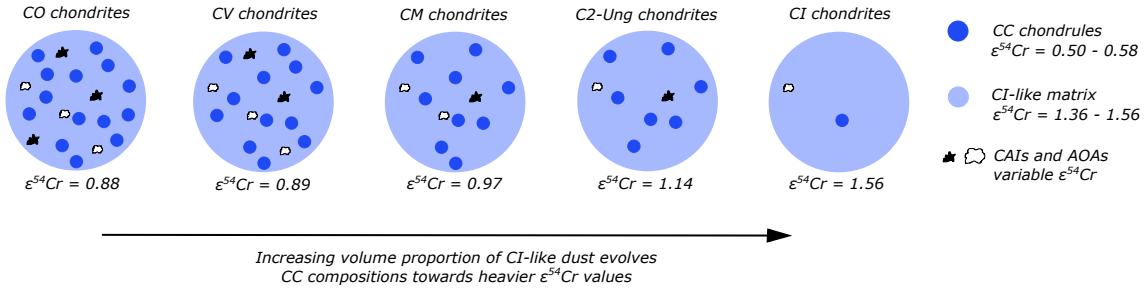

Figure 4.16: Variation in chondrule and matrix fractions observed in CC chondrite groups. Chondrites that display higher matrix fractions accrete with greater amounts of CI-like dust, evolving towards heavier bulk ε^{54}Cr compositions. Bulk chondrite and chondrule compositions sourced from results reported in this study and those referenced in Fig. 1.6. Not to scale.

4.4.3 Formation of the CC parent bodies

Much of the debate surrounding formation of the CC parent bodies focuses on the provenance of the CAIs, AOAs, chondrules and matrix material observed in chondrites. CAIs and AOAs are thought to from in close proximity to the proto-Sun before they are transported to greater radial distances to the CC reservoir (Yang and Ciesla, 2012; Desch et al., 2018). The mechanisms behind chondrule formation are still enigmatic, however, isotopic compositions can help determine whether chondrules and matrix sample material from the same local reservoir, or if they are formed in different regions of the disk.

Results from this study indicate that chondrules in the CO, CV, CM, and C2-Ung chondrites share a similar average ε^{54}Cr composition, close to that measured previously in pooled CV chondrules (Schneider et al., 2020). This composition is distinct to the recovered matrix compositions, which display similar, higher ε^{54}Cr values in all CC groups, within error of CI chondrites. The different chondrule and matrix compositions observed here indicate that these components form from/sample different reservoirs and acquire different isotopic signatures before they are transported and accreted into the chondrite parent bodies. Different chondrite parent bodies accrete with varying amounts of matrix material, forming the different CC chondrite groups observed (Fig. 4.16). Parent bodies that accrete with higher proportions of matrix material (e.g., CM and C2-Ung chondrites) exhibit greater PVE concentrations and larger ε^{54}Cr anomalies, due to their higher fractions of compositionally CI-like matrix.

This result disagrees with models of chondrite formation that suggest complementarity

CC group	CAIs and AOAs (vol%)	Matrix (vol%)	Chondrule (vol%)
CO	13	31.7	55.3
CV	10	37.7	82.3
CM	5	63.1	31.9
C2-Ung	0.2	62.0	37.8

Table 4.4: Inferred chondrule abundances based on CAI and AOA volume percentages reported by Scott and Krot (2004) and Schrader et al. (2024a), and matrix volume fractions calculated in this study.

in the major element compositions of chondrule and matrix. Though some evidence of complementary Si/Mg and Fe/Mg ratios has been observed in the CR and NC chondrites (Bland et al., 2005; Friend et al., 2017; Hezel et al., 2018a; Ebel et al., 2024), this model disagrees with the observation of isotopically distinct chondrules and matrix seen here. By definition, models of complementarity require chondrules and matrix to be formed from a shared reservoir of material. This would result in chondrules and matrix exhibiting different, but complementary, major element ratios - the signature of which can be obscured due to later alteration. However, if chondrules are formed from the same reservoir as matrix material they should display the same ε^{54}Cr isotopic compositions. This assumes that the carrier of the ε^{54}Cr anomaly would be incorporated equally into both chondrules and matrix, and would not be destroyed via mechanisms such as thermal processing. Interestingly, Budde et al. (2016b) observe that chondrules and matrix in Allende display distinct but complementary ^{183}W anomalies that could be explained by a localised dust-grain sorting mechanism (Hubbard, 2016), but Sanders and Scott (2022) attribute this to later hydrothermal alteration on the parent body.

The chondrite formation mechanism proposed here instead supports recent studies that suggest that the CC chondrite parent bodies form from mixtures of chondrules, CI-like matrix, and RIs (Alexander, 2019b; Bryson and Brennecka, 2021; Hellmann et al., 2023). A summary of recovered chondrule, matrix, CAI, and AOA proportions present in each CC group is displayed in Table 4.4. These estimates neglect the contribution of metal (often $<$5 vol%), and, in general, provide greater estimated chondrule fractions than those reported in the literature (Scott and Krot, 2004). This could reflect the difficulty in identifying smaller, μm-sized chondrule fragments and mischaracterising them as matrix, leading to higher reported matrix fractions in the literature, and lower reported chondrule

abundances (Schrader et al., 2011).

This chondrite formation mechanism also agrees with observed trends in the mass-dependent fractionation of PVEs in CC chondrites, which indicate that the compositions of CC chondrites can be replicated by mixing of volatile-enriched matrix with a volatile-depleted component, assumed to be chondrules (Morton et al., 2024). Marrocchi et al. (2023) also suggest that the μ^{54}Fe compositions of CC chondrites display a similar trend to what is observed in this work, as the μ^{54}Fe composition of CC chondrites can be recovered through mixing of CI-like dust and a non-matrix component, assumed to represent chondrules.

Since CO chondrules display the lowest matrix fractions, the oldest chondrule ages (Zhu et al., 2019a), and the oldest accretion ages (Bryson and Brennecka, 2021), it is likely that increased matrix fractions (and higher ε^{54}Cr compositions) correlate with later formation of chondrite parent bodies. This agrees with the findings of Bryson and Brennecka (2021) who report CC chondrite accretion ages of 2.5 Ma, 2.7 Ma, 3.25 Ma, and 3.25 Ma for the CO, CV, CM, and C2-Ung chondrites, respectively. The correlation of decreasing age with increasing matrix fractions could indicate that the proportion of matrix material (i.e., CI-like dust) within the chondrite formation region increased over time. If CC chondrules of all groups formed in a restricted location, as suggested by their similar average ε^{54}Cr compositions, this implies that CI-like material must continually be transported into the chondrite forming region. The amount of CI-like dust in this region must increase in concentration over time to form chondrites that exhibit higher fractions of matrix. This is proposed by Bryson and Brennecka (2021) as an explanation for the apparent increase in CI-like signatures observed in CC chondrites over time.

4.4.4 Dynamics of solid transport in the CC reservoir

If the matrix and chondrules of CC chondrites display distinct ε^{54}Cr compositions, this indicates that they sample different reservoirs within the protoplanetary disk. Understanding where these reservoirs originate and how chondrules and matrix subsequently accrete can shed light on the history of solid transport in the protoplanetary disk.

The matrix in CC chondrites displays comparatively enriched ε^{54}Cr compositions com-

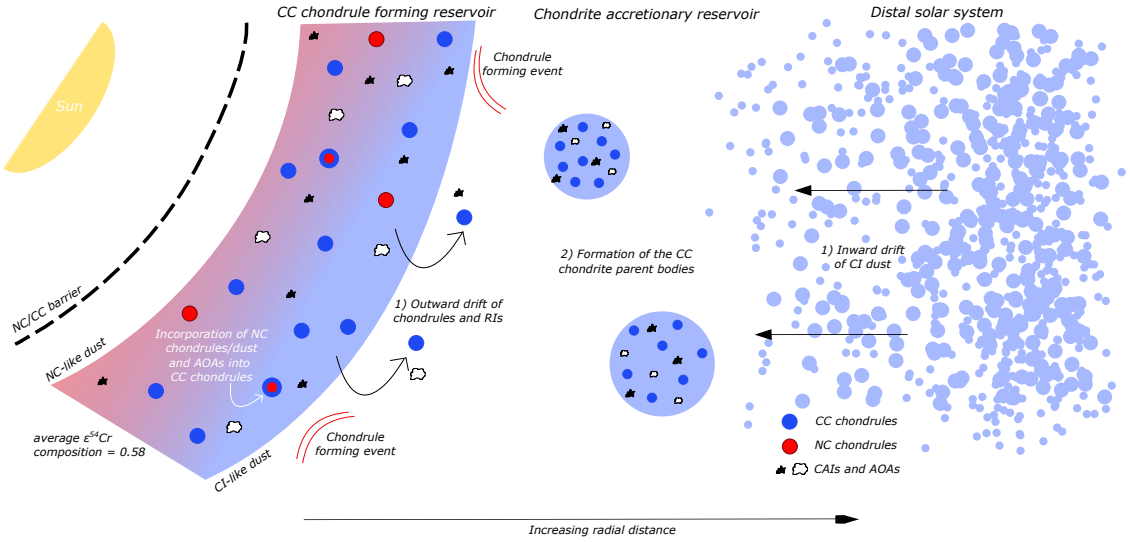

Figure 4.17: CC chondrules form in a reservoir close to the barrier between the NC and CC reservoirs. This chondrule formation reservoir contains AOAs, CAIs, and small amounts of NC-like dust and/or chondrules that are incorporated into the CC chondrules. The average chondrule ε^{54}Cr composition is ~0.58. CC chondrules and RIs are transported out of the chondrule forming reservoir and accrete at greater radial distances with inwardly drifting CI-like dust that forms the matrix within CC chondrite parent bodies. Different CC groups accrete with varying proportions of CI-like dust, chondrules, and RIs. Not to scale.

pared to CC chondrules, indicating the presence of higher proportions of the carrier of the *r*-process-enriched ^{54}Cr anomaly. The ε^{54}Cr composition of matrix is within error of CI chondrites, which display the most enriched ε^{54}Cr compositions of all chondrite groups. Due to their high volatile abundances (Krot et al., 2014), solar-like compositions (Palme et al., 2014), high degrees of aqueous alteration (King et al., 2015a), and scarcity of chondrules and CAIs (Frank et al., 2023), CI chondrites are thought to represent some of the most distal material in our solar system. The enriched isotopic composition of CI chondrites implies a radial distribution of carriers of the ^{54}Cr anomaly, with more distal material displaying enriched isotopic compositions. This suggests that the matrix material in CC chondrites originates from a more distal reservoir compared to the CC chondrules, which display lower ε^{54}Cr compositions and are thought to form in a restricted reservoir, possibly at the water-ice line (see section 4.4.3).

If chondrules and matrix in the CC chondrites are formed at different radial distances in the protoplanetary disk, large scale transport of material is required to allow these components to mix and accrete to form the CC parent bodies. If chondrules do form close to the water-ice line over a protracted period of time, as suggested by Hellmann

et al. (2023), the CI-like matrix material must drift inwards from the outer regions of the protoplanetary disk towards the chondrule forming region. This model is also proposed by Bryson and Brennecka (2021) in their formation scenarios for the CC chondrites. However, this dust must not pollute the chondrule forming region, or chondrules would display an evolving ε^{54}Cr composition over time, which is not observed (Zhu et al., 2019a). Instead, chondrules must also be transported out of their formation reservoir, into a region where the CC parent bodies accrete with infalling CI dust (Fig. 4.17).

The dynamics of how chondrules and matrix-bound dust move around in the early solar system can help identify which mechanisms of solid transport and accretion were dominant in the outer solar system. The movement of matrix and/or chondrules suggested in this study implies the large-scale movement of solids in the CC reservoir, though it should be noted that inward drift of dust grains is an expected occurrence within protoplanetary disks (Drazkowska et al., 2022). Widespread movement is consistent with models of pebble accretion used to explain the rapid formation of the gas giants in the outer solar system (Lambrechts et al., 2019; Levison et al., 2015; Drazkowska et al., 2022). Unlike models of planetesimal formation which sample spatially restricted zones, pebble accretion models depict large feeding regions of growing planetesimals, facilitated by the accretion of mm - cm-sized dust particles that are able to drift large distances in the protoplanetary disk. The large scale outward drift of pebble-sized chondrules and inward drift of mm-scale CI-like dust into the CC forming regions is indicative of a dynamically active CC reservoir. This does not provide definitive evidence for the action of pebble accretion in the outer solar system, but does imply widespread inward and outward movement of solids in the outer protoplanetary disk. Any dynamical model that attempts to describe planetesimal formation in the outer solar system must encapsulate the movement of CC chondrules and CI-like dust proposed in this work.

4.5 Conclusions

Coupled ε^{54}Cr and PVE concentrations were measured of subsamples of CO chondrite DOM 08006, CV chondrite Allende, CM chondrite NWA 11345, and C2-Ung chondrite Tarda to investigate the formation of the CC chondrites.

Bulk ε^{54}Cr compositions, Zn concentrations, and matrix volume fractions of each chondrite are provided in table 4.5. Also included are the chondrule and matrix compositions of each chondrite group, recovered from isotopic mixing lines plot through the subsamples.

Chondrite	**Bulk ε^{54}Cr** 2σ	**Chondrule ε^{54}Cr** 2σ	**Matrix ε^{54}Cr** 2σ	**Zn (ppm)**	**Matrix volume fraction**
CO DOM 08006	0.73 ±0.08	0.74 ±0.17	0.78 ±0.45	99	0.317
CV Allende	0.68 ±0.34	0.32 ±0.80	1.35 ±1.80	118	0.377
CM NWA 11345	1.09 ±0.27	0.64 ±2.52	1.40 ±1.83	197	0.631
C2-Ung Tarda	0.94 ±0.31	0.71 ±0.80	1.18 ±0.64	194	0.620

Table 4.5: Summary of bulk CC chondrite compositions recovered from this study.

As mixing lines plot through each CC chondrite subsample set have large errors associated with the lack of spread of matrix fractions, a mixing line was also plot through all the measured CC chondrite subsamples. This recovers chondrule and matrix ε^{54}Cr compositions of 0.50 ± 0.17 and 1.36 ± 0.22, respectively.

The compositional similarity of chondrules from the CO, CV, CM, and C2-Ung chondrites implies that chondrules from all CC groups form in a restricted region, and their isotopically distinct ε^{54}Cr matrix composition implies that matrix material samples a different region of the protoplanetary disk compared to CC chondrules.

As matrix material displays higher ε^{54}Cr compositions, within error of CI chondrites, this implies that matrix originates from more distal locations in the protoplanetary disk compared to the chondrule forming region, which is likely located at the water-ice line. CI-like matrix material may have drifted inwards, and CC chondrules outwards from their formation reservoir, to co-accrete and form the different CC chondrite parent bodies.

CC chondrites that display higher fractions of matrix and higher ε^{54}Cr compositions (i.e., CM and C2-Ung chondrites) likely accrete later compared to those that display lower matrix fractions and smaller ε^{54}Cr anomalies (i.e., CO and CV chondrites).

The formation mechanism of CC chondrites described here requires the large scale transport of CI-like dust and/or CC chondrules before accretion of the chondrite parent bodies. This inferred extensive solid movement in supports planetary formation models that include wide-scale solid movement, such as pebble accretion.

Chapter 5

Accretionary history of the CR chondrites

5.1 Introduction

5.1.1 Background

The Renazzo-like (CR) chondrites are a group of carbonaceous chondrites which represent some of the most primitive and pristine meteorites in our collections. This is evidenced by the presence of unaltered, unequilibrated silicates in their matrix (Schrader et al., 2011) and the preservation of high abundances of presolar grains within insoluble organic matter (Davidson et al., 2014). CR chondrites show evidence for a range of aqueous alteration extents (between grades CR1 - CR2.8), but show evidence of minimal thermal metamorphism (Weisberg et al., 2006; Harju et al., 2014; Schrader et al., 2015).

The CR chondrites display relatively low matrix abundances (35 vol% (Schrader et al., 2011)) compared to the range seen in other carbonaceous chondrites (30 - 80 vol%). However, a few anomalous CR chondrites show elevated matrix abundances, of 68.5 vol% and 65.8 vol% seen in Al Rais and GRO 95577, respectively (Schrader et al., 2011).

Chondrules make up ∼64 area% of CR chondrites, and refractory inclusions (RIs) ∼0.4 area% (Abreu et al., 2020). The CR chondrites contain three types chondrules: abundant MgO-rich, FeO-poor Type I chondrules which comprise up to 63% of the total area

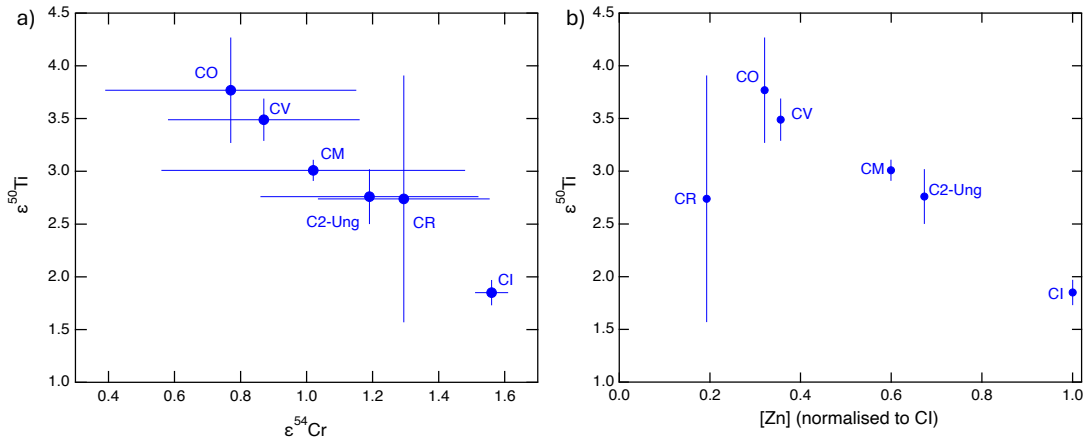

Figure 5.1: Plot displaying the a)ε^{50}Ti vs ε^{54}Cr of CC chondrites. b) ε^{50}Ti vs matrix volume fraction of CC chondrites. ε^{50}Ti and Zn concentration data is sourced from Bryson and Brennecka (2021) and Braukmüller et al. (2018).

of chondrite sections; MgO-poor, FeO-rich Type II chondrules which are relatively rare occupying 2.3% of CR chondrites; and rare anorthite rich chondrules (ARCs) that only occupy 0.5 area% (Schrader et al., 2011). Recent work has further divided the type I chondrules seen in CR chondrites into two groups, *type I-CR* and *type I-CO*, based on their chondrule diameters, textures, and oxygen isotopic compositions (Marrocchi et al., 2022). Most CR chondrules are porphyritic olivine (PO) and porphyritic olivine/pyroxene (POP) indicating that some chondrule precursors had experienced total melting before their incorporation into the CR parent body (Hewins et al., 2005; Schrader et al., 2015).

CR chondrites differ from the "main group" CC chondrites (interpreted here as CO, CM, CV, and CI chondrites) in various aspects, prompting further study into the conditions of their formation in the protoplanetary disk. Notably, Pb-Pb, Al-Mg, and Hf-W dating of CR chondrules consistently indicate formation ages of ∼3.4 - 4 Ma after CAI formation, nearly ∼1 - 2 Ma later than other CC chondrite groups (Amelin et al., 2002; Budde et al., 2018; Schrader et al., 2017). This is corroborated by Mn-Cr dating of aqueous alteration on CR chondrites, which is shown to have occurred at later times, implying later accretion and alteration of the CR parent body (Jilly-Rehak et al., 2017).

In ε^{50}Ti-ε^{54}Cr isotopic space, the CR chondrites follow the trend defined by "main group" CC chondrites, displaying the largest positive ε^{54}Cr anomalies and lowest ε^{50}Ti anomalies, only exceeded by CI chondrites (Fig. 5.1a) (Warren, 2011). Interestingly though, they

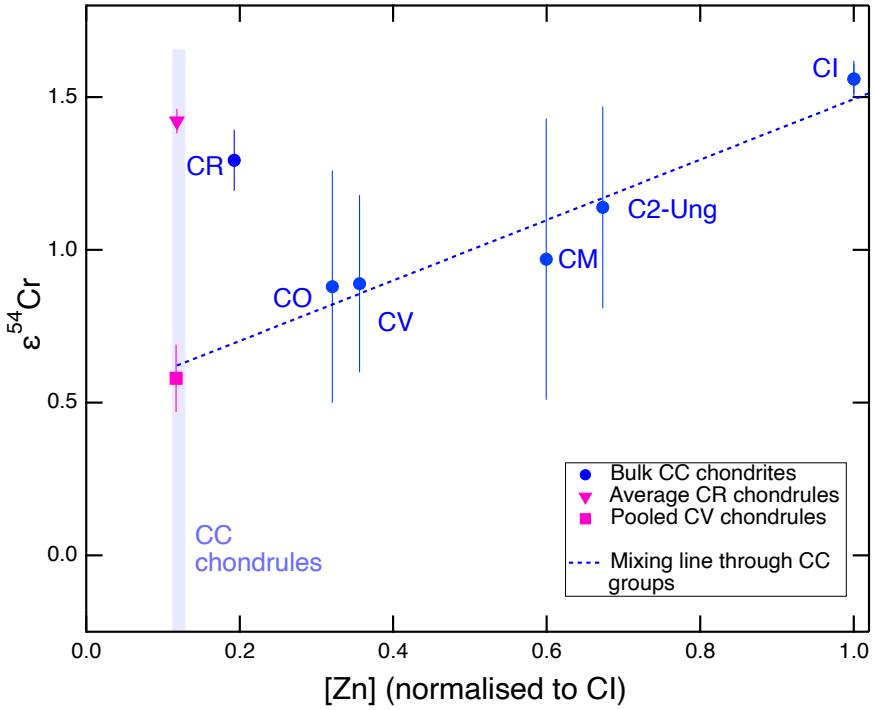

Figure 5.2: Plot displaying the average reported ε^{54}Cr compositions of CC chondrites, CV chondrules, and CR chondrules plotted against their Zn concentration (normalised to CI). Bulk chondrite and chondrule data is sourced from: Olsen et al. (2016), van Kooten et al. (2016), and references listed in Fig. 1.6.

do not fall on this same trend in plots of ε^{54}Cr and ε^{50}Ti vs matrix fraction (Fig. 5.1b). This could indicate that though CR chondrites share similar trends in isotopic anomalies to the other CC chondrites, these anomalies are now decoupled from their initial carriers as they are no longer correlated to matrix fraction. This deviation could be the result of reprocessing events affecting the matrix, chondrule, and RI compositions. Suggestions of reprocessing and devolatilisation affecting the composition and petrology of CR chondrites have been previously proposed by Connolly et al. (2008), Schrader et al. (2015), Hellmann et al. (2020), Bryson and Brennecka (2021), Marrocchi et al. (2022), and Pinto et al. (2024).

The majority of CR chondrites are also depleted in PVEs compared to CIs (∼10% CI abundances), though rare, matrix-rich samples MIL 090001 and Al Rais show larger enrichments (∼60% CI) (Bryson and Brennecka, 2021). Questions then arise as to why certain CR chondrites show anomalously high matrix and volatile abundances compared to the rest of the CR chondrite group, and whether this is related to the material available

for accretion in the local environment, and/or mechanisms of volatile loss during accretion of the CR parent body.

In light of these observations, investigating the formation of CR chondrules and matrix, and the accretion CR chondrite parent body compared to the "main group" CC chondrites, should allow us to determine whether mechanisms of chondrite formation were consistent throughout the CC reservoir and how they may have changed over time. The ε^{54}Cr compositions of CC chondrites imply that the CO, CM, CV, and C2-Ung chondrites form from variable mixtures of CI-like dust and isotopically distinct chondrules (see Chapter 4). CR chondrites appear to fall off this trend, displaying high ε^{54}Cr values but low matrix fractions and depleted PVE abundances (Fig. 5.2). Characterising the composition of chondrules and matrix in the CR chondrites would allow us to compare them with other CC chondrites, to investigate whether all CC groups sample the same chondritic components and accrete in a similar manner. This would also allow us to comment on the conditions present in the formation reservoir of the CR parent body; specifically, the composition of the material available for accretion and the local concentration of dust. This would provide insight on how the dynamics and composition of material present in the CC reservoir changed over the first ~4 Ma of the solar system.

5.1.2 This work

In this chapter I will investigate the accretionary history of the CR chondrites by measuring the coupled ε^{54}Cr and Zn concentrations of subsamples of CR MIL 090001. These results will then be used to determine the compositions of chondrules and matrix within the CR chondrites. I will compare the average chondrule composition recovered here to those measured in previous studies, and suggest a history of reprocessing that can explain the differences in observed compositions. This will be used to propose the existence of an "initial" CR chondrite and detail a history of accretion of the CR parent body that would bring the formation of the CR chondrites in line with our understanding of how the remaining CC chondrites accreted.

5.2 Methods

One CR chondrite, MIL 090001, was analysed to determine the coupled ε^{54}Cr isotopic compositions and PVE concentrations of its subsamples. This was acquired from JSC (loan no. 3712) and processed at the University of Oxford.

The 900 mg sample was cut into 9 subsamples using a diamond wire saw. Subsamples ranged in weight between 6.7 - 32.9 mg. The subsamples were then digested by the protocol described in section 2.1.3, and a 0.8 ml aliquot was preserved for determining PVE concentrations and initial Cr abundance. A 0.5 ml aliquot was then subjected to the Cr purification procedure detailed in section 2.2. Yields of 63 - 95% were achieved during column chemistry, with 6 subsamples displaying yields greater than 80%. Initial Cr concentrations, PVE abundances, and purity and yield of the column chemistry were measured using Quadrupole ICP-MS, as described in section 2.3.2.

The column chemistry had a procedural blank of Cr below the Method Detection Limit (MDL) of the Quadrupole ICP-MS, indicating the presence of a negligible Cr blank.

Matrix mass fractions were calculated using the CI-normalised Zn concentrations of each subsample as described in section 2.3.4.

For calculation ε^{54}Cr, measured $\frac{^{54}Cr}{^{52}Cr}$ ratios of each subsamples are normalised to the average processed NIST-979 standard values, as described in section 2.3.1.6.

An isotopic mixing line was fit through the ε^{54}Cr and CI-normalised Zn compositions of subsamples of MIL 090001 to determine the ε^{54}Cr composition of chondrules and matrix present. Details of the mixing line are provided in section 2.4.

The bulk ε^{54}Cr composition and CI-normalised Zn concentration of MIL 090001 was calculated using the weighted average of their subsample compositions. The error associated with the bulk ε^{54}Cr composition is the uncertainty associated with the measurement of the isotopic compositions of the subsamples (as described in section 2.3.1.7).

5.3 Results

5.3.1 MIL 090001 chemical and isotopic composition

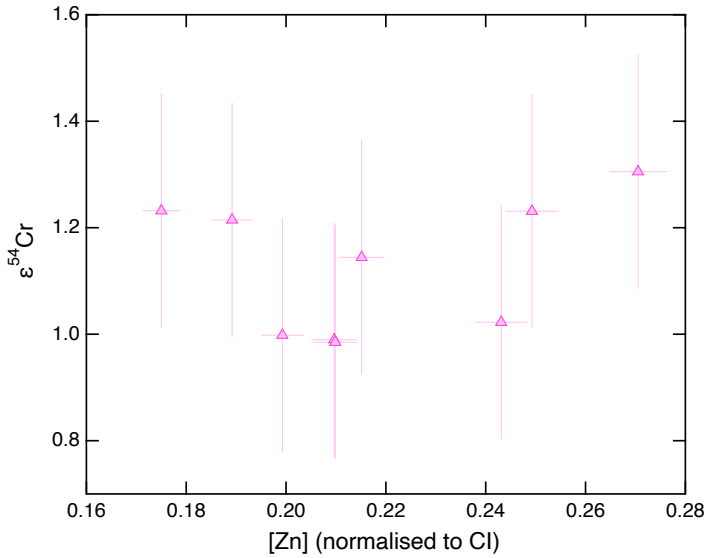

Figure 5.3: Calculated matrix volume fractions of subsamples of CR chondrite MIL 090001, represented by their CI-normalised Zn concentration, plotted against their ε^{54}Cr composition.

The coupled ε^{54}Cr and PVE composition of 9 subsamples of CR chondrite MIL 090001 are reported in Table 5.1. The subsamples span a range of ε^{54}Cr compositions between 0.99 - 1.31, and Zn concentrations between 55 - 84 ppm, resulting in a calculated matrix volume fraction range of 0.175 - 0.271 and matrix mass fraction range of 0.156 - 0.665 (Tables 5.1 and 5.2).

The range of matrix volume fractions in LoV 171 subsamples displays a RSD of 28.2%, indicating a heterogenous population of subsamples (Stracke et al., 2012).

The bulk ε^{54}Cr composition of MIL 090001 is 1.11 $\pm$ 0.22 and the bulk Zn concentration is 66 ppm. The average matrix volume fraction of the subsamples was 0.211.

The ε^{54}Cr compositions and matrix fractions of MIL 090001 subsamples are displayed in Fig. 5.3. There appears to be weak-to-no correlation between matrix fraction and Cr isotopic compositions, with all subsamples plotting within error of their ε^{54}Cr compositions. This is supported by a ρ of 0.25, indicating little correlation between the ε^{54}Cr value and matrix fraction of different CR subsamples.

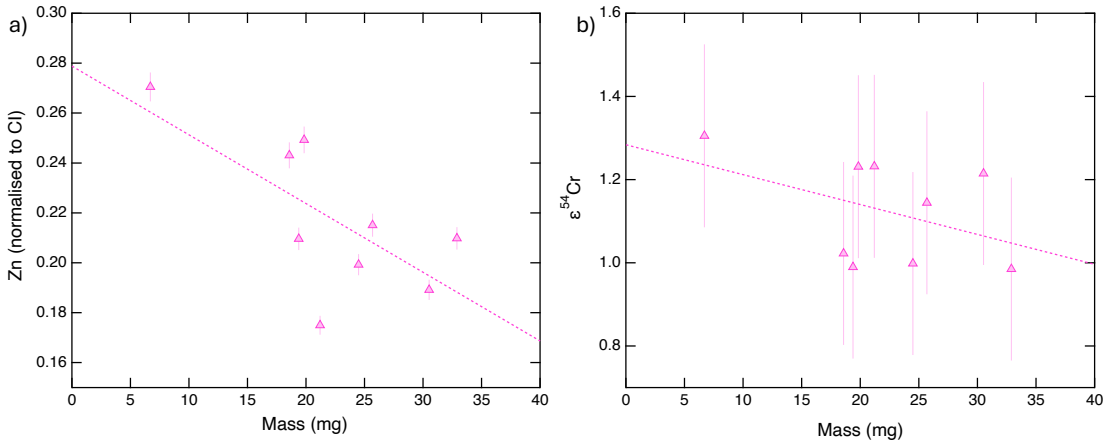

Figure 5.4: a) Plot of CI normalised Zn concentration vs mass (mg) of subsamples of CR chondrite MIL 090001. Slight trend is seen between subsample mass and Zn concentration. b) Plot of ε^{54}Cr vs mass (mg) of subsamples of CR chondrite MIL 090001. No relationship is seen between ε^{54}Cr and mass.

There is no apparent relationship between the mass of each subsample and its ε^{54}Cr or the calculated matrix volume fraction (CI-normalised Zn) (Fig. 5.4). Subsample CR1 which has the smallest mass of 6.8 mg displays a higher matrix volume fraction and slightly elevated ε^{54}Cr value, though its Cr isotopic composition is within error of the remaining subsamples.

I.D.	ε^{54}Cr	Cr	Zn	Ge	Se	Cd	Sn	Te	Pb
		(ppm)	(ppm)	(ppm)	(ppm)	(ppm)	(ppm)	(ppm)	(ppm)
	±0.22	±3.51%	±2.14%	±1.55%	±2.22%	±1.21%	±0.55%	±2.01%	±0.98%
	2σ	2RSD	2RSD	2RSD	2RSD	2RSD	2RSD	2RSD	2RSD
CR1	1.31	3231	84.4	0.44	7.72	0.28	8.05	0.53	0.52
CR2	1.23	3377	77.8	0.22	7.59	0.44	7.03	0.57	0.72
CR3	0.99	4940	65.4	0.18	7.08	0.34	5.04	0.43	0.53
CR4	1.00	3416	62.2	0.18	6.61	0.32	5.66	0.42	0.53
CR5	1.14	3504	67.1	0.17	7.14	0.36	5.11	0.48	0.54
CR6	1.21	3368	59.0	0.15	7.38	0.31	4.85	0.47	0.51
CR7	1.02	3287	75.8	0.21	7.95	0.40	7.34	0.54	0.60
CR8	0.99	3424	65.5	0.15	6.63	0.33	26.32	0.46	0.55
CR9	1.23	3597	54.6	0.20	5.23	0.29	4.92	0.40	0.44

Table 5.1: ε^{54}Cr compositions and PVE concentrations of MIL 090001 subsamples. σ = Standard deviation. RSD = Relative standard deviation.

I.D.	Matrix volume fraction	Matrix mass fraction
CR1	0.271	0.200
CR2	0.249	0.177
CR3	0.210	0.133
CR4	0.199	0.122
CR5	0.215	0.139
CR6	0.189	0.111
CR7	0.243	0.170
CR8	0.210	0.133
CR9	0.175	0.095

Table 5.2: Calculated matrix volume fraction (Zn normalised to CI) and calculated matrix mass fraction of MIL 090001 subsamples.

5.3.2 Mixing line

5.3.2.1 MIL 090001

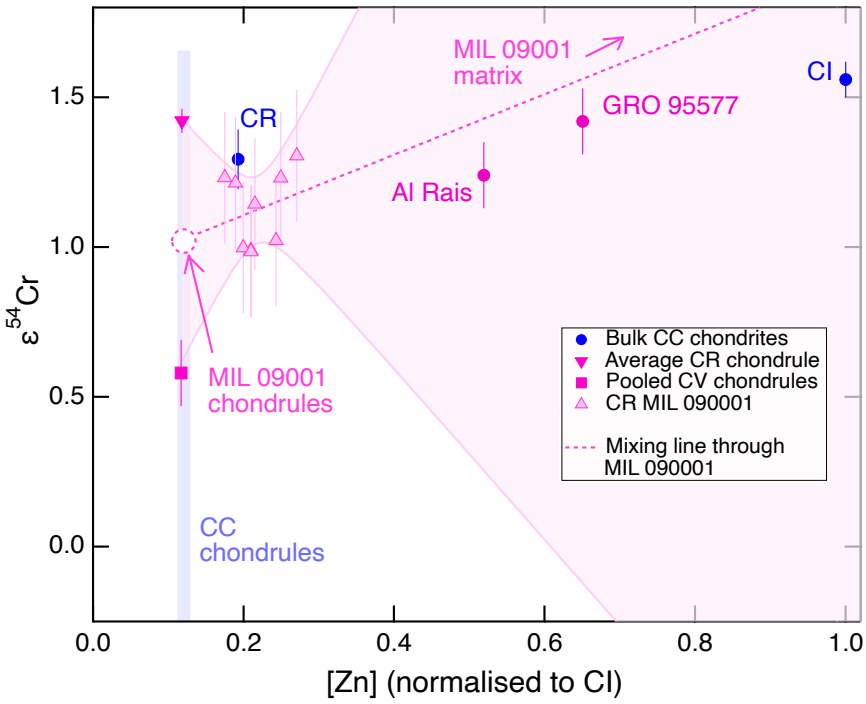

Figure 5.5: Plot displaying the composition of measured subsamples of CR chondrite MIL 090001, the reported compositions of anomalous CR chondrites Al Rais, and GRO 95577, and the CI chondrites, the average reported composition of CR and CC chondrules, and the range of CC chondrules. A mixing line has been fitted through subsamples of CR chondrite MIL 090001. A shaded 95% confidence interval has been included. Bulk chondrite and chondrule data is sourced from: Olsen et al. (2016), van Kooten et al. (2016), Mahan et al. (2018), Abreu et al. (2020), Hellmann et al. (2023), and references listed in Figs. 1.6 and 5.5.

An isotopic mixing line (details in section 2.4) was fitted to the measured CR chondrite subsamples and provided with initial values of: 0.58 and 1.56 for the ε^{54}Cr composition of chondrules and matrix. This was due to the CI-like matrix observed in few CR chondrites reported in the literature. Values of 1.0 and 0.118 were used for the ratio of Cr concentrations in chondrules:matrix, and 0.118 for the Zn concentration in chondrules (normalised to CI), respectively.

When the Zn and Cr concentrations in chondrules and matrix are held constant, the best fit mixing line passes through a value of 1.91 ± 2.79 for the ε^{54}Cr composition of matrix and 1.02 ± 0.37 for chondrules. This mixing line is plotted in Figure 4.8a. Wide 95% confidence interval bands and the large errors associated with the calculated chondrule

and matrix compositions indicate the poor fit of this mixing line. When the initial ε^{54}Cr compositions for chondrules and matrix were varied between 0.6 - 1.6, the recovered ε^{54}Cr compositions for both components varied minimally, indicating that the initial values used were a reasonable estimate.

5.3.2.2 MIL 090001 and anomalous CR chondrites Al Rais and GRO 95577

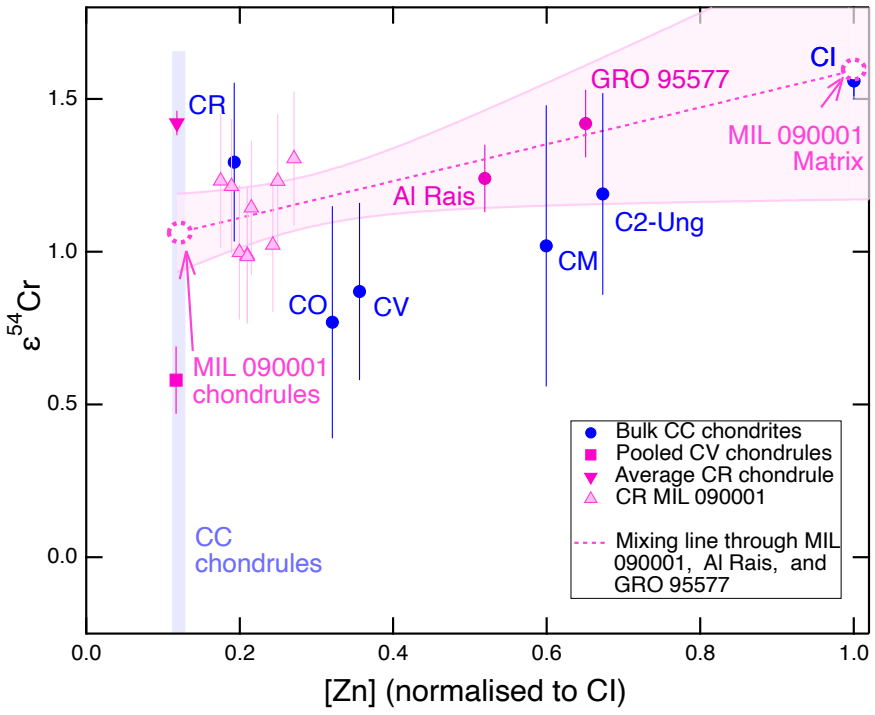

Figure 5.6: Plot displaying the composition of measured subsamples of CR chondrite MIL 090001, the reported compositions of anomalous CR chondrites Al Rais, and GRO 95577, and the CI chondrites, the average reported composition of CR and CC chondrules, and the range of CC chondrules. A mixing line has been fitted through subsamples of CR chondrite MIL 090001, Al Rais, and GRO 95577. A shaded 95% confidence interval has been included. Bulk chondrite and chondrule data is sourced from references listed in Figs. 1.6 and 5.5.

Including literature data for anomalous CR chondrites Al Rais and GRO 95577 into the fit of a mixing line through subsamples of MIL 090001 reproduces similar ε^{54}Cr compositions of chondrules and matrix generated by the mixing line seen in Figure 5.6. This mixing line uses initial values of: 0.58 and 1.56 for the ε^{54}Cr composition of chondrules and matrix, 1.0 for the ratio of Cr concentrations in chondrules:matrix, and 0.118 for the Zn concentration in chondrules (normalised to CI).

This mixing line is plotted in Figure 5.8, and generates a ε^{54}Cr composition of 1.06 $\pm$ 0.12 for chondrules and 1.59 $\pm$ 0.40 for matrix. This line also has a poor fit demonstrated by a wide 95% confidence interval bands.

5.4 Discussion

5.4.1 Bulk composition

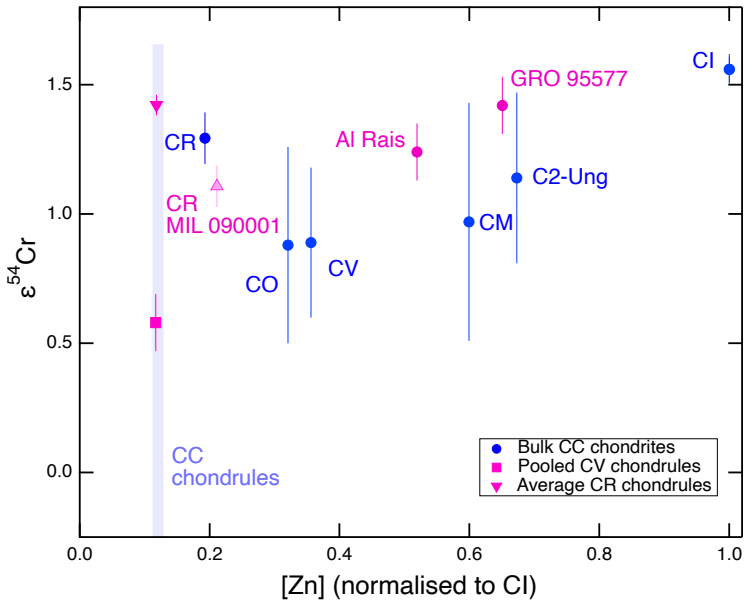

Figure 5.7: Average composition of MIL 090001 compared to literature data. Bulk chondrite and chondrule data is sourced from references listed in Figs. 1.6 and 5.5.

Chemical and isotopic compositions are used to determine chondrite grouping. Each chondritic group is understood to have experienced unique thermal and aqueous alteration histories and undergone varying amounts of reprocessing. Previous studies have questioned whether MIL 090001 should be classified as CR chondrite, or if it should instead be reported as part of the CV clan due to it's anomalously high ^{15}N isotope composition and light bulk H isotopic composition (Alexander et al., 2012, 2013). Conversely, O isotopes and ε^{48}Ca (Alexander et al., 2013; Zhu et al., 2023) compositions indicate that this meteorite should be classified as a CR chondrite. The ε^{54}Cr composition and Zn concentration of MIL 090001 have not previously been measured but could provide further evidence for its classification. The bulk ε^{54}Cr isotopic composition of MIL 090001 measured in this study is 1.11 ± 0.22. This agrees within error to the average composition of CR chondrites (1.31 ± 0.1, see Fig 5.7) (Bryson and Brennecka, 2021), supporting its classification as a CR chondrite.

The average bulk Zn concentration of MIL 090001 (66 ppm) is similar compared to the

average CR chondrite Zn concentration (60.1 ppm), and the calculated matrix volume fraction (0.211) is lower than the average reported values (0.35), and just outside of the range measured by Schrader et al. (2011) (0.235 - 0.685). Previous studies report matrix volume fractions based on petrographic analysis, and so could mistakenly quantify small fragments of minerals, chondrules, and CAIs as matrix, leading to higher calculated matrix fractions (Schrader et al., 2011). This effect is observed by Schrader et al. (2011) who demonstrate that mischaracterising larger mineral and chondrule fragments as matrix leads to a ∼7% difference in calculated matrix fraction in the CR chondrite PCA 91082. In light of this, the calculated matrix volume fraction seen here is similar to the average CR chondrite matrix fraction reported in the literature, assuming literature values are slight overestimates.

5.4.2 ε^{54}Cr composition of chondrules and matrix

Characterising the isotopic compositions of chondrules and matrix in the CR chondrites allows for direct comparison to other CC chondrites groups, and provides insight into the history of CR parent body accretion.

Assuming Zn concentrations provide a good proxy for matrix amounts in the CR chondrite group (Hellmann et al., 2020), it is clear that there is no obvious correlation between the amount of matrix present in a subsample of a CR chondrite and its ε^{54}Cr composition (see Fig. 5.3). Over a spread of ∼0.10 matrix volume fraction, there is little variability in the isotopic compositions of subsamples, implying that the matrix and chondrules in CR chondrites share similarly enriched ε^{54}Cr compositions. Large uncertainties associated with the fit of a mixing line through CR chondrite subsamples make it difficult to accurately determine the compositions of chondrules and matrix via this method. Regardless of the large uncertainty margins, this mixing line indicates that CR chondrules display higher average compositions than those observed in CC chondrites (ε^{54}Cr of 1.02 vs 0.58, respectively) (Schneider et al., 2020). A mixing line plot through MIL 090001 subsamples and anomalously matrix-rich CR chondrites Al Rais and GRO 95577 constrains the errors associated with the fit due to the wider range of matrix fraction covered. This mixing line recovers an average chondrule ε^{54}Cr composition of 1.06 ± 0.12 and a matrix composition

of 1.59 ± 0.40. These compositions indicate that the CR chondrites contain isotopically heterogeneous chondrules and matrix, with chondrules displaying lower ε^{54}Cr compositions and matrix displaying CI-like compositions. However, this heterogeneity is notably smaller than that observed in other CC chondrites (Chapter 4).

5.4.3 Isotopic evidence for different chondrule populations

The average chondrule ε^{54}Cr composition recovered from the mixing line shown in Fig. 5.6 (1.06 ± 0.12) is isotopically depleted compared to previous measurements of isolated, extracted chondrules, which report an average value of 1.44 ± 0.14 (Olsen et al., 2016; van Kooten et al., 2016; Schneider et al., 2020; Marrocchi et al., 2022), and a compositional range spanning 1.21 - 1.66 ε^{54}Cr (Olsen et al., 2016). This difference could indicate that the method utilised in this work highlights the presence and contribution of a previously unmeasured, isotopically depleted population of chondrules.

Previous studies have identified different populations of chondrules within the CR chondrites, based on their sizes, textures, and oxygen isotopic compositions (Tenner et al., 2015, 2019; Schrader et al., 2020b; Piralla et al., 2021; Marrocchi et al., 2022). The first population, termed the *type I-CR* chondrules by Marrocchi et al. (2022), typically display ^{16}O-poor ($\Delta^{17}O > -4‰$) compositions and are texturally complex, often with larger diameters and smaller chondrule-like objects embedded within them (Abreu et al., 2020; Marrocchi et al., 2022). These chondrules exhibit similar ε^{54}Cr and ε^{50}Ti compositions to bulk CR chondrites, specifically showing little variability in ε^{54}Cr compositions (1.44 ± 0.14) compared to those seen in CM, CV, and CO chondrules (0.66 ± 0.49) (Marrocchi et al., 2022).

The second population, termed the *type I-CO* chondrules due to their similarity to chondrules observed in CO chondrites, are characterised by smaller diameters (∼0.6 mm) and ^{16}O-rich compositions (Schrader et al., 2020a; Marrocchi et al., 2022). Though the ε^{54}Cr composition of these smaller chondrules has not been measured, it could be assumed that these chondrules also show comparatively lower average Cr isotopic compositions, similar in value to those observed in the CO, CV, and CM chondrites (∼0.58 (Schneider et al., 2020)). The *type I-CO* chondrules could then represent the population of isotopically de-

pleted chondrules that are responsible for the lower average ε^{54}Cr composition recovered for CR chondrites from the mixing lines in this study.

If the average CR chondrule ε^{54}Cr composition recovered in this study (1.06) is a mixture of isotopically enriched *type I-CR* and isotopically depleted *type I-CO* chondrules, this indicates a ratio of approximately 60:40 of *type I-CR*:*type I-CO* chondrules in the CR chondrites. This estimate roughly agrees with Tenner et al. (2015) and Marrocchi et al. (2022), who propose a 30:10 ratio of *type I-CR*:*type I-CO* chondrules based on a count of the number of chondrules displaying ^{16}O-poor and ^{16}O-rich compositions. The higher proportion of *type I-CO* seen in this study may be related to sampling bias in previous studies towards measuring the compositions of larger chondrules, due to analytical ease.

5.4.4 Evidence of reprocessing and an initial CR reservoir

5.4.4.1 Reprocessing

Though the CR chondrites are widely accepted to represent some of the most primitive and pristine chondrites in our collections, compelling arguments suggest that these meteorites have experienced a complex history of recycling and reprocessing (Connolly et al., 2008; Schrader et al., 2015; Hellmann et al., 2020; Bryson and Brennecka, 2021; Marrocchi et al., 2022; Pinto et al., 2024).

Various studies have suggested that *type I-CR* chondrules are formed through reprocessing of *type I-CO* chondrules due to the observation of relict grains within *type I-CR* chondrules that display ^{16}O-rich compositions, similar to those measured in *type I-CO* chondrules (Tenner et al., 2015; Marrocchi et al., 2022). Tenner et al. (2019) also show that *type I-CO* chondrules predate *type I-CR* chondrules due to excesses in ^{26}Mg in chondrules with lower Δ^{17}O values and no observable excesses in *type I-CR* chondrules, indicating *type I-CO* chondrules formed first and were later incorporated into *type I-CR* chondrules. Further evidence for this history of reprocessing is seen in the scarcity of Fe-sulfides and the low S contents observed in Type I chondrules, associated with multiple heating and reprocessing events (Jacquet et al., 2013; Schrader et al., 2008; Wasson and Rubin, 2009).

Type II chondrules also display evidence for reworking. These rare chondrules are mainly

present as fragments in the matrix of CR chondrites, highlighting the highly energetic conditions they experienced (Schrader et al., 2015). Multiple type II chondrules plot in the same oxygen isotopic space as type I chondrules (Connolly et al., 2008; Tenner et al., 2015; Pinto et al., 2024). Connolly et al. (2008) and Pinto et al. (2024) argue that this compositional overlap indicates that type II chondrules are formed from the same reservoir as type I chondrules, or that they represent type I chondrules reprocessed under more oxidising conditions, forming the FeO-rich mineralogy observed.

The ε^{54}Cr compositions of CR chondrules recovered in this study cannot be used to comment further on the relationships between different chondrule populations. However, the low measured PVE abundances in MIL 090001 subsamples may provide some evidence for reprocessing. Though CR chondrites fall on the trend between matrix volume fraction and PVE concentrations (Hellmann et al., 2020), they exhibit markedly lower PVE concentrations compared to other CC chondrites that display enriched ε^{54}Cr compositions. Further evidence for PVE loss in the CR chondrites is discussed by Marrocchi et al. (2022) who note that if the original CR reservoir contained higher amounts of CI-like dust, their coupled δ^{128}Te-ε^{54}Cr composition would align with the correlation observed in other CC groups. The lighter observed δ^{128}Te composition in CR chondrites, away from this expected initial value, is attributed to evaporative loss associated with reprocessing and formation of the *type I-CR* chondrules.

Bryson and Brennecka (2021) suggest that the reprocessing evidenced by low reported PVE abundances, constrained ε^{54}Cr chondrule compositions, and similarity in chondrule and bulk CR isotopic compositions in CR chondrites, could be due to energetic impacts between asteroid-sized bodies (Johnson et al., 2015). If the initial CR parent body was matrix-rich and displayed ^{54}Cr-enriched compositions, this could explain the enriched ε^{54}Cr compositions of CR chondrites compared to other CC groups. This would also help explain the low PVE abundances observed in MIL 090001 subsamples as thermal processing of chondrules and matrix during impacts could result in volatile loss. δ^{128}Te-ε^{54}Cr compositions of CR chondrites also suggest the evaporative loss of volatiles (Marrocchi et al., 2022), supporting suggestions of a impact-laden history. Further evidence for an impact history of the CR chondrites lies in their isotopic similarity to CB and CH chon-

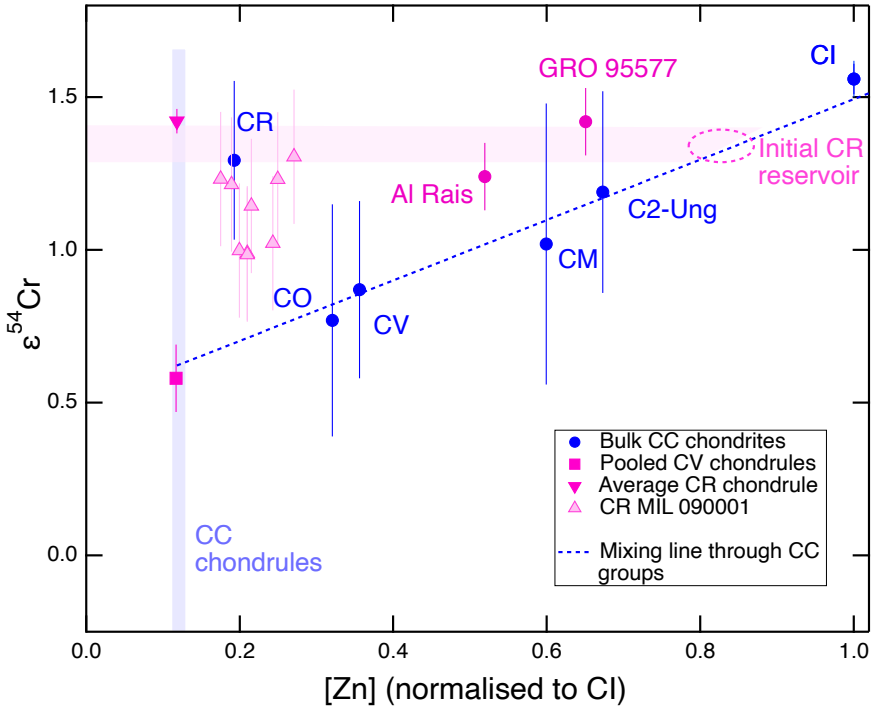

Figure 5.8: Plot displaying the composition of: measured subsamples of CR chondrite MIL 090001; anomalous CR chondrites Al Rais and GRO 95577; the average reported compositions of CC groups; the average reported composition of CR and CC chondrules; and the range of CC chondrules. A mixing line is fit through the CC groups (barring CR chondrites (blue line)). The pink shaded region indicates the ε^{54}Cr compositional range displayed by CR chondrules and bulk CR chondrites. The intercept is the presumed composition of the initial CR reservoir. Bulk chondrite and chondrule data is sourced from references listed in Fig. 1.6 and 5.5.

drites. CH and CB chondrites display similar excess in ε^{54}Cr compared to CR chondrites, with CBs displaying a similar compositional range of bulk ε^{54}Cr (1.5 ± 0.01, 1.36 ± 0.30, and 1.29 ± 0.26, respectively (Zhu et al., 2021c). This isotopic similarity could indicate that CB, CH, and CR chondrites may they share a similar origin (Zhu et al., 2021c; Wölfer et al., 2023). CB and CH chondrites are thought to form in an impact-generated vapour-melt plume at similar times compared to the CR chondrites, which may imply that CR chondrites could have also experienced impacts between asteroid-sized bodies (Wölfer et al., 2023). However, preservation of pristine matrix mineralogy implies that CR chondrites are not similarly melt-plume-derived (Davidson et al., 2014).

5.4.4.2 The initial CR reservoir

As CR chondrites have undergone reprocessing that altered their chondrule compositions and PVE abundances, these compositions could be used to determine the nature of the

initial CR chondrite reservoir/parent body. Assuming CR chondrites display the same trend as other CC chondrites in ε^{54}Cr vs matrix fraction plots, their measured ε^{54}Cr compositions can be used to define the chondrule and matrix fractions present in the initial CR reservoir. An estimate of the composition of the initial CR reservoir is depicted in Fig. 5.8, where the reported ε^{54}Cr compositions of *type I-CR* chondrules and bulk CR chondrites is assumed to record the isotopic composition of the initial CR reservoir/parent body. The intercept in Fig. 5.8 indicates that the original CR chondrite reservoir exhibited high matrix contents of ∼80 vol% and relatively low chondrule contents of ∼20 vol%. This interpretation relies on the assumption that CR chondrules and chondrites preserve the ε^{54}Cr composition of the initial reservoir and that this composition is unaffected by later alteration.

A similar estimated initial matrix abundance in the CR reservoir has been proposed by Marrocchi et al. (2022) and Bryson and Brennecka (2021) based on O and Cr isotopes of bulk CR chondrites and chondrules. These studies suggest the existence of an initial reservoir populated by ∼30% *type I-CO* chondrules and ∼70% CI-like dust which underwent reprocessing to produce the observed compositions of CR chondrites and *type I-CR* chondrules. This would explain why *type I-CR* chondrules exhibit enriched isotopic compositions, closer to CI, compared to those observed in CO, CV, and CM chondrites. Further evidence for incorporation of CI-like dust to form *type I-CR* chondrules is seen from the presence of <1 - 80 μm-sized dust in and around grains within CR chondrules (Schrader et al., 2018b).

This assumed initial CR reservoir displays higher matrix abundances and more positive ε^{54}Cr anomalies than most other CC chondrite groups, except for CB, CH, and CI chondrites. Though similarities in Cr and O isotopes and bulk chemical compositions has led to the CB and CH chondrites being previously associated with a "CR-clan" (Krot et al., 2014), distinct Mo and Ti isotopes point towards these chondrites being formed in a similar region to, but separate from, the CR chondrites (Wölfer et al., 2023).

Higher matrix fractions in the initial CR reservoir also bring the CR chondrites back in line with the other CC chondrites in a plot of ε^{50}Ti vs matrix volume fraction (Fig. 5.9).

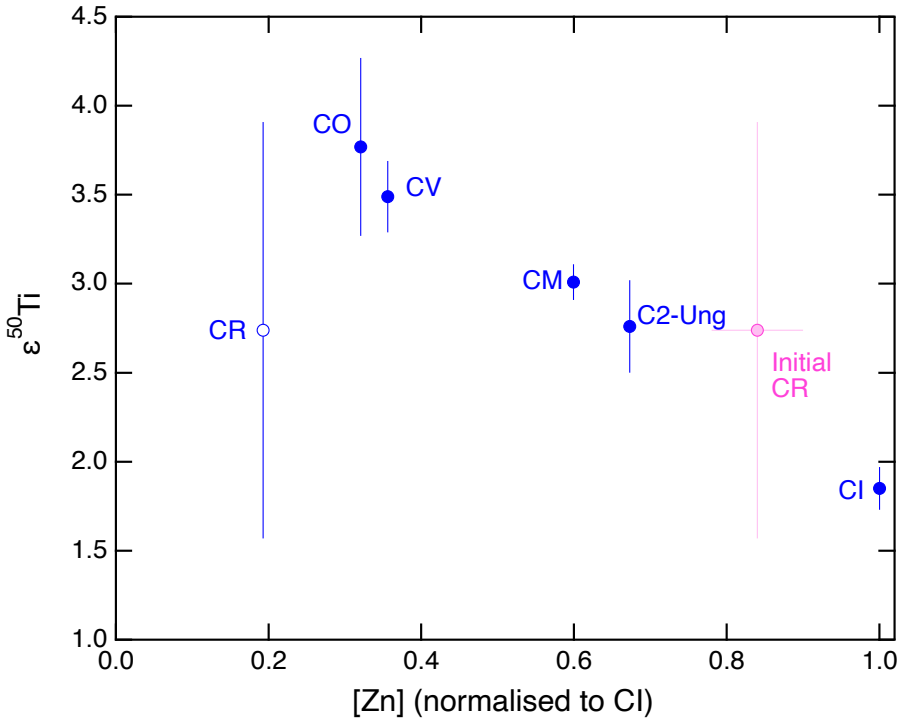

Figure 5.9: Plot displaying the ε^{50}Ti vs matrix volume fraction of CC chondrites, including the new calculated initial CR reservoir. Data is sourced from Bryson and Brennecka (2021), Braukmüller et al. (2018), and references within.

5.4.5 Formation of the CR parent body

Textural and isotopic evidence for reprocessing of CR chondrules in dust rich environments, combined with the existence of CR chondrites with anomalously high matrix and volatile element abundances (e.g., Al Rais, GRO 95577, NWA 852), has lead to suggestions that the main CR chondrites we observe today are the final products of reprocessing of a dust-rich initial CR chondrite reservoir (Schrader et al., 2018a; Abreu et al., 2020; Bryson and Brennecka, 2021; Marrocchi et al., 2022).

The recovered chondrule and matrix compositions from Fig. 5.6 indicate the presence of: isotopically enriched *type I-CR* chondrules; isotopically depleted *type I-CO* chondrules; and CI-like matrix within the CR chondrites. The enriched ε^{54}Cr composition of *type I-CR* chondrules, and the evidence of reprocessing discussed in section 5.4.4.1, indicates that these chondrules form in a dust-rich reservoir via the remelting and incorporation of CI-like dust with *type I-CO* chondrules (Fig. 5.10). The bulk composition of this initial reservoir is likely reflected in the composition of the *type I-CR* chondrules (ε^{54}Cr of 1.41, Fig. 5.8), and

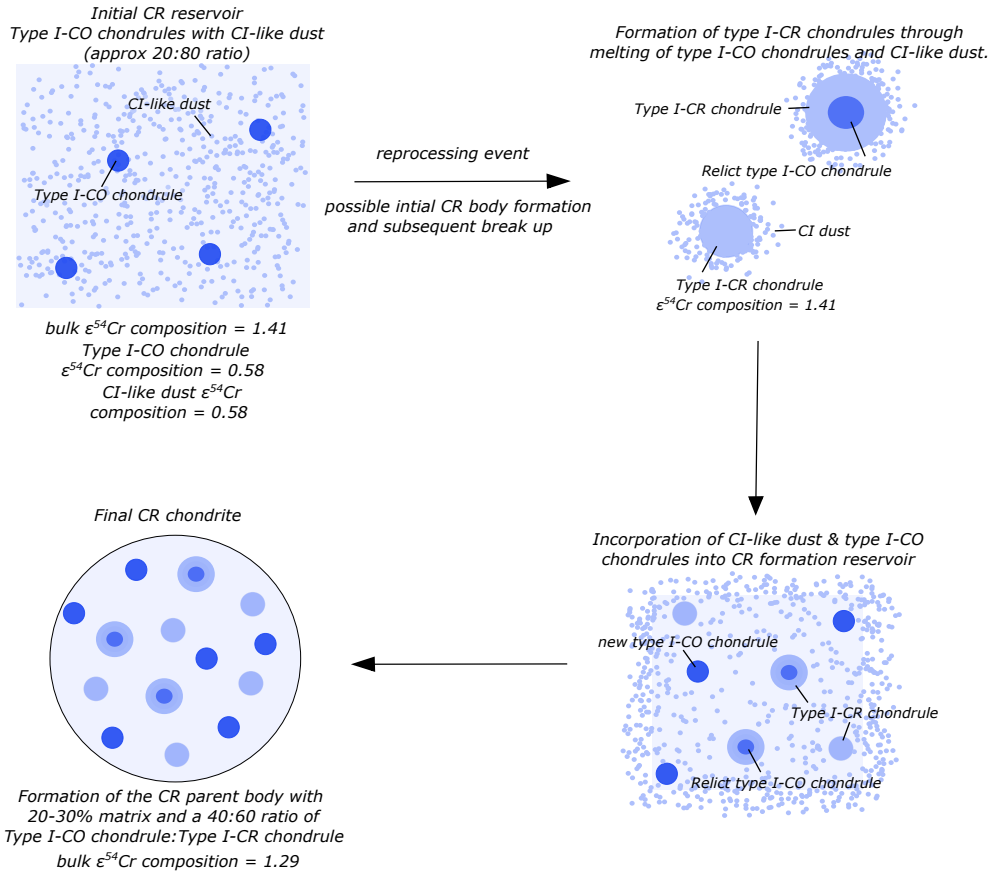

Figure 5.10: Schematic displaying the formation of *type I-CR* chondrules through reprocessing of *type I-CO* chondrules with CI dust in a dust rich initial CR reservoir. These two chondrule populations later mix and accrete with CI dust to form the final CR parent body.

corresponds to an approximately 80:20 ratio of CI-like dust:chondrules in the initial CR reservoir. Few *type I-CO* chondrules survived this reprocessing, with rare chondrules being preserved as relict grains within *type I-CR* chondrules. This reprocessing event may have been due an impact between asteroid-sized bodies, which generated the conditions required for conversion of of CI-like dust and *type I-CO* chondrules into *type I-CR* chondrules (Bryson and Brennecka, 2021; Marrocchi et al., 2022). This reprocessing would result in the volatile loss observed in CR chondrites, and conserve the distinctive high ε^{54}Cr isotopic signature seen in *type I-CR* chondrules which reflects the bulk composition of their initial reservoir. Subsequently, the newly formed *type I-CR* chondrules mix and accrete with more *type I-CO* chondrules (continually formed in the CC chondrule formation reservoir, discussed in Chapter 4), and inwardly drifting, matrix-bound CI-like dust, forming the CR chondrites observed today (Fig. 5.10).

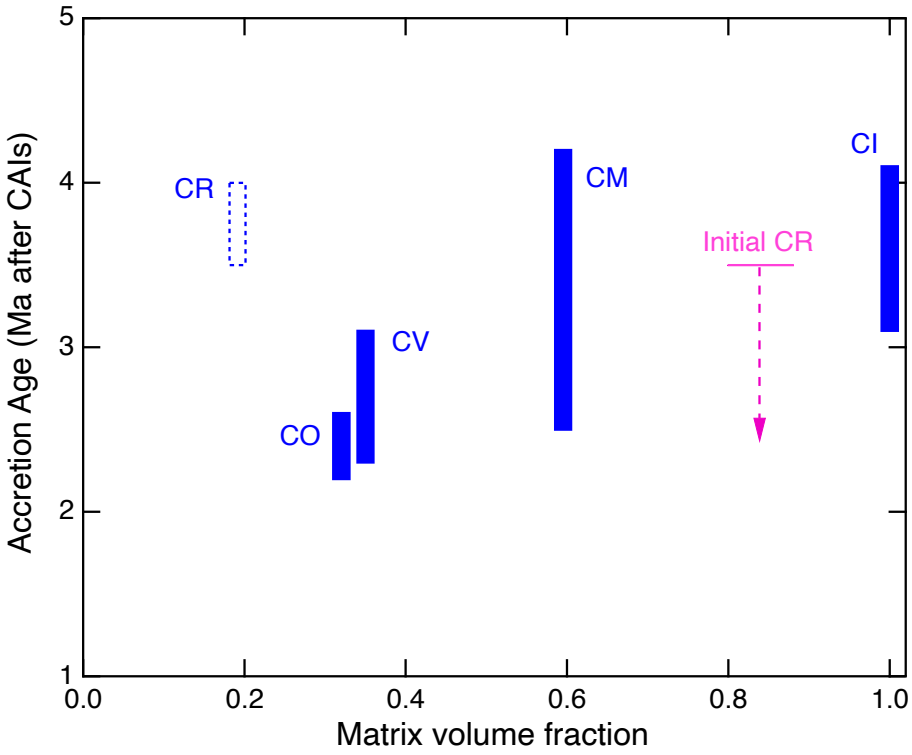

Figure 5.11: Plot displaying the accretion ages of CC chondrites plotted against their matrix volume fraction (calculated by Zn concentrations). The calculated matrix fraction of the initial CR reservoir is included in this plot. Data is sourced from Hellmann et al. (2023) and Braukmüller et al. (2018).

This formation mechanism agrees with suggestions of an original reservoir dominated by CI dust (Tenner et al., 2015) and estimates of a predominantly matrix rich (∼80 vol%) initial CR parent body proposed by Bryson and Brennecka (2021). Reworking of CR chondrules with pristine CI-like dust could also explain the high abundance of presolar grains and primitive amino acids observed in the matrix of CR chondrites (Glavin et al., 2010; Davidson et al., 2014). The incorporation of volatile enriched CI-like dust in CR chondrite components could also facilitate the formation of MVE-enriched type II chondrules, as these are proposed to have formed in a more oxidizing environment, with enhanced dust-to-gas ratios compared to type I chondrules (Jacquet et al., 2015; Tenner et al., 2018; Schrader et al., 2013; Pinto et al., 2024). Anomalously matrix-rich CR chondrites may reflect different regions of the CR parent body that exhibit larger amounts of matrix, or they may originate from different parent bodies that form alongside the parent body from which the matrix-poor CR chondrites originate.

If Cr isotopic anomalies can be used to trace CI-like material in CC chondrites, as proposed in this study and by Hellmann et al. (2020), Bryson and Brennecka (2021), and Hellmann et al. (2023), the initial CR parent body likely accreted with higher amounts of CI-like dust compared to most other CC chondrites (barring CI chondrites). According to accretion models by Bryson and Brennecka (2021), this could imply that the initial CR body accretes at a later time, or at further radial distances than the other main CC groups (as discussed in section 4.4.3). Young chondrule and accretion ages for the CR chondrites have been reported by multiple studies (Schrader et al., 2017; Budde et al., 2018; Desch et al., 2018). A higher matrix proportion present in the initial CR reservoir would bring its initial accretion age back in line with the remaining CC groups, completing a trend of increasing younger CC chondrites forming with greater fractions of matrix/CI-like material, as seen in Fig. 5.11 (Bryson and Brennecka, 2021; Hellmann et al., 2023). However, care must be taken with this interpretation as the ages of CR chondrules may represent the later formed *type I-CR* chondrules, and instead provide a maximum age for the initial CR reservoir.

5.5 Conclusions

The coupled ε^{54}Cr compositions and PVE concentrations of subsamples of CR chondrite MIL 090001 were measured to probe the mechanism of formation and the history of reprocessing of the CR chondrites.

MIL 090001 has a bulk ε^{54}Cr composition of 1.11 ± 0.22, and Zn concentration of 66 ppm, resulting in a calculated average matrix volume fraction of 0.211. This measured Cr isotopic value is within error of the reported average CR chondrite value, providing further evidence to support the classification of MIL 090001 as a CR chondrite.

Subsamples of MIL 090001 do not show large differences in their ε^{54}Cr values, implying their chondrules and matrix display similarly enriched compositions. A mixing line plot through subsamples of MIL 090001 and the compositions of matrix-rich CR chondrites GRO 95577 and Al Rais recovers average chondrule and matrix compositions of 1.06 ± 0.12 and 1.59 ± 0.40, respectively. Including Al Rais and GRO 95577 in the fit of the mixing line allowed for a greater range of matrix proportions to be sampled, and therefore narrowed the uncertainty associated with recovering the isotopic compositions of chondrules and matrix.

The recovered average CR chondrule composition (ε^{54}Cr of 1.06) is isotopically depleted compared to those previously measured (∼1.41), indicating the presence of an unmeasured population of CR chondrules that exhibit lower ε^{54}Cr compositions. These are likely the *type I-CO* chondrules proposed by Marrocchi et al. (2022), and resemble the average chondrule population observed in CO, CM, and CV chondrites, with an average ε^{54}Cr composition of 0.58 (Schneider et al., 2020).

The enriched ε^{54}Cr composition of CR chondrites and evidence of PVE loss could imply the existence of an initial CR reservoir that was matrix-rich, likely comprised of ∼80 vol% CI-like dust and ∼20 vol% *type I-CO* chondrules. This reservoir likely existed at later times or at further distances than the locations of CO, CM, and CV chondrite accretion, as it displays comparatively higher ε^{54}Cr compositions. After reprocessing and incorporation of CI dust into *type I-CO* chondrules, the signature of the CI dust may have been recorded in *type I-CR* chondrules that display enriched, restricted ε^{54}Cr compositions, as measured

by previous studies.

The final CR parent body may have subsequently accreted with the newly formed *type I-CR* chondrules, chondrules with lower ε^{54}Cr compositions similar to those seen in CO, CV, and CM chondrites (*type I-CO* chondrules), and more inwardly drifting CI-like dust that forms the matrix.

This implies that CR chondrites form in a similar manner to CC chondrites, from isotopically distinct chondrules and CI-like dust, sourced from different regions of the outer solar system.

Chapter 6

Synthesis

6.1 Summary

In this study I have measured the coupled PVE concentrations and ε^{54}Cr compositions of subsamples of a range of carbonaceous (CC) and non-carbonaceous (NC) chondrites to investigate how their parent bodies formed. PVE concentrations were used to determine the fraction of matrix present in each chondrite subsample. An isotopic mixing line was fitted through the coupled PVE and ε^{54}Cr compositions of the subsamples to determine the Cr isotopic compositions of chondrules and matrix in each chondrite.

NC chondrites

NC chondrites display isotopically depleted ε^{54}Cr compositions compared to CC chondrites. Ordinary chondrite (OC) subsamples appear to show no relationship between ε^{54}Cr composition and matrix fraction, indicating that chondrules and matrix share the same isotopic composition. This isotopic homogeneity implies that the chondrules and matrix present in OCs were sourced from the same reservoir. Rumuruti (R) chondrites display larger isotopic excesses compared to the OCs. It is unclear whether their chondrules and matrix display differing isotopic compositions, however, their higher ε^{54}Cr values indicate enrichment of neutron-rich material, possibly sourced from the CC reservoir (Fig. 6.1a).

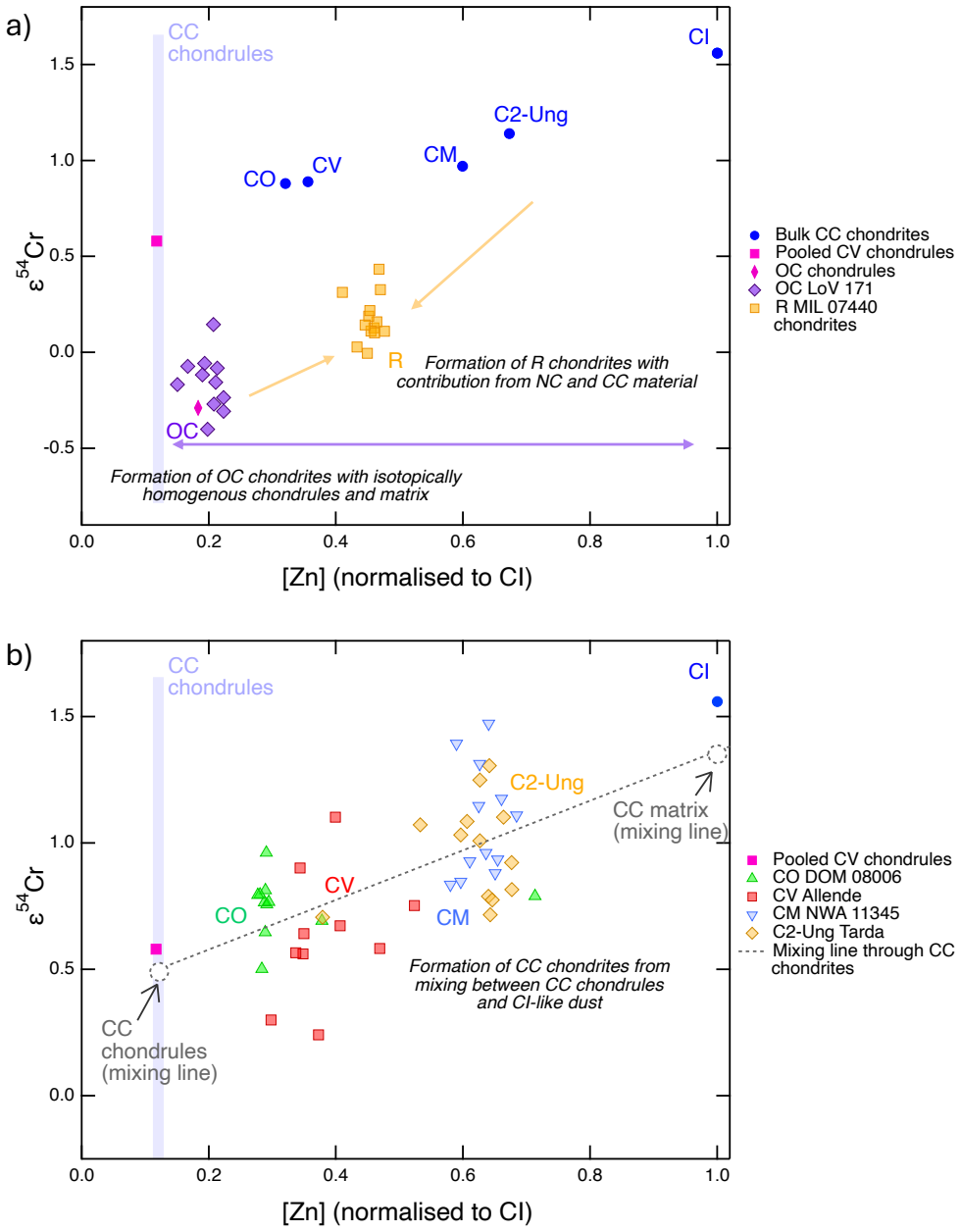

Figure 6.1: Coupled ε^{54}Cr and Zn concentrations of a) NC and b) CC chondrite subsamples measured in this study. OCs form from isotopically homogenous chondrules and matrix, R chondrites reflect contribution from the CC reservoir. All CC chondrites form from a mixture of varying proportions of CC chondrules and isotopically distinct matrix, close to CI in composition. Bulk chondrite and chondrule data is sourced from references listed in Fig. 1.6.

CC chondrites

CC chondrites display higher ε^{54}Cr compositions with increasing matrix fractions. Subsamples of each chondrite group indicate that the ε^{54}Cr compositions of chondrules and matrix in CC chondrites vary, with matrix displaying enriched isotopic compositions com-

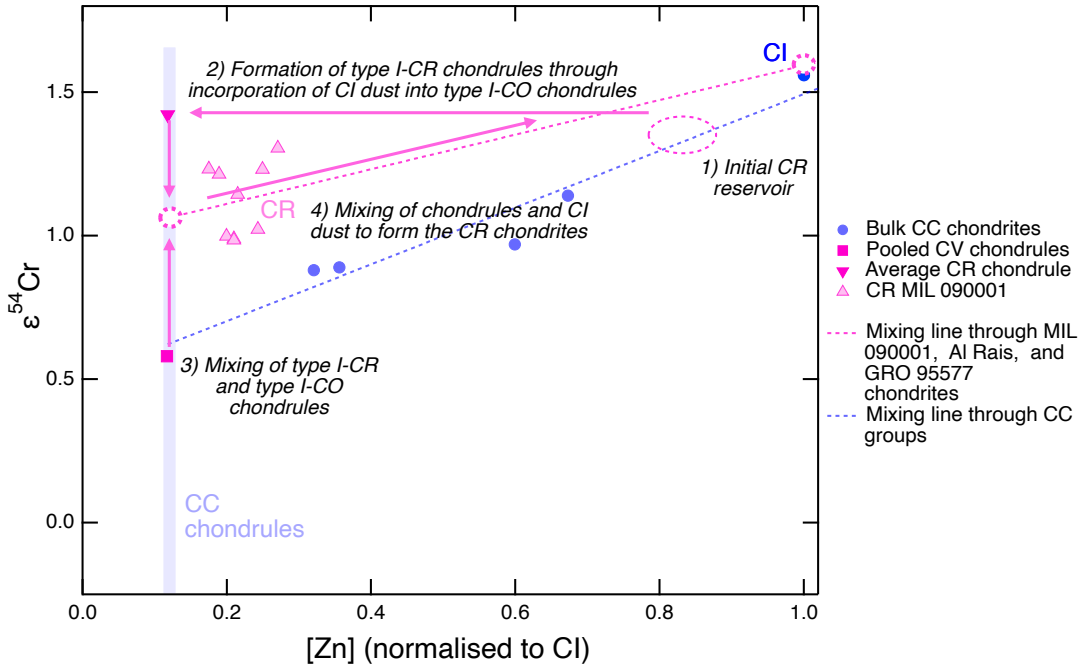

Figure 6.2: Coupled ε^{54}Cr and Zn concentrations of CR chondrite subsamples measured in this study. The formation pathways of chondrules observed in CR chondrites is detailed, along with their accretion with CI dust to form the final CR parent bodies. Bulk chondrite and chondrule data is sourced from references listed in Fig. 1.6 and 5.2.

pared to chondrules. A mixing line plot through all CC groups indicates that the matrix in all CC chondrites is enriched in ^{54}Cr, with isotopic compositions within error of CI chondrites. All CC chondrites, excluding the CR chondrites, appear to share the same average chondrule ε^{54}Cr composition. This implies that the chondrules and matrix present in CC chondrites are sourced from different regions of the CC reservoir, before they are transported and accreted into the CC parent body. CC chondrites that accrete with greater fractions of CI-like matrix display higher ε^{54}Cr compositions (Fig. 6.1b).

CR chondrites

CR chondrites display higher average ε^{54}Cr chondrule compositions than the other CC groups. These chondrites likely underwent reprocessing where CI-like dust was incorporated into chondrules, imparting an enriched isotopic signature, before accretion with CI-like dust to form the final CR parent body (Fig. 6.2).

6.2 Suitability of the subsampling method

One aim of this work was to assess whether subsampling individual chondrites would allow for better characterisation of chondrule and matrix compositions within chondrite groups. This was reliant on subsamples of a chondrite successfully producing a large range of chondrule:matrix ratios, which would enable me to isolate the contribution of chondrules and matrix to the bulk composition of a chondrite using fitted mixing lines.

Difficulties in generating range of matrix fractions

It is evident from this study that it is difficult to cut subsamples small enough to display large heterogeneities in matrix fractions. In general, subsamples <20 mg displayed the largest variations in calculated matrix fractions within a chondrite (see Figs. 3.4, 3.7, 4.12, and 5.4). However, these variations were often still too small to generate large spreads in matrix fractions, with most groups displaying variations of ∼10 vol% (excluding a few subsamples which showed anomalously high or low matrix fraction compared to the others in CO DOM 08006). The exception to this was the CV chondrite Allende, which showed variations of ∼23 vol%. This is likely due to CV chondrites typically displaying the largest average chondrule diameter (see table 6.1). The smaller the diameter of chondrules present, the harder it becomes to sample heterogenous proportions of chondrules:matrix, especially as subsamples were typically orders of magnitude larger than the chondrule diameters. Since CV chondrites contain larger chondrules, it is easier to sample differing amounts of them in each subsample. The inability to sample large ranges of matrix content in each chondrite subset led to difficulty in recovering reliable chondrule and matrix compositions from fitted isotope mixing lines, as demonstrated with a hypothetical spread of data in Fig. 6.3a. This resulted in fits which had wide 95% confidence intervals outside of the matrix range populated by subsamples, leading to large associated errors in the recovered ε^{54}Cr chondrule and matrix compositions.

To work around this limitation, in Chapter 4 I fit the mixing line through all the measured CC chondrite subsets to determine whether all groups shared similar average chondrule and matrix ε^{54}Cr compositions. This combined dataset provided a larger range of matrix

Chondrite group	Chondrule diameter (mm)	Matrix volume fraction range
LL	0.10 - 2.60[1]	0.07
R	0.40[3]	0.07
CO	0.15[2,3]	0.10 - 0.44
CV	0.9[2]	0.23
CM	0.27 - 0.37[4,5]	0.10
C2-Ung (Tarda)	0.26[6]	0.08 - 0.30
CR	0.7[7]	0.10

Table 6.1: Average chondrule diameters reported in the literature and the obsereved matrix volume fraction range seen in this study. CO and C2-Ung display the ranges including and without the anomalous subsamples. References: [1] Friedrich et al. (2015), [2] Rubin (2010), [3] Rubin (2000), [4] Rubin and Wasson (1986), [5] Schrader and Davidson (2017), [6] Schrader et al. (2024a), [7] Kallemeyn et al. (1996).

fractions which allowed the end member compositions of chondrules and matrix to be better constrained, with narrower 95% confidence intervals. In a similar fashion, in Chapter 5 I used previously reported compositions of anomalously matrix-rich CR chondrites in conjunction with the subsamples measured to fit a mixing line that spanned wider matrix ranges to better constrain the compositions of the CR chondrules and matrix. Future work utilising this method could similarly sample multiple chondrites from each group to attempt to generate a dataset with a larger represented matrix range.

Effects of chondrule isotopic heterogeneity

An additional problem encountered with this method was the compositional scatter associated with sampling varying amounts of chondrules in each subsample. Previous studies have reported large variations in the isotopic compositions of individual chondrules in the CC chondrites. This is particularly pronounced in the CV chondrites whose chondrule compositions have been more extensively studied (possibly due to the relative ease of isolating their relatively larger chondrules). If the individual subsamples are too small their chondrules might fail to represent the average compositions of these spherules, and instead be shifted towards more isotopically enriched/depleted compositions compared to the mean. This would make it hard to use these subsamples to define a mixing line for recovery of the average chondrule and matrix isotopic compositions within a chondrite group. This effect would induce scatter into the dataset, widening the 95% confidence envelopes and increasing the uncertainties on the recovered compositions of chondrules

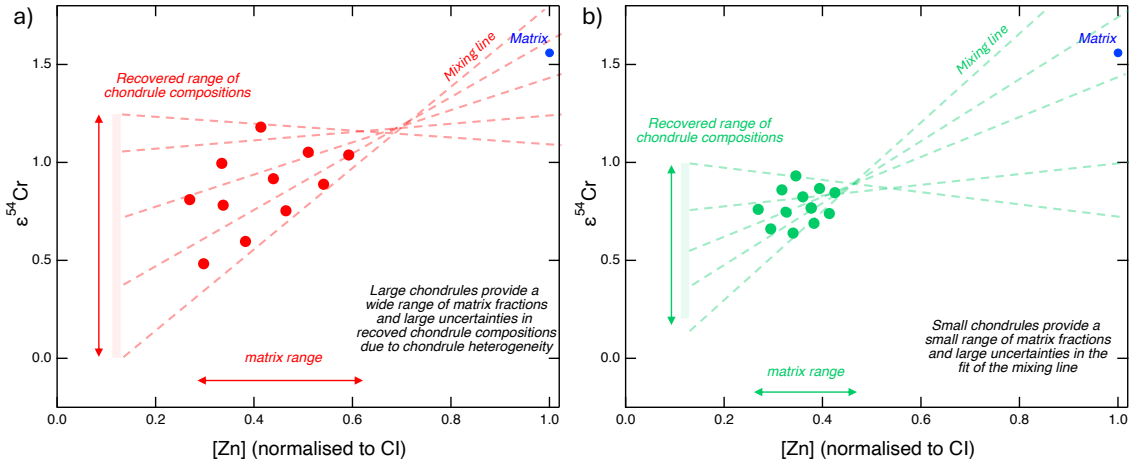

Figure 6.3: a) Small subsample sizes result in larger matrix ranges but increased spread in recovered chondrule composition as deviations are not averaged out. b) Large subsample size leads to reduced spread in chondrule composition but poor over all fit mixing line and recovery of matrix composition due to small spread in matrix range.

and matrix. The effects of this were discussed previously in section 4.4.2.3 where it is evident that subsamples of each CC chondrite display large variations in ε^{54}Cr compositions, broadly defining a trend but suffering from scatter that introduces large uncertainties into a fitted mixing line. It is possible this effect is seen to a greater degree in the CV chondrite data as these subsamples display the greatest variations in ε^{54}Cr compositions. Since CV chondrites contain some of the largest chondrules it is harder for a subsample to contain enough chondrules to represent an average composition. As such, it is likely that the large range observed in ε^{54}Cr compositions is due to this "nugget" effect.

It is difficult to reconcile needing to cut larger subsamples to average out variations in chondrule compositions (Fig. 6.3b), and requiring smaller subsamples to generate wide ranges of chondrule-to-matrix fractions (Fig. 6.3a). Larger subsamples result in greater uncertainties in the recovered chondrule and matrix compositions, while smaller subsamples do not accurately represent the average chondrule compositions in each chondrite group. This is a major limitation of this method, and could possibly be alleviated by measuring subsamples of multiple chondrites within each group to generate wider matrix fraction ranges, as suggested above.

6.3 Chondrite formation and solid dynamics in the inner and outer solar system

NC chondrites represent material formed in the inner region of the protoplanetary disk whilst CC chondrites accreted in the outer portions of the disk. Chapters 3 and 4 of this thesis focus on each chondrite group independently, however, comparing the differences in formation histories of NC and CC chondrites allows us to investigate how the dynamics of solid transport and planet formation varied across the protoplanetary disk.

Though NC irons display older ages compared to CC irons, both NC and CC parent bodies form between 2 - 3 Ma (Kruijer et al., 2020). CC chondrites also show a more protracted period of accretion, with CM and CR bodies accreting between 3 - 4 Ma after CAI formation. Chondrules in both the NC and CC reservoirs show overlapping ages, between 0 - 3.3 Ma (Desch et al., 2018; Zhu et al., 2019a), indicating that chondrules form and chondrite parent bodies accrete at similar times in the inner and outer solar system. CR chondrites represent the exception to this as they display chondrule ages of 3 - 4 Ma (Desch et al., 2018; Kruijer et al., 2020), later than most other chondrite groups. Since the majority of NC and CC chondrites form at similar times, comparing their accretion mechanisms can provide a more complete understanding of how planetesimals formed across the solar system.

Chondrule formation in the NC and CC reservoirs

Though chondrules in NC and CC chondrites have experienced extensive recycling and remelting, characterising their mass-independent isotopic compositions allows us to determine the behaviour of their final formation reservoirs and the processes by which they formed (Tenner et al., 2018; Piralla et al., 2021; van Kooten et al., 2021; Fukuda et al., 2024; Rubin et al., 2024; Marrocchi et al., 2024; Pinto et al., 2024). CC and NC chondrites display distinct ε^{54}Cr chondrule compositions, indicating that they form in different regions of the solar system, with CC chondrules displaying higher ε^{54}Cr values of $\sim$0.50 $\pm$ 0.17, and NC chondrules displaying a lower recovered compositional range between -1.44 ($\pm$ 1.88) to 0.06 ($\pm$ 1.17) (Chapters 3 and 4). Previous studies that characterise the

ε^{54}Cr and O isotopic compositions of NC and CC chondrules can provide addition insight regarding chondrule formation across the solar system.

CC, OC, and R chondrite chondrules all display similar compositional and textural characteristics, indicating that they generally form from similar processes throughout the solar system (i.e., formation processes controlled by gas–melt interactions between chondrule precursors and SiO- and Mg-rich gas) (Piralla et al., 2021; Regnault et al., 2022). However, similar to the isotopic dichotomy seen in Cr isotopes, NC chondrules display ^{17}O- and ^{18}O-enrichments compared to CC chondrules (Trinquier et al., 2007; Qin et al., 2011; Tenner et al., 2013, 2015; Olsen et al., 2016; Tenner et al., 2018; Williams et al., 2020; Zhu et al., 2020, 2019a; Piralla et al., 2021). Within the NC chondrites, EC chondrules display distinct O isotopic compositions to OC and R chondrules, indicating that chondrules from each NC group may form at several differnt locations within the NC reservoir (Weisberg et al., 2021). This is supported by the ε^{54}Cr compositions of EC chondrules, which differ from OC chondrule values (0.06 and -0.29, respectively) (Schneider et al., 2020; Zhu et al., 2020). Though OCs and R chondrite chondrules display similar O isotopic compositions (Regnault et al., 2022; Marrocchi et al., 2024), chondrules in R chondrites display increased Δ^{17}O compositions, implying a scarcity of ^{16}O-rich chondrules within the R chondrites compared to OCs (Ali et al., 2017; Regnault et al., 2022). Considered together, Δ^{17}O and ε^{54}Cr compositions indicate that within the NC reservoir, different NC chondrite groups are characterised by distinct chondrule compositions, implying that EC, OC, and R chondrules may form in different regions in the NC reservoir. This differs to the CC chondrites, where all groups appear to share a similar average ε^{54}Cr chondrule composition, and display a common range of O isotopic compositions (Tenner et al., 2018). This similarity in CC chondrule compositions argues that they all formed at the same location within the CC reservoir. As such, a difference in chondrule formation regions exists between the two reservoirs, with chondrules forming at several locations in the NC reservoir and seemingly only at one location within the CC reservoir. This contrast could be used to investigate the processes that form chondrules throughout the disk.

Provenance of accreting material

Comparing the isotopic compositions of chondrules and matrix within chondrite groups allows us to determine their provenance. The results from Chapter 3 indicate that NC chondrites accrete with chondrules and matrix that share a similar ε^{54}Cr isotopic composition. Contrastingly, Chapter 4 indicates that CC chondrites consist of chondrules and matrix which exhibit different ε^{54}Cr compositions. This implies that the NC and CC chondrites source their respective components from different locations and suggest distinct formation histories and mechanisms for the components in these chondrites.

NC chondrites sample a more restricted reservoir where chondrules and matrix form in the same region and acquire a similar isotopic signature. This varies from the CC chondrites, whose differing chondrule and matrix isotopic compositions imply that these components are sourced from different regions before they are mixed and accrete together. Within the CC reservoir, the lower ε^{54}Cr values of chondrules recovered from mixing lines in section 4.3 indicates that they form at smaller radial distances, possibly near the ice line, whilst the enriched ε^{54}Cr compositions of matrix implies it is sourced from more distal, inwardly drifting CI-like dust. The suggestion from this study that the matrix in CC chondrites is composed of CI-like dust agrees with chemical and isotopic measurements from volatile contents (Braukmüller et al., 2018; Hellmann et al., 2020; Morton et al., 2024) and previous compilation studies (Alexander, 2019b; Bryson and Brennecka, 2021; Yap and Tissot, 2023). A constant supply of inwardly drifting CI-like matrix could also explain the protracted formation timescales of CC chondrite formation compared to NC chondrites. The continuous drift of CI-matrix inwards insinuates large scale pollution of the disk by outer solar system material, also proposed by Bryson and Brennecka (2021), van Kooten et al. (2024), and Morbidelli et al. (2024). In particular, van Kooten et al. (2024) and Morbidelli et al. (2024) stress this point by reporting evidence of cometary material present in CC chondrites from the presence of ^{15}N-rich, D-rich, and ^{16}O-poor isotope signatures.

In contrast, the lower and less variable ε^{54}Cr compositions of OC chondrules and matrix observed in Chapter 3 and the literature (Qin et al., 2010) indicate that the NC chondrites sample a more restricted reservoir located between the proto-sun and the barrier between

the NC and CC reservoirs. It is likely that the barrier separating the NC and CC reservoirs prevented new material from drifting inwards. Addition of *r*-process-depleted material to the NC reservoir was thought to occur in the first <1 Ma, setting the conditions for the observed isotope dichotomy (Nanne et al., 2019; Brennecka et al., 2020; Kruijer et al., 2020). Evidence for later addition of large amounts of CI-like material is not evident in OCs. The R chondrites, however, may provide evidence for the pollution of small amounts of more distally derived, CC-like material within the outer regions of the NC reservoir. Their comparatively enriched ε^{54}Cr compositions compared to OCs reported in Chapter 3 and by Larsen et al. (2011) and Zhu et al. (2021b) indicate the presence of ^{54}Cr-enriched material in the R chondrite accretion region. It is possible that this enrichment could be due to the inward drift of small dust particles, possibly hosting ^{54}Cr-enriched anomalies, unhindered by the barrier or the higher concentration of this material at the outskirts of the reservoir. Evidence for this lies in the presence of small, <200 μm-sized CAIs observed in some NC chondrites (assumed to drift inwards past the NC-CC barrier) (Haugbølle et al., 2019), and small chondrules that display CC-like Δ^{17}O values in O chondrites (Marrocchi et al., 2024).

Locations of accretion of the NC and CC chondrite parent bodies

Based on the geochemical constraints identified in this study, the locations in which the NC and CC chondrites accreted can be investigated. Due to the isolated nature of the NC reservoirs (implied by the shared ε^{54}Cr compositions of chondrules and matrix); the observations of major element complementarity (Ebel et al., 2024); the identification of distinct groupings in ^{50}Ti isotopes (Rüfenacht et al., 2023); and the differing Δ^{17}O and ε^{54}Cr compositions of chondrules in NC groups (Schneider et al., 2020; Zhu et al., 2020; Weisberg et al., 2021; Regnault et al., 2022); it is possible that the NC chondrites (and chondrules) formed in isolated ring structures that prevented widespread movement of solids within the inner solar system (Fig. 6.4). Some models suggest that early planetesimal formation requires the drift and pile up of particles in ring structures to generate high local dust-to-gas ratios (Morbidelli et al., 2024), and early ring-like structures have been observed in ALMA images of protoplanetary disks (Dullemond et al., 2018). These models and observations lend further support to the model of accretion in the inner solar

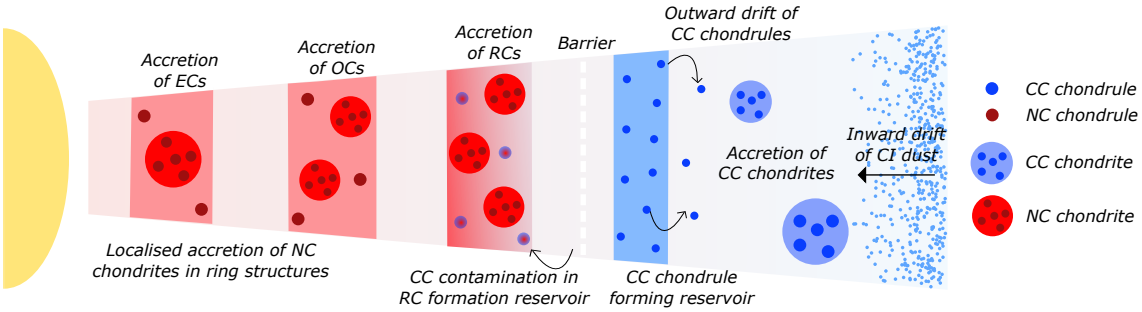

Figure 6.4: Schematic of the formation locations of NC and CC chondrites. NC chondrules form in the same region as NC chondrtie parent body accretion, likely in distinct rings in the inner solar system. CC chondrites form in the outer solar system from a mixture of inwardly drifting CI dust, and outwardly drifting CC chondrules that form in a reservoir closer to the barrier between the NC and CC reservoirs. Not to scale.

system being localised in rings.

The CC chondrites likely accreted at greater radial distances compared to the NC chondrites, evidenced by their higher ε^{54}Cr compositions. They appear to accrete with chondrules that formed in the inner regions on the CC reservoir (over a protracted time period) and with dust sourced from greater radial distances. This inwardly drifting dust could not have continually polluted the chondrule forming reservoir itself, as this would be reflected in increasingly isotopically enriched chondrules forming over time which are not seen in this study, or in others. Instead, chondrite parent body accretion likely occurred just outside of the chondrule formation region, with different CC groups forming over time with increasing amounts of inwardly drifting CI-like dust (Fig. 6.4). Chondrules and refractory inclusions (RIs) may have continually moved out of the chondrule forming region to be accreted within the CC chondrite parent bodies, since their abundances appear to co-vary (Hellmann et al., 2023). This accretion may also occur in a ring-like structure, similar to what is proposed for the NC chondrites. This structure, however, would have to be permeable to outwardly drifting pebble-sized chondrules. Rings have been observed in protoplanetary disks at distances up to 100 AU, so this is a plausible scenario for the CC reservoir (Dullemond et al., 2018). Rings located at greater radial distances than the region of chondrite accretion may act as filters that allow small CI-like dust to drift inwards, instead of barriers that stop the total flow of material.

Mechanisms of chondrite parent body accretion in the inner and outer solar system

The evidence of limited solid movement in the inner solar system contrasts with wide scale dust transport inferred in the outer solar system. This difference could indicate that mechanisms of planetesimal accretion varied across the protoplanetary disk.

The limited movement and mixing of solids in the NC reservoir, and the assumption of focussed accretion in ring structures, agrees with planetesimal models of planet formation in the inner solar system. This model of accretion is generally accepted to best replicate the formation of the terrestrial planets located between the Sun and Jupiter (Drazkowska et al., 2022; Morbidelli et al., 2025). Other mechanisms have also been suggested, i.e., pebble accretion, which sample volatile-enriched material from the outer solar system to explain the observed chemical and isotopic compositions of Earth (Schiller et al., 2018; Johansen et al., 2021). These models, however, are inconsistent with the compositions of OC and R chondrites reported in chapter 3, which display a lack of substantial CC-like enrichment compared to what is proposed by proponents of pebble accretion.

The movement of CC chondrules outwards into a chondrite forming region, and the large-scale inward drift of CI-like dust required for CC chondrite formation indicates substantial radial movement of solids in the outer solar system. Inward drift of dust is expected in protoplanetary disks due to gas drag (Drazkowska et al., 2022). Taking this into consideration, this dust migration itself may not provide strong evidence for large-scale transport of pebble-like objects in the outer disk. However, the transport of chondrules to greater radial distances to accrete within the CC parent body may be reminiscent of the movement of pebbles, albeit in the net opposite direction to the pebble accretion hypothesis. Pebble accretion in the outer solar system is thought to successfully explain the rapid formation of the gas and ice giants (Levison et al., 2015; Drazkowska et al., 2022). This cannot be successfully proven or disproven in this work, however, there is evidence of substantial dust and minor chondrule movement in the outer solar system.

If planetesimal accretion is the dominant mechanism of planetary formation in the inner solar system, and pebble accretion possibly occurs in the outer regions of the disk, this

change in accretionary mechanism must be related to disk conditions within each region. Factors influencing the mechanisms of accretion can include local turbulence, the dust-to-gas ratio, and the availability/infall of more material (Drazkowska et al., 2022). Further work focussed on identifying why different mechanisms of formation might be dominant in the inner and outer solar system, as inferred from this study, will allow us to better understand the dynamics of solid movement in the protoplanetary disk.

6.4 Formation of the CC chondrites vs CR chondrites: changing conditions over time

The carbonaceous chondrites contain multiple groups which each display variations in their petrology and chemical and isotopic composition. CR chondrites are a subset of CC chondrites that display younger chondrule and parent body accretion ages (Amelin et al., 2002; Budde et al., 2018; Schrader et al., 2017) as well as evidence of extensive reprocessing (Jacquet et al., 2013; Marrocchi et al., 2022; Pinto et al., 2024). Evaluating how the CR chondrites formed in comparison to other CC chondrites would allow us to investigate how mechanisms of chondrite parent body accretion varied over time in the outer solar system.

As seen in Chapter 5 and widely reported in literature data (Zhu et al., 2021c), the CR chondrites display enriched ε^{54}Cr compositions compared to most other CC groups, barring the CI chondrites. A mixing line plot through CR chondrite subsamples measured in Chapter 5, and anomalously matrix-rich CR chondrites Al Rais and GRO 95577, indicates that the compositions of CR chondrites can be replicated through mixtures of CI-like dust (forming the matrix) and chondrules that display depleted ε^{54}Cr compositions (Fig. 5.6). This indicates that accretion of CI dust was an integral component of CC chondrite accretion up to 2 Ma after the first CC chondrites formed. This is further supported by previous work that suggest that CR chondrites display abundant dark inclusions, unaltered presolar grains, and primitive amino acids, often associated with pristine CI-like dust and relatively unaltered matrix (Glavin et al., 2010; Davidson et al., 2014; Abreu et al., 2020).

The average CR chondrule composition (ε^{54}Cr = 1.06) recovered in Chapter 5 is higher than the average recovered for CC chondrites in Chapter 4 (ε^{54}Cr = 0.50), but is lower than those measured in previous studies of individual, extracted chondrules (ε^{54}Cr = 1.41) (Qin et al., 2011; Olsen et al., 2016; van Kooten et al., 2016; Schneider et al., 2020). This difference could be due to sampling bias when measuring chondrule compositions. Larger chondrules (>0.9 mm) are easier to isolate and measure compared to smaller chondrules and chondrule fragments, and likely represent the *type I-CR* chondrules identified by

Marrocchi et al. (2022). Marrocchi et al. (2022) and Tenner et al. (2015) note that smaller chondrules in CR chondrites display ^{16}O-enriched compositions, closer to those observed in CO-CV-CM chondrules; these are termed *type I-CO* chondrules. Though the ε^{54}Cr compositions of these small chondrules have not yet been measured, it is reasonable to assume they may reflect similar ε^{54}Cr values to chondrules present in CO, CM, CV, and C-Ung chondrites due to their similar oxygen isotopic composition. The lower average CR chondrule composition observed in Chapter 6 possibly reflects contribution from both chondrule populations. The formation of the isotopically enriched *type I-CR* chondrules is possibly linked to their formation within a reservoir that was previously enriched in isotopically CI-like dust, as proposed in Chapter 6 (see Fig. 5.10) and by Bryson and Brennecka (2021) and Marrocchi et al. (2022).

Since the CR chondrites appear to contain contributions from CI-like dust, isotopically "CO-like" chondrules (with compositions assumed to match those observed in the CO, CM and CV chondrites), and ^{54}Cr enriched chondrules, this implies that conditions of parent body accretion in the CC reservoir did not drastically differ over time. CI dust and a population of "CC-like" chondrules (analogous to *type I-CO* chondrules) must have been present in the initial CR reservoir to form the *type I-CR* chondrules (Fig. 5.10). These components were then both present during the subsequent accretion of the CR parent body at ∼4 Ma after the reprocessing event that formed the *type I-CR* chondrules. This indicates that CI-like dust continuously drifted inwards from the time of accretion of the CO chondrite parent body until the CR parent body formed. Schrader et al. (2018b) also argue for the prolonged presence of fine-grained dust (here assumed to be CI-like) in the outer solar system until ∼3.7 Ma due to observations of small <1 - 80 μm dust-sized silicates present in some CR chondrule olivines. This indicates that the CR chondrite parent body and chondrules formed in a dusty environment, lending further support for the presence of CI-like dust being present.

Overall, though the CR chondrites record evidence of reprocessing that form chondrules with enriched ε^{54}Cr compositions compared to the average composition seen in other CC chondrites, they also reflect accretion of isotopically heterogenous chondrules and matrix. Matrix compositions are likely isotopically CI-like, implying that the overall mechanism

of CC chondrite parent body formation from isotopically distinct chondrules and CI-like matrix was constant over time in the outer solar system. The initial CR chondrite body/reservoir is assumed to have high proportions of matrix compared to chondrules, consistent with their later formation and the trend seen in CC chondrites where parent bodies that accrete later form with greater fractions of matrix (see Fig. 5.11). This highlights that the CR chondrites, though distinct in their history of reprocessing, provide valuable insights into how mechanisms of parent body formation in the CC reservoir remained constant over the lifetime of the protoplanetary disk, as well as how this mechanism was modified by stochastic processes.

Chapter 7

Conclusions

This work utilised a novel method of subsampling chondrites to identify and characterise variations in their chondrule and matrix isotopic compositions. This was used to investigate whether chondrules and matrix display homogeneous or heterogenous isotopic compositions, and to determine the mechanisms of accretion of the non-carbonaceous (NC) and carbonaceous (CC) chondrites.

Success of the novel subsampling method

The subsampling method developed in this study, paired with the fitting of an isotopic mixing line, aimed to characterise the ε^{54}Cr compositions of chondrules and matrix in chondrites. This method struggles in some instances (e.g., R chondrites, CO chondrites) due to the difficulty of generating subsamples that are small enough to exhibit large variations in matrix proportions. This small spread of matrix proportions results in difficulty fitting an isotopic mixing line through the compositions of chondrite subsamples to recover accurate and precise ε^{54}Cr compositions of chondrules and matrix. The fitted mixing line, and recovered chondrule and matrix compositions, have large uncertainties associated with this poor fit. Additionally, isotopic variations between chondrules may not be averaged out in subsamples of CC chondrites leading to large scatter away from the mixing line. Problems associated with the narrow spread of subsamples and data scatter were minimised by considering larger datasets with multiple chondrite samples that cover a wider range of matrix fractions, as demonstrated in Chapter 4, or including literature values as

seen in Chapter 5.

NC chondrites

The coupled ε^{54}Cr compositions and plateau volatile element concentrations of subsamples of an OC and R chondrite were measured to investigate chondrite formation in the NC reservoir.

LL chondrite LoV 171 has a bulk ε^{54}Cr composition of -0.16 ± 0.39 and displays a matrix volume fraction of 0.199. This represents the first reported ε^{54}Cr composition of this OC and agrees with the compositions of other measured OCs and LL chondrites. A mixing line through subsamples of LoV 171 displays a poor fit and large uncertainties, leading to recovered chondrule and matrix compositions of -0.14 ± 0.13 and -1.45 ± 5.37, respectively. A qualitative assessment of the compositions of individual subsamples of LoV 171 indicates that there is no apparent variation in Cr isotopic composition between subsamples. This consistency indicates that OCs display similar chondrule and matrix ε^{54}Cr compositions. This similarity implies that chondrules in OCs formed in the same local reservoir as the matrix, such that both acquire a similar isotopic composition.

R chondrite MIL 07440 displays a bulk ε^{54}Cr composition of 0.18 ± 0.31 and a matrix volume fraction of 0.450. This measured ε^{54}Cr composition may be slightly elevated due to isotopic fractionation effects during column chemistry that were uncorrected for. This composition indicates that R chondrites show enrichment in ^{54}Cr, reflected by their comparatively enriched ε^{54}Cr compositions compared to OCs. The compositions of individual subsamples of MIL 07440 cannot help distinguish whether this isotopic enrichment is present in both chondrules and matrix or if it is solely hosted in the matrix. Therefore, it is also difficult to ascertain if chondrules and matrix in the R chondrites display heterogenous or homogeneous isotopic compositions. A mixing line through subsamples of MIL 07440 displays a poor fit and large uncertainties in chondrule and matrix compositions, leading to recovered values of 0.06 ± 1.17 and 0.49 ± 3.28, respectively. The ^{54}Cr-enrichment observed in R chondrites is likely due to a small contribution of CC-like material to material with an OC isotopic signature within the R chondrite accretion region. The location of the R chondrite reservoir may be at greater radial distances compared to

Chondrite	Bulk ε^{54}Cr 2σ	Chondrule ε^{54}Cr 2σ	Matrix ε^{54}Cr 2σ	Matrix volume fraction
LL LoV 171	-0.16 ±0.39	-0.14 ±0.13	-1.45 ±5.37	0.199
R MIL 07440	0.18 ±0.31	0.06 ±1.17	0.49 ±3.28	0.450
CO DOM 08006	0.73 ±0.08	0.74 ±0.17	0.78 ±0.45	0.317
CV Allende	0.68 ±0.34	0.32 ±0.80	1.35 ±1.80	0.377
CM NWA 11345	1.09 ±0.27	0.64 ±2.52	1.40 ±1.83	0.631
C2-Ung Tarda	0.94 ±0.31	0.71 ±0.80	1.18 ±0.64	0.620
CR MIL 090001	1.11 ±0.22	1.06 ±0.12	1.59 ±0.40	0.211

Table 7.1: Summary of bulk NC and CC chondrite, chondrule, and matrix compositions recovered from this study

the OCs and closer to the barrier between the NC and CC reservoirs. A leaky barrier, or a pre-existing compositional gradient at the outer edges of the NC reservoir, could result in the CC-like enrichments observed in the R chondrites.

CC chondrites

The coupled ε^{54}Cr compositions and plateau volatile element concentrations of subsamples of various CC chondrites were measured to investigate the mechanisms of chondrite formation in the CC reservoir.

The bulk ε^{54}Cr compositions of CO DOM 08006, CV Allende, CM NWA 11345, and C2-Ung Tarda were measured and display values of 0.73 ± 0.23, 0.68 ± 0.34, 1.09 ± 0.27, and 0.94 ± 0.27, respectively. Zn concentrations indicate that each chondrite displays matrix volume fractions of 0.317, 0.377, 0.631, and 0.620, respectively.

Isotopic mixing lines plotted through subsamples of each chondrite have large uncertainties but generate chondrule ε^{54}Cr compositions of 0.74 ± 0.17, 0.32 ± 0.80, 0.64 ± 2.52, and 0.71 ± 0.80 for CO, CV, CM, and C2-Ung chondrites, respectively. These recovered values are within error of CC chondrule compositions previously measured.

Due to the large errors associated with fitting through the subsamples, these mixing lines are unable to reliably distinguish whether matrix in each measured chondrite displays

the same or different isotopic compositions to chondrules. The recovered matrix ε^{54}Cr compositions are 0.78 ± 0.45, 1.35 ± 1.80, 1.40 ± 1.83, and 1.18 ± 0.64 for CO, CV, CM, and C2-Ung chondrites, respectively.

A mixing line fit through all measured CC chondrite subsamples displays smaller uncertainties and recovers an average chondrule ε^{54}Cr composition of 0.50 ± 0.17 and matrix composition of 1.36 ± 0.22. This implies that all CC chondrites share an average chondrule composition similar to that recovered from pooled chondrules measured by Schneider et al. (2020), and these chondrites contain matrix that is CI-like in composition. CC chondrites from different groups contain varying proportions of chondrules and matrix, which controls their bulk ε^{54}Cr compositions. Chondrites that contain higher proportions of matrix display higher ε^{54}Cr compositions, with increasingly enriched compositions seen in the CO, CV, CM, and C2-Ung chondrites.

As the chondrules and matrix present in CC chondrites display different ε^{54}Cr compositions, it is likely these components formed in different reservoirs. Matrix displays enriched isotopic compositions, within error of CI chondrites, implying that it is sourced from more distal regions of the protoplanetary disk compared to the isotopically depleted chondrules. Since all CC chondrules show similar average compositions, they likely all formed in a shared reservoir over a protracted period of time. As CO chondrites accrete the earliest and display the oldest chondrule ages, this indicates that the matrix fraction present in CC chondrites increases over time. CV, CM, and C2-Ung chondrites thus reflect a trend of increasingly younger CC chondrites that accreted with greater amounts of CI-like dust.

The presence of isotopically heterogeneous chondrules and matrix in CC chondrites implies that these components were formed in different regions of the outer solar system before they were both transported and accreted in the CC chondrite forming region. CI-like dust continually drifted inwards towards the CC chondrite accretion region and chondrules were transported outwards from their formation reservoir, indicating large-scale transport of material in the outer protoplanetary disk.

CR chondrites

The coupled ε^{54}Cr compositions and plateau volatile element concentrations of subsamples of a CR chondrite were measured to investigate how chondrite formation differed over time in the CC reservoir.

CR chondrite MIL 090001 has a bulk ε^{54}Cr composition of 1.11 ± 0.22 and displays a matrix volume fraction of 0.211. There is no apparent variation in the Cr isotopic composition of chondrules and matrix in this CC chondrite. An isotopic mixing line plotted through subsamples of MIL 090001 and compositions of anomalously matrix rich CR chondrite Al Rais and GRO 95577 indicates that the compositions of CR chondrites can be reproduced by mixing of CI dust (ε^{54}Cr composition of 1.59 ± 0.19) and isotopically depleted chondrules (ε^{54}Cr composition of 1.06 ± 0.12). This recovered chondrule composition is lower than what has previously measured in isolated, large CR chondrules, but could reflect the contribution of smaller chondrules that display similar ε^{54}Cr compositions to the average chondrule composition observed in other CC chondrites (∼0.50).

The initial CR chondrite reservoir was probably matrix-rich, indicated by the enriched bulk CR and measured chondrule ε^{54}Cr compositions. The reprocessing event that formed the ^{54}Cr-enriched chondrules was likely followed by accretion of the final CR parent body with additional CI-like matrix and isotopically depleted, CC-like chondrules.

Though the formation of the CR chondrites is overprinted by reprocessing events that have altered the isotopic composition of some chondrules, in general, the CR chondrites initially appear to have accreted via similar mechanisms to the earlier formed CC chondrites. This is evidenced by their accretion from CC-like chondrules with isotopically depleted ε^{54}Cr compositions, and infalling CI dust. This implies that chondrite formation mechanisms in the CC reservoir remained constant over time, with increasing contribution of CI dust to the chondrite accretion region.

Accretionary mechanisms in the protoplanetary disk

NC chondrites accrete in the inner regions of the protoplanetary disk and display minimal isotopic variation, with little evidence of contribution of material from the outer

solar system. These chondrites accrete from local material, potentially in isolated ring structures. This model of formation depicts chondrite accretion from a compositionally restricted reservoir, akin to planetesimal accretions models. This is inconsistent with scenarios of pebble accretion which model terrestrial planet formation from material sourced from across the protoplanetary disk (i.e., includes material that originates from the distal solar system).

CC chondrites accrete chondrules and matrix that form in different regions of the outer protoplanetary disk. CI-like matrix is likely sourced from the outer protoplanetary disk and chondrules form closer to the barrier between the NC and CC reservoirs. This suggests wide-scale radial movement of CI-like dust and chondrules towards the accretion region of the CC chondrite parent bodies. This indicates that, compared to the NC reservoir, solids in the outer protoplanetary disk undergo large-scale transport, possibly supporting the suggestion of pebble accretion acting in the outer solar system. The transport of CI dust into the CC chondrite accretion reservoir, and the formation and reprocessing of chondrules, occurred over a protracted period of time as evidenced by the CR chondrites. This implies that the mechanisms of CC chondrite accretion remained fairly constant over 2 - 4 Ma after CAI formation.

From this, it is clear that the dominant mechanisms of accretion differ in the inner and outer protoplanetary disk. NC chondrites provide evidence of accretion within a restricted reservoir in the inner solar system, while CC chondrites accrete from material across the disk in an environment that experiences extensive solid movement. It is likely that the dynamic regimes controlling chondrite formation in the inner and outer protoplanetary disk differed due to variations in local dust-to-gas ratios, the availability of material, and barriers to the movement of solids. These differences in dynamic regime could also be the source of the different accretion mechanisms identified in this study that operate in the inner and outer solar system.

Bibliography

Abreu, N., Aponte, J., Cloutis, E., and Nguyen, A. (2020). The Renazzo-like carbonaceous chondrites as resources to understand the origin, evolution, and exploration of the solar system. *Geochemistry*, 80(4):125631.

Alexander, C. (2019a). Quantitative models for the elemental and isotopic fractionations in chondrites: The carbonaceous chondrites. *Geochimica et Cosmochimica Acta*, 254:277–309.

Alexander, C. (2019b). Quantitative models for the elemental and isotopic fractionations in the chondrites: The non-carbonaceous chondrites. *Geochimica et Cosmochimica Acta*, 254:246–276.

Alexander, C., Cody, G., De Gregorio, B., Nittler, L., and Stroud, R. (2017). The nature, origin and modification of insoluble organic matter in chondrites, the major source of Earth's C and N. *Geochemistry*, 77(2):227–256.

Alexander, C., Howard, K., Bowden, R., and Fogel, M. (2013). The classification of CM and CR chondrites using bulk H, C and N abundances and isotopic compositions. *Geochimica et Cosmochimica Acta*, 123:244–260.

Alexander, C., McKeegan, K., and Altwegg, K. (2018). Water Reservoirs in Small Planetary Bodies: Meteorites, Asteroids, and Comets. *Space Science Reviews*, 214.

Alexander, C. M. O., Bowden, R., Fogel, M. L., Howard, K. T., and Greenwood, R. C. (2012). The Classification of CM and CR Chondrites Using Bulk H Abundances and Isotopes. page 2799. Conference Name: 43rd Annual Lunar and Planetary Science Conference ADS Bibcode: 2012LPI....43.2799A.

Alexander, R., Pascucci, I., Andrews, S., Armitage, P., and Cieza, L. (2014). The Dispersal of Protoplanetary Disks. In *Protostars and Planets VI*. University of Arizona Press.

Ali, A., Nasir, S. J., Jabeen, I., Al Rawas, A., Banerjee, N. R., and Osinski, G. R. (2017). Geochemical and oxygen isotope perspective of a new R chondrite Dhofar 1671: Affinity with ordinary chondrites. *Meteoritics & Planetary Science*, 52(9):1991–2003.

Amelin, Y., Krot, A. N., Hutcheon, I. D., and Ulyanov, A. A. (2002). Lead Isotopic Ages of Chondrules and Calcium-Aluminum-Rich Inclusions. *Science*, 297(5587):1678–1683.

Anand, A. and Mezger, K. (2023). Early solar system chronology from short-lived chronometers. *Geochemistry*, 83(3):126004.

Barosch, J., Ebel, D. S., Hezel, D. C., Alpert, S., and Palme, H. (2020). Formation of chondrules and matrix in Kakangari chondrites. *Earth and Planetary Science Letters*, 542:116286.

Bates, H. (2020). *Understanding the formation and evolution of asteroids through analysis of carbonaceous chondrites*. PhD Thesis, University of Oxford.

Bates, H. C., Aspin, R., Fu, C. Y., Harrison, C. S., Feaver, E., Branagan-Harris, E., King, A. J., Bryson, J. F. J., Sridhar, S., and Nichols, C. I. O. (2024). Extent of alteration, paleomagnetic history, and infrared spectral properties of the Tarda ungrouped carbonaceous chondrite. *Meteoritics & Planetary Science*, 59(9):2411–2431.

Bekaert, D. V., Auro, M., Shollenberger, Q. R., Liu, M.-C., Marschall, H., Burton, K. W., Jacobsen, B., Brennecka, G. A., McPherson, G. J., von Mutius, R., Sarafian, A., and Nielsen, S. G. (2021). Fossil records of early solar irradiation and cosmolocation of the CAI factory: A reappraisal. *Science Advances*, 7(40):eabg8329.

Bermingham, K., Füri, E., Lodders, K., and Marty, B. (2020). The NC-CC Isotope Dichotomy: Implications for the Chemical and Isotopic Evolution of the Early Solar System. *Space Science Reviews*, 216.

Bermingham, K. and Meyer, B. (2024). Nucleosynthetic Isotope Anomalies in Cosmochemistry and Geochemistry. In *Oxford Research Encyclopedia of Planetary Science*. Oxford University Press.

Bischoff, A., Vogel, N., and Roszjar, J. (2011). The Rumuruti chondrite group. *Geochemistry*, 71(2):101–133.

Black, D. and Pepin, R. (1969). Trapped neon in meteorites — II. *Earth and Planetary Science Letters*, 6(5):395–405.

Bland, P. A., Alard, O., Benedix, G. K., Kearsley, A. T., Menzies, O. N., Watt, L. E., and Rogers, N. W. (2005). Volatile fractionation in the early solar system and chondrule/matrix complementarity. *Proceedings of the National Academy of Sciences*, 102(39):13755–13760.

Bland, P. A., Jackson, M. D., Coker, R. F., Cohen, B. A., Webber, J. B. W., Lee, M. R., Duffy, C. M., Chater, R. J., Ardakani, M. G., McPhail, D. S., McComb, D. W., and Benedix, G. K. (2009). Why aqueous alteration in asteroids was isochemical: High porosity /= high permeability. *Earth and Planetary Science Letters*, 287(3-4):559–568.

Bollard, J., Connelly, J. N., Whitehouse, M. J., Pringle, E. A., Bonal, L., Jørgensen, J. K., Nordlund, Å., Moynier, F., and Bizzarro, M. (2017). Early formation of planetary building blocks inferred from Pb isotopic ages of chondrules. *Science Advances*, 3(8):e1700407.

Brasser, R. and Mojzsis, S. J. (2020). The partitioning of the inner and outer Solar System by a structured protoplanetary disk. *Nature Astronomy*, 4(5):492–499.

Braukmüller, N., Wombacher, F., Hezel, D. C., Escoube, R., and Münker, C. (2018). The chemical composition of carbonaceous chondrites: Implications for volatile element depletion, complementarity and alteration. *Geochimica et Cosmochimica Acta*, 239:17–48.

Brennecka, G. A., Borg, L. E., and Wadhwa, M. (2013). Evidence for supernova injection into the solar nebula and the decoupling of r-process nucleosynthesis. *Proceedings of the National Academy of Sciences*, 110(43):17241–17246.

Brennecka, G. A., Burkhardt, C., Budde, G., Kruijer, T. S., Nimmo, F., and Kleine, T.

(2020). Astronomical context of Solar System formation from molybdenum isotopes in meteorite inclusions. *Science*, 370(6518):837–840.

Bryson, J., Weiss, B., Biersteker, J., King, A., and Russell, S. (2020a). Constraints on the Distances and Timescales of Solid Migration in the Early Solar System from Meteorite Magnetism. *The Astrophysical Journal*, 896.

Bryson, J. F. J. and Brennecka, G. A. (2021). Constraints on Chondrule Generation, Disk Dynamics, and Asteroid Accretion from the Compositions of Carbonaceous Meteorites. *The Astrophysical Journal*, 912(2):163.

Bryson, J. F. J., Weiss, B. P., Lima, E. A., Gattacceca, J., and Cassata, W. S. (2020b). Evidence for Asteroid Scattering and Distal Solar System Solids From Meteorite Paleomagnetism. *The Astrophysical Journal*, 892(2):126.

Budde, G., Burkhardt, C., Brennecka, G. A., Fischer-Gödde, M., Kruijer, T. S., and Kleine, T. (2016a). Molybdenum isotopic evidence for the origin of chondrules and a distinct genetic heritage of carbonaceous and non-carbonaceous meteorites. *Earth and Planetary Science Letters*, 454:293–303.

Budde, G., Burkhardt, C., and Kleine, T. (2019). Molybdenum isotopic evidence for the late accretion of outer Solar System material to Earth. *Nature Astronomy*, 3(8):736–741.

Budde, G., Kleine, T., Kruijer, T. S., Burkhardt, C., and Metzler, K. (2016b). Tungsten isotopic constraints on the age and origin of chondrules. *Proceedings of the National Academy of Sciences*, 113(11):2886–2891.

Budde, G., Kruijer, T. S., and Kleine, T. (2018). Hf-W chronology of CR chondrites: Implications for the timescales of chondrule formation and the distribution of 26Al in the solar nebula. *Geochimica et Cosmochimica Acta*, 222:284–304.

Burkhardt, C., Dauphas, N., Hans, U., Bourdon, B., and Kleine, T. (2019). Elemental and isotopic variability in solar system materials by mixing and processing of primordial disk reservoir. *Geochimica et Cosmochimica Acta*, 261:145–170.

Burkhardt, C., Kleine, T., Oberli, F., Pack, A., Bourdon, B., and Wieler, R. (2011). Molybdenum isotope anomalies in meteorites: Constraints on solar nebula evolution and origin of the Earth. *Earth and Planetary Science Letters*, 312(3-4):390–400.

Burkhardt, C., Spitzer, F., Morbidelli, A., Budde, G., Render, J. H., Kruijer, T. S., and Kleine, T. (2021). Terrestrial planet formation from lost inner solar system material. *Science Advances*, 7(52):eabj7601.

Clayton, R. N. (2008). Oxygen Isotopes in the Early Solar System – A Historical Perspective. *Reviews in Mineralogy and Geochemistry*, 68(1):5–14.

Clayton, R. N. and Mayeda, T. K. (1999). Oxygen isotope studies of carbonaceous chondrites. *Geochimica et Cosmochimica Acta*, 63(13-14):2089–2104.

Clayton, R. N., Mayeda, T. K., Goswami, J., and Olsen, E. J. (1991). Oxygen isotope studies of ordinary chondrites. *Geochimica et Cosmochimica Acta*, 55(8):2317–2337.

Colmenares, M. J., Lambrechts, M., Van Kooten, E., and Johansen, A. (2024). Thermal processing of primordial pebbles in evolving protoplanetary disks. *Astronomy & Astrophysics*, 685:A114.

Connelly, J., Bollard, J., and Bizzarro, M. (2017). Pb–Pb chronometry and the early Solar System. *Geochimica et Cosmochimica Acta*, 201:345–363.

Connelly, J., Schiller, M., and Bizzarro, M. (2019). Pb isotope evidence for rapid accretion and differentiation of planetary embryos. *Earth and Planetary Science Letters*, 525:115722.

Connelly, J. N., Bizzarro, M., Krot, A. N., Nordlund, Å., Wielandt, D., and Ivanova, M. A. (2012). The Absolute Chronology and Thermal Processing of Solids in the Solar Protoplanetary Disk. *Science*, 338(6107):651–655.

Connolly, H. C., Huss, G. R., Nagashima, K., Weisberg, M. K., Ash, R. D., Ebel, D. S., Schrader, D. L., and Lauretta, D. S. (2008). Oxygen Isotopes and the Nature and Origins of Type-II Chondrules in CR2 Chondrites. page 1675. Conference Name: 39th Annual Lunar and Planetary Science Conference ADS Bibcode: 2008LPI....39.1675C.

Creech, J. and Moynier, F. (2019). Tin and zinc stable isotope characterisation of chondrites and implications for early Solar System evolution. *Chemical Geology*, 511:81–90.

Dauphas, N. (2017). The isotopic nature of the Earth's accreting material through time. *Nature*, 541(7638):521–524.

Dauphas, N., Chen, J. H., Zhang, J., Papanastassiou, D. A., and Davis, A. M. (2014). Calcium-48 isotopic anomalies in bulk chondrites and achondrites: Evidence for a uniform isotopic reservoir in the inner protoplanetary disk. *Earth and Planetary Science Letters*, 407:96–108.

Dauphas, N., Hopp, T., and Nesvorný, D. (2024). Bayesian inference on the isotopic building blocks of Mars and Earth. *Icarus*, 408:115805.

Dauphas, N., Remusat, L., Chen, J. H., Roskosz, M., Papanastassiou, D. A., Stodolna, J., Guan, Y., Ma, C., and Eiler, J. M. (2010). Neutron-rich chromium isotope anomalies in supernova nanoparticles. *The Astrophysical Journal*, 720(2):1577–1591.

David, J.-C. and Leya, I. (2019). Spallation, cosmic rays, meteorites, and planetology. *Progress in Particle and Nuclear Physics*, 109:103711.

Davidson, J., Busemann, H., Nittler, L. R., Alexander, C. M., Orthous-Daunay, F.-R., Franchi, I. A., and Hoppe, P. (2014). Abundances of presolar silicon carbide grains in primitive meteorites determined by NanoSIMS. *Geochimica et Cosmochimica Acta*, 139:248–266.

Davidson, J., Schrader, D., Alexander, C., Nittler, L., and Bowden, R. (2019). Re-examining thermal metamorphism of the Renazzo-like (CR) carbonaceous chondrites: Insights from pristine Miller Range 090657 and shock-heated Graves Nunataks 06100. *Geochimica et Cosmochimica Acta*, 267:240–256.

Desch, S. J., Kalyaan, A., and Alexander, C. M. O. (2018). The Effect of Jupiter's Formation on the Distribution of Refractory Elements and Inclusions in Meteorites. *The Astrophysical Journal Supplement Series*, 238(1):11.

Doyle, P., Jogo, K., Nagashima, K., Krot, A., Wakita, S., Ciesla, F., and Hutcheon, I. (2015). Early aqueous activity on the ordinary and carbonaceous chondrite parent bodies recorded by fayalite. *Nature Communications*, 6.

Drazkowska, J., Bitsch, B., Lambrechts, M., Mulders, G. D., Harsono, D., Vazan, A., Liu, B., Ormel, C. W., Kretke, K., and Morbidelli, A. (2022). Planet Formation Theory in the Era of ALMA and Kepler: from Pebbles to Exoplanets. Publisher: arXiv Version Number: 3.

Dullemond, C. P., Birnstiel, T., Huang, J., Kurtovic, N. T., Andrews, S. M., Guzmán, V. V., Pérez, L. M., Isella, A., Zhu, Z., Benisty, M., Wilner, D. J., Bai, X.-N., Carpenter, J. M., Zhang, S., and Ricci, L. (2018). The Disk Substructures at High Angular Resolution Project (DSHARP). VI. Dust Trapping in Thin-ringed Protoplanetary Disks. *The Astrophysical Journal Letters*, 869(2):L46.

Dunham, E. T., Sheikh, A., Opara, D., Matsuda, N., Liu, M.-C., and McKeegan, K. D. (2023). Calcium–aluminum-rich inclusions in non-carbonaceous chondrites: Abundances, sizes, and mineralogy. *Meteoritics & Planetary Science*, 58(5):643–671.

Ebel, D. (2006). Condensation of Rocky Material in Astrophysical Environments. *Meteorites and the Early Solar System II*, 943.

Ebel, D. S., Gemma, M. E., Alpert, S. P., Bayron, J., Lobo, A. H., and Weisberg, M. K. (2024). Abundance, sizes, and major element compositions of components in CR and LL chondrites: Formation from single reservoirs. *Meteoritics & Planetary Science*, 59(9):2276–2295.

Floss, C. and Haenecour, P. (2016). Presolar Silicate Abundances in the Unequilibrated Ordinary Chondrites Meteorite Hills 00526 and Queen Alexandra Range 97008. *79th Annual Meeting of the Meteoritical Society*.

Frank, D. R., Huss, G. R., Zolensky, M. E., Nagashima, K., and Le, L. (2023). Calcium-aluminum-rich inclusion found in the Ivuna CIchondrite: Are CI chondrites a good proxy for the bulk composition of the solar system? *Meteoritics & Planetary Science*, 58(10):1495–1511.

Friedrich, J. M., Weisberg, M. K., Ebel, D. S., Biltz, A. E., Corbett, B. M., Iotzov, I. V., Khan, W. S., and Wolman, M. D. (2015). Chondrule size and related physical properties: A compilation and evaluation of current data across all meteorite groups. *Geochemistry*, 75(4):419–443.

Friend, P., Hezel, D. C., Palme, H., Bischoff, A., and Gellissen, M. (2017). Complementary element relationships between chondrules and matrix in Rumuruti chondrites. *Earth and Planetary Science Letters*, 480:87–96.

Fu, R. R., Volk, M. W. R., Bilardello, D., Libourel, G., Lesur, G. R. J., and Ben Dor, O. (2021). The Fine-Scale Magnetic History of the Allende Meteorite: Implications for the Structure of the Solar Nebula. *AGU Advances*, 2(3).

Fujiya, W., Sugiura, N., Sano, Y., and Hiyagon, H. (2013). Mn–Cr ages of dolomites in CI chondrites and the Tagish Lake ungrouped carbonaceous chondrite. *Earth and Planetary Science Letters*, 362:130–142.

Fukami, Y., Ariizumi, R., Ijichi, Y., Ohno, T., Kashiwabara, T., Shibuya, T., Suzuki, K., and Hirata, T. (2024). Variation in the relationship between odd isotopes of tin in mass-independent fractionation induced by the magnetic isotope effect. *Proceedings of the National Academy of Sciences*, 121(17):e2321616121.

Fukuda, K., Hibiya, Y., Kastelle, C. R., Suzuki, K., Iizuka, T., Yamashita, K., Helser,

T. E., and Kita, N. T. (2024). Radial transport and nebular thermal processing of millimeter-sized solids in the Solar protoplanetary disk inferred from Cr-Ti-O isotope systematics of chondrules. *Meteoritics & Planetary Science*, page maps.14276.

Garenne, A., Beck, P., Montes-Hernandez, G., Chiriac, R., Toche, F., Quirico, E., Bonal, L., and Schmitt, B. (2014). The abundance and stability of "water" in type 1 and 2 carbonaceous chondrites (CI, CM and CR). *Geochimica et Cosmochimica Acta*, 137:93–112.

Glavin, D. P., Callahan, M. P., Dworkin, J. P., and Elsila, J. E. (2010). The effects of parent body processes on amino acids in carbonaceous chondrites: Amino acids in carbonaceous chondrites. *Meteoritics & Planetary Science*, 45(12):1948–1972.

Göpel, C., Birck, J.-L., Galy, A., Barrat, J.-A., and Zanda, B. (2015). Mn–Cr systematics in primitive meteorites: Insights from mineral separation and partial dissolution. *Geochimica et Cosmochimica Acta*, 156:1–24.

Greenwood, R. C., Burbine, T. H., and Franchi, I. A. (2020). Linking asteroids and meteorites to the primordial planetesimal population. *Geochimica et Cosmochimica Acta*, 277:377–406.

Gregory, T., Luu, T.-H., Coath, C. D., Russell, S. S., and Elliott, T. (2020). Primordial formation of major silicates in a protoplanetary disc with homogeneous 26Al/27Al. *Science Advances*, 6(11):eaay9626.

Grossman, J. and Brearley, A. (2005). The onset of metamorphism in ordinary and carbonaceous chondrites. *Meteoritics & Planetary Science*, 40:87–122.

Halliday, A., Rehkämper, M., Lee, D.-C., and Yi, W. (1996). Early evolution of the Earth and Moon: new constraints from Hf-W isotope geochemistry. *Earth and Planetary Science Letters*, 142(1-2):75–89.

Harju, E., Rubin, A., Ahn, I., Choi, B., Ziegler, K., and Wasson, J. (2014). Progressive aqueous alteration of CR carbonaceous chondrites. *Geochimica et Cosmochimica Acta*, 139:267–292.

Haugbølle, T., Weber, P., Wielandt, D. P., Benítez-Llambay, P., Bizzarro, M., Gressel, O., and Pessah, M. E. (2019). Probing the Protosolar Disk Using Dust Filtering at Gaps in the Early Solar System. *The Astronomical Journal*, 158(2):55.

Hellmann, J., Hopp, T., Burkhardt, C., and Kleine, T. (2020). Origin of volatile element depletion among carbonaceous chondrites. *Earth and Planetary Science Letters*, 549.

Hellmann, J. L., Budde, G., Willhite, L. N., and Walker, R. J. (2024). Hf–W isotope systematics of bulk chondrites: Implications for early Solar System evolution. *Geochimica et Cosmochimica Acta*, 387:38–52.

Hellmann, J. L., Schneider, J. M., Wölfer, E., Drążkowska, J., Jansen, C. A., Hopp, T., Burkhardt, C., and Kleine, T. (2023). Origin of Isotopic Diversity among Carbonaceous Chondrites. *The Astrophysical Journal Letters*, 946(2):L34.

Hewins, R. H., Connolly, H. C., Lofgren, G. E. J., and Libourel, G. (2005). Experimental Constraints on Chondrule Formation. 341:286. Conference Name: Chondrites and the Protoplanetary Disk ADS Bibcode: 2005ASPC..341..286H.

Hezel, D. and Palme, H. (2008). Constraints for chondrule formation from Ca–Al distribution in carbonaceous chondrites. *Earth and Planetary Science Letters*, 265(3-4):716–725.

Hezel, D. C., Bland, P. A., Palme, H., Jacquet, E., and Bigolski, J. (2018a). Composition of Chondrules and Matrix and Their Complementary Relationship in Chondrites. In Russell, S. S., Connolly Jr., H. C., and Krot, A. N., editors, *Chondrules*, pages 91–121. Cambridge University Press, 1 edition.

Hezel, D. C., Harak, M., and Libourel, G. (2018b). What we know about elemental bulk chondrule and matrix compositions: Presenting the ChondriteDB Database. *Geochemistry*, 78(1):1–14.

Hibiya, Y., Iizuka, T., Yamashita, K., Yoneda, S., and Yamakawa, A. (2019). Sequential Chemical Separation of Cr and Ti from a Single Digest for High-Precision Isotope Measurements of Planetary Materials. *Geostandards and Geoanalytical Research*, 43(1):133–145.

Horányi, M., Morfill, G., Goertz, C., and Levy, E. (1995). Chondrule Formation in Lightning Discharges. *Icarus*, 114(1):174–185.

Hubbard, A. (2016). Partioning tungsten between matrix precursors and chondrule precusors through relative settling. *The Astrophysical Journal*, 826(2):151.

Huss, G. R. and Lewis, R. S. (1995). Presolar diamond, SiC, and graphite in primitive chondrites: Abundances as a function of meteorite class and petrologic type. *Geochimica et Cosmochimica Acta*, 59(1):115–160.

Isa, J., Rubin, A. E., and Wasson, J. T. (2014). R-chondrite bulk-chemical compositions and diverse oxides: Implications for parent-body processes. *Geochimica et Cosmochimica Acta*, 124:131–151.

Jacquet, E., Alard, O., and Gounelle, M. (2015). Trace element geochemistry of ordinary chondrite chondrules: The type I/type II chondrule dichotomy. *Geochimica et Cosmochimica Acta*, 155:47–67.

Jacquet, E., Paulhiac-Pison, M., Alard, O., Kearsley, A. T., and Gounelle, M. (2013). Trace element geochemistry of CR chondrite metal. *Meteoritics & Planetary Science*, 48(10):1981–1999.

Javoy, M. (1995). The integral enstatite chondrite model of the Earth. *Geophysical Research Letters*, 22(16):2219–2222.

Jilly-Rehak, C. E., Huss, G. R., and Nagashima, K. (2017). 53 Mn– 53 Cr radiometric dating of secondary carbonates in CR chondrites: Timescales for parent body aqueous alteration. *Geochimica et Cosmochimica Acta*, 201:224–244.

Johansen, A., Ronnet, T., Bizzarro, M., Schiller, M., Lambrechts, M., Nordlund, Å., and Lammer, H. (2021). A pebble accretion model for the formation of the terrestrial planets in the Solar System. *Science Advances*, 7(8):eabc0444.

Johansen, A., Ronnet, T., Schiller, M., Deng, Z., and Bizzarro, M. (2023). Anatomy of rocky planets formed by rapid pebble accretion: II. Differentiation by accretion energy and thermal blanketing. *Astronomy & Astrophysics*, 671:A75.

Johnson, B. C., Minton, D. A., Melosh, H. J., and Zuber, M. T. (2015). Impact jetting as the origin of chondrules. *Nature*, 517(7534):339–341.

Kallemeyn, G. W., Rubin, A. E., and Wasson, J. T. (1996). The compositional classification of chondrites: VII. The R chondrite group. *Geochimica et Cosmochimica Acta*, 60(12):2243–2256.

King, A., Schofield, P., Howard, K., and Russell, S. (2015a). Modal mineralogy of CI and CI-like chondrites by X-ray diffraction. *Geochimica et Cosmochimica Acta*, 165:148–160.

King, A., Solomon, J., Schofield, P., and Russell, S. (2015b). Characterising the CI and CI-like carbonaceous chondrites using thermogravimetric analysis and infrared spectroscopy. *Earth, Planets and Space*, 67.

Kleine, T., Budde, G., Burkhardt, C., Kruijer, T., Worsham, E., Morbidelli, A., and Nimmo, F. (2020). The Non-carbonaceous–Carbonaceous Meteorite Dichotomy. *Space Science Reviews*, 216.

Krietsch, D., Busemann, H., Riebe, M. E., King, A. J., M.O'D. Alexander, C., and Maden, C. (2021). Noble gases in CM carbonaceous chondrites: Effect of parent body aqueous and thermal alteration and cosmic ray exposure ages. *Geochimica et Cosmochimica Acta*, page S0016703721003318.

Krot, A., Keil, K., Scott, E., Goodrich, C., and Weisberg, M. (2014). Classification of Meteorites and Their Genetic Relationships. In *Treatise on Geochemistry*, pages 1–63. Elsevier.

Krot, A. N., Nagashima, K., Lyons, J. R., Lee, J.-E., and Bizzarro, M. (2020). Oxygen isotopic heterogeneity in the early Solar System inherited from the protosolar molecular cloud. *Science Advances*, 6(42):eaay2724.

Kruijer, T., Kleine, T., and Borg, L. (2020). The great isotopic dichotomy of the early Solar System. *Nature Astronomy*, 4:32–40.

Kruijer, T. S., Burkhardt, C., Budde, G., and Kleine, T. (2017). Age of Jupiter inferred from the distinct genetics and formation times of meteorites. *Proceedings of the National Academy of Sciences*, page 201704461.

Lambrechts, M., Morbidelli, A., Jacobson, S. A., Johansen, A., Bitsch, B., Izidoro, A., and Raymond, S. N. (2019). Formation of planetary systems by pebble accretion and migration: How the radial pebble flux determines a terrestrial-planet or super-Earth growth mode. *Astronomy & Astrophysics*, 627:A83.

Larsen, K., Wielandt, D., Schiller, M., and Bizzarro, M. (2016). Chromatographic speciation of Cr(III)-species, inter-species equilibrium isotope fractionation and improved chemical purification strategies for high-precision isotope analysis. *Journal of Chromatography A*, 1443:162–174.

Larsen, K. K., Trinquier, A., Paton, C., Schiller, M., Wielandt, D., Ivanova, M. A., Connelly, J. N., Nordlund, Å., Krot, A. N., and Bizzarro, M. (2011). Evidence for magnesium isotope heterogeneity in the solar protoplanetary disk. *The Astrophysical Journal*, 735(2):L37.

Leshin, L. A., Rubin, A. E., and McKeegan, K. D. (1997). The oxygen isotopic composition of olivine and pyroxene from CI chondrites. *Geochimica et Cosmochimica Acta*, 61(4):835–845.

Levison, H. F., Kretke, K. A., and Duncan, M. J. (2015). Growing the gas-giant planets by the gradual accumulation of pebbles. *Nature*, 524(7565):322–324.

Lewis, R. S., Ming, T., Wacker, J. F., Anders, E., and Steel, E. (1987). Interstellar diamonds in meteorites. *Nature*, 326(6109):160–162.

Lichtenberg, T., Dra?żkowska, J., Schönbächler, M., Golabek, G. J., and Hands, T. O. (2021). Bifurcation of planetary building blocks during Solar System formation. *Science*, 371(6527):365–370.

Lichtenberg, T., Golabek, G. J., Dullemond, C. P., Schönbächler, M., Gerya, T. V., and Meyer, M. R. (2018). Impact splash chondrule formation during planetesimal recycling. *Icarus*, 302:27–43.

Lodders, K. (2003). Solar System Abundances and Condensation Temperatures of the Elements. *The Astrophysical Journal*, 591(2):1220–1247.

Mahan, B., Moynier, F., Beck, P., Pringle, E. A., and Siebert, J. (2018). A history of violence: Insights into post-accretionary heating in carbonaceous chondrites from volatile element abundances, Zn isotopes and water contents. *Geochimica et Cosmochimica Acta*, 220:19–35.

Marrocchi, Y., Avice, G., and Barrat, J.-A. (2021a). The Tarda Meteorite: A Window into the Formation of D-type Asteroids. *The Astrophysical Journal Letters*, 913(1):L9.

Marrocchi, Y., Bekaert, D., and Piani, L. (2018). Origin and abundance of water in carbonaceous asteroids. *Earth and Planetary Science Letters*, 482:23–32.

Marrocchi, Y., Bonal, L., Gattacceca, J., Piani, L., Beck, P., Greenwood, R., Eschrig, J., Basque, A., Nuccio, P. M., and Martin, F. F. (2020). The Piancaldoli meteorite: A forgotten primitive LL3.10 ordinary chondrite. *Meteoritics & Planetary Science*, 55(8):maps.13552.

Marrocchi, Y., Delbo, M., Gounelle, M., and Timothy Jull, A. J. (2021b). The astrophysical context of collision processes in meteorites. *Meteoritics & Planetary Science*, 56(7):1406–1421.

Marrocchi, Y., Longeau, A., Goupil, R. L., Dijon, V., Pinto, G., Neukampf, J., Villeneuve, J., and Jacquet, E. (2024). Isotopic evolution of the inner solar system revealed by size-dependent oxygen isotopic variations in chondrules. *Geochimica et Cosmochimica Acta*, 371:52–64.

Marrocchi, Y., Piralla, M., Regnault, M., Batanova, V., Villeneuve, J., and Jacquet, E. (2022). Isotopic evidence for two chondrule generations in CR chondrites and their relationships to other carbonaceous chondrites. *Earth and Planetary Science Letters*, 593:117683.

Marrocchi, Y., Piralla, M., and Tissot, F. L. H. (2023). Iron Isotope Constraints on the Structure of the Early Solar System. *The Astrophysical Journal Letters*, 954(1):L27.

Marti, K., Fischer-Gödde, M., and Proksche, C. (2023). Meteoritic Molybdenum and Ruthenium Isotopic Abundances Document Nucleosynthetic p-process Components. *The Astrophysical Journal*, 956(1):7.

Martins, R., Kuthning, S., Coles, B. J., Kreissig, K., and Rehkämper, M. (2023). Nucleosynthetic isotope anomalies of zinc in meteorites constrain the origin of Earth's volatiles. *Science*, 379(6630):369–372.

Mayer, B., Wittig, N., Humayun, M., and Leya, I. (2015). Palladium isotopic evidence for nucelosynthetic and cosmogenic isotope anomalies in IVB iron meteorites. *The Astrophysical Journal*, 809(2):180.

McCord, T. B., Adams, J. B., and Johnson, T. V. (1970). Asteroid Vesta: Spectral Reflectivity and Compositional Implications. *Science*, 168(3938):1445–1447.

McDonough, W. and Sun, S.-s. (1995). The composition of the Earth. *Chemical Geology*, 120(3-4):223–253.

Meech, K. and Raymond, S. N. (2019). Origin of Earth's water: sources and constraints. Publisher: arXiv Version Number: 1.

Miller, K., Lauretta, D., Connolly, H., Berger, E., Nagashima, K., and Domanik, K. (2017). Formation of unequilibrated R chondrite chondrules and opaque phases. *Geochimica et Cosmochimica Acta*, 209:24–50.

Morbidelli, A., Baillié, K., Batygin, K., Charnoz, S., Guillot, T., Rubie, D. C., and Kleine, T. (2021). Contemporary formation of early Solar System planetesimals at two distinct radial locations. *Nature Astronomy*, 6(1):72–79.

Morbidelli, A., Kleine, T., and Nimmo, F. (2025). Did the terrestrial planets of the solar system form by pebble accretion? *Earth and Planetary Science Letters*, 650:119120.

Morbidelli, A., Marrocchi, Y., Ali Ahmad, A., Bhandare, A., Charnoz, S., Commerçon, B., Dullemond, C. P., Guillot, T., Hennebelle, P., Lee, Y.-N., Lovascio, F., Marschall, R., Marty, B., Maury, A., and Tamami, O. (2024). Formation and evolution of a protoplanetary disk: Combining observations, simulations, and cosmochemical constraints. *Astronomy & Astrophysics*, 691:A147.

Morris, M. A., Weidenschilling, S. J., and Desch, S. J. (2016). The effect of multiple particle sizes on cooling rates of chondrules produced in large-scale shocks in the solar nebula. *Meteoritics & Planetary Science*, 51(5):870–883.

Morton, E. M., Pickard, H., Wombacher, F., Huang, Y., Palk, E., Martins, R., Kuthning, S., Schönbächler, M., and Rehkämper, M. (2024). Volatile Element Depletion of Carbonaceous Chondrites—Insights from Mass-dependent Zinc, Cadmium, and Tellurium Isotope Variations. *The Astrophysical Journal*, 977(1):53.

Nanne, J. A., Nimmo, F., Cuzzi, J. N., and Kleine, T. (2019). Origin of the non-carbonaceous–carbonaceous meteorite dichotomy. *Earth and Planetary Science Letters*, 511:44–54.

Nesvorný, D., Roig, F. V., and Deienno, R. (2021). The Role of Early Giant-planet Instability in Terrestrial Planet Formation. *The Astronomical Journal*, 161(2):50.

Noronha, B. A. and Friedrich, J. M. (2014). Chemical compositions and classifica tion of five thermally altered carbonaceous chondrites. *Meteoritics & Planetary Science*, 49(8):1494–1504.

Olsen, M. B., Wielandt, D., Schiller, M., Van Kooten, E. M., and Bizzarro, M. (2016). Magnesium and 54Cr isotope compositions of carbonaceous chondrite chondrules – Insights into early disk processes. *Geochimica et Cosmochimica Acta*, 191:118–138.

Onyett, I. J., Schiller, M., Makhatadze, G. V., Deng, Z., Johansen, A., and Biz-

zarro, M. (2023). Silicon isotope constraints on terrestrial planet accretion. *Nature*, 619(7970):539–544.

Palme, H., Lodders, K., and Jones, A. (2014). Solar System Abundances of the Elements. In *Treatise on Geochemistry*, pages 15–36. Elsevier.

Palme, H. and Zipfel, J. (2022). The composition of CI chondrites and their contents of chlorine and bromine: Results from instrumental neutron activation analysis. *Meteoritics & Planetary Science*, 57(2):317–333.

Pape, J., Mezger, K., Bouvier, A.-S., and Baumgartner, L. (2019). Time and duration of chondrule formation: Constraints from 26Al-26Mg ages of individual chondrules. *Geochimica et Cosmochimica Acta*, 244:416–436.

Patzer, A., Bullock, E. S., and Alexander, C. M. O. (2021). Testing models for the compositions of chondrites and their components: I. CO chondrites. *Geochimica et Cosmochimica Acta*, 304:119–140.

Pedersen, S. G., Schiller, M., Connelly, J. N., and Bizzarro, M. (2019). Testing accretion mechanisms of the H chondrite parent body utilizing nucleosynthetic anomalies. *Meteoritics & Planetary Science*, 54(6):1215–1227.

Peters, S. T., Münker, C., Pfeifer, M., Elfers, B.-M., and Sprung, P. (2017). Distribution of p-process 174 Hf in early solar system materials and the origin of nucleosynthetic Hf and W isotope anomalies in Ca–Al rich inclusions. *Earth and Planetary Science Letters*, 459:70–79.

Petitat, M., Birck, J.-L., Luu, T. H., and Gounelle, M. (2011). The chromium isotopic composition of the ungrouped carbonaceous chondrite Tagish Lake. *The Astrophysical Journal*, 736(1):23.

Piani, L., Marrocchi, Y., Rigaudier, T., Vacher, L. G., Thomassin, D., and Marty, B. (2020). Earth's water may have been inherited from material similar to enstatite chondrite meteorites. *Science*, 369(6507):1110–1113.

Pinto, G. A., Jacquet, E., Corgne, A., Olivares, F., Villeneuve, J., and Marrocchi, Y. (2024). Deciphering recycling processes during solar system evolution from magnesium-rich relict olivine grains in type II chondrules. *Geochimica et Cosmochimica Acta*, 364:65–78.

Pinto, G. A., Marrocchi, Y., Jacquet, E., and Olivares, F. (2022). Formation of chondrule fine-grained rims from local nebular reservoirs. *Meteoritics & Planetary Science*, 57(5):1004–1017.

Piralla, M., Villeneuve, J., Batanova, V., Jacquet, E., and Marrocchi, Y. (2021). Conditions of chondrule formation in ordinary chondrites. *Geochimica et Cosmochimica Acta*, 313:295–312.

Piralla, M., Villeneuve, J., Schnuriger, N., Bekaert, D. V., and Marrocchi, Y. (2023). A unified chronology of dust formation in the early solar system. *Icarus*, 394:115427.

Qin, L., Alexander, C. M., Carlson, R. W., Horan, M. F., and Yokoyama, T. (2010). Contributors to chromium isotope variation of meteorites. *Geochimica et Cosmochimica Acta*, 74(3):1122–1145.

Qin, L. and Carlson, R. W. (2016). Nucleosynthetic isotope anomalies and their cosmochemical significance. *Geochemical Journal*, 50(1):43–65.

Qin, L., Nittler, L., Alexander, C., Wang, J., Stadermann, F., and Carlson, R. (2011). Extreme 54Cr-rich nano-oxides in the CI chondrite Orgueil – Implication for a late supernova injection into the solar system. *Geochimica et Cosmochimica Acta*, 75(2):629–644.

Raymond, S. N. and Izidoro, A. (2017). Origin of water in the inner Solar System: Planetesimals scattered inward during Jupiter and Saturn's rapid gas accretion. *Icarus*, 297:134–148.

Raymond, S. N. and Morbidelli, A. (2022). Planet Formation: Key Mechanisms and Global Models. In Biazzo, K., Bozza, V., Mancini, L., and Sozzetti, A., editors, *Demographics of Exoplanetary Systems*, volume 466, pages 3–82. Springer International Publishing, Cham. Series Title: Astrophysics and Space Science Library.

Regnault, M., Marrocchi, Y., Piralla, M., Villeneuve, J., Batanova, V., Schnuriger, N., and Jacquet, E. (2022). Oxygen isotope systematics of chondrules in Rumuruti chondrites: Formation conditions and genetic link with ordinary chondrites. *Meteoritics & Planetary Science*, 57(1):122–135.

Render, J., Brennecka, G. A., Burkhardt, C., and Kleine, T. (2022). Solar System evolution and terrestrial planet accretion determined by Zr isotopic signatures of meteorites. *Earth and Planetary Science Letters*, 595:117748.

Render, J., Brennecka, G. A., Wang, S.-J., Wasylenki, L. E., and Kleine, T. (2018). A Distinct Nucleosynthetic Heritage for Early Solar System Solids Recorded by Ni Isotope Signatures. *The Astrophysical Journal*, 862(1):26.

Reynolds, J. H. and Turner, G. (1964). Rare gases in the chondrite Renazzo. *Journal of Geophysical Research*, 69(15):3263–3281.

Rubin, A., Trigo-Rodríguez, J., Huber, H., and Wasson, J. (2007). Progressive aqueous alteration of CM carbonaceous chondrites. *Geochimica et Cosmochimica Acta*, 71:2361–2382.

Rubin, A. E. (2000). Petrologic, geochemical and experimental constraints on models of chondrule formation. *Earth-Science Reviews*, 50(1-2):3–27.

Rubin, A. E. (2010). Physical properties of chondrules in different chondrite groups: Implications for multiple melting events in dusty environments. *Geochimica et Cosmochimica Acta*, 74(16):4807–4828.

Rubin, A. E., Dunn, T. L., Garner, K., Cecchi, M., and Hernandez, M. (2024). Barred olivine chondrules in ordinary chondrites: Constraints on chondrule formation. *Meteoritics & Planetary Science*, 59(4):670–684.

Rubin, A. E. and Pernicka, E. (1989). Chondrules in the Sharps H3 chondrite: Evidence for intergroup compositional differences among ordinary chondrite chondrules. *Geochimica et Cosmochimica Acta*, 53(1):187–195.

Rubin, A. E. and Wasson, J. T. (1986). Chondrules in the Murray CM2 meteorite and compositional differences between CM-CO and ordinary chondrite chondrules. *Geochimica et Cosmochimica Acta*, 50(2):307–315.

Rubin, A. E. and Wasson, J. T. (1987). Chondrules, matrix and coarse-grained chondrule rims in the Allende meteorite: Origin, interrelationships and possible precursor components. *Geochimica et Cosmochimica Acta*, 51(7):1923–1937.

Rüfenacht, M., Morino, P., Lai, Y.-J., Fehr, M. A., Haba, M. K., and Schönbächler, M. (2023). Genetic relationships of solar system bodies based on their nucleosynthetic Ti isotope compositions and sub-structures of the solar protoplanetary disk. *Geochimica et Cosmochimica Acta*, 355:110–125.

Sanders, I. S. and Scott, E. R. D. (2022). Complementary nucleosynthetic isotope anomalies of Mo and W in chondrules and matrix in the Allende carbonaceous chondrite: The case for hydrothermal metamorphism and its implications. *Meteoritics & Planetary Science*, 57(2):450–471.

Savage, P. S., Moynier, F., and Boyet, M. (2022). Zinc isotope anomalies in primitive meteorites identify the outer solar system as an important source of Earth's volatile inventory. *Icarus*, 386:115172.

Schiller, M., Bizzarro, M., and Fernandes, V. A. (2018). Isotopic evolution of the protoplanetary disk and the building blocks of Earth and the Moon. *Nature*, 555(7697):507–510.

Schiller, M., Bizzarro, M., and Siebert, J. (2020). Iron isotope evidence for very rapid accretion and differentiation of the proto-Earth. *Science Advances*, 6(7):eaay7604.

Schneider, J. M., Burkhardt, C., Marrocchi, Y., Brennecka, G. A., and Kleine, T. (2020). Early evolution of the solar accretion disk inferred from Cr-Ti-O isotopes in individual chondrules. *Earth and Planetary Science Letters*, 551:116585.

Schrader, D. and Davidson, J. (2017). CM and CO chondrites: A common parent body or asteroidal neighbors? Insights from chondrule silicates. *Geochimica et Cosmochimica Acta*, 214:157–171.

Schrader, D., Davidson, J., Zega, T., Russell, S., and McCoy, T. (2020a). The Fe/S Ratio of Pyrrhotite in Carbonaceous Chondrites Relevant to Bennu and Ryugu: An Indicator of Parent Asteroid Aqueous and Thermal Alteration. *51st Lunar and Planetary Science Conference*.

Schrader, D. L., Cloutis, E. A., Applin, D. M., Davidson, J., Torrano, Z. A., Foustoukos, D., Alexander, C. M. O., Domanik, K. J., Matsuoka, M., Nakamura, T., Zega, T. J., Brennecka, G. A., and Render, J. (2024a). Tarda and Tagish Lake: Samples from the same outer Solar System asteroid and implications for D- and P-type asteroids. *Geochimica et Cosmochimica Acta*, 380:48–70.

Schrader, D. L., Connolly, H. C., and Lauretta, D. S. (2008). Opaque phases in type-II chondrules from CR2 chondrites: Implications for CR parent body formation. *Geochimica et Cosmochimica Acta*, 72(24):6124–6140.

Schrader, D. L., Connolly, H. C., Lauretta, D. S., Nagashima, K., Huss, G. R., Davidson, J., and Domanik, K. J. (2013). The formation and alteration of the Renazzo-like carbonaceous chondrites II: Linking O-isotope composition and oxidation state of chondrule olivine. *Geochimica et Cosmochimica Acta*, 101:302–327.

Schrader, D. L., Connolly, H. C., Lauretta, D. S., Zega, T. J., Davidson, J., and Domanik, K. J. (2015). The formation and alteration of the Renazzo-like carbonaceous chondrites

III: Toward understanding the genesis of ferromagnesian chondrules. *Meteoritics & Planetary Science*, 50(1):15–50.

Schrader, D. L., Franchi, I. A., Connolly, H. C., Greenwood, R. C., Lauretta, D. S., and Gibson, J. M. (2011). The formation and alteration of the Renazzo-like carbonaceous chondrites I: Implications of bulk-oxygen isotopic composition. *Geochimica et Cosmochimica Acta*, 75(1):308–325.

Schrader, D. L., Fu, R. R., Desch, S. J., and Davidson, J. (2018a). The background temperature of the protoplanetary disk within the first four million years of the Solar System. *Earth and Planetary Science Letters*, 504:30–37.

Schrader, D. L., Nagashima, K., Davidson, J., McCoy, T. J., Ogliore, R. C., and Fu, R. R. (2020b). Outward migration of chondrule fragments in the early Solar System: O-isotopic evidence for rocky material crossing the Jupiter Gap? *Geochimica et Cosmochimica Acta*, 282:133–155.

Schrader, D. L., Nagashima, K., Krot, A. N., Ogliore, R. C., Yin, Q.-Z., Amelin, Y., Stirling, C. H., and Kaltenbach, A. (2017). Distribution of 26Al in the CR chondrite chondrule-forming region of the protoplanetary disk. *Geochimica et Cosmochimica Acta*, 201:275–302.

Schrader, D. L., Nagashima, K., Waitukaitis, S. R., Davidson, J., McCoy, T. J., Connolly, H. C., and Lauretta, D. S. (2018b). The retention of dust in protoplanetary disks: Evidence from agglomeratic olivine chondrules from the outer Solar System. *Geochimica et Cosmochimica Acta*, 223:405–421.

Schrader, D. L., Torrano, Z. A., Foustoukos, D. I., Alexander, C. M., Render, J., and Brennecka, G. A. (2024b). Reassessing the proposed "CY chondrites": Evidence for multiple meteorite types and parent bodies from Cr-Ti-H-C-N isotopes and bulk elemental compositions. *Geochimica et Cosmochimica Acta*, page S0016703724006604.

Scott, E. and Krot, A. (2004). Chondrites and Their Components. In Holland, H. D. and Turekian, K. K., editors, *Treatise on geochemistry*. Elsevier/Pergamon, Amsterdam ; Boston, 1st ed edition.

Shukolyukov, A. and Lugmair, G. (2006). Manganese–chromium isotope systematics of carbonaceous chondrites. *Earth and Planetary Science Letters*, 250(1-2):200–213.

Steele, R. C., Elliott, T., Coath, C. D., and Regelous, M. (2011). Confirmation of mass-independent Ni isotopic variability in iron meteorites. *Geochimica et Cosmochimica Acta*, 75(24):7906–7925.

Steller, T., Burkhardt, C., Yang, C., and Kleine, T. (2022). Nucleosynthetic zinc isotope anomalies reveal a dual origin of terrestrial volatiles. *Icarus*, 386:115171.

Stracke, A., Palme, H., Gellissen, M., Münker, C., Kleine, T., Birbaum, K., Günther, D., Bourdon, B., and Zipfel, J. (2012). Refractory element fractionation in the Allende meteorite: Implications for solar nebula condensation and the chondritic composition of planetary bodies. *Geochimica et Cosmochimica Acta*, 85:114–141.

Sugiura, N. and Fujiya, W. (2014). Correlated accretion ages and ε ^{54} Cr of meteorite parent bodies and the evolution of the solar nebula. *Meteoritics & Planetary Science*, 49(5):772–787.

Suttle, M., King, A., Schofield, P., Bates, H., and Russell, S. (2021). The aqueous alteration of CM chondrites, a review. *Geochimica et Cosmochimica Acta*.

Tenner, T. J., Nakashima, D., Ushikubo, T., Kita, N. T., and Weisberg, M. K. (2015). Oxygen isotope ratios of FeO-poor chondrules in CR3 chondrites: Influence of dust enrichment and H2O during chondrule formation. *Geochimica et Cosmochimica Acta*, 148:228–250.

Tenner, T. J., Nakashima, D., Ushikubo, T., Tomioka, N., Kimura, M., Weisberg, M. K., and Kita, N. T. (2019). Extended chondrule formation intervals in distinct physicochemical environments: Evidence from Al-Mg isotope systematics of CR chondrite chondrules with unaltered plagioclase. *Geochimica et Cosmochimica Acta*, 260:133–160.

Tenner, T. J., Ushikubo, T., Kurahashi, E., Kita, N. T., and Nagahara, H. (2013). Oxygen isotope systematics of chondrule phenocrysts from the CO3.0 chondrite Yamato 81020: Evidence for two distinct oxygen isotope reservoirs. *Geochimica et Cosmochimica Acta*, 102:226–245.

Tenner, T. J., Ushikubo, T., Nakashima, D., Schrader, D. L., Weisberg, M. K., Kimura, M., and Kita, N. T. (2018). Oxygen Isotope Characteristics of Chondrules from Recent Studies by Secondary Ion Mass Spectrometry. In Russell, S. S., Connolly Jr., H. C., and Krot, A. N., editors, *Chondrules*, pages 196–246. Cambridge University Press, 1 edition.

Torrano, Z. A., Alexander, C. M., Carlson, R. W., Render, J., Brennecka, G. A., and Bullock, E. S. (2024). A common isotopic reservoir for amoeboid olivine aggregates (AOAs) and calcium-aluminum-rich inclusions (CAIs) revealed by Ti and Cr isotopic compositions. *Earth and Planetary Science Letters*, 627:118551.

Torrano, Z. A., Schrader, D. L., Davidson, J., Greenwood, R. C., Dunlap, D. R., and Wadhwa, M. (2021). The relationship between CM and CO chondrites: Insights from combined analyses of titanium, chromium, and oxygen isotopes in CM, CO, and ungrouped chondrites. *Geochimica et Cosmochimica Acta*, 301:70–90.

Trinquier, A., Birck, J.-L., and Allegre, C. J. (2007). Widespread 54Cr Heterogeneity in the Inner Solar System. *The Astrophysical Journal*, 655(2):1179–1185.

Trinquier, A., Birck, J.-L., and Allègre, C. J. (2008). High-precision analysis of chromium isotopes in terrestrial and meteorite samples by thermal ionization mass spectrometry. *Journal of Analytical Atomic Spectrometry*, 23(12):1565.

Trinquier, A., Birck, J.-L., and Jean Allègre, C. (2006). The nature of the KT impactor. A 54Cr reappraisal. *Earth and Planetary Science Letters*, 241(3-4):780–788.

Trinquier, A., Elliott, T., Ulfbeck, D., Coath, C., Krot, A. N., and Bizzarro, M. (2009). Origin of Nucleosynthetic Isotope Heterogeneity in the Solar Protoplanetary Disk. *Science*, 324(5925):374–376.

Van Clepper, E. and Ciesla, F. J. (2023). Tracking trajectories of solids in a sculpted disk. *86st Annual Meeting of The Meteoritical Society*.

van Kooten, E., Cavalcante, L., Wielandt, D., and Bizzarro, M. (2020). The role of Bells in the continuous accretion between the CM and CR chondrite reservoirs. *Meteoritics & Planetary Science*, 55(3):575–590.

van Kooten, E. and Moynier, F. (2019). Zinc isotope analyses of singularly small samples

(<5 ng Zn): Investigating chondrule-matrix complementarity in Leoville. *Geochimica et Cosmochimica Acta*, 261:248–268.

van Kooten, E., Schiller, M., Moynier, F., Johansen, A., Haugbølle, T., and Bizzarro, M. (2021). Hybrid Accretion of Carbonaceous Chondrites by Radial Transport across the Jupiter Barrier. *The Astrophysical Journal*, 910(1):70.

van Kooten, E., Zhao, X., Franchi, I., Tung, P.-Y., Fairclough, S., Walmsley, J., Onyett, I., Schiller, M., and Bizzarro, M. (2024). The nucleosynthetic fingerprint of the outermost protoplanetary disk and early Solar System dynamics. *Science Advances*, 10(24):eadp1613.

van Kooten, E. M., Schiller, M., and Bizzarro, M. (2017). Magnesium and chromium isotope evidence for initial melting by radioactive decay of 26Al and late stage impact-melting of the ureilite parent body. *Geochimica et Cosmochimica Acta*, 208:1–23.

van Kooten, E. M. M. E., Moynier, F., and Agranier, A. (2019). A unifying model for the accretion of chondrules and matrix. *Proceedings of the National Academy of Sciences*, 116(38):18860–18866.

van Kooten, E. M. M. E., Wielandt, D., Schiller, M., Nagashima, K., Thomen, A., Larsen, K. K., Olsen, M. B., Nordlund, Å., Krot, A. N., and Bizzarro, M. (2016). Isotopic evidence for primordial molecular cloud material in metal-rich carbonaceous chondrites. *Proceedings of the National Academy of Sciences*, 113(8):2011–2016.

Van Schmus, W. and Wood, J. (1967). A chemical-petrologic classification for the chondritic meteorites. *Geochimica et Cosmochimica Acta*, 81:747–765.

Varela, M. E., Sylvester, P., Engler, A., and Kurat, G. (2012). Nonporphyritic chondrules from equilibrated Rumuruti and ordinary chondrites: Chemical evidence of secondary processing: Nonporphyritic chondrules. *Meteoritics & Planetary Science*, 47(10):1537–1557.

Warren, P. H. (2011). Stable-isotopic anomalies and the accretionary assemblage of the Earth and Mars: A subordinate role for carbonaceous chondrites. *Earth and Planetary Science Letters*, 311(1-2):93–100.

Wasson, J. and Kallemeyn, G. W. (1988). Compositions of chondrites. *Philosophical Transactions of the Royal Society of London. Series A, Mathematical and Physical Sciences*, 325(1587):535–544.

Wasson, J. T. and Rubin, A. E. (2009). Composition of matrix in the CR chondrite LAP 02342. *Geochimica et Cosmochimica Acta*, 73(5):1436–1460.

Weisberg, M., McCoy, T., and Krot, A. (2006). Systematics and Evaluation of Meteorite Classification. In *Meteorites and the Early Solar System II*, pages 19–52.

Weisberg, M. K., Kita, N. T., Fukuda, K., Siron, G., and Ebel, D. S. (2021). Micro-distribution of oxygen isotopes in unequilibrated enstatite chondrites. *Geochimica et Cosmochimica Acta*, 300:279–295.

Weisberg, M. K., Prinz, M., Clayton, R. N., Mayeda, T. K., Grady, M. M., Franchi, I., Pillinger, C. T., and Kallemeyn, G. W. (1996). The K (Kakangari) chondrite grouplet. *Geochimica et Cosmochimica Acta*, 60(21):4253–4263.

Weisberg, M. K., Prinz, M., Kojima, H., Yanai, K., Clayton, R. N., and Mayeda, T. K. (1991). The Carlisle Lakes-type chondrites: A new grouplet with high δ17O and evidence for nebular oxidation. *Geochimica et Cosmochimica Acta*, 55(9):2657–2669.

Williams, C. D., Sanborn, M. E., Defouilloy, C., Yin, Q.-Z., Kita, N. T., Ebel, D. S., Yamakawa, A., and Yamashita, K. (2020). Chondrules reveal large-scale outward transport of inner Solar System materials in the protoplanetary disk. *Proceedings of the National Academy of Sciences*, 117(38):23426–23435.

Wölfer, E., Budde, G., and Kleine, T. (2023). Age and genetic relationships among CB, CH and CR chondrites. *Geochimica et Cosmochimica Acta*, 361:288–301.

Worsham, E. A., Burkhardt, C., Budde, G., Fischer-Gödde, M., Kruijer, T. S., and Kleine, T. (2019). Distinct evolution of the carbonaceous and non-carbonaceous reservoirs: Insights from Ru, Mo, and W isotopes. *Earth and Planetary Science Letters*, 521:103–112.

Yamakawa, A., Yamashita, K., Makishima, A., and Nakamura, E. (2009). Chemical Separation and Mass Spectrometry of Cr, Fe, Ni, Zn, and Cu in Terrestrial and Extraterrestrial Materials Using Thermal Ionization Mass Spectrometry. *Analytical Chemistry*, 81(23):9787–9794.

Yamakawa, A. and Yin, Q.-Z. (2014). Chromium isotopic systematics of the Sutter's Mill carbonaceous chondrite: Implications for isotopic heterogeneities of the early solar system. *Meteoritics & Planetary Science*, 49(11):2118–2127.

Yamashita, K., Maruyama, S., Yamakawa, A., and Nakamura, E. (2010). ^{53} Mn-^{53} Cr chronometry of CB chondrite: Evidence for the uniform disribution of ^{53} Mn in the early solar system. *The Astrophysical Journal*, 723(1):20–24.

Yang, L. and Ciesla, F. J. (2012). The effects of disk building on the distributions of refractory materials in the solar nebula. *Meteoritics & Planetary Science*, 47(1):99–119.

Yap, T. E. and Tissot, F. L. (2023). The NC-CC dichotomy explained by significant addition of CAI-like dust to the Bulk Molecular Cloud (BMC) composition. *Icarus*, 405:115680.

Yokoyama, T., Wadhwa, M., Iizuka, T., Rai, V., Gautam, I., Hibiya, Y., Masuda, Y., Haba, M. K., Fukai, R., Hines, R., Phelan, N., Abe, Y., Aléon, J., Alexander, C. M. O., Amari, S., Amelin, Y., Bajo, K.-i., Bizzarro, M., Bouvier, A., Carlson, R. W., Chaussidon, M., Choi, B.-G., Dauphas, N., Davis, A. M., Di Rocco, T., Fujiya, W., Hidaka, H., Homma, H., Hoppe, P., Huss, G. R., Ichida, K., Ireland, T., Ishikawa, A., Itoh, S., Kawasaki, N., Kita, N. T., Kitajima, K., Kleine, T., Komatani, S., Krot, A. N., Liu, M.-C., McKeegan, K. D., Morita, M., Motomura, K., Moynier, F., Nakai, I., Nagashima, K., Nguyen, A., Nittler, L., Onose, M., Pack, A., Park, C., Piani, L., Qin, L., Russell, S., Sakamoto, N., Schönbächler, M., Tafla, L., Tang, H., Terada, K., Terada, Y., Usui, T., Wada, S., Walker, R. J., Yamashita, K., Yin, Q.-Z., Yoneda, S., Young, E. D., Yui, H., Zhang, A.-C., Nakamura, T., Naraoka, H., Noguchi, T., Okazaki, R., Sakamoto, K., Yabuta, H., Abe, M., Miyazaki, A., Nakato, A., Nishimura, M., Okada, T., Yada, T., Yogata, K., Nakazawa, S., Saiki, T., Tanaka, S., Terui, F., Tsuda, Y., Watanabe, S.-i., Yoshikawa, M., Tachibana, S., and Yurimoto, H. (2023). Water circulation in Ryugu asteroid affected the distribution of nucleosynthetic isotope anomalies in returned sample. *Science Advances*, 9(45):eadi7048.

Youdin, A. N. and Goodman, J. (2005). Streaming Instabilities in Protoplanetary Disks. *The Astrophysical Journal*, 620(1):459–469.

Zhu, K., Liu, J., Moynier, F., Qin, L., Alexander, C. M. O., and He, Y. (2019a). Chromium Isotopic Evidence for an Early Formation of Chondrules from the Ornans CO Chondrite. *The Astrophysical Journal*, 873(1):82.

Zhu, K., Moynier, F., Alexander, C. M. O., Davidson, J., Schrader, D. L., Zhu, J.-M., Wu, G.-L., Schiller, M., Bizzarro, M., and Becker, H. (2021a). Chromium Stable Isotope Panorama of Chondrites and Implications for Earth Early Accretion. *The Astrophysical Journal*, 923(1):94.

Zhu, K., Moynier, F., Schiller, M., Alexander, C. M., Barrat, J.-A., Bischoff, A., and Bizzarro, M. (2021b). Mass-independent and mass-dependent Cr isotopic composition of the Rumuruti (R) chondrites: Implications for their origin and planet formation. *Geochimica et Cosmochimica Acta*, 293:598–609.

Zhu, K., Moynier, F., Schiller, M., Alexander, C. M., Davidson, J., Schrader, D. L., van Kooten, E., and Bizzarro, M. (2021c). Chromium isotopic insights into the origin of chondrite parent bodies and the early terrestrial volatile depletion. *Geochimica et Cosmochimica Acta*, 301:158–186.

Zhu, K., Moynier, F., Schiller, M., and Bizzarro, M. (2020). Dating and Tracing the Origin of Enstatite Chondrite Chondrules with Cr Isotopes. *The Astrophysical Journal Letters*, 894(2):L26.

Zhu, K., Schiller, M., Moynier, F., Groen, M., Alexander, C. M., Davidson, J., Schrader, D. L., Bischoff, A., and Bizzarro, M. (2023). Chondrite diversity revealed by chromium, calcium and magnesium isotopes. *Geochimica et Cosmochimica Acta*, 342:156–168.

Zhu, K., Sossi, P. A., Siebert, J., and Moynier, F. (2019b). Tracking the volatile and magmatic history of Vesta from chromium stable isotope variations in eucrite and diogenite meteorites. *Geochimica et Cosmochimica Acta*, 266:598–610.

Zinner, E. (2014). Presolar Grains. In *Treatise on Geochemistry*, pages 181–213. Elsevier.

Zinner, E., Ming, T., and Anders, E. (1987). Large isotopic anomalies of Si, C, N and noble gases in interstellar silicon carbide from the Murray meteorite. *Nature*, 330(6150):730–732.